The University of Nottingham

UNITED KINGDOM · CHINA · MALAYSIA

Reduction of torsional vibrations due to electromechanical interaction in aircraft systems

Constanza Ahumada Sanhueza

Thesis submitted to the University of Nottingham
for the degree of Doctor of Philosophy

May 2018

Abstract

With the growth of electrical power onboard aircraft, the interaction between the electrical systems and the engine will become significant. Moreover, since the drivetrain has a flexible shaft, higher load connections can excite torsional vibrations on the aircraft drivetrain. These vibrations can break the shaft if the torque induced is higher than the designed value, or reduce its lifespan if the excitation is constant. To avoid these problems, the electromechanical interaction between the electrical power system and the drivetrain must be evaluated. Past studies have identified the electromechanical interaction and introduced experimental setups that allow its study. However, strategies to reduce the excitation of the torsional vibrations have not been presented.

This thesis aims to analyse the electromechanical interaction in aircraft systems and develop an advanced electrical power management system (PMS) to mitigate its effects. The PMS introduces strategies based on the load timing requirements, which are built on the open loop Posicast compensator. The strategies referred as Single Level Multi-edge Switching Loads (SLME), Multilevel Loading (MLL), and Multi-load Single Level Multi-edge Switching Loads (MSLME) are applied to different loads, such as pulsating loads, ice protection system, and time-critical loads, such as the control surfaces.

The Posicast based strategies, eliminate the torsional vibrations after a switching event, by the addition of zeros that cancel the poles of the system. For this reason, the knowledge of the natural frequencies of the mechanical system is necessary. Experimentally, the system parameters are obtained through Fourier analysis of the step response and the strategies are applied. A robust analysis of the strategies allows the establishment of the range of uncertainty on the frequencies that allow the proper operation of the strategies. Simulation and experimental results show that the torsional vibrations can be reduced to values close to zero by the application of the strategy. Therefore, the PMS mitigates the electromechanical interaction between the electrical power system and the aircraft drivetrain.

Acknowledgements

First, I wish to thank my supervisor Prof Seamus Garvey for his continuous guidance and support during my PhD. The discussions with him allowed me to learn, get ideas, and enjoy the research. I would also like to thank my supervisors Prof Patrick Wheeler for giving me this opportunity and Dr Tao Yang for his advice during the thesis.

Also, I would like to thank Dr Ponggorn Kulsangcharoen for his guidance in the building of the experimental rig and Dr Michele Degano for offering the universal motor machine and its information.

Next, I wish to thank Prof Doris Sáez and Prof Roberto Cárdenas for encouraging me to pursue this PhD and for supporting me all this time. I wouldn't be here if you haven't been my supervisors during my master and taught me about control and research.

I would also like to thank my friends and colleagues in the University of Nottingham for the discussions and the fun. Chiara, Adrian, Luca, Savvas, Stefano, Sharmila, Matias, Tim, Lalo, ATC lunch breaks group, and so many others in the PEMC group, you have made this a wonderful experience.

As well, I wish to thank my parents for teaching me to think, to be independent, and to laugh about myself. A special thanks to Bea for challenging me and not wanting to play Barbies with me.

Finally, I wish to thank my partner Dr Luca Tarisciotti, for his infinite patience, for listening to me, complain and celebrate, and for believing in me even when I did not.

Contents

List of Figures

List of Tables

Acronyms

- MEA: More Electric Aircraft
- AEA: All Electric Aircraft
- EMD: Empirical Mode Decomposition
- SLME: Single Level Multi-edge Switching
- MLL: Multilevel Loading Switching
- MSLME: Multiload Single Level Multi-edge Switching
- FFT: Fast Fourier Transform
- ECS: Environmental Control System
- IPS: Ice Protection System
- FBW: Fly by Wire
- PBW: Power by Wire
- GCU: Generator Control Unit
- EMF: Electromotive Force
- PMS: Power Management System

Chapter 1

Introduction

1.1 Background

Civil air traffic has increased 9% each year since 1960, and it is expected to keep growing at a rate between 5 and 7% [1], [2]. Likewise, cargo traffic has grown at a mean value of 8.3% [3]. However, aircraft systems already produce 2% of the worlds CO_2 emissions [4], and with the ongoing rise in passengers, it is estimated that the emissions will be 3% by 2050. To decrease the effect on the environment, the Advisory Council for Aviation Research and Innovation in Europe (ACARE) has set the challenge of reducing by 2020 and 2050 the CO_2 emissions in 50% and 75% respectively, the NO_x in 80% in 90% respectively, and the noise in 50% and 65% respectively [4], [5]. To achieve these goals and reduce cost of air travel, fuel efficiency must be improved [3], [4], [6], [7].

To meet these requirements, the following approaches can be taken:

- Lighter aircraft: reduced weight and hence the fuel consumption.
- More aerodynamically shaped aircraft: reduced drag and hence the fuel consumption.
- Improved efficiency: reduce the wasteful use of energy sources.

Conventional aircraft have a mechanical, hydraulic, pneumatic and electric power system [8], which are described in detail in chapter 2. To obtain lighter aircraft and improve the efficiency, the All Electric Aircraft (AEA), in which the propulsion and auxiliary systems are electrical, and the More Electric Aircraft (MEA), in which only the auxiliary systems are electrical, are introduced [8]–[10]. Thus, there is no need for hydraulic and pneumatic systems. The use of an electrical system allows the elimination of expensive and cumbersome hydraulics. Consequently, the weight of the aircraft can be reduced, by up to 10% and the fuel consumption by 9% according to [11]. Moreover, the design, development, and testing costs are reduced, and advanced diagnostics methods are easier to apply. Overall, the efficiency increases and the maintenance decreases [12] [3], [6]–[8]. The MEA and its systems are described in chapter 2.

The first civilian aircraft using MEA technology appeared in 2000's with the Airbus A380 and Boeing B787. In them, the technology Power-by-Wire (PBW) was introduced. PBW replaces some or all of the hydraulic circuits with electric ones, increasing the electric loads up to 850kW and 1.4MW in each aircraft respectively [11], [13]. Figure 1.1 illustrates the electrical power system installed on Airbus and Boeing civil aircraft.

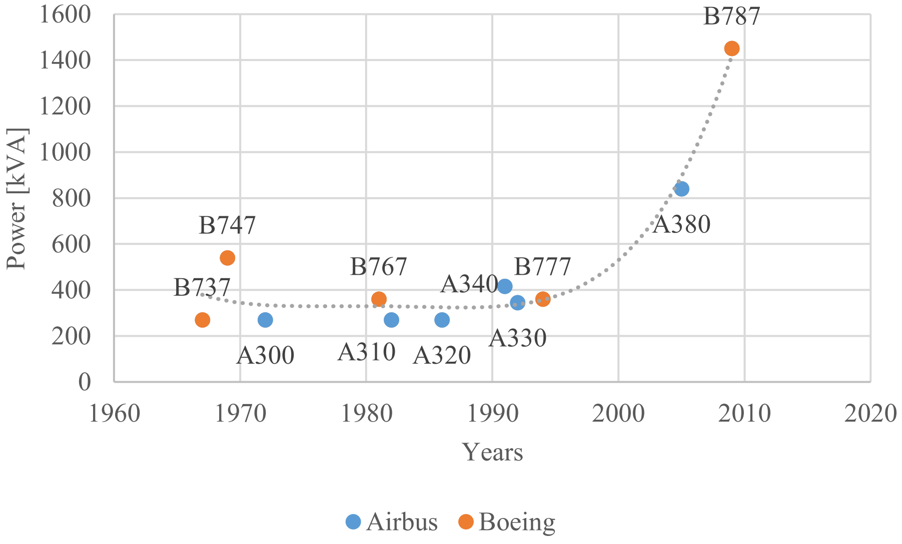

Figure 1.1: Increment of electric power system in civil aircraft (Data from [1], [14], [15]).

The more electric aircraft has introduced new electric loads, such as high-powered, transient (e.g. actuators), pulsating, or constant power (e.g. motor driven pumps), and power electronics [16]. Between the challenges of working with new electric load is the higher coupling between the electrical power system and the aircraft's drivetrain. As shown in Figure 1.2, the engine is connected to the generator through a drivetrain, and the generator is connected to the electrical power system of the aircraft. Since the generator shaft is flexible, the higher load connections may induce torsional vibrations. Moreover, each of these loads can affect the system differently, for example pulsating loads can produce resonances, and high power and transient loads can create torque peaks [17].

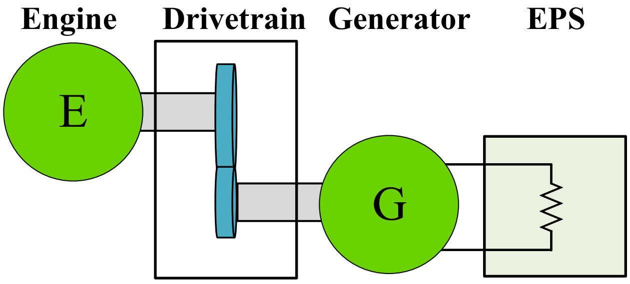

Figure 1.2: System diagram.

Since the study of electromechanical interaction in aircraft system is new, few studies on the topic have been presented. Most of the existing work is by T. Feehally in [18] and G. Moore in [19] and is focused on the modelling of the interaction. Therefore, to reduce the excitation of torsional vibrations by the connection of electrical loads, the solutions presented for the marine system, wind turbines, and traction systems, among other ground operation, are analysed in this thesis.

However, in most ground based systems, the weight and size are not usually significant constraints. Therefore, the solutions to mitigate the torsional vibrations consist of increasing the system damping (by the use of larger shafts) [20], [21], or by the use of observers that determinate the drive speeds that need to be avoided [21], [22]. Moreover, all the solutions that use controllers to diminish the vibrations are focused on slowing down the machine dynamics, instead of analysing the system [18], [21], [23], [24].

In this thesis strategies to suppress the excitation of torsional vibrations due to electromechanical interaction, which are centred on the management of the power system of an aircraft are proposed. The strategies presented are based on the load timing requirements, as shown in chapter 5.

1.2 Aims and Objectives

This thesis aims to analyse the electromechanical interaction in aircraft electrical power system and develop strategies to suppress the excitation of torsional vibrations. The specific objectives to achieve the aim are:

- Show the electromechanical interaction in an aircraft system, identifying the effects of different sources. Propose mitigation strategies for them.
- A theoretical understanding of the dynamic interaction between load connections and the system response. Understand the importance of the timing in the connection and introduced strategies based on it to minimise the effects of torque impacts.
- Develop a power management system (PMS) that minimises the drivetrain torsional vibrations produced by the connection of electrical loads with different characteristics and requirements.
- Build an experimental setup to test the electromechanical interaction and the strategies that suppress the excitation of torsional vibrations.

1.3 Contributions

The contributions of this thesis are:

- A study of the state of the art, which describes the current state of aircraft systems and electromechanical interaction, is presented.
- Different sources of electromechanical interaction in aircraft system are presented and analysed. Past studies have shown the effect of electrical load step connection. In this thesis, electrical load step and pulsating loads are analysed. Moreover, the effects of the Generator Control Unit (GCU) on the electromechanical interaction is shown.
- A strategy to supress the excitation of the drivetrain torsional vibrations centred on the electrical loads connected is developed. This strategy is based

on the Posicast compensator and the analysis of the electrical load switching.

- A PMS that can be applied to different electrical loads present in an aircraft is proposed. The PMS applies different switching strategies according to the electrical load being connected and hence eliminates the excitation of torsional vibrations.
- A reduced model to study the electromechanical interaction in aircraft systems is presented. In the past it has been shown that the mechanical system can be reduced to one with two natural frequencies. In this thesis, to that reduction is added that to study the electromechanical interaction, the electrical system can be represented by a DC system. This reduction allows the reduction of the experimental setup cost.
- A validation methodology for sensorless systems is proposed. This methodology allows the obtention of experimental results which are comparable with the theory.
- A sensibility analysis that shows the relationship between the strategies behaviour and the tuning accuracy is carried out.
- Finally, an improved method to apply the strategies to inductive loads, and which can be extended to capacitive loads is proposed.

1.4 Thesis Structure

The rest of the thesis is organised as follows:

In chapter 2 and chapter 3 the literature review is presented. Chapter 2 provides an overview of aircraft systems and its development. For this purpose, the evolution of aircraft from traditional models and to the adoption of More Electric Aircraft technology is analysed. The changes in power distribution technologies and the increase in the electrical system power is presented. Finally, a gas turbine and a typical drivetrain for aircraft systems are described.

In chapter 3 a review about electromechanical system interaction is presented. First, the reasons why torsional vibrations are excited in the mechanical drivetrain are presented including step and pulsating load connections, grid faults, sub-synchronous currents, and machine control systems. The effects of the torsional vibrations on the mechanical system are described, and the applications in which electromechanical interaction is found presented. Finally, the solutions traditionally used in the literature to mitigate the effects of the interaction are considered.

Chapter 4, introduces a functional model of the aircraft system used in this study. Using this model the stability of the system is analysed; the poles are identified, and the torsional vibrations modes are shown. Later, the electromechanical interaction is considerd. The cases of load connection (step and pulsating) and machine control systems are analysed. Techniques to minimise the effect of pulsating load connections and the machine control are presented.

In chapter 5, a PMS that eliminates the drivetrain torsional vibrations excited by the connection of electrical loads is described. The strategies used by the PMS are based on the Posicast method that suppresses vibrations using a compensator. This compensator introduces a series of step delays that depend on the frequency that is being cancelled. A detailed description of the method equations and its implementation are presented. Finally, strategies based on this approach are introduced and applied to some of the different electrical loads found in an aircraft, such as ailerons, ice protection systems, and a radar.

The experimental setup to test the effectiveness of the PMS strategies is described in chapter 6. The components used and the design torsional vibrations are presented. The theoretical vibrations models associated with each frequency are studied.

In chapter 7, the experimental results are presented. To test the Posicast strategies described in chapter 5, the torsional vibrations are identified using a combined method of Fourier analysis, Empirical Mode Decomposition (EMD) and Hilbert Transform. Moreover, the methods employed to measure the torque of the mechanical system are introduced. The results obtained by each method are compared. Finally, the electromechanical interaction due to the connection of resistive loads is shown, and the PMS is tested.

An analysis of the robustness of the Posicast based strategies is presented in chapter 8. In this chapter, improvements to the method are introduced. The effect of inductance on the machine is considered, and sensitivity is studied.

Finally, in chapter 9 the conclusions and summary of this thesis are presented. Also, further areas for future research are discussed.

Chapter 2

Aircraft Systems

2.1 Introduction

Since the beginning of aircraft systems, innovation has been its main characteristic. These changes have been transversal to every area of study: engines, airframes, controls, airline business models, materials, and electrical power system among others [25]. Now, the changes in aircraft technologies are centred on meeting the market needs, protecting the environment by reducing the emissions, and ensuring safety and security [4]. To decrease the effect on the environment, the FlightPath 2050 has set the target that the CO_2 emissions should reduce 50% by 2020, the NO_x and noise should reduce in 80%, and 50% respectively [4].

Steps towards a more efficient aircraft have been taken since the beginning of the aerospace history. The use of the pneumatic, hydraulic, mechanical, and electrical energies have been the main topic of discussion, as shown in the timeline in Figure 2.1.

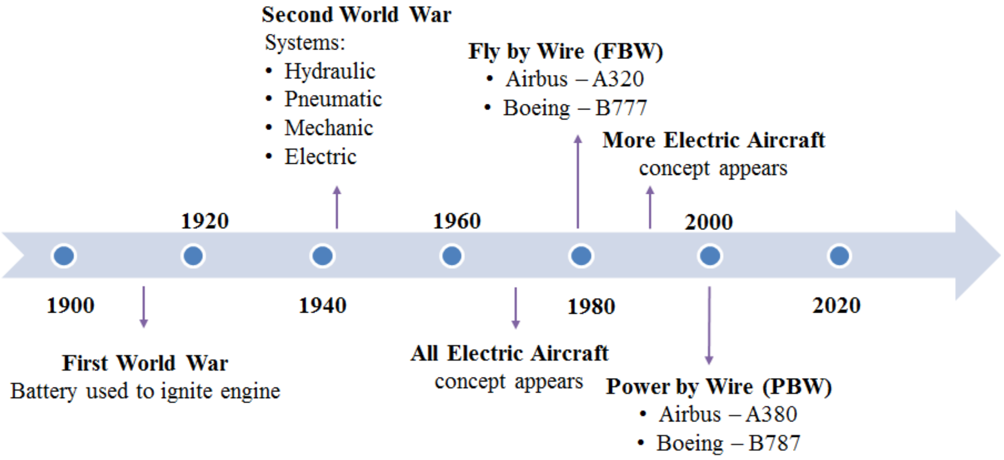

Figure 2.1: Aircraft time line. (Data from [3], [6]–[8], [10]–[13], [19], [26]).

The electrical power system at the time of the First World War consisted in a 12V DC battery for the engine ignition. This battery was also used to supply power to instruments, landing lights, radio receivers and transmitters [10]. However, with the expansion of the size of civil aircraft and accordingly an increase in passengers, a need of faster flights, and better radio equipment, the battery power became insufficient. As a consequence, an electrical power system was incorporated in aircraft systems. The transmission (AC or DC), voltage and frequency of the electrical power system were not agreed.

By the time of the Second World War, the aircraft had electrical, hydraulic and pneumatic systems, but their functions varied between models even of the same characteristics. For this reason, in the 1940s the systems were standardised [8]:

- Hydraulic System: For applications operating with high torque and short time intervals as undercarriages and ailerons.
- Pneumatic System: For air conditioning and pressurisation.
- Electrical System: For avionics and airframe utilities.

The use of a single power system to reduce the complexity was discussed in the 1970's, and the All Electric Aircraft (AEA) concept was introduced [8], [10]. In [12], the AEA is defined as an aircraft with only electrical power off-take, with only electrical loads and electric propulsion. Additionally, in the 1990s the More Electric Aircraft (MEA) concept was introduced [3], [6]–[8]. The MEA, described in section 2.3, aims to change the pneumatic, hydraulic, and mechanical systems to electrical systems while keeping the actual propulsion system. Thus, there is no need for hydraulic and pneumatic systems. The use of an electrical system allows the elimination of expensive and cumbersome hydraulics. Moreover, the design, development, and testing costs are reduced, and advanced diagnostics technology is easier applied. Overall, the efficiency increases and the maintenance decreases [12].

The first step towards the AEA and MEA were taken in the decade of 1980 when Fly-by-Wire (FBW) systems were introduced and used in Airbus A320 and Boeing B777. FBW uses electrical control systems to regulate the flight control surfaces, such as aileron, elevator, rudder, and spoiler; replacing the mechanical and hydro-mechanical ones used before. Thus, the aircraft have less weight, improved reliability, and an easier and safer control system [13].

The first MEA appeared with the introduction of Power-by-Wire (PBW) systems in 2000's in Airbus A380 and Boeing B787. PBW replaces the hydraulic circuits by electric ones, increasing the electric loads up to 850kW and 1.4MW in each aircraft respectively [11], [13]. As a consequence of the MEA and AEA concept, the electric demand in aircraft has increased drastically in 20 years [26].

In next sections, the conventional aircraft power systems and the More Electric Aircraft (MEA) are discussed. Later the aero gas turbine and the drivetrain torsional vibrations are described. Finally, the chapter summary is presented.

2.2 Conventional Aircraft

For a conventional aircraft, engines are mainly used to produce the propulsion thrust of the plane (about 40MW for propulsion). Another 1.7MW of the generated power is consumed by the pneumatic, hydraulic, mechanic and electrical power system as shown in Figure 2.2 [1], [9].

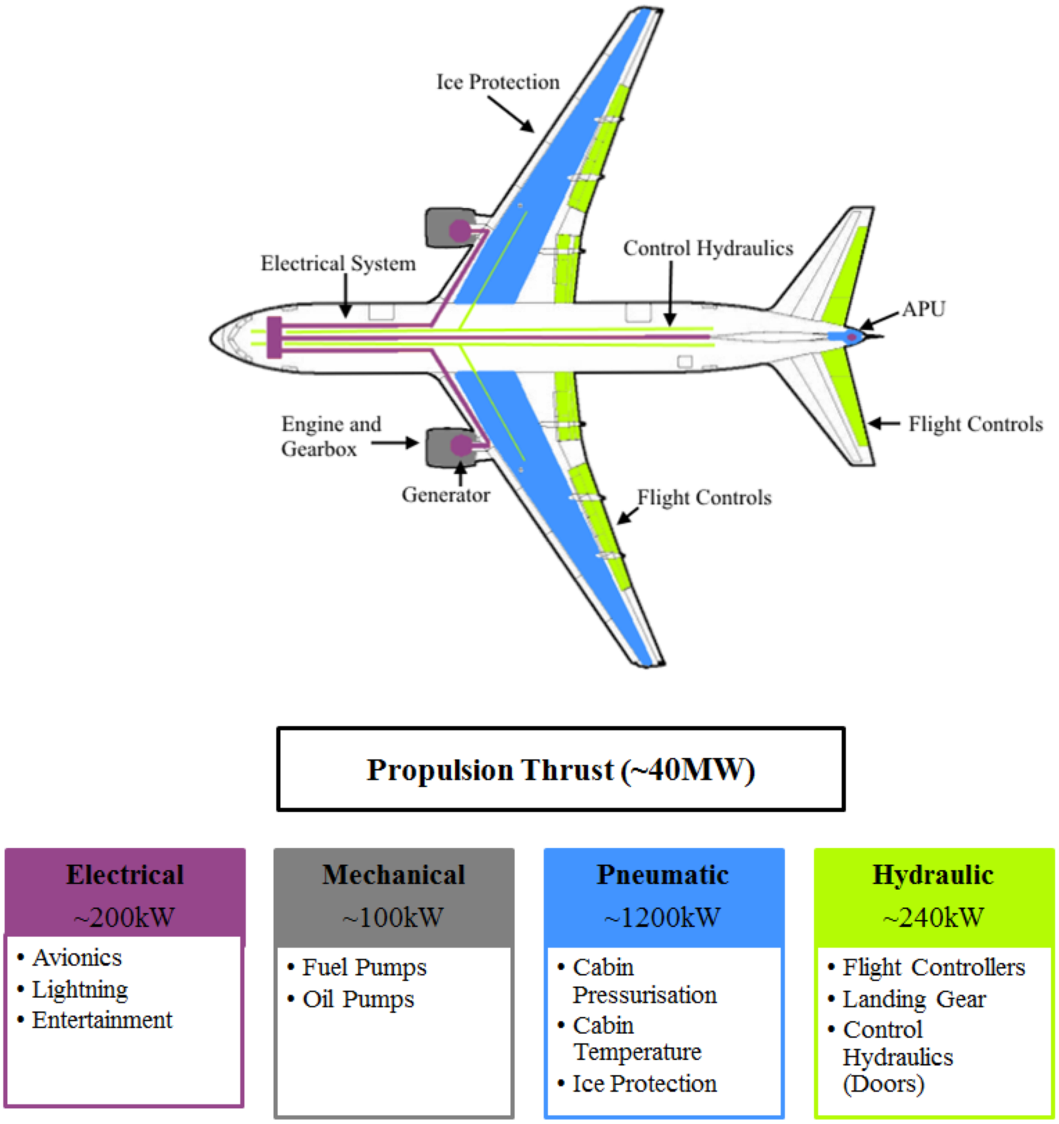

Figure 2.2: Conventional aircraft power (Data from [3], [15], [27], [28]).

2.2.1 Mechanical Power

On a conventional aircraft, the mechanical power is derived from a gearbox connected to the engine and is used to drive the hydraulic pumps, oil pumps as well as the electrical generators. The main disadvantage of this the gearbox is that it is normally very heavy and requires regular maintenance [1], [12].

2.2.2 Hydraulic Power

The hydraulic system has been used in the aircraft from the 1930s when a retractable undercarriage was introduced. Since then, the hydraulic system has been used to manage the flight actuators, including the rudders, the elevators the ailerons, and the landing gear, among others [1].

The hydraulic system consists of two pressurised circuits supplied by hydraulic pumps which are driven by a gearbox, as shown in green lines in Figure 2.2. Through these pipes, the fluid is distributed to all the actuators for aircraft flight control actuators.

The main advantages of hydraulic systems include high reliability, robustness, and high power density. However, the hydraulic system has a abundant weight and requires regular maintenance [1].

2.2.3 Pneumatic Power

The pneumatic power is the highest one after the thrust, as can be seen in Figure 2.2. This type of power is derived by bleeding air from the engine core. In reality, about 2- 8% of the air flux is bled from the engine. The air bled from the engine is mainly used for the environmental control system and the ice protection system [1], [12]:

- Environmental Control System (ECS): its functions are the pressurisation and the thermal regulation of the cabin. The air bled from the engine is regulated by pressure valves in a heat exchanger and is cooled down by ambient air. The fans, valves and monitoring and control are electrical.
- Ice Protection System (IPS): its function is to heat the engine intake and aircraft wings, protecting from the ice and rain. The bleed air is used to heat the wings, while its control is electric.

The advantages are its simple design and high reliability. However, as the pressurised air of the bleed system comes from the engine, its temperature and pressure are high. To be able to use the bleed air, it must be cooled down, causing a significant waste of energy [12], [14].

2.2.4 Electrical Power

The electrical power in a conventional aircraft is used for the avionics, cabin and aircraft lighting, monitoring and control of ECS, etc. [1]. As shown in purple in Figure 2.2 and in Figure 2.3, the electrical system consists of two identical subsystems: the left side power system and the right side power system. Each subsystem has an electrical generator which generates an AC 115Vrms three-phase electrical power operating at 400Hz constant frequency [6], [29], [30].

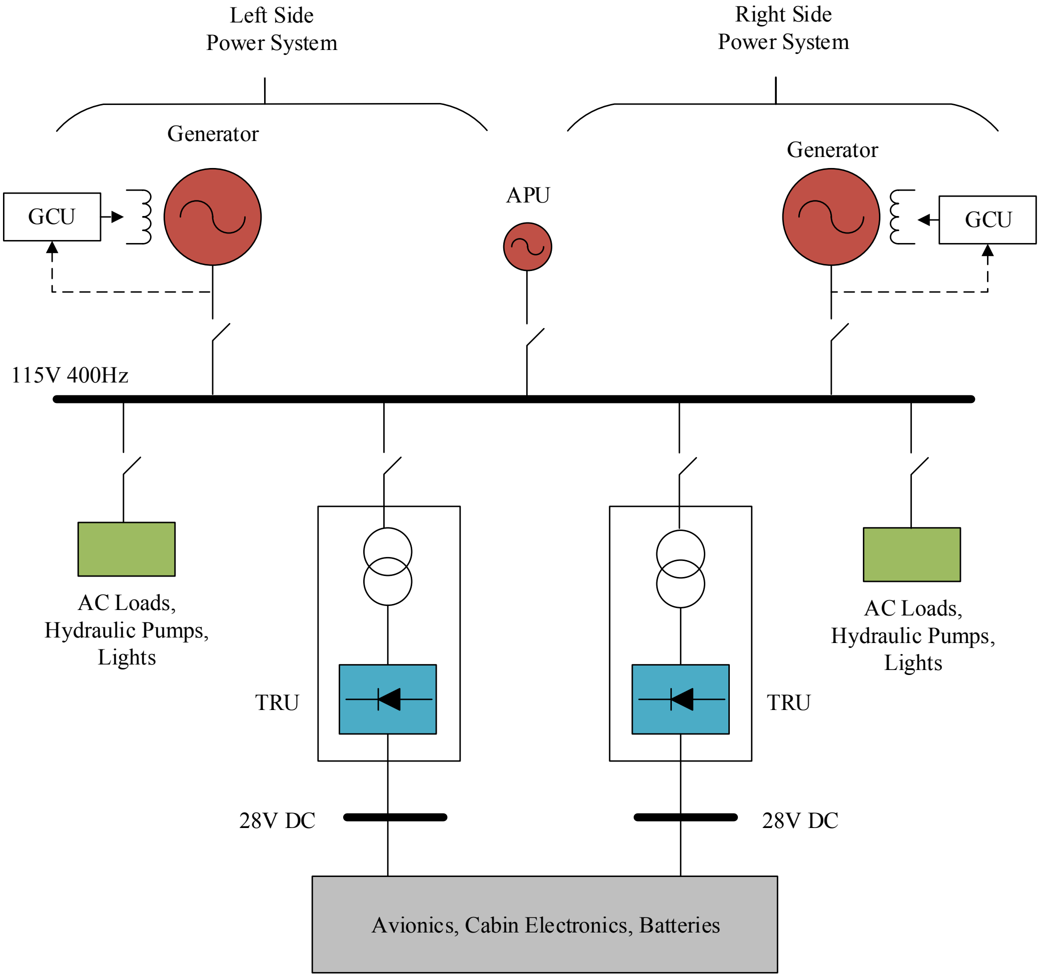

Figure 2.3: Electrical system.

To achieve a constant frequency, the generator speed needs to be constant. This is achieved through a Constant Speed Drive (CSD) which transforms a variable engine shaft speed to a constant one. The CSD, shown in Figure 2.4, is essentially a hydro-mechanical automatic gearbox. The CSD is mechanically complex and needs oil and maintenance [9].

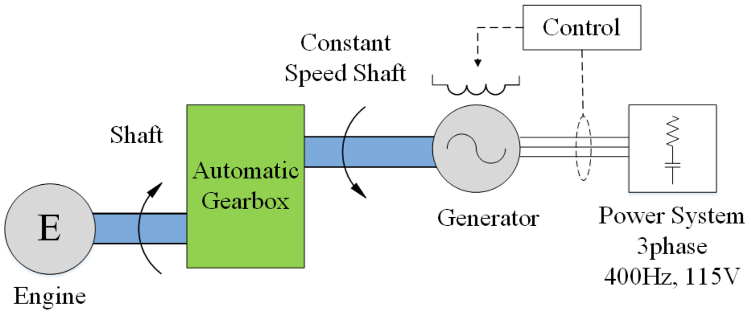

Figure 2.4: CSD configuration.

Each generator has its own Generator Control Unit (GCU) to keep the voltage amplitude of the generator at a desired value (115Vrms). Electrical loads such as lighting, entertainment system and auxiliary hydraulic pumps are directly fed by the HVAC bus [1], [12]. The avionics, cabin electronics and backup batteries are connected to a 28V DC bus. As shown in Figure 2.3, a Transformer Rectifier Unit (TRU) is used to change from AC to DC voltage [10].

The advantages of using electrical systems are its high efficiency and low maintenance. For these two reasons, in MEA aircraft, the hydraulic and pneumatic systems are replaced by electrical ones to improve the overall system efficiency.

2.3 More Electric Aircraft

The More Electric Aircraft (MEA) aims to replace the pneumatic, hydraulic and mechanical system by electrical ones [6], [29]–[32]. For this reason, the MEA's engine would only require fuel, a control interface, and electrical power connections as presented in section 2.3.1 [3].

To reduce the mechanical system, the fuel and oil pump systems can be driven by electrically powered pumps [7], [31]. In the same way, the drivetrain will need to be removed, and hence the speed of the generator will not be constant. For this reason, new drive strategies are necessary as presented in section 2.3.2.

To reduce the hydraulic system, the hydraulic actuators will be replaced by Electro-Hydraulic Actuator (EHA), and Electromechanical Actuators (EMA) [32], [33]. Both are described in section 2.3.3.

The elimination of the pneumatic power will result in a bleedless engine, which may improve the engine efficiency by 3- 4 % [4]. For this reason, the ice protection system (IPS) and environmental control system (ECS) will be electrical. These two systems are described in section 2.3.3.

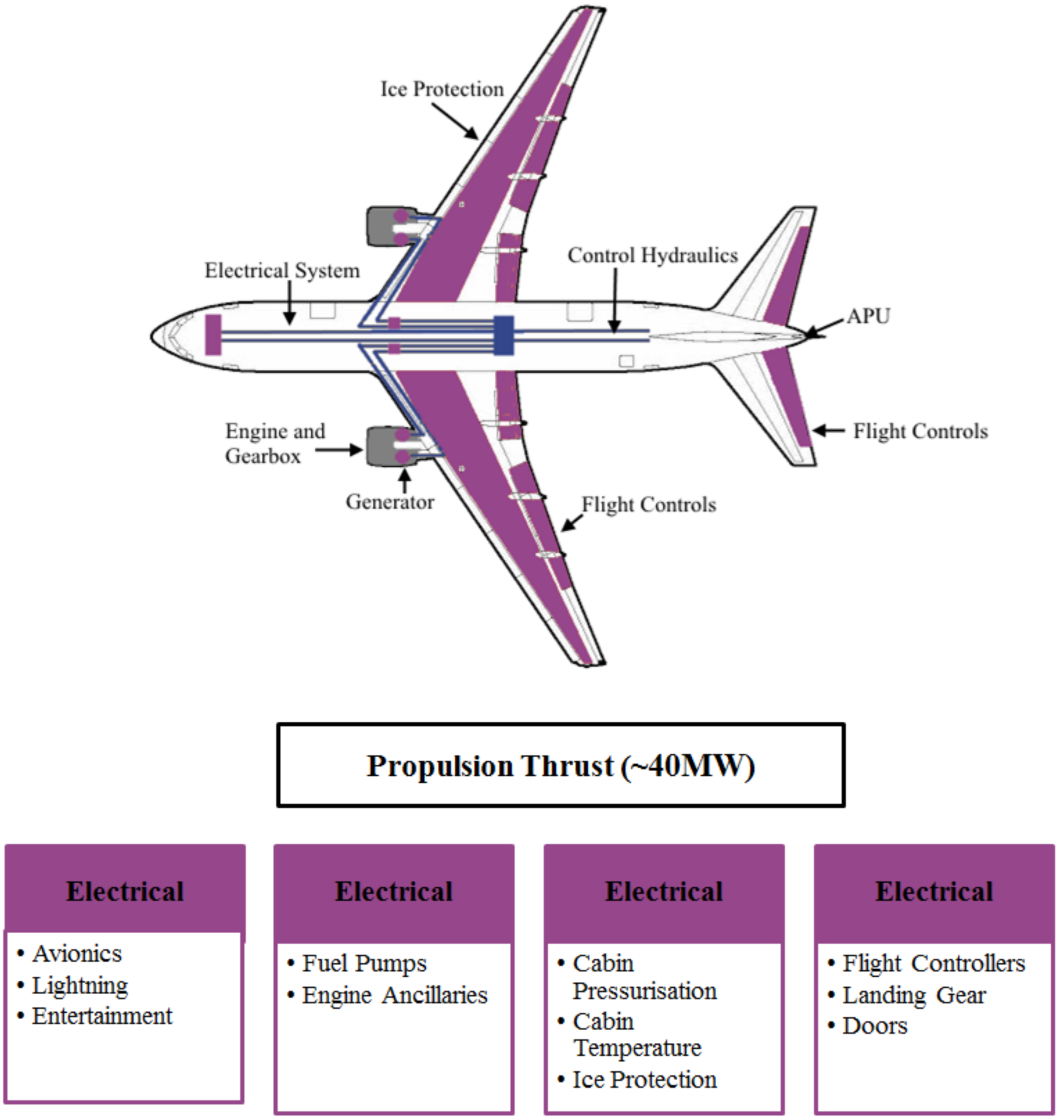

Figure 2.5: More electric aircraft power.

Figure 2.5 shows the MEA's power system, in which the hydraulic, pneumatic and mechanical systems from Figure 2.2 have been replaced by electrical ones. Typical load values on a large MEA according to [9] are fuel pumps (10kW), flight controls (2-35kW), environmental control system (4*70kW), ice protection system (250kW), landing gear (5-70kW), and the starting of the engine (200kW). A higher electrical power system will require new electrical network configurations. Furthermore, in a higher power system, high power disturbances are now passed on to the drivetrain, and electromechanical interaction needs to be studied. Chapter 3 presents the reasons and effects for electromechanical interaction, and in the rest of this thesis, solutions are proposed.

In the following sections, the aircraft engines, electrical power generation strategies, the new electrical loads (such as EHAs, EMAs, IPS, and ECS), the electrical power system, and cases of the MEA will be introduced.

2.3.1 Aircraft Engines

To have a more electric system, new technologies for the engine has also been proposed. The main ones are the Bleedless Engine, and the More Electric Engine (MEE).

2.3.1.1 Bleedless Engine

In a conventional aircraft, the ECS and IPS use pneumatic power. This power comes from air bled from the HP spool in the gas turbine [34]. However, the bleed air temperature is much higher than the one required normally, up to 350°F in the LP spool and 1200°F in the HP spool at a pressure of up to 500psig. For this reason, the air must be cool down to around 150°F and the pressure reduced to approximately 30 psig before it is used in the ECS and IPS. Therefore, pressure regulating valves and a pre-cooler arrangement are used [34].

Because the process of heat exchange has a lower thermal and energy efficiency, the use of bleed air reduces the efficiency of the engine. Furthermore, the bleed air is responsible for higher aeroplane drag and the noise production [35].

For Boeing B787, the bleed air has been drastically reduced and is only used as anti-icing at the engine cowl. For the ECS and IPS, bleed air is not used anymore. Instead, these systems operate electrically [14].

The advantages are [35]:

- Improved fuel consumption (1 to 2% in cruise and 3% overall)
- Reduced maintenance cost, because the bleed system has been eliminated.
- Reduce weight, since the bleed system has been removed. Consequently, the fuel consumption reduces and the operation range expands.

2.3.1.2 More Electric Engine

The More Electric Engine (MEE) is directly related to the MEA, as it aims to reduce the hydraulic, pneumatic, and mechanical system in the aircraft engine to reduce the weight, the required thrust, and the fuel burn [3], [36]. Also, the interface between the engine and the aircraft would be simplified, as the system has been reduced to electric power and fuel only [3].

With this objective, the following components will be eliminated in the MEE [3]:

- Lubrication system: It will be replaced by Active Magnetic Bearings (AMB).
- Gearbox and associated shaft: A motor/generator, combined with an AMB, will be embedded into the IP and HP spools. In this way, the inter-shaft power transfer would improve the operability of the engine, and the compressors and valves will be reduced. These changes will allow the removal of the radial driveshaft, internal and external drivebox, and lubrication systems.
- Hydraulic system: Electric power from the generator will be used to power an electric motor hydraulic pump, allowing the replacement of the hydraulic system with a fan shaft generator.
- Pneumatic engine starting system: Gas turbine engines have traditionally been started with an air motor applying torque to the accessory drivetrain to turn the GT spools. In the MEE an HP motor/generator will be used to launch the engine electrically.
- Bleed air offtake: As mentioned before, the system will be bleedless.

The first steps towards an MEE have been taken in the B787, in which the bleed air has been removed, and the engine is started electrically [37].

2.3.2 Electrical Generation Strategies

In section 2.2.4 was mentioned that most electrical loads need to operate at a constant frequency and that normally a CSD is used. Since the CSD is a complex mechanical system, which needs regular maintenance, in this section, two new strategies to keep the load's frequency constant are presented: Variable Speed Constant Frequency (VSCF), and Variable Frequency (VF) operation.

2.3.2.1 Variable Speed Constant Frequency

In the Variable Speed Constant Frequency (VSCF) methodology, the generator is connected directly to the engine, removing the automatic gearbox. The generator produces variable frequency proportional to the speed of the shaft.

As shown in Figure 2.6, to keep the frequency of the network constant at 400Hz, a power electronic converter is used between the electrical generator and the 115Vac 400Hz power systems. Usually, a cyclo-converter or converter with DC-link is used [9]. Historically, cyclo-converters have been mainly employed in military applications, while the DC-link method has been applied to civil aircraft like B373, MD-90 and IPTN N250 [12].

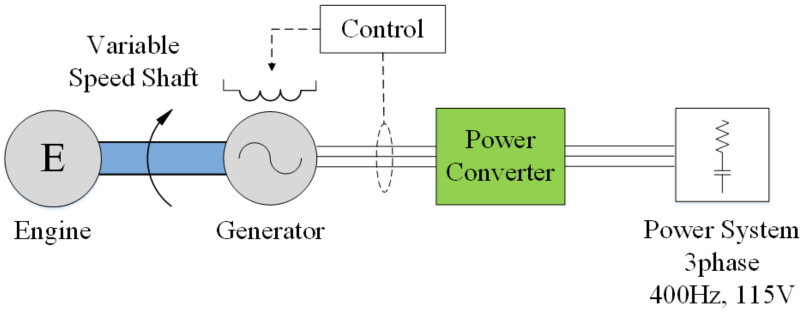

Figure 2.6: VSCF configuration.

While the VSCF allows the elimination of the mechanical gearbox, its main disadvantage is only one power converter is used to obtain the desired frequency. Since a failure of the power converter will result in the disconnection of the whole electric system, the system is not robust enough [9].

2.3.2.2 Variable Frequency

To overcome the problem of the VSCF strategy, the operation of the electrical network with a Variable Frequency (VF) is used [9], [27]. In the VF strategy, the generator is connected directly to the engine and the frequency of the grid changes between 320 and 720Hz, as shown in Figure 2.7. To each load operating at constant speed, a power converter is connected if necessary. In this way, a single failure point is removed, and each connection can be fixed independently [9], [12], [31].

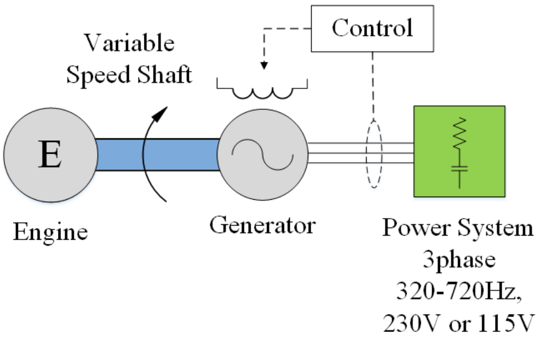

Figure 2.7: VF configuration.

The advantage of this method is the elimination of the mechanical CSD and that there is no single connection point failure problem as in the VSCF strategy. However, the number of power converters required is high, since nearly all aircraft loads required constant frequency [9], [31]. For this reasons, the VF strategy is used in Boeing B787 and Airbus A380.

2.3.3 Emerging New Loads

In the MEA, a variety of power loads with different requirements and effects on the system can be found [14], [38], [39], for example:

- Pulsating Loads: Can be solid-state radars and digital loads.
- Constant Power Loads: Motor driven pump can operate as constant power loads.
- High Power Loads: The ECS and undercarriage are high power loads which are connected to the DC bus to avoid additional AC-DC converter. As the ECS consumes high electrical energy, it might add harmonics to the system if connected through AC-DC-AC converters.

- Transient Loads: EHA and EMA loads are transient. They are fed from the essential buses which can be powered by backup batteries under emergency. In general, they are connected to the essential AC bus, but the need of AC-DC converters suggests the use of an essential DC bus instead.

In the next sections, different loads on board MEA such as the actuators, environmental control system and ice-protection systems will be described.

2.3.3.1 Actuators

For the MEA operation, two actuators are considered: Electro-Hydraulic Actuator (EHA) and Electromechanical Actuator (EMA). The main advantages of electric actuators compared to the hydraulic ones are the decrease in the weight and an increased efficiency. The weight is reduced because the use of electric actuators allows the removal of the hydraulic pipes, replacing them with a lighter electrical network. The use of a PBW connection makes the installation and replacement of actuators more accessible as they are line-replaceable [40].

Secondly, electric actuators are more efficient because they consume power only when the control surface moves or overcomes a load, instead of being continuously active like the hydraulic system.

Electro-hydraulic Actuator

Electro-hydraulic actuators (EHA) are employed to localize the hydraulic system used on the flight control surfaces, such as rudders, elevators and ailerons. The use of EHA allows the elimination of the central hydraulic pumps (driven by the engine gearbox) and the replacement of hydraulic distribution pipes by electrical cables thus reduce the weight and maintenance cost. As shown in Figure 2.8, EHA consists of an electrically driven pump which pressurises a local hydraulic system. The fixed displacement pump is connected to a motor, and the position of the actuator moves a fixed amount per revolution [9].

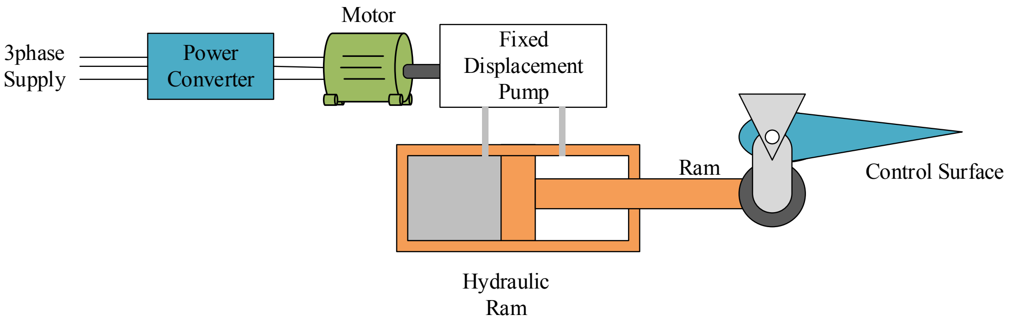

Figure 2.8: Electro-hydraulic actuator.

There are several advantages of EHA. First, because there is no direct mechanical connection between the motor and actuator, the failure possibility of the system is reduced. Second, the technology is more similar to hydraulic actuators [9]. Currently, EHA is used as backup systems of Boeing B787 and Airbus 380, where is connected in parallel to conventional hydraulic systems [9].

Electromechanical Actuator

An alternative to the EHA, is the Electromechanical Actuator (EMA). As shown in Figure 2.9, in an EMA, an electric motor is connected to a gearbox which drives a ball screw to amplify the machine's torque and provide linear actuation force. The linear force allows the movement of the flight surface. With the use of the gearbox and the ball screw, the local hydraulic system is removed [9].

The EMA can be used for surface control, landing gear and undercarriage with reduced cost, less complexity and maintenance cost, and increased reliability [9], [32]. However, due to the mechanical connection on the ball-screw, jamming may occur. This limits the EMA to be used only for secondary control actuation (flaps and slats) [9].

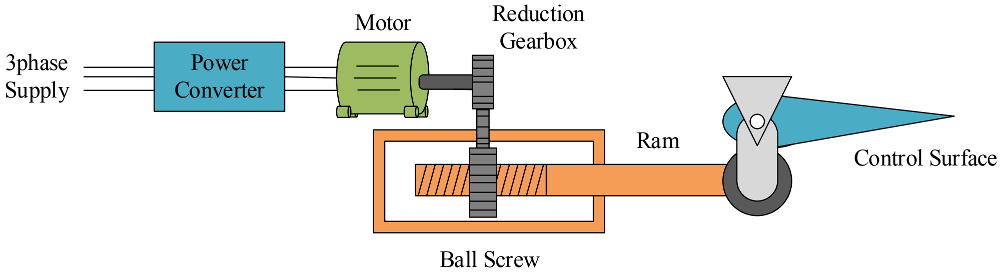

Figure 2.9: Electromechanical actuator.

2.3.3.2 Environmental Control System

The Environmental Control System (ECS), is used to control the temperature and air of the cabin. Conventionally, it consists of one or two stages compressor connected to the main engine. However, to reduce the bleed air, an electric ECS is used [15].

In the electric ECS, instead of pneumatic power, electric motors and converters are used to drive a compressor which provides air for the pressurisation. To adjust the temperature of the pressurised air, an electrical heating/cooling plant is used [7], [9], [15], [31], [35].

The advantage of this method is the elimination of the bleeding air from the engine, which will improve the efficiency of the aircraft. The main challenge is sizing the overall system and calculating the required electrical power for every phase of the flight [15].

2.3.3.3 Ice-Protection System

Traditionally, the Ice-Protection System (IPS) uses the bleed air to heat the wings [1], [12]. Instead, in the MEA, the IPS is achieved using electrical power with thermal mats embedded in the wing leading edges. These thermal mats, formed by resistive materials will generate heat for de-icing or anti-icing functions when powered on. For anti-icing protection, the thermal mats can be energised simultaneously, while for de-icing protection in the wing leading edge, the mats can be connected sequentially [35].

Compared with conventional ways, these electrical IPS solutions are more controllable and have a more flexible and lighter interface than pressure pipes [7], [31]. Moreover, since no excess energy is used, the system is more efficient [35]. This kind of IPS is used in the Boeing 787.

The electrical loads described can make the system unstable. For instance, after a perturbation or load connection, currents are induced in the machine circuits. The velocity with which these currents decay depends on the components of the system

[41]. As a result, the modelling of the load's behaviour and the system stability analysis are fundamental. In [33], [39], [42], [43] the stability of the electric power system is studied with pole analysis through small-signal model analysis. In [44] a stability analysis for a hybrid AC-DC system has been studied, in [45] the impact of pulsating loads over the electrical power system is evaluated considering a storage system, and in [46] a secondary control for voltage restoration is presented. In [18], the effect of the electrical load connection over the mechanical drivetrain has been studied. However, no studies to minimise the effects of the electromechanical interaction have been presented.

The disturbances in the electrical system can pass to the mechanical one, generating electromechanical interaction. For example, high electrical transients can produce mechanical transients, or pulsating electrical loads can resonate with the mechanical system. Although the electromechanical interaction has been acknowledged in [17], [18], no solution has been proposed to attenuate these electromechanical interactions.

2.3.4 Electrical Power System

The electrical power on board has increased from 100-200kW to over 1MW in a large civilian aircraft such as the Boeing B787 during last few decades [9]. Electrical power systems with higher capabilities imply new challenges that need to be assessed. This makes the study and design of the electrical power system fundamental.

In general, an electrical power system can be DC, AC, or hybrid with a variable voltages or variable frequencies. Most systems operate with an AC distribution because it is easier to implement. On the other hand, DC systems are more reliable for high transient systems because the DC-link capacitors can help in maintaining the voltage. Since no agreement has been reached in the advantages of the different electrical systems, the MEA can operate with a DC, AC, or hybrid architecture [11].

A possible hybrid configuration is presented in Figure 2.10. In that case, 230Vrms VF is used for generation, 270V DC for distribution, and 28V DC for lower loads as shown in Figure 2.10 [11], [14], [47]. The generators of the proposed configuration produce 230Vrms of 320-720Hz (or 360-720Hz in other aircraft models) since the mechanical drivetrain has been removed to make the electrical power generation more efficient. A higher voltage (230Vrms instead of 115Vrms) is used to reduce the conduction losses [6], [18], [29]–[32]. Moreover, as shown in the figure, the generators are connected to the 230Vrms variable frequency buses. To this bus, the IPS and the 270V DC bus are connected. The 270V DC bus is connected to an Auto-Transformer Rectifier Unit (ATRU), and to this, a 28V DC bus is connected to be used with the legacy loads, such as avionics [14].

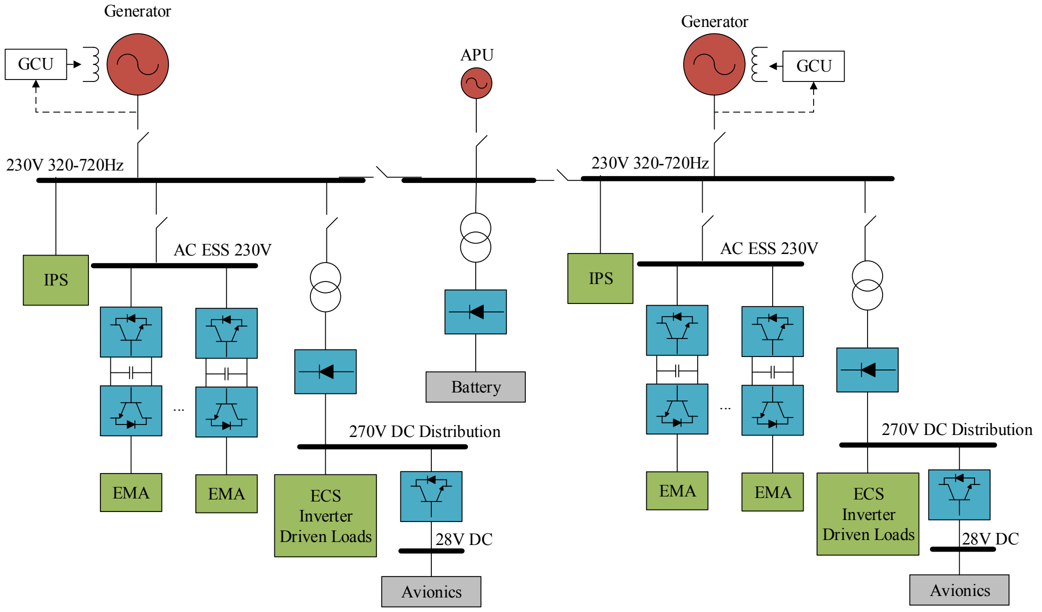

Figure 2.10: Possible electrical power system of and hybrid MEA.

2.3.5 Cases of MEA

While the MEA concept originated in 1990, the electrical power systems in aircraft have been studied since 1930, first with the use of a battery to start the engine, and then with the AEA concept. The military aircraft, known as the British V-Bombers (Valiant, Vulcan, and Victor) are an example of steps taken towards the use of electrical systems in the 1950s. Valiant had electrically powered hydraulics and electrically powered landing gear actuation. Whereas, Vulcan and Victor had electrically powered Integrated Actuator Packages [8]. In civil applications, the VC-10, the Lockheed Electra and the Lockheed P-3, used electrically driven hydraulic pumps [10].

In modern aircraft, the Airbus A380 and A350, and Boeing B787 are examples of MEA. In them, the number of centralised hydraulic system has been reduced, connecting EHA backup systems [9]. In the A380 a more electric flight control is used. Instead in B787 maintains centralised hydraulic systems, but the ECS and IPS are done electrically [37].

Next, the functions of the pneumatic, hydraulic, and electrical systems in the B787 and A380 are described.

2.3.5.1 Boeing B787

The case of the Boeing B787 is the one with more MEA features. The characteristic of its power systems are:

- Pneumatic system: is only used for the anti-icing of the engine cowl, and the ECS and IPS are both electrical. In the first, the air is pressurised and warmed electrically using 280kW. While in the second, a thermal mat protects the wing of the ice consuming 250kW. Moreover, the engine, Rolls-Royce Trent 1000, is the first large commercial aircraft to be equipped with electric engine starter [37].
- Hydraulic system: a conventional hydraulic system is combined with EHA to decrease the hydraulic and keep redundancy at the same time [9].
- Electrical system: its power network is hybrid, combining AC and DC buses. It has four 250kVA Hamilton-Sundstrand variable frequency generators (2 per engine) connected to a 230V AC voltage bus. The variable frequency generator allows a more efficient energy conversion so that the fuel can be reduced. On the other hand, the operation at a higher voltage than the conventional aircraft (115V AC) decreases the losses in the transmission lines. Hence, less wiring is required on the plane, and the weight is reduced [19].

2.3.5.2 Airbus A380

The power systems characteristics of Airbus A380 are:

- Pneumatic system: the ECS is conventional, and hence the pneumatic system has been retained.
- Hydraulic system: uses EHAs. In conventional aircraft, the actuators are connected in pairs to give redundancy to the network. In the A380, one hydraulic actuator has been replaced with two EHA. In other control surfaces (as the rudders), backup EHAs have been implemented parallel to the traditional hydraulic ones. This connection also used in the V-bombers, allows the choosing which actuator to use: hydraulic or EHA [40].
- Electrical system: has four engines, and to each of them, an Aerolec 150kVA variable frequency (370-770Hz) generators are connected [37]. Also, there are two 120kVA 400Hz auxiliary power unit (APU) generators, each of which is driven by the APU. Each generator is connected to VF bus. These buses cannot be paralleled.

2.4 Aero Gas Turbine

The Gas Turbine (GT) introduced in the 1940s is one of the best methods to produce mechanical power [34], [37], [48]. It involves the compression and heating of a fluid at high temperatures. Later this fluid is expanded, generating power. The main three stages of the GT are:

- Compressor: The air entering the turbine is compressed.
- Combustion chamber: Fuel combustion is used to rise the temperature of the fluid before the expansion to increase the produced power.
- Turbine: The hot fluid expands generating power.

The advantage of the GT is that it has high power to weight ratio and high thrust speeds [37]. Because of this reason, the GT replaced other engines for all aircraft but the light ones [48].

In the case of the Aero Gas Turbine, the behaviour is equivalent as shown in Figure 2.11. The fluid, air, enters the turbine through an intake; it goes through the compressor, combustion chamber and turbine; and finally, it is expelled through the nozzle propelling the jet at a high velocity [48].

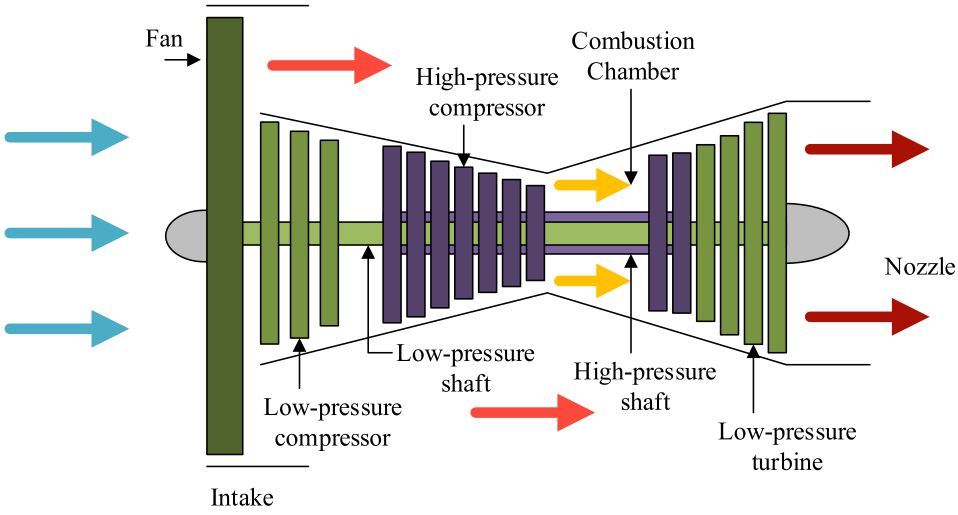

Figure 2.11: Three spool turbine system.

A turbofan is connected to obtain a higher efficiency. It consists of connecting further turbines to drive a larger diameter fan after the first gas exhaustion [17], [34], [37], [48]. Thus, the exhaust gas can be used to drive one or more additional spools. These spools are not attached to each other, but their operation is coupled through the air flow, and their speed is related to the level of pressure and the thrust generated. In general two and three spool shaft are used. The spools will be referred as High Pressure (HP), Intermediate Pressure (IP), and Low Pressure (LP) spool according to their position. Three-spool systems are preferred for a long-haul flight, where fuel burn is a higher fraction of the cost. Two spool systems are preferred for short haul operation [37]. The turbine from Figure 2.11 has three spool turbine, like the one from Rolls-Royce Trent 1000 [18]. The three spools are represented in purple (HP), blue (IP), and green (LP). In this configuration, the generator is connected to the IP shaft through the drivetrain. For a two spool system, the generator is connected to the HP shaft. The studies presented in this thesis can be applied to the two and three spool configurations.

2.5 Torsional Vibrations on Aircraft Drivetrain

Generally, aircraft drivetrains are formed by a set of rotating shaft and gears connected to the IP or HP spool of the engine as shown in Figure 2.13. Rotating mechanical systems, such as an aircraft one, are subjected to three types of vibrations: axial vibrations, torsional vibrations, and transversal vibrations. The axial vibrations occur along the shaft length axis as shown in Figure 2.12(a). The torsional vibrations produce a twist motion around the rotor shaft (Figure 2.12(b)), and the lateral or transversal vibrations cause horizontal and vertical displacements of the rotor (Figure 2.12(c)) [49]. In this thesis, the critical speeds that enhance transversal vibrations are identified, and strategies to minimize the torsional vibrations of the aircraft mechanical system are studied.

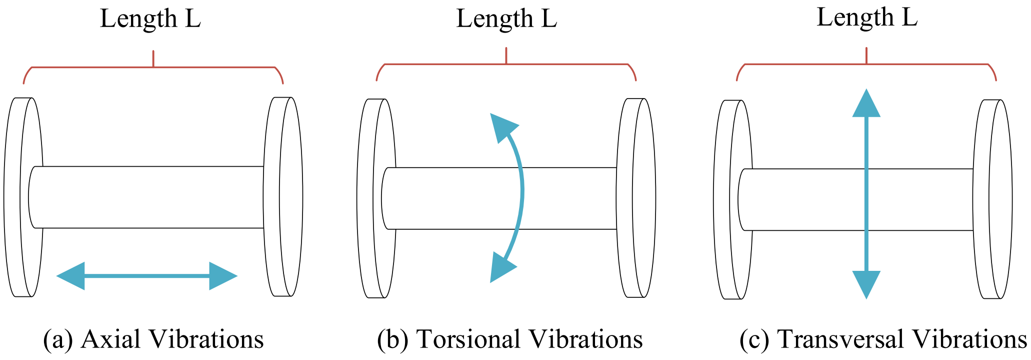

(a) Axial Vibrations (b) Torsional Vibrations (c) Transversal Vibrations

Figure 2.12: Drivetrain vibrations.

Transversal vibrations increase the displacement of the rotating components of a drivetrain and are excited when the rotation speed of shaft and gears is the same of the critical speeds. Hence, in order to avoid the excitation of transversal vibrations, in the experimental setup of this research, the critical speeds are identified, and the operation at these values avoided [49].

On the other hand, torsional vibrations are produced due to the excitation of the natural frequencies of a mechanical system when a torque is being applied. The excitation torque can be impulsive (transient loads as EHA, EMA) or periodic (pulsating loads, high power loads). The damage of the torsional vibration on a mechanical component increases with each oscillation producing small cracks that propagate along the material. Fatigue of the material occurs when the cross-section of the material is lower than the required for the torque applied [49]–[51].

In general, systems with large inertias have low natural frequencies. Instead, the natural frequencies of systems with small inertial values and stiff mechanical components are high [50]. In aircraft systems, due to the large engine inertia and the flexible shaft used to reduce weight, two vibrations modes below 100Hz can be found [18], [19]. When the electrical network share of loads is weak, and there are dynamic loads, the likelihood of electromechanical interaction increases [18]. In [18] it was shown that the torsional torques produced by the electrical system could affect the mechanical one, and hence the electromechanical interaction studies must be carried out.

The maximum torsional vibration allowed depends on the duration and the amplitude of the stress. For higher amplitude stresses, the number of times the stress can occur reduces. The life of the component can be predicted studying its fatigue. To analyse the torsional vibrations, the rotating system must be reduced to a model. The complexity of the model depends on the system and the purpose of the study. When a model aims to identify potential problems, it can be represented by a simple motor, couplings and a driven load. Instead, to predict the component life and the exact torsional oscillations complex models with gearboxes and multiple inputs or loads are used [50].

Moreover, a conventional aircraft drivetrain, connecting the gas turbine to the generator is shown in Figure 2.13 [18]. The drivetrain consists of three subsystems: the spool coupling, the transmission, and the accessory load gearbox [18], [37].

The drivetrain is connected to a spool in the engine, the IP spool in the case of a three pressure spool, and the HP in the case of a two spool system [18], [35]. The spool operates at a variable speed, and a fixed ratio bevel gear is used for the coupling. Since the engine inertia is much higher than the rest of the drivetrain, when the aircraft is not in idle, the speed of the system is fixed by the gas turbine that acts as the ground of the system [18], [37].

From the spool coupling, the power is mechanically transmitted through a series of shaft (radial driveshaft and angular driveshaft) till the transfer gearbox on the outer fan casting and then to the accessory gearbox. The shaft goes through the central core of the gas turbine and the bypass region, therefore to minimise the airflow disruption, the shaft diameter is small. Moreover, since the shaft is also long, the flexibility is high [18], [37].

Finally, to the accessory gearbox all the loads, feed mechanically, are connected. The two (or the number in the corresponding aircraft model) electrical generators, the oil pump, the de-oiler, the fuel pump, the hydraulic pump, and the permanent magnet alternator (used for electrical power backup) are connected. The accessory loads are designed to have a low mass, which together with the flexible shaft are responsible for the low frequencies of the aircraft mechanical drivetrain [18], [37], [49].

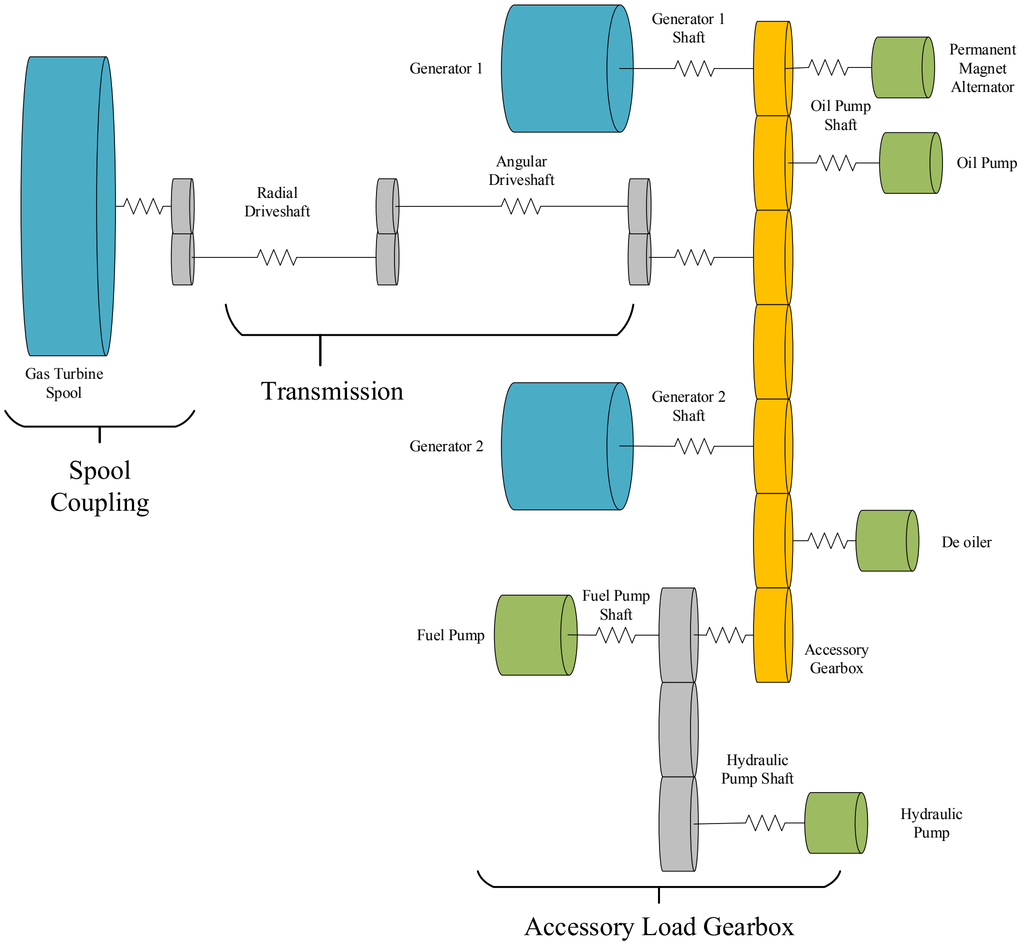

Figure 2.13: Engine mechanical system.

In [18], was shown that the drivetrain system presented in Figure 2.13 could be reduced from 9 to 2 natural frequencies and keep the firsts two vibration modes within 5% of the original ones. These two vibrations modes are the lower ones, which are responsible for the system torsional vibrations. Hence, a simple system can be used to analyse the electromechanical interaction in an aircraft. Chapter 4 presents the reduced mechanical model used for the electromechanical interaction studies in this thesis.

2.6 Summary

In this chapter, the aircraft systems and the migration towards an MEA have been presented. The MEA comprises the development of a whole new set of technologies, such as the MEE, the EHA and EMA actuators, new generation strategies such as VF, and a whole new design of the aircraft electrical power system.

Moreover, the electrical and the mechanical system of a plane have been described. To understand the interaction between these two systems, in next chapter a review on electromechanical interactions and its solutions is presented. Then, in chapter 4 the electromechanical system in the study is modelled. In chapter 5 a power management system (PMS) to suppress the excitation of the drivetrain torsional vibrations is proposed.

Chapter 3

Electromechanical Interaction

3.1 Introduction

Studies on mechanical and electrical stabilities have been carried out from as early as 1937. However, the first study on electromechanical interaction started after a shaft failure at the Mohave Generating Station in Southern Nevada in the early 1970s [52]. A similar case was discussed in [53] where two motor shafts, driving a compressor, failed, one after 3400 hours of operation and the other after 7000 hours of operation.

These two incidences were due to electromechanical interaction as only the electrical natural frequencies were considered in the design and not the mechanical ones. The electrical natural frequencies are dependent on its controllers, resistances and other components, while the mechanical natural frequencies are dependent on the inertias and stiffness of the components on the drivetrain. Since the machines are the interface between the electrical and mechanical systems, some disturbances can pass from one to the other, and resonant modes can be excited [18], [54]. However, frequently when studying machines and drives, the mechanical system is simplified, and the torsional elements are not considered. Because of the lack of electromechanical studies, transient torque can be produced at various points on the drive during a fault or switching event [55], [56].

The evolution of the electromechanical interaction studies is shown in Figure 3.1. As can be seen, the first cases analysed in the 1970s are associated with traction systems [23], [53] and ground generation (for example the Mohave case) [52]. However, during this period, the studies of electromechanical interaction were mainly associated with the modelling of the systems and the identification of vibration modes. It was at the beginning of this century, with the ongoing growth of electrical systems (automotive, aerospace, marine, drives, and wind turbines) that the studies on electromechanical interaction became significant.

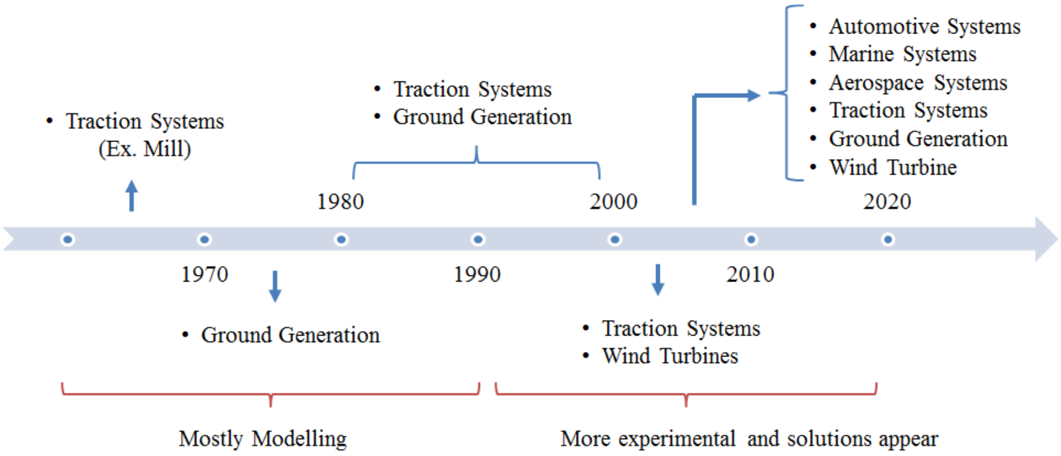

Figure 3.1: Electromechanical interaction through the years.

The rest of the chapter is organised as follows: First, the sources of electromechanical interaction are introduced, and then the effects of the torsional vibration of the system are studied. Third, different applications subjected to electromechanical interaction are detailed. Finally, solutions to minimise the interaction are presented followed by a summary.

3.2 Sources of Torsional Vibrations due to Electromechanical Interaction

In this section, different components that produce interaction in an electromechanical system are described. A general layout, like the one shown in Figure 3.2, consists of two electrical machines connected through a gearbox. This schematic characterises applications from electric power systems to traction systems and hence is used as a general representation of the electromechanical system. For example, Machine 1 can be a motor acting as a prime mover for a generator represented by Machine 2. Likewise, Machine 2 can be a motor connected to a rotating load, such as a mill, represented by Machine 1.

Independently of the operation case, the electromechanical system has a controller and loads connected. The controller (or drive), electrical power system connected to the generator, and flywheels can produce or be affected by torsional vibrations excited by electromechanical interaction. Next, the sources of this interaction are described: step and pulsating load connections, grid faults, sub-synchronous currents, and control systems.

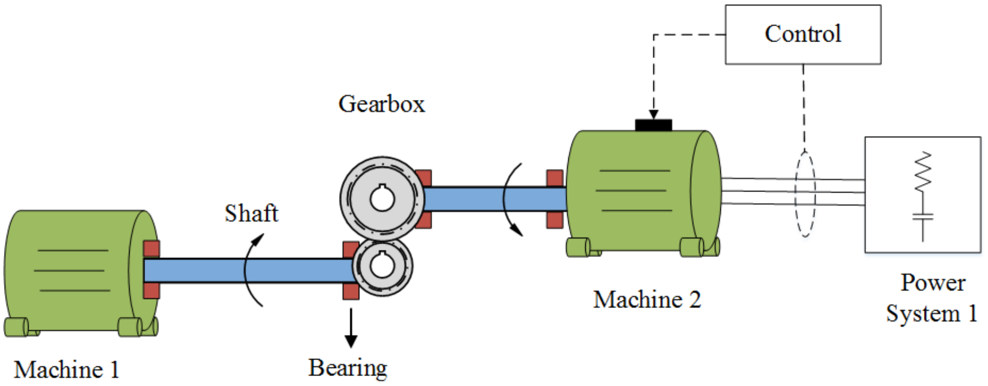

Figure 3.2: General electromechanical interaction system layout.

3.2.1 Step Load

The transient of the electrical load will produce a short-time disturbance in the mechanical system through the generator. This induced torque disturbance may result in mechanical vibrations and produce speed fluctuations. Furthermore, mechanical torque variations can change the speed and produce vibrations which are transmitted to the electrical system [18]. In general, higher load connections produce higher disturbance, and thus the magnitude of the connection is limited [57].

The load changes are especially relevant in isolated electrical systems, such as aerospace and marine, in which the effect of the connection and disconnection of an electrical load affects the generators [8] directly. In contrast, in most ground power systems the effect of a load connection is shared among the whole grid and thus the generator, and consequently, the mechanical system is not affected. However, breakers operation in power systems is equivalent to load connections in isolated systems, and the connection and disconnection of grid buses and faults can produce transient torques [57].

3.2.2 Grid Faults

As step connections in isolated power systems, grid faults can also produce torsional vibrations [58], [59]. Faults and instabilities of a power system can generate oscillations on the shaft due to the resultant high electromagnetic torque at the generator [58], [59]. For this reason, it is essential to have a good voltage control on circuit breaker and relays to avoid peak torques being produced [57], [58].

In [60], a zone of vulnerability of a power plant is defined. This zone is shaped by the regions in which an electrical disturbance damages a critical shaft due to torsional stress. These characteristics (fault location, type, clearing time, load of the line and generating unit, the effect of series capacitors, and distance of the fault) define the magnitude and set time of the torque applied to the generator, and which are the ones that excite the mechanical system [57], [60].

3.2.3 Pulsating Load

Pulsating loads can be found in mechanical and electrical systems, and in both cases, their effects have to be taken into account to avoid resonance [54]. Regarding electrical loads, many applications use pulsating loads, such as radars [18], [61]. These electrical loads can create resonance in mechanical systems if their period is close to the natural frequency of the mechanical system. Therefore the effect of the pulsating load over the mechanical system depends on its period [23], [62], [63].

In the case of mechanical loads, the pulsating loads can be found as cyclic rotational disturbance caused by eccentric or unbalanced rolls, bent shafts, seams in felts or wires, and mechanical misalignment. Their principal effect is imposing a periodic load change on the machine electrical drive [23].

Some systems have mechanical pulsating loads, like in [64] where its effect on an induction motor is studied. While in other cases mechanical and electric pulsating loads are present. For example, in marine systems, the pulsating loads can be of both origins, mechanical, such as the vibrations produced by the waves, and electrical, such as the radar connected to the system. The torsional vibrations can affect the mechanical system and the drive [65].

3.2.4 Sub-synchronous Currents

The AC current in an electrical system is composed of two components, the fundamental ($i_F(t)$) and the harmonics ($i_H(t)$), as shown in equation (3.1). The fundamental, shown in equation (3.2), has an amplitude A and oscillates at a frequency f_0, normally 50 or 60Hz. On the other hand, the harmonics, shown in equation (3.3), have an amplitude B_i and oscillate at the electrical system natural frequencies f_i with an exponential decay given by the damping ratio ξ_i [66].

$$i(t) = i_F(t) + i_H(t) \tag{3.1}$$

$$i_F(t) = A\sin(2\pi f_0\, t + \phi_0) \tag{3.2}$$

$$i_H(t) = \sum_i B_i \exp(-2\pi f_i \xi_i t)\sin\left(2\pi f_i \sqrt{1-\xi^2}t + \phi_i\right) \tag{3.3}$$

Figure 3.3 shows a simplified electromechanical system with one mechanical natural frequency and one electrical natural frequency. The mechanical frequencies are given by the inertia J, the stiffness K, and the damping D, while the electrical ones are given by the resistance R, the inductance L, and the capacitance C.

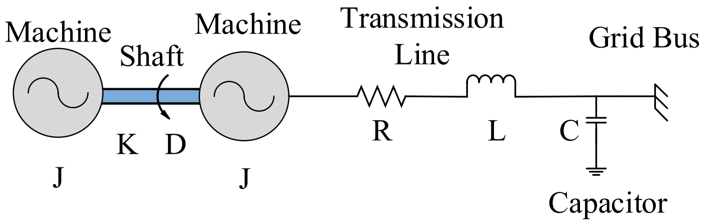

Figure 3.3: Sub-synchronous system.

Equations (3.4) and (3.5) show the electrical natural frequencies of the system with and without capacitance connected respectively. As given in equation (3.5), if there is no capacitance connected, the damping ratio is unitary thus there is no oscillation due to the current harmonic after an excitation to the system. However, as shown in equation (3.4), when the capacitances are connected close to the generator, the damping ratio is not unitary, and thus the oscillatory component of equation (3.1) is present after an excitation to the system.

$$f_1 = \frac{1}{2\pi}\frac{1}{\sqrt{LC}} \text{ and } \xi = \frac{R}{2}\sqrt{\frac{C}{L}} \tag{3.4}$$

$$f_1 = \frac{1}{2\pi}\frac{R}{L} \text{ and } \xi = 1 \tag{3.5}$$

When a capacitance is connected, the current harmonics are present. The current harmonic with frequency f_1 flowing into the generator's armature produce a rotating magnetic field in the machine, which induces currents on the rotor at frequencies $f_0 \mp f_1$. The current produced by $f_r = f_0 - f_1$ is called sub-synchronous current because its value is below the power system frequency and can generate shaft torques [51], [57], [66], [67]. For this reason, a capacitor can produce steady state or transient currents at sub-synchronous frequencies [67]. If the induced rotor current frequency f_r is close to the mechanical natural frequency f_m, the system oscillates producing resonance. This is known as sub-synchronous resonance [51], [52], [57], [66], [67].

An example of this is the Mohave case, in which the plant shaft failed because the second torsional mode was excited by sub-synchronous currents, which in general cause no harm to the electrical system [52]. Sub-synchronous currents also produce these problems in wind turbines which generally use capacitors next to the generators.

Another effect of the sub-synchronous currents is the self-excitation of the induction machine. The rotor resistance of an induction machine viewed from the armature terminals depends on the system frequency by the factor $f_r/(f_r - f_0)$, its value produced by sub-synchronous currents is negative as $f_r < f_0$. For this reason, if the rotor resistance referred to the armature is higher than the armature and network resistance the electrical system is self-excited [68], [69]. This self-excitation is passed to the mechanical system, producing higher and increasing torque vibrations.

3.2.5 Control Systems

Control systems or drives regulating electrical machines speed or voltage are found in every application. Among them, variable speed drives are increasing in use, due to their performance and low cost. These drives can potentially produce vibrations because their bandwidth can get close to the vibration modes of mechanical systems [22], [50] and since their control system can produce negative damping over the mechanical vibrations.

The effect of the drive bandwidth is accentuated when there is a backlash on the system, and the shaft is not stiff enough [60]. To avoid the excitation of the vibration modes, the drives and controllers must be designed with a bandwidth far from the natural frequencies of the vibration modes [18], [22], [70]. For this, electromechanical interaction analysis must be executed.

Alternatively, large drive or controller gains, which are used to improve transient responses, can produce negative damping over the mechanical system. Negative damping produces a continuous rise in the torsional vibrations, making the system unstable [71]. In general, adjustable frequency controllers can be found in aircraft actuators, marine systems, wind turbines or robot servo systems [18], [22], [63].

3.3 Effect of Electromechanical Interaction

The effect of the electromechanical interaction on the mechanical system is the generation of torsional vibrations. Depending on the source, these vibrations can make the system unstable if they are generated due to negative damping or resonance, or break the shaft or reduce its lifespan if the oscillations have a high amplitude (load connection or electrical fault) or are constant (pulsating loads) [50], [59].

In general, the effect of stresses on the shaft depends on their magnitude and duration, and the maximum that can be withstood by a material depends on the following two properties [72].

- Ultimate stress: Peak magnitude of oscillation.
- Endurance stress: Duration of oscillation.

Subsequently, the shaft of a system sustains damage if the torque applied is more than the maximum it can stand, or if the maximum amount of vibrations that it can hold has been reached, producing fatigue. For example, pulsating loads can generate vibrations under the maximum allowed but sustained on time. In this case, the lifespan of the shaft is reduced [53]. Likewise, the presence of backlash can produce extended vibrations after a speed change in the system [23], [24], [73], [74]. On the other hand, if the peak of torque is too high, the material can break [50], [75], as it happened in the Mohave Generation Plant in [52].

In particular, for induction machines, overload, fatigue, and corrosion are a common reason for shaft failure [76].

3.4 Electromechanical Interaction in Applications

Electromechanical interaction is a transversal problem that can be found in different applications. In general, every system with drivetrains with multiple stages has electromechanical interaction. In this thesis, the applications susceptible to electromechanical interaction are separated into two categories: Ground Systems, and Transport Systems. In ground systems, the applications of wind turbines, generation and power systems, and traction systems like paper machines and mills are studied. While in transport systems, three subgroups are distinguished, automotive, marine, and aerospace.

The timeline in Figure 3.1 showed the evolution of electromechanical interaction studies. The first cases presented were traction systems, like a paper machine, followed by generation and power systems. Later, wind turbines started to be analysed, and finally, the case of automotive, marine, and aircraft became relevant.

Other areas in which the electromechanical interaction has been investigated is devices and robotics, but they are not discussed for being out of the scope of this thesis. The only exception is the study presented in [77], in which to suppress the electromechanical interaction on devices such as MEMS (RF switches) the method of input shaping was used. This case is relevant because of its similitude to the solution to eliminate torsional vibrations due to electromechanical interaction developed in thesis and presented in chapter 5. Next, the ground and transport cases studied are presented.

3.4.1 Ground Systems

Ground systems are the primary area of research in which electromechanical interaction has been analysed, and can be divided into three: traction systems, and generation – power systems, wind turbines.

3.4.1.1 Traction Systems

Usually, traction systems such as rolling mill, and paper machines have low natural frequencies or vibrations modes (10-20Hz) because their shafts are long and henceforth have low stiffness [23], [24], [55], [78]. As the natural frequencies are low, they can be of the same order of the drive ones, and so these systems are susceptible to electromechanical interaction like vibrations or resonances. As most traction systems have reducers is usual to find backlash, which makes the duration of the vibrations longer [24].

Moreover, these systems work with servo drives [76], [79], which are affected by the torsional vibrations produced by disturbances due to misalignment, unbalance, or mechanical pulsating loads [23].

3.4.1.2 Generation – Power Systems

In the case of power systems, load connections, such as step load and pulsating loads do not produce electromechanical interaction because the whole power system controls their switching and not only one generator. However, grid faults, sub-synchronous currents, and machine controllers are known to excite torsional modes since early 1970 when the shaft of the Mohave Station broke due to electromechanical interaction [52].

To minimise the effect of grid faults or electrical system disturbances, such as breakers, the mechanical systems are designed to have high damping or frequencies far from the electrical ones [51], [57], [59], [80]. Instead, to avoid the effect of sub-synchronous currents, the connection of capacitances close to the machines is studied, and observers strategies used [18], [81], [82].

3.4.1.3 Wind Turbines

In wind turbines, which operate with variable speed controllers, the control systems, and the grid faults can be sources of electromechanical interaction. The power system disturbances or faults can produce vibrations on the mechanical components of the generator [83], [84] and the gearbox can extend its duration due to backlash [18]. Moreover, the control system can induce negative damping on the shaft, and resonance must be avoided [21]. Also, in some configurations, flywheels, which are susceptible to the vibrations, are used to store energy [21].

3.4.2 Transport Systems

3.4.2.1 Automotive Systems

Internal combustion engines are being replaced by electric and hybrid vehicles, which reduce the emission and the fuel consumption. These vehicles use integrated powertrains to reduce size, weight, and cost. However, integrated powertrains have no mechanical dampers, such as the clutch, flying wheel, and flexible joints, which were present in internal combustion engines. Therefore, the electric motor is directly coupled to the mechanical system, and perturbations in the electrical system can be passed into the mechanical one, increasing the wear [37], [85], [86]. Strategies to eliminate the mechanical vibrations through the power system control are being studied in [85], [86].

3.4.2.2 Marine Systems

Marine systems have increased their power system considerably in the last decades since their mechanical and hydraulic power systems are being replaced with electrical ones. A higher electric system increases the design flexibility, optimises the power management, reduces the fuel consumption and the maintenance, and increases operational flexibility [65], [87].

In the more electric marine systems, auxiliary loads as cargo handling equipment, sensor and navigation systems, and passenger and crew amenities have been integrated using variable speed propulsion drives [63]. Consequently, resonance and negative damping must be analysed [63]. Likewise, marine systems have instability due to waves, which can produce pulsating torques and hence torsional vibrations on the mechanical system [18], [65]. These effects have to be accounted for on the drive, to avoid further problems.

A particular research case on marine systems is the one from the AMEPS project [87] in which different universities have come together to study and integrate different parts of the marine system.

3.4.2.3 Aerospace Systems

Electromechanical interaction on aerospace systems has been known since its beginning, but most studies on the topic are new and have been presented in [18], [19], [88] by T. Feehally and G. Moore.

As with marine systems, new aircraft have higher power demands as their hydraulic and mechanical systems are being replaced by electrical ones. Higher electrical power demand implies that larger disturbances pass to the mechanical system.

Nowadays different electrical loads can be found: high powered, transient (e.g. actuators), pulsating, or constant power (e.g. motor driven pumps). Each of these loads can affect the system in a different way, for example, pulsating loads can produce resonances, and high power and transient loads can create torque peaks. Moreover, the aircraft systems have variable speed, which makes the study of its control necessary to review to avoid negative damping and resonance [17].

3.5 Solutions

The solutions found in the literature to minimise the effects of electromechanical interaction in the different applications can be separated into three groups: System Analysis, System Design and Controller Design. In the first case, the system has been analysed to know which are the natural frequencies of the mechanical system and avoid them. In the second, the applications are being designed to prevent the cases in which electromechanical interaction are found. Finally, on the third case, the control systems are being adapted to minimise the effect of electromechanical interaction.

3.5.1 System Analysis

In most electromechanical interaction studies to avoid torsional vibrations and resonance, the electromechanical system has been analysed. Once the system is known, the vibration modes or natural frequencies of the mechanical system can be identified and avoided [18], [56], [57], [67], [81].

To analyse the vibration modes, the system must be modelled. Since the modelling of the electrical and mechanical system has high computational requirements (computer time, program size and data space), reduction techniques must be used [57]. For example, on the first electromechanical interaction studies, due to computational processing limitations, the electrical system was modelled independently [57], and then only its torque was applied to a model of the mechanical system.

Likewise, in most models, the non-linearity of the mechanical system, such as backlash and torsional coupling, are simplified [56]. However, as studies have shown that in ground applications, such as a mill, the backlash is a source of torsional vibrations that can affect the electrical drive, its effects have been modelled in [74].

More improvements on the modelling have been made in [54], in which a new modelling approach for pulsating torques that helps with the integration of the overall model has been proposed. In [59], [76] the fatigue of the system has been modelled. In [65], [87] the electromechanical interaction of a marine system is modelled, and in the study of wind turbines typically the mechanical model FAST is used [83].

Despite the frequent use of this methodology to avoid torsional vibrations, in [59] is mentioned that predicting the values of the frequencies has not been enough to predict the vibrations produced by electromechanical interaction in cases such as the sub-synchronous currents. For this reason, the solutions of the next sections are studied.

3.5.2 System Design

As presented in the last case, most initial studies consisted of modelling the system and then identifying the natural frequencies to avoid them. One approach is to design the controllers to operate at different bandwidth, which is presented in section 3.5.3. The other method, which was initially used, was to design the mechanical components, such as shaft and inertias to move the vibration modes far from possible resonances [18], [23].

Two methods are used to avoid vibrations: increase the damping of the mechanical system, or change the stiffness to move the natural frequencies values.

3.5.2.1 Damping

A higher damping ratio produces less vibration on a system as shown in Figure 3.4. For this reason, when possible it is desired to increase the damping of the system. However, higher damping requires higher weight and size, which is not desired in aircraft applications [21], [24].

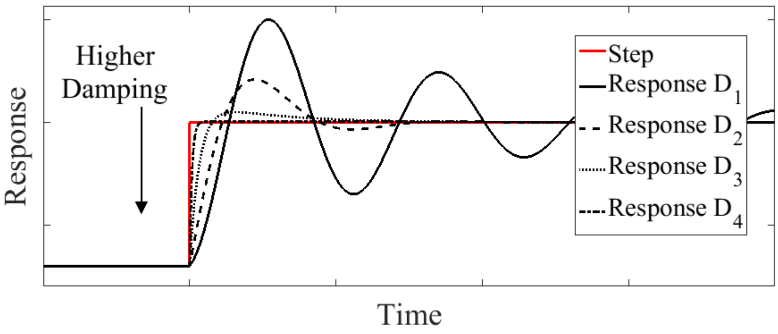

Figure 3.4: Damping plot.

3.5.2.2 Stiffness

From the mechanical point of view, there are two possible cases for electrical machines, to have rigid or flexible shaft:

- Rigid shaft: the lowest frequency (critical speed) is 130% or more than the maximum operating speed. They have no problem in operating at a wide range of speeds.
- Flexible shaft: is the case in which the critical speed is under 130% of the maximum speed. The flexible shaft is recommended for machines that

operate at constant speed, but not for adjustable speed operations, as at some speeds there may be high vibrations [89].

Most torsional vibrations are due to systems with a flexible shaft and hence low stiffness. For this reason, increasing the stiffness of the mechanical system, mainly of the shaft has been a traditional solution to avoid interaction and resonance [21], [23]. Higher stiffness can be obtained using a shaft with larger diameters, but this is not always sought as also the weight increases. For this reason, in [24] is presented the use of hollow shafts to increase stiffness and not weight. Nonetheless, this method can be expensive in a system with space restrictions as marine and aircraft ones [78].

3.5.3 Controller Design

A standard closed-loop control is shown in Figure 3.5. In it, a signal is being controlled, in general, the speed or the voltage of the machine. Due to this control, a step or pulsating torque is being applied to a mechanical system $G_p(s)$, and this generates vibrations on the shaft.

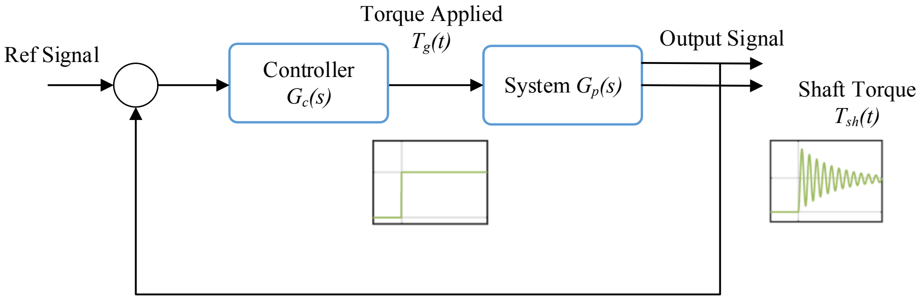

Figure 3.5: Closed-loop diagram.

To avoid extreme vibrations, like resonance, the first step is to design the controller operating at a different bandwidth without overlapping the natural frequency of the shaft [21], [22]. However as this does not eliminate all the vibrations, other strategies are desired. To minimise the torsional vibrations in the drivetrain, many strategies have been developed recently and can be categorized into three groups: Ramp torque control, torque feedback in the control loop, use of anti-resonant filters in the control loop.

3.5.3.1 Ramp Torque Control

The use of electrical drives that apply a ramp torque (or similar) to the mechanical system, as shown in Figure 3.6., has been proposed in [20], [78], [90] [62], [78], [90]. The application of a ramp torque to the mechanical system instead of a step, can eliminate the excitation of torsional vibrations or reduce them. When the proper slope is chosen, the torque does not excite the mechanical natural frequencies [20]. On the other hand, slope values different from the optimal, reduce the vibrations on the drivetrain because the dynamic response of a ramp is slower than a step [19], [62], [78], [90]. However, this solution is not always desirable, since a ramp connection can take a long time, extending the duration of the transient response and slowing down the system dynamics.

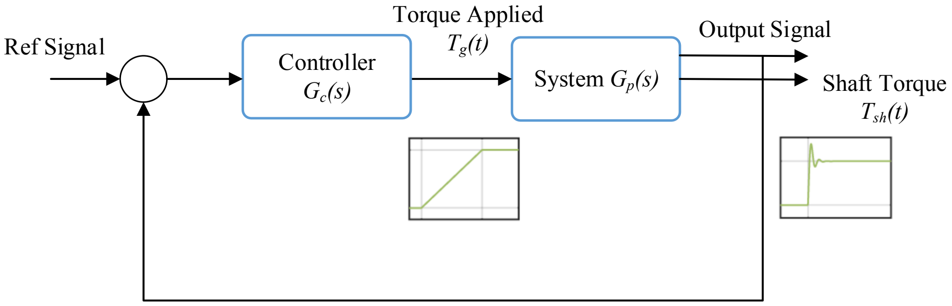

Figure 3.6: Closed-loop diagram with ramp torque.

3.5.3.2 Torque Feedback

Another method to suppress the torsional vibrations is to feedback the measured torque to the output of the controller as shown in Figure 3.7. The feedback will compensate the disturbance in the torque. Since not every system has torque measurements, observers have been used in [22], [55], [82]. The observers estimate the torque on the system based on the system models and thus depend on the knowledge of the stiffness K, inertia J, and the damping D of the mechanical system.

Since these parameters are not always easy to derive [78], others method to obtain the torque have been proposed. In [91], the shaft torque is estimated as the difference of angles at both ends. Another alternative, presented in [64], [92], is the use of a repetitive controller instead of an observer. The repetitive controller can reduce the torsional vibration of the V/f controller of an induction motor with pulsating torque load.

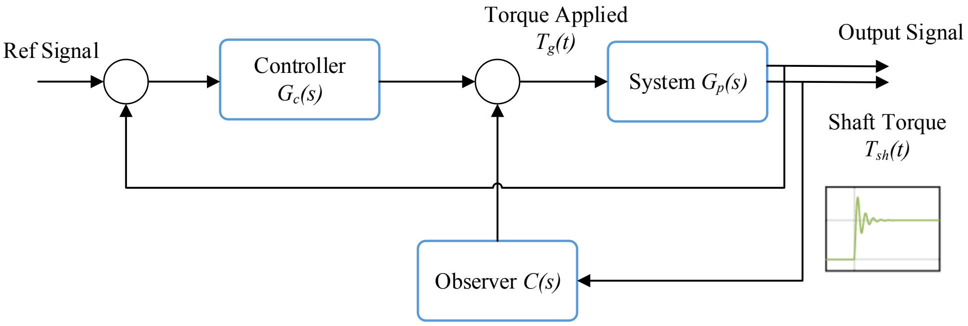

Figure 3.7: Closed-loop diagram torque feedback.

Like in the case of the ramp connection, the main problem of this type of strategy is that the controller reduces torque applied to the system at once, slowing down the connection. Since the response of the mechanical system is not directly analysed, the strategies do not give an optimal solution and slow down the dynamics of the overall system.

3.5.3.3 Anti-resonant Filter

Another approach to reduce the vibrations is to use a filter in the closed loop as shown in Figure 3.8. Contrary to the last case, the filter connected in line with the controller reduces the torsional vibrations by studying the mechanical system and filtering the frequencies that produce the excitation. The most common filters used are low pass, notch, and input shaping [77], [79].

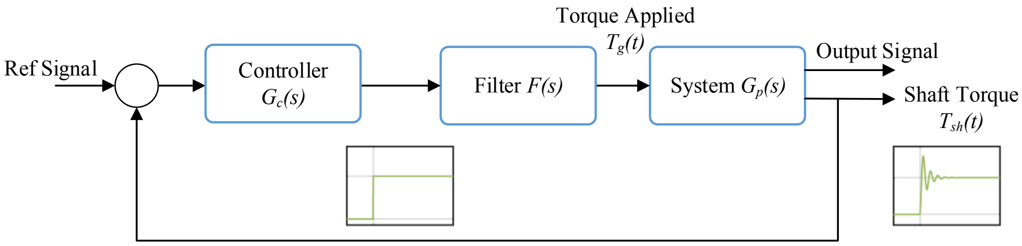

Figure 3.8: Closed-loop diagram with filter.

The low pass and phase-lead compensation filters are used to reduce the gain of the resonance frequency. These filters are easy to apply, but are not efficient for low resonant frequencies, since they filter a wide range of frequencies and not the resonant frequency alone [55], [78], [79].

To overcome this problem, notch filters are used. A notch filter is a filter designed to use the numerator roots or zeros to cancel each resonant poles. However, while these filters can be designed to cancel more than one frequency, they work better filtering one natural frequency at the time. In practice, they are used to cancel one natural frequency in traction systems such as rolling mill drives, paper machines, and machining centres [24], [55], [60], [78], [79].

A different approach was taken in [77], were input shaping was used for micro-electromechanical system (MEMS) devices used in the computer storage and automobile industry. Input shaping consists in modelling the shape of a load or torque applied such that the excitation of the mechanical natural frequencies is cancelled [93]. The input shaping strategy and its derivative the Posicast compensator are further explained in chapter 5.

Since anti-resonant filters, such as the input shaping, are designed considering the drivetrain torsional vibrations, the response of the system is faster than the one using torque feedback and applying directly a ramp connection. For this reason, the strategies proposed in this thesis are centred on this solution.

Moreover, in general the solutions to reduce or eliminate the excitation of torsional vibrations have been centred in the control of the machine. This thesis proposes to apply the input shaping strategies directly to the loads being connected. This approach is taken since the load connection following patterns, which can be given by input shaping (or Posicast compensator), is already present in aircraft systems. For example, the switches used to connect loads present a rebound in their connection which can be seen as a short pulse. Thus, the application of these strategies does not disrupt the dynamics of the electrical system.

3.6 Summary

In this chapter, the sources, effects, applications and solutions of electromechanical interaction have been presented. It has been shown that the problem is transversal to diverse engineering fields and that due to the development of more electric systems, the studies on electromechanical interaction are increasing.

However, as most of the electromechanical interaction studies are associated with the modelling of the system and simulation, there is a lack of feasible solutions to eliminate the torsional vibrations produced. Moreover, all the solutions that use controllers to diminish the vibrations are focused on adapting the controller of the machine, and do not consider the dynamics of the mechanical system. Furthermore, these control strategies do not take into consideration the load or timings requirements. Contrary, the use of anti-resonant filters, such as the strategies given by input-shaping, allow the obtention of an optimal response. Since their application is focused on the mechanical system model, the time connections are faster than the one obtained in torque feedback cases.

In the case of aircraft systems, which is studied in this thesis, few studies have been carried out, and no solutions have been presented. For this reason, in this thesis strategies to eliminate the electromechanical interaction centred on input shaping strategies are going to be proposed. Next chapters present a study on the sources of electromechanical interaction in aircraft system and a power management system (PMS) to eliminate these effects.

Chapter 4

Analysis of Electromechanical Interaction

4.1 Introduction

In this chapter, the electromechanical interaction in aircraft systems is introduced. The effects of step load connections, pulsating loads, and the negative damping of a generator controller are studied. To analyse this interaction, the electromechanical interaction system is modelled using reduction techniques for the drivetrain and the electrical system.

The rest of the chapter is organised as follows. First model reductions are described. Then, the electromechanical system model is presented. Thirdly, the stability of the system and the vibration modes are assessed. Fourthly, the effect of electrical load connections over the mechanical system is shown. After, the effect of a Generator Control Unit (GCU) on the mechanical system is analysed. Finally, the chapter summary is presented.

4.2 System Modelling

As presented in chapter 3, for the studies of electromechanical interaction the simplification of the systems has always been relevant. The presence of low and high natural frequencies of the mechanical and electrical system implies that simulations take a high time to run. To decrease the complexity of systems, and hence reduce the number of equations and simulation time, systems are reduced [94], [95]. In the electrical system, the reductions are presented in terms of modelling precision levels, while in the mechanical system, reduction strategies that allow the maintaining of the desired accuracy are going to be shown. Next, the mechanical and electrical system modelling and their reduction strategies are presented.

4.2.1 Mechanical System Modelling

When working with mechanical models, the prediction of the exact torsional oscillations and component life are complex and time-consuming. However, the identification of torsional vibrations and the potential problems associated use simplified systems [50]. Because of this, the systems can be reduced to model only the lower vibration modes or natural frequencies, which allows the analysis of electromechanical interaction as shown in [18], [88]. Therefore, as shown in [18], [88], [96], a turbine drivetrain can be represented as a lumped mass model as the one from Figure 4.1. The system is modelled by equation (4.1), which is formed by the inertias (J), stiffness (K) and damping (D) matrices, and the angular displacements θ, speeds $\dot{\theta}$, accelerations $\ddot{\theta}$ vectors. u is the vector of externally applied torques. Rotating parts, such as machines, flywheels, and gears are represented as inertias, while the connections, such as shafts and couplings, are represented in terms of stiffness and damping.

$$J\ddot{\theta} + D\dot{\theta} + K\theta = u \tag{4.1}$$

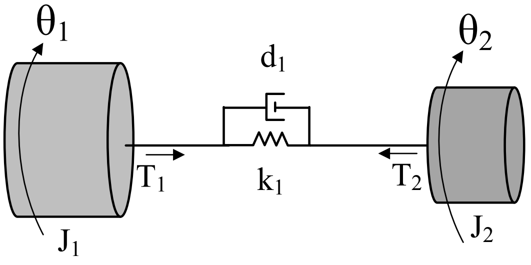

Figure 4.1: Lumped mass system.

Next, the modelling of the components of the lumped mass system is presented. After, reduction methods to decrease the computational power needed are presented.

4.2.1.1 Modelling

In this section, the modelling of the inertia, stiffness, and damping, along with its equations are presented.

Inertia

The mass moment of inertia J_1 is described as the object's opposition to an absolute angular acceleration $\ddot{\theta}_1$ measured in an inertial frame of reference, which produces a reaction torque T_1 as shown in equation (4.2).

$$T_1 = J_1\ddot{\theta}_1 \tag{4.2}$$

The inertia value depends on the axis of rotation. Therefore, each flywheel or gear used in this thesis is modelled as a rotating cylinder, with inner radius r_i, outer radius r_o, mass M, or density ρ and length L its value is given by equation (4.3) [37].

$$J = \frac{\pi\rho L}{2}(r_o^4 - r_i^4) = \frac{1}{2}M(r_i^2 + r_o^2) \tag{4.3}$$

Torsional Stiffness

The stiffness k of a component is the opposition to a relative angular displacement between two points (θ_1 and θ_2) which results in a reaction torque T_s as shown in equation (4.4) [37].

$$T_S = k(\theta_1 - \theta_2) \tag{4.4}$$

The stiffness of a solid shaft is calculated by equation (4.5), with G the material shear modulus, r the shaft radius, and L the shaft length.

$$k = \frac{G\pi r^4}{2L} \tag{4.5}$$

Damping

The damping of an element d is any effect that tends to reduce the vibrations, for example the internal friction. It is described by equation (4.6), in which $\dot{\theta}_1$ and $\dot{\theta}_2$ are the speed at both ends of the shaft and T_d is the produced torque [37].

$$T_d = d(\dot{\theta}_1 - \dot{\theta}_2) \tag{4.6}$$

4.2.1.2 Reduction Methods

To simplify the number of equations of a mechanical system and add constraints to the system, the equation system are reduced using methods such as Direct Reduction, Guyan Reduction, and Balance Reduction [94], [95], [97]–[99].

In all of these methods, a reduction matrix T, which obeys equation (4.7), is used. The methodology to obtain T changes in each method. In the Direct Reduction, equations that relate the states to reduce to the remaining states must be found using the characteristics of the system. For the Guyan Reduction, the states of the system are divided into masters and slaves. The slaves are written as a function of the master and reduced [100]. The Balance Reduction method is applied to the state space system and is able to reduce the order of a large-scale system independently if all the variables are decoupled or not. This method, was originally developed by Enns in [101], and consists in selecting the states that are less observable or controllable for elimination, previous balancing the system, as explained by Moore in [102].

As a result, of the Direct, Guyan, and Balanced reduction, the reduction matrix T is replaced on the lumped mass system as shown in equations (4.8) and (4.9), and the reduced system from equation (4.10) is obtained.

$$T'T = I \tag{4.7}$$

$$\left.\begin{aligned} \theta_R &= T'\theta \\ u_R &= T'u \end{aligned}\right\} \tag{4.8}$$

$$\left.\begin{aligned} J_R &= T'JT \\ D_R &= T'DT \\ K_R &= T'KT \end{aligned}\right\} \tag{4.9}$$

$$J_R\ddot{q}_R + D_R\dot{q}_R + K_R q_R = u_R \tag{4.10}$$

In this thesis, the lumped mass system of equation (4.1), which is a model reduction representation of the system, is used. Moreover, to add constraints on the gearbox speed, Direct Reduction is applied as shown in section 4.3.

4.2.2 Electrical System Modelling

In the case of the electrical system modelling, to maximise the computational efficiency, while keeping the required accuracy, the multilevel paradigm, presented in [47], is used. As shown in Figure 4.2, four modelling levels with different complexities can be identified: Architectural, Functional, Behavioural, and Component. The lower in the pyramid, the more detail is needed.

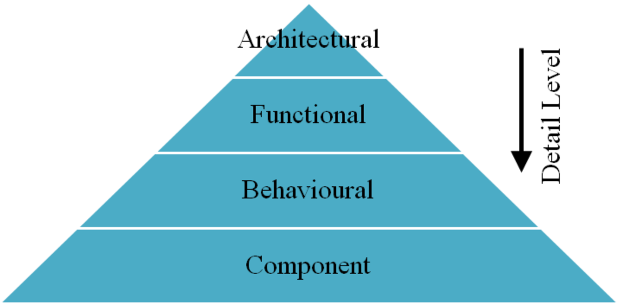

Figure 4.2: Multilevel modelling of electrical systems (Data from [47]).

The Component Level models the behaviour of each element up to the region of MHz, such as solid-state switches. Still, as high-frequency switching makes the system slower, the Behaviour Level models the system up to kHz, including converter switching and harmonics and non-linearity. In the Functional Level, the components are modelled up to hundreds of Hz (200-300Hz) with a time waveform accuracy of 5% respect to the Behaviour Level. Its primary focus is the power system performance, stability, and transient response. The switching of the converters is not modelled. Finally, Architecture Level computes the steady state of a system and is typically used to calculate weight, and cost of systems [103].

The transients of each component are not necessary to study the electromechanical interaction. Therefore, in this thesis, the Functional Level modelling is used, and the following simplifications are assumed:

- Reduced systems of the mechanical and electrical systems are used. The drivetrain reduction is based on the studies presented by Gareth Moore and Thomas Feehally in [18], [19]. While for the electrical case, the system is DC because from a control point of view its behaviour is equivalent.

- Only the connection of resistive loads is studied. Non-linear loads are proposed for further research. Moreover, the electrical loads are connected through IGBTs to the generator. No converter is used to avoid the modelling of the switching.
- The effect of the machine over the transversal vibrations is not studied. Only the critical speeds are identified.
- No grid instabilities are considered (no negative impedance due to converters, or three phase).

4.3 Functional Modelling of Electromechanical Systems

In this section, the system used to show the electromechanical interaction is presented. As shown in Figure 4.3, the electromechanical interaction system is composed of the engine, drivetrain (shafts and gearbox), generators and the electrical loads. Next, the modelling of each part of the system is presented.

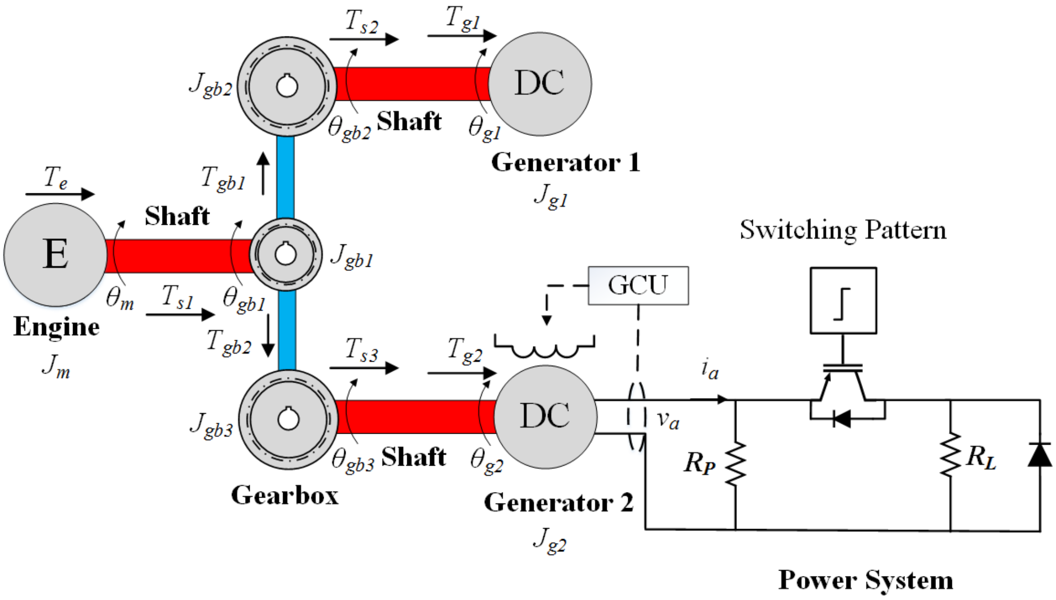

Figure 4.3: Electromechanical interaction system.

4.3.1 Modelling of the Drivetrain

Because in an aircraft 95% of the strain energy is concentrated at the generator end, for simplicity the connection between the engine and the two generators is modelled as a shaft connected from the engine spool (middle or high pressure spool according to the engine model) to the generators shaft through a gearbox formed by three inertias as shown in Figure 4.3 [18]. It is assumed there is no backlash in the system since aircraft drivetrains are designed to have a minimal one, as stated in [19]. Also because backlash only happens with full torque reversals and those are rare.

Furthermore, as mentioned in section 4.2.1, the mechanical system can be represented as a lumped mass model. As shown in Figure 4.4, the electromechanical interaction system is modelled by 6 inertias: the engine (J_m), the gearbox (J_{gb1},J_{gb2},J_{gb3}) and generator rotors (J_{g1} and J_{g2}). These inertias are connected through shafts (red connections) or directly in the case of the gears (blue connections). Each connection has an associated stiffness and damping. The stiffness and damping of each shaft are given by k_{s1}, k_{s2}, and k_{s3} and d_{s1}, d_{s2}, and d_{s3} respectively, while the gear mesh stiffness and damping are given by k_{gb1}, k_{gb2} and d_{gb1} and d_{gb2} respectively.

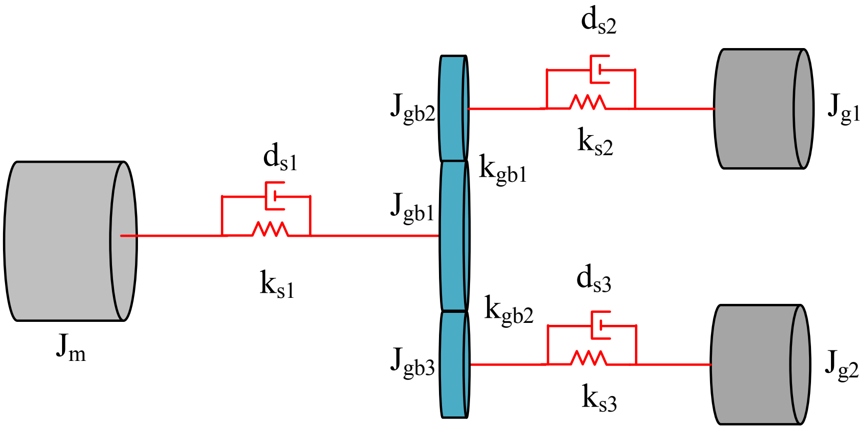

Figure 4.4: Mechanical layout.

The torque acting over each inertia is shown in Figure 4.3. Their modelling was described in section 4.2.1.1. For the engine inertia J_m (in kgm^2), equation (4.11) models the torque applied, with T_E the torque (in Nm) applied by the engine, and T_{s_1} the torque (in Nm) transported by the shaft connecting the engine J_m through the gearbox J_{gb_1}. T_{s_1} can be calculated by equation (4.12), with θ_m, $\dot{\theta}_m$, and $\ddot{\theta}_m$, the position (in rad), speed (in rad/s), and acceleration (in rad/s^2) of the engine inertia, and θ_{gb_1}, $\dot{\theta}_{gb_1}$, and $\ddot{\theta}_{gb_1}$ the values associated with the gear.

$$J_m\ddot{\theta}_m = T_E - T_{s_1} \tag{4.11}$$

$$T_{s_1} = k_{s_1}\left(\theta_m - \theta_{gb_1}\right) + d_{s_1}(\dot{\theta}_m - \dot{\theta}_{gb_1}) \tag{4.12}$$

The equations for the rest of the system are obtained repeating the same methodology used for the engine inertia and are shown in equations (4.13) and (4.14). With T_{s_1}, T_{s_2} and T_{s_3} the shafts torque, T_{gb_1} and T_{gb_2} the gearshaft torque, and $\theta_{gb_1}, \theta_{gb2}, \theta_{gb3}, \theta_{g1}, \theta_{g2}$ the angles associated with each inertia as shown in Figure 4.3 and Figure 4.4.

$$\left.\begin{aligned}
J_{gb_1}\ddot{\theta}_{gb_1} &= T_{s_1} - T_{gb_1} - T_{gb_2}\\
J_{gb_2}\ddot{\theta}_{gb_2} &= T_{gb_1} - T_{s_2}\\
J_{gb_3}\ddot{\theta}_{gb_3} &= T_{gb_2} - T_{s_3}\\
J_{g_1}\ddot{\theta}_{g_1} &= T_{s_2} - T_{g_1}\\
J_{g_2}\ddot{\theta}_{g_2} &= T_{s_3} - T_{g_2}
\end{aligned}\right\} \tag{4.13}$$

$$\left.\begin{aligned}
T_{s_2} &= k_{s_2}\left(\theta_{gb_2} - \theta_{g_1}\right) + d_{s_2}(\dot{\theta}_{gb_2} - \dot{\theta}_{g_1})\\
T_{s_3} &= k_{s_3}\left(\theta_{gb_3} - \theta_{g_2}\right) + d_{s_3}(\dot{\theta}_{gb_3} - \dot{\theta}_{g_2})\\
T_{gb_1} &= k_{gb_1}\left(\theta_{gb_1} - \theta_{gb_2}\right) + d_{gb_1}\left(\dot{\theta}_{gb_1} - \dot{\theta}_{gb_2}\right)\\
T_{gb_2} &= k_{gb_2}\left(\theta_{gb_1} - \theta_{gb_3}\right) + d_{gb_2}(\dot{\theta}_{gb_1} - \dot{\theta}_{gb_3})
\end{aligned}\right\} \tag{4.14}$$

Sorting out equations (4.11)-(4.14), the lumped mass system of equation (4.15) is obtained. The inertia matrix J, the stiffness matrix K, the damping matrix D, the input vector u, and the variables vector of the second order system θ are given in equation (4.16).

$$J\ddot{\theta} + D\dot{\theta} + K\theta = u \tag{4.15}$$

$$\left.\begin{gathered}
J = \begin{bmatrix} J_m & 0 & 0 & 0 & 0 & 0 \\ 0 & J_{gb_1} & 0 & 0 & 0 & 0 \\ 0 & 0 & J_{gb_2} & 0 & 0 & 0 \\ 0 & 0 & 0 & J_{gb_3} & 0 & 0 \\ 0 & 0 & 0 & 0 & J_{g_1} & 0 \\ 0 & 0 & 0 & 0 & 0 & J_{g_2} \end{bmatrix} \\
D = \begin{bmatrix} d_{s_1} & -d_{s_1} & 0 & 0 & 0 & 0 \\ -d_{s_1} & d_{s_1} + d_{g_1} + d_{g_2} & -d_{g_1} & -d_{g_2} & 0 & 0 \\ 0 & -d_{g_1} & d_{g_1} + d_{s_2} & 0 & -d_{s_2} & 0 \\ 0 & -d_{g_2} & 0 & d_{g_2} + d_{g_3} & 0 & -d_{s_3} \\ 0 & 0 & -d_{s_2} & 0 & d_{s_2} & 0 \\ 0 & 0 & 0 & -d_{s_3} & 0 & d_{s_3} \end{bmatrix} \\
K = \begin{bmatrix} k_{s_1} & -k_{s_1} & 0 & 0 & 0 & 0 \\ -k_{s_1} & k_{s_1} + k_{g_1} + k_{g_2} & -k_{g_1} & -k_{g_2} & 0 & 0 \\ 0 & -k_{g_1} & k_{g_1} + k_{s_2} & 0 & -k_{s_2} & 0 \\ 0 & -k_{g_2} & 0 & k_{g_2} + k_{g_3} & 0 & -k_{s_3} \\ 0 & 0 & -k_{s_2} & 0 & k_{s_2} & 0 \\ 0 & 0 & 0 & -k_{s_3} & 0 & k_{s_3} \end{bmatrix} \\
u = \begin{bmatrix} T_E \\ 0 \\ 0 \\ 0 \\ -T_{g_1} \\ -T_{g_2} \end{bmatrix} \\
\theta = \begin{bmatrix} \theta_m \\ \theta_{gb_1} \\ \theta_{gb_2} \\ \theta_{gb_3} \\ \theta_{g_1} \\ \theta_{g_2} \end{bmatrix}
\end{gathered}\right\} \qquad (4.16)$$

Because the gear mesh stiffness is assumed infinite, and its damping zero, the speeds $\dot{\theta}_{gb_1}$, $\dot{\theta}_{gb_2}$, and $\dot{\theta}_{gb_3}$ can be related by equations (4.17), with r the speed ratio between gear J_{gb_1} and gears J_{gb_2} and J_{gb_3}. Then, using Direct Reduction and equations (4.17), the transformation matrix of equation (4.18) is found. Finally, the reduced matrices J_R, K_r, D_R, u_R, and θ_R are obtained as shown in equations (4.19).

$$\left.\begin{aligned}\dot{\theta}_{gb_1} &= r\dot{\theta}_{gb_2}\\ \dot{\theta}_{gb_1} &= r\dot{\theta}_{gb_3}\end{aligned}\right\} \quad (4.17)$$

$$T = \begin{bmatrix} r_1 & 0 & 0 & 0\\ 0 & r_1 & 0 & 0\\ 0 & 1 & 0 & 0\\ 0 & 1 & 0 & 0\\ 0 & 0 & 1 & 0\\ 0 & 0 & 0 & 1 \end{bmatrix} \quad (4.18)$$

$$\left.\begin{aligned} J_R &= T'JT\\ K_R &= T'KT\\ D_R &= T'DT\\ u_R &= T'u = \begin{bmatrix} T_E\\ 0\\ -T_{g_1}\\ -T_{g_2}\end{bmatrix}\\ \theta_R &= T'\theta = \begin{bmatrix}\theta_m\\ \theta_{gb}\\ \theta_{g_1}\\ \theta_{g_2}\end{bmatrix}\end{aligned}\right\} \quad (4.19)$$

The drivetrain is related to the rest of the system through the torque applied, T_E, T_{g_1} and T_{g_2}. In the next section the engine and the electrical system are modelled in order to obtain these values.

4.3.2 Modelling of the Engine

As shown in equation (4.19), the engine applies a torque T_E on the drivetrain. In this thesis the modelling of the engine is not in study, hence it can be considered as a big inertia that keeps the speed constant. Consequently, the torque T_E is going to be modelled as a linear equation depending on the engine speed ($\dot{\theta}_m = \omega_m$) as shown in (4.20), in which A_{Te} and B_{Te} are the slope and the position constant.

$$T_E = A_{Te}\omega_m + B_{Te} \quad (4.20)$$

Figure 4.5 shows the linear equation that describes T_E. The value of A_{T_e} and B_{T_e} are obtained as shown in equations (4.21). Since the torque is inversely proportional to the speed, the value of the slope is negative. To keep the speed value almost constant, and hence represent the engine when is not in idle, the slope must be steep.

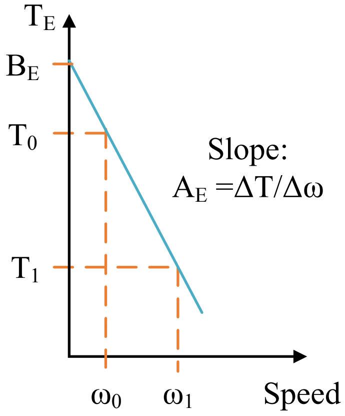

Figure 4.5: Linear behaviour engine.

$$\left.\begin{aligned} A_{T_e} &= \frac{T_0 - T_1}{\omega_0 - \omega_1} \\ B_{T_e} &= T_0 - \frac{T_0 - T_1}{\omega_0 - \omega_1}\omega_0 \end{aligned}\right\} \tag{4.21}$$

The value of T_E is integrated with the rest of the system in section 4.3.4. Next the generator and electrical power system are modelled.

4.3.3 Modelling of the Generator and Electrical Power System

In this section, the relationship between the generators and the mechanical system is modelled. As both electrical systems and generators are equivalent, only one of them is modelled (T_{g_2}), while the other is considered to be electrically disconnected, assuming $T_{g_1} = 0$ all the time. Moreover, if the values of inertias and stiffness of the system are symmetrical, and the gears receive exactly the same torque, some torsional modes are not excited. This is known as the vibration absorber and is shown in Appendix II.

Since the modelling is based on the Functional Level described in section 4.2.2, the aircraft electrical power system presented in chapter 2 is simplified. As shown in

Figure 4.3 and Figure 4.6, the electrical power system is represented by resistive banks ($R_{L_1}, R_{L_2}, \dots, R_{L_n}$) connected to the generator through IGBTs. The IGBTs are switched on and off only to connect and disconnect the loads. Moreover, the generator is modelled as a DC machine as from a control point of view, the control of a DC and AC system are the same.

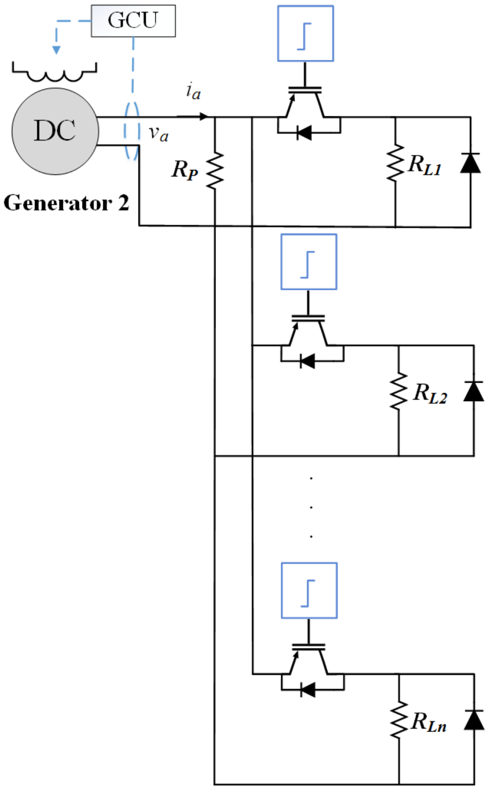

Figure 4.6: Electrical power system.

The generator is modelled as a single phase DC machine operating with independent field connection. Its equations are given by (4.22) and (4.23), in which k is the rotational inductance, i_f is the field current, i_a is the armature current, E is the induced voltage, v_a is the armature voltage at the terminals of the machine, R_a and L_a are the armature resistance and inductance respectively, and V_0 is the voltage drop in the machine brushes.

$$E = R_a i_a + L_a \frac{di_a}{dt} + v_a + V_0 \tag{4.22}$$

$$E = k i_f \dot{\theta}_{g_2} \tag{4.23}$$

The generator armature voltage v_a can be kept reasonably constant using a Generator Control Unit (GCU), which is shown in section 4.6. However, in most of this thesis the system operates without a GCU, and the field current i_f is kept constant instead.

The electrical power system is modelled as a resistive load R_P always connected in parallel to the machine terminal, and resistive loads $R_{L_1}, R_{L_2}, \dots, R_{L_n}$, connected through IGBTs to the machine as shown in Figure 4.6. The IGBT allows the switching of the electrical loads according to different connection patterns which are studied in this thesis and presented in chapter 5. The resistance R_P is a protection resistance to guard the machine of the inductance current when the loads R_{L_n} are disconnected. To protect the IGBTs during the disconnection, diodes are connected parallel to the load resistances.

The electrical loads are related to the generator through equation (4.24), in which R_{eq} is the equivalent resistance of the parallel connection of R_P and the load resistances R_L.

$$v_a = R_{eq} i_a \tag{4.24}$$

Combining equations (4.22) - (4.24), the state variable of the electrical power system, i_a, is obtained and given by equation (4.25).

$$\frac{di_a}{dt} = \frac{1}{L_a}\left(k i_f \dot{\theta}_{g_2} - \left(R_a + R_{eq}\right) i_a - V_0\right) \tag{4.25}$$

The torque applied to the mechanical system is given by equation (4.26), in which T_e is the torque producing the electromotive force and $T_{windage}$ is the torque consumed by the windage of the machine. In Appendix I was shown that the windage torque of the machine is small, therefore, the torque applied to the mechanical system is modelled as the torque that produces the electromagnetic force T_e and shown in equation (4.27). When operating with constant field current, the torque applied to the mechanical system depends only on the armature current.

$$T_{g_2} = T_e + T_{windage} \tag{4.26}$$

$$T_{g_2} = T_e = k i_f i_a \tag{4.27}$$

Finally, equation (4.25) and (4.27) are integrated to the drivetrain model as shown in the next section.

4.3.4 Integrated Model

The equations (4.19)-(4.27) can be modelled in Simulink and PLECS, which allows the simulation of the electromechanical interaction system. To study the stability of the integrated electromechanical system, the state system must be obtained. Consequently, the torques T_E, T_{g_1}, and T_{g_2}, along with the state i_a must be connected to the system of equation (4.19).

In the case of the engine, the engine's torque is modelled linearly by equation (4.20) and depends on the speed $\dot{\theta}_m$. Hence, only the damping matrix D_R and the input u_R changes as shown in equations (4.28). The new damping matrix includes the slope of the engine linear equation A_{T_e}, while the input of the system have the equation constant value B_{T_e}. Keeping the matrices J_R and K_R presented in section 4.3.1, the lumped mass system equation (4.29) is obtained.

$$\left.\begin{aligned} D_{Engine} &= D_R + \begin{bmatrix} -A_{T_e} & 0_{3x1} \\ 0_{1\mathrm{x}3} & 0_{3x3} \end{bmatrix} \\ u_{Engine} &= \begin{bmatrix} B_{T_e} \\ 0 \\ -T_{g_1} \\ -T_{g_2} \end{bmatrix} \end{aligned}\right\} \tag{4.28}$$

$$J_R \ddot{\theta}_R + D_{Engine} \dot{\theta}_R + K_R \theta_R = u_{Engine} \tag{4.29}$$

The state space system, given by equation (4.30) can be obtained from the second order lumped mass system as shown in equations (4.31) - (4.32) [95]. The states are given by the angle θ_R and speed $\dot{\theta}_R$ of each inertia, while the input of the system remains the same.

$$\dot{x}_{Engine} = A_{Engine} x_{Engine} + B_{Engine} u_{Engine} \tag{4.30}$$

$$x_{Engine} = \begin{bmatrix} \theta_R \\ \dot{\theta}_R \end{bmatrix} \tag{4.31}$$

$$\left.\begin{aligned} A_{Engine} &= \begin{bmatrix} 0 & I \\ -J_R^{-1}K_R & -J_R^{-1}D_{Engine} \end{bmatrix} \\ B_{Engine} &= \begin{bmatrix} 0 \\ J_R^{-1} \end{bmatrix} \end{aligned}\right\} \tag{4.32}$$

After obtaining the state system of the engine and drivetrain, the effects of the electrical system can be added. The values of $T_{g_1} = 0$ and T_{g_2} given by equation (4.27) are used. Moreover, the state equation for i_a given by equation (4.25) is added to the system. Since the field current i_f is constant, the equations do not need to be linearized.

The state system of the electromechanical interaction, which allows the study of the stability, is shown in equation (4.33) with the matrices and vector given by equations (4.34) and (4.35). In next section, the stability of the described system is analysed, and in sections 4.5 and 4.6 the electromechanical interaction is shown.

$$\dot{x}_T = A_T x_T + B_T u_T \tag{4.33}$$

$$\left.\begin{aligned} A_T &= \begin{bmatrix} A_{Engine} & 0_{8x1} \\ \begin{bmatrix} 0_{1x7} & \frac{ki_f}{L_a} \end{bmatrix} & -\frac{1}{L_a}\left(R_a + R_{eq}\right) \end{bmatrix} \\ B_T &= \begin{bmatrix} B_{Engine} \\ -\dfrac{1}{L_a} \end{bmatrix} \end{aligned}\right\} \tag{4.34}$$

$$\left.\begin{aligned} x_T &= \begin{bmatrix} x_{Engine} \\ i_a \end{bmatrix} \\ u_T &= \begin{bmatrix} u_{Engine} \\ V_0 \end{bmatrix} \end{aligned}\right\} \tag{4.35}$$

4.4 Stability of the System

To study the stability of the electromechanical interaction system the mechanical vibration modes and later the poles of the whole system are analysed. The parameters of the engine and drivetrain are shown in Table 4.1. Their values were chosen to have two mechanical natural frequencies under 100Hz, which are characteristics of aircraft drivetrains. The engine inertia value is 10 times the generator inertia to represent an aircraft engine system and be considered as the drivetrain ground. For the same reason, the constants A_{T_e} and B_{T_e} are chosen to keep the engine speed almost constant. Their values are calculated as shown in equation (4.21) with $T_0 = 100\text{Nm}$, $T_1 = 200\text{Nm}$, $\omega_0 = 1501\text{rpm}$, and $\omega_1 = 1499\text{rpm}$[1] [2], [18], [37], [104]. These constants were chosen to operate with low power to be representative of the parameters used in the experimental test presented in chapter 6.

Table 4.1. Parameters of the engine and the drivetrain.

Parameter	**Value**
Engine Inertia	$J_m = 0.386\ \text{kgm}^2$
Gears Inertia	$J_{gb1} = 0.0093\ \text{kgm}^2$ $J_{gb2} = 4.7e - 4\ \text{kgm}^2$ $J_{gb3} = 0.0091\ \text{kgm}^2$
Generator 1 Inertia	$J_{g1} = 0.0386\ \text{kgm}^2$
Generator 2 Inertia	$J_{g2} = 0.0376\ \text{kgm}^2$
Shaft Stiffness	$k_{s1} = 2.1598e3\ \text{Nm/rad}$ $k_{s2} = 2.2398e3\ \text{Nm/rad}$ $k_{s3} = 2.2398e3\ \text{Nm/rad}$
Shaft Damping	$d_{s1} = 0.5\ \text{Nmrad/s}$ $d_{s2} = 0.5\ \text{Nmrad/s}$ $d_{s3} = 0.5\ \text{Nmrad/s}$
Gearbox Ratio	$r = 2$
Engine Constants	$A_{T_e} = -119.3662\ \text{Nmrad/s}$ $B_{T_e} = 1.8787e4\ \text{Nm}$

---

[1] The speed values are transformed in rad/s before the calculation.

The generator parameters are presented in Table 4.2. Their values are the same as those of the experimental generator which are used for the experimental test in chapter 6 and chapter 7.

Table 4.2. Generator parameters.

Parameter	**Value**
Armature resistance	$R_a = 4.025\ \Omega$
Field resistance	$R_f = 2\ \Omega$
Armature Inductance	$L_a = 0.019\mathrm{H}$
Field Inductance	$L_f = 0.02\mathrm{H}$
Rotational inductance	$k = 0.0713\ \mathrm{ln} - \mathrm{in/A}$
Drop Voltage Brushes	$V_0 = 12.247\ \mathrm{V}$

4.4.1 Torsional Vibration Modes of the System

The vibration modes of the drivetrain are analysed to prove that the reduced electromechanical interaction model in the study is representative of an aircraft drivetrain. For this, the electromechanical interaction of Figure 4.4 is modelled in TorTrans, a Matlab Toolbox written by Seamus Garvey, which allows the analysis of the torsional vibrations of a lumped mass system.

The torsional mode shapes obtained are presented in Figure 4.7. The circles symbolise the inertias, while the red and blue connections denote the shafts and gearbox respectively. The vertical green lines represent the inertias referred angles in each operation mode. It is observed that the system has four modes, a rigid mode at 0Hz (Figure 4.7 (a)), and three vibration modes at 11.98Hz (Figure 4.7 (a)), 38.59Hz (Figure 4.7 (b)), and 109.7Hz (Figure 4.7 (c)).

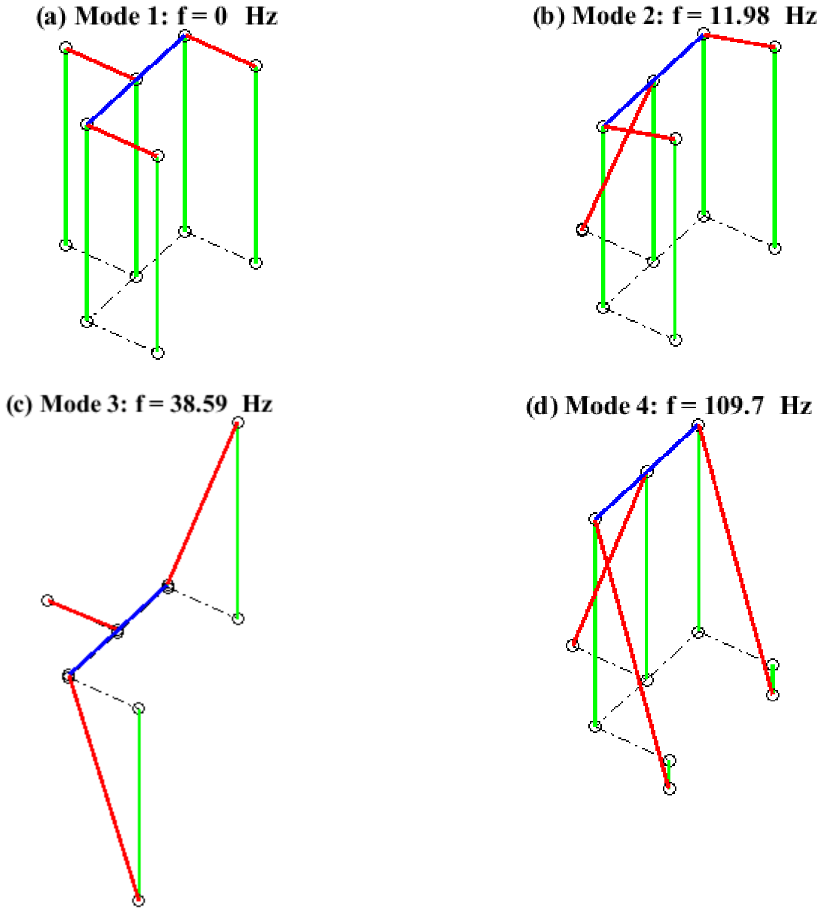

Figure 4.7: Torsional mode shapes.

The modes of the system are:

- Rigid Mode – 0Hz: the whole system moves together.
- Second Mode – 11.98Hz: the two generators move in phase, and oscillate against the engine. Moreover, the oscillation of the engine is minimum, since its inertia value has been chosen to be higher than the rest of the system and thus act as the system's ground.
- Third Mode – 38.59Hz: the two generators oscillate out of phase.
- Fourth Mode – 109.7Hz: the gearbox oscillates out of phase respect to the system machines (engine and generators).

As a result, the system modelled has two vibration modes under 100Hz, which is the same that can be found in a typical aircraft drivetrain, like the one of the Rolls Royce Trent 1000 engine [18], [19].

4.4.2 Poles of the System

The state system presented in section 4.3.4 is used to analyse the stability through poles analyses. Figure 4.8 shows the poles of the electromechanical interaction system. Since all the poles are in the left hemisphere the system in study is stable. Moreover, through participation factor analysis the states with a higher correlation to each pole are found. These are circled in red in the figure, observing that the poles associated with the engine and the electrical power system are further from the origin than the ones related to the mechanical system or drivetrain as was expected.

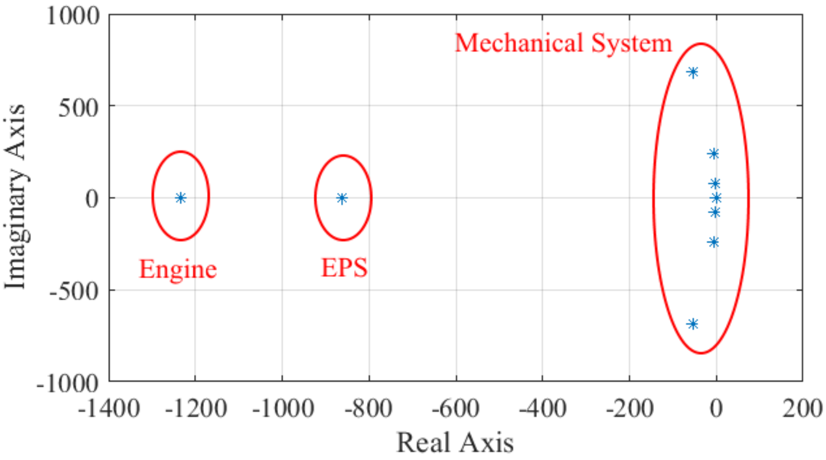

Figure 4.8: Poles of the system.

The natural frequencies and damping ratio are obtained using equation (4.36), in which a and b are the real and imaginary part of the eigenvalue respectively, and ξ, ω_n, and f_n are the damping ratio, natural frequency in rad/s and natural frequency in Hz.

$$\left.\begin{aligned} s &= -a \pm jb = -\xi\omega_n \pm \omega_n\sqrt{1-\xi^2} \\ f_n &= \frac{\omega_n}{2\pi} \end{aligned}\right\} \tag{4.36}$$

The obtained natural frequencies and damping ratios are:

- $f_0 = 0\text{Hz}, \xi_0 = 1$
- $f_1 = 11.9443\text{Hz}, \xi_1 = 0.0362$

- $f_2 = 38.5982\text{Hz}$, $\xi_2 = 0.0276$
- $f_3 = 109.7207\text{Hz}$, $\xi_3 = 0.0774$
- $f_4 = 137.4276\text{Hz}$, $\xi_4 = 1$
- $f_5 = 196.3611\text{Hz}$, $\xi_5 = 1$

The participation analysis of the poles shows that the first four frequencies are predominantly associated with the mechanical system. This is the same that was obtained through the vibration mode analysis, proving that the poles closer to the origin are the drivetrain vibration modes.

Furthermore, the poles allow finding the settling time of the electromechanical interaction to a step connection. This is the time that the system's response takes to reach a set range of the steady-state value. To obtain this, the envelope of the system response given by equation (4.37) is used.

$$y_{envelope}(t) = 1 \pm \frac{\exp(-\xi\omega_n t)}{\sqrt{1-\xi^2}} \tag{4.37}$$

For $\xi = 1$ the settling time is given by the time constant of the system. Instead, for $\xi < 1$, the settling time is obtained by calculating the value at which the signal envelope has the desired value, as shown in equation (4.38) and Figure 4.9. S is the settling value to be used. For $S = 1\%$, equation (4.39) can be used to obtain the settling time associated with each natural frequency [105].

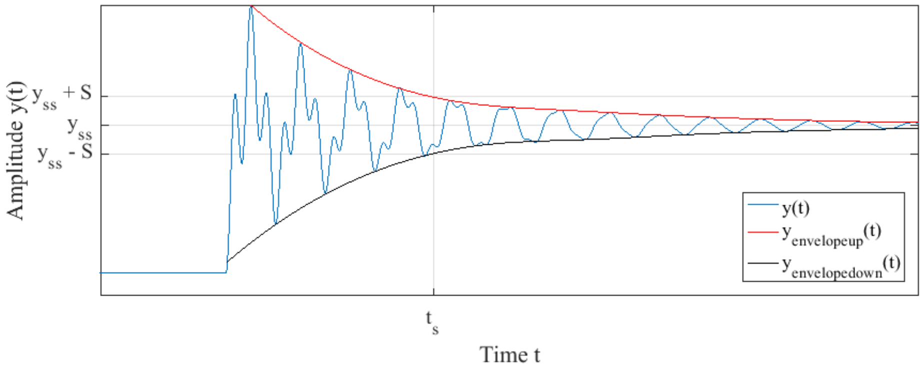

Figure 4.9: Settling time diagram.

$$y_{envelope}(t) \leq (1 \pm S) \tag{4.38}$$

$$\frac{\exp(-\xi\omega_n t_s)}{\sqrt{1-\xi^2}} = 0.01 \Rightarrow t_s = -\frac{\log\left(0.01\sqrt{1-\xi^2}\right)}{\xi\omega_n} \tag{4.39}$$

The settling times are:

- $f_1 = 11.9443\text{Hz}$ → $t_{s1} = 1.6953\text{s}$
- $f_2 = 38.5982\text{Hz}$ → $t_{s2} = 0.6881\text{s}$
- $f_3 = 109.7207\text{Hz}$ → $t_{s3} = 0.0864\text{s}$
- $f_4 = 137.4276\text{Hz}$ → $t_{s4} = 0.0073\text{s}$
- $f_5 = 196.3611\text{Hz}$ → $t_{s5} = 0.0051\text{s}$

Finally, the settling times of the mechanical system are higher than the ones of the electrical system. This difference in timing allows the modelling of the power system as torque step connections.

4.5 Load Connections

Until now, the modelling of the electromechanical interaction has been presented, and its stability has been assessed. In this section, the effects of step load connections and pulsating load connections are shown.

4.5.1 Step Connection

To test the step connection, a 5Ω resistive load is connected to the system operating in steady state with a field current $i_f = 6.2\text{A}$ and only the protection resistance $R_P = 60\Omega$ connected. Table 4.3 shows the steady state operation values before and after the connection. It is observed that as the speed of the system is controlled by the engine, the step only produces a low drop on its value, regardless of the 2.5Nm change in torque.

Table 4.3: Steady state values.

Parameter		**Value** **Before Connection**	 **After Connection**
Armature Current	i_a	0.8947 A	2.307 A
Armature Voltage	v_a	53.68 V	30.59 V
Field Current	i_f	6.2 A	6.2 A
Field Voltage	v_f	11.16 V	11.16 V
Electrical Power	P_E	48.03 W	202.8 W
Electrical Torque	T_{g_2}	0.3952 Nm	2.928 Nm
Shaft Torque	T_{s_3}	0.3952 Nm	2.928 Nm
Generator Speed	ω_{g2}	1503 rpm	1502.8 rpm

The electrical results of the step connection are shown in Figure 4.10. Since the field current is externally given, its value and the field voltage value do not change as a result of the connection. However, the armature current is higher because a higher load must be fed. The armature voltage drops, due to the higher current consumption in the machine windings. As the electromotive voltage, given by $E = ki_f\omega$, depends only on the speed its value is virtually constant since the speed is fixed by the engine, and hence is practically constant as shown in Table 4.3. Therefore, the change in armature voltage is only due to the higher current consumption on the armature windings.

The consumed power and the torque needed at the machine are higher after the load connection. The temporary drop in power after the load connection is due to the drop in voltage, produced by the presence of inductances in the system. Moreover, it is observed that the transient lasts 7ms (for a settling time of 1%), which agrees with the 7.3ms time constant obtained for 137Hz. Small vibrations can be observed after 7ms, which are due to the lower natural frequencies associated with the drivetrain of the system. The maximum load connection depends on the electrical characteristics and the value of the voltage overshoot according to [106].

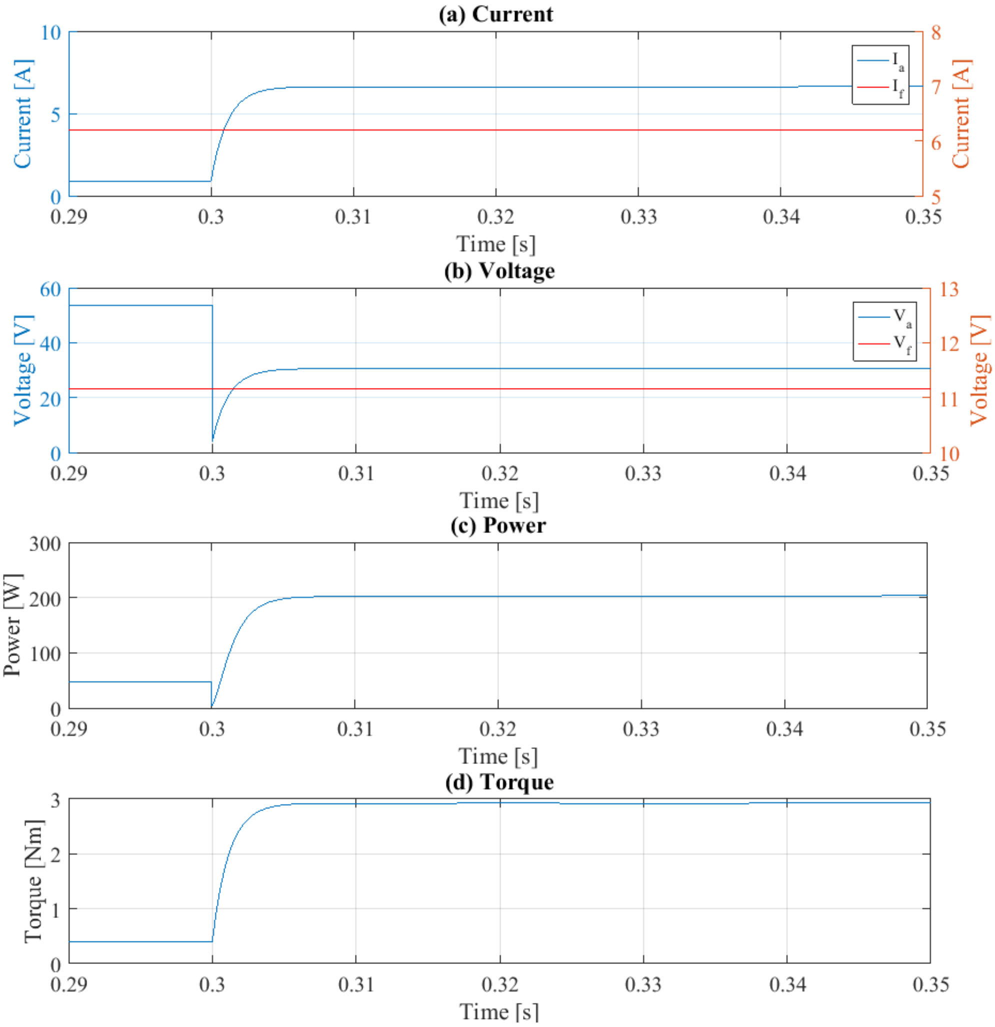

Figure 4.10: Electrical step response of the system.

The mechanical response of the system: the speed (a), acceleration (b) of each inertia in the drivetrain, along with the torque in the generator shaft (c) are shown in Figure 4.11. It is observed that the connection of the electrical load produces vibrations in these variables along the whole drivetrain. Hence, a change in the electrical load produces a transient in all the components of the system. In (a), and (b) the vibrations of the engine shaft are observed in blue. These vibrations are considerably lower than the ones of the rest of the system due to the higher damping and inertia of the engine, which acts as the ground of the mechanical system. This behaviour is consistent with an aircraft drivetrain in which the size of the engine is much higher than the one of the electrical system as its power is used to move the plane and not only power the electrical power system.

Moreover, it can be seen that the transients are longer than the one presented on the electrical system, with values of the order of 1.3s. This is consistent with having lower natural frequencies with lower damping and between the theory settling times obtained for f_1 and f_2.

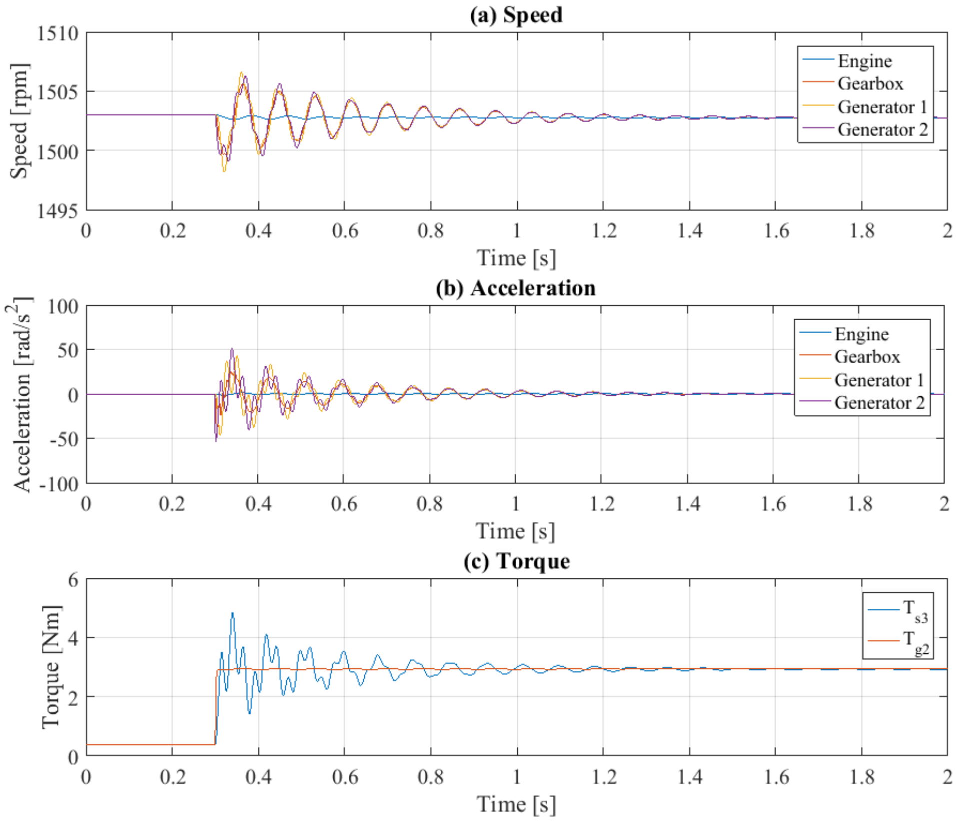

Figure 4.11: Mechanical step response of the system.

In Figure 4.11 (c), the changes in electrical torque (in red) and shaft torque (in blue) are observed. T_{g_2} can be approximated by a step, with a settling time much lower than the one of the mechanical system, as was already mentioned. This connection is reduced and modelled as a perfect step connection for simplification from chapter 5 to 7.

Since the effect of an electrical step connection is the production of vibrations on the shaft of the system, electromechanical interaction has been demonstrated. As presented in chapter 3, the torsional vibrations can reduce the lifespan of the mechanical components and produce fatigue. To decrease the effect of the electromechanical interaction, and consequently, reduce the torsional vibrations, vibration suppression methods must be analysed.

The most common solution, presented in chapter 3, is to increase the damping of the system. To analyse the damping effect on the electromechanical interaction, the overshoot given by equation (4.40) and the settling time are calculated for different damping values.

$$Overshoot = \frac{Y_{max} - Y_{SS}}{Y_{SS}} * 100 \tag{4.40}$$

Figure 4.12 shows the generator shaft torque T_{S_3} for different values of shaft damping d_{s1}. Table 4.4 shows the overshoot and settling time of each case (low, medium, and high). As expected for higher damping the vibrations are lower and hence the overshoot and settling time decrease.

Table 4.4: Performance of the system for different damping.

Case	Damping Value $\left[\frac{\text{Nmrad}}{\text{s}}\right]$	Overshoot [%]	Settling Time [s]
Low	0.5	65.1981	1.261
Medium	1.5	45.1844	0.3840
High	11.02	7.0355	0.0645

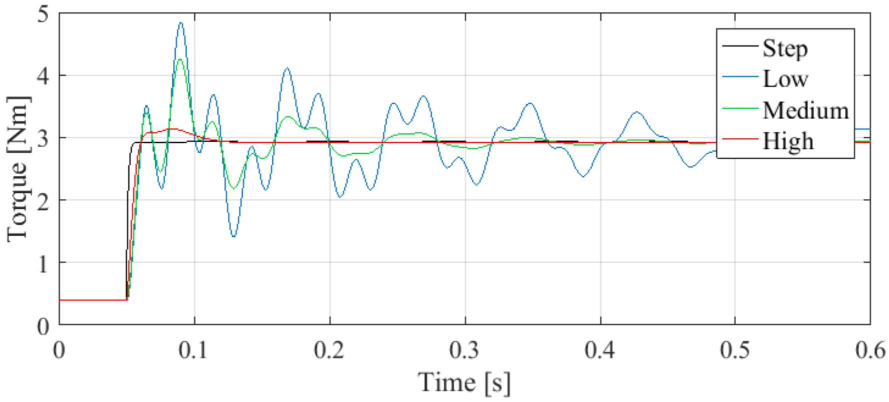

Figure 4.12: Generator 2 shaft torque for different damping.

The overshoot and settling time decreases until the damping of the system equals the critical damping, which is the damping value that stops the vibrations of the system. For a one inertia system, it can be calculated by equation (4.41), with d_c the critical damping, j the inertia, and k the stiffness.

$$d_c = \sqrt{4jk} \tag{4.41}$$

In summary, the vibrations of the system decrease more rapidly as the damping increases. Therefore, as presented in chapter 3, a method to reduce the vibrations of a system is to increase the damping. However, in an aircraft, this is not desired due to the associated increase in space and weight. For this reason, chapter 5 presents strategies that allow the elimination of the transient vibrations without the need for an increase in the damping of the system.

4.5.2 Pulsating Load Connections

Many loads, such as the heating system of an aircraft and the radar systems are pulsating loads [37], [107]. This section evaluates the effect of the carrier frequency and the duty cycle of a pulsating load over the drivetrain in terms of vibrations on the shaft torque.

To model the pulsating load, the electrical load R_{L_1} is connected and disconnected in a pulse pattern. Consequently, the electrical torque T_{g_2} applied to the shaft is pulsating. Figure 4.13 presents the pulse applied to the drivetrain, in which $T = 1/f$ is the period in seconds, D is the duty cycle or percentage of one pulse on, T_{mean} the average value of the pulse in Nm, and T_{max} and T_{min} are the maximum and minimum value of the pulse respectively in Nm.

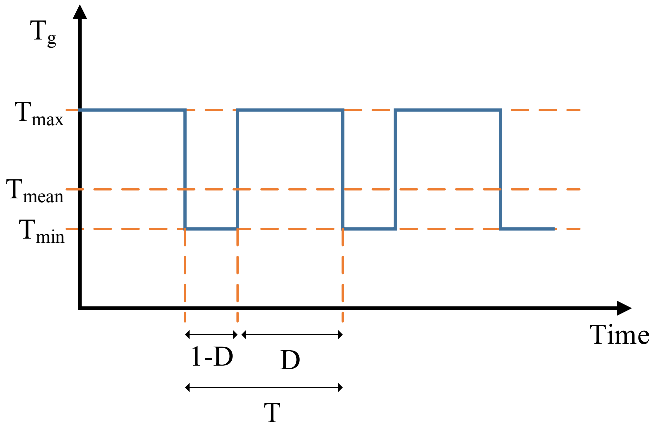

Figure 4.13: Pulsating load.

The response to the shaft torque T_{s_3} is analysed for different values of duty cycle D and pulse frequencies f, while maintaining the mean value T_{mean} of the electrical torque T_{g_2} constant. The parameters used are the same as were used to analyse the stability and the step load connection. The shaft damping is $d_{s1} = 0.5\mathrm{Nmrad/s}$ and $d_{s2} = d_{s3} = 0.5\mathrm{Nmrad/s}$. The minimum value of the electrical torque is $T_{min} = 0.3952\mathrm{Nm}$, which is the torque obtained when only $R_P = 60\Omega$ is connected. The maximum torque T_{max} is calculated from equation (4.42), in which T_{mean} is the mean torque applied to the system, and its value is 2.928Nm, corresponding to the torque obtained when a resistance R_{L_1} is connected.

$$T_{max} = \frac{T_{mean} - T_{min}(1 - D)}{D} \tag{4.42}$$

Figure 4.14 presents the results obtained when a pulse with a duty cycle $D = 75\%$ and frequencies of 1Hz (a), 11.94Hz (b), and 200Hz (c) are connected. In the three cases the generator torque T_{g_2} applied is shown in red, while the shaft torque T_{s_3} is presented in blue.

When a 1Hz pulse is used as shown in Figure 4.14 (a), each connection presents a transient response, due to the long time between the pulses. This case, which is observed in aircraft heating systems, can be considered as a series of step load connections and thus apply the same strategies to eliminate the vibrations. These strategies are presented in chapter 5. In the second case, shown in Figure 4.14 (b), a frequency equals to the natural frequency of the drivetrain 11Hz is used. This generates resonance, and thus a high amplitude sustained vibration on the shaft. Therefore, the operation at the natural frequency values must be avoided. Finally, when a high-frequency pulse is applied, as in Figure 4.14 (c), the system reaches steady state as if the load applied would be equal to a single step connection. Therefore, only an initial overshoot and settling time are observed. Now, low frequencies are going to be defined as those under the lower resonance value, while higher frequencies are the ones over.

(a) f = 1Hz and D = 75%

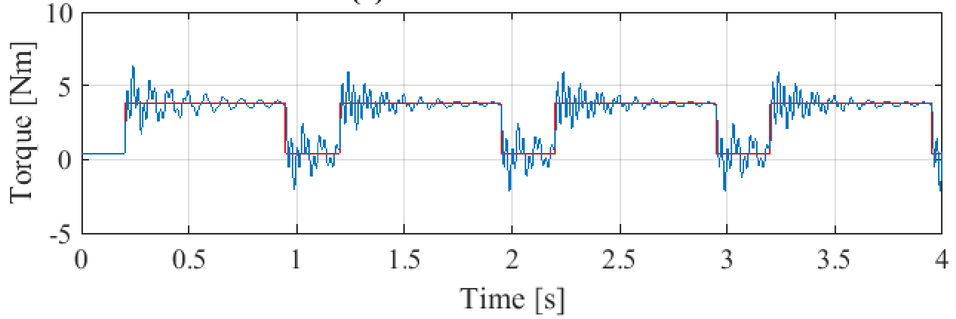

(b) f = 11.94Hz and D = 75%

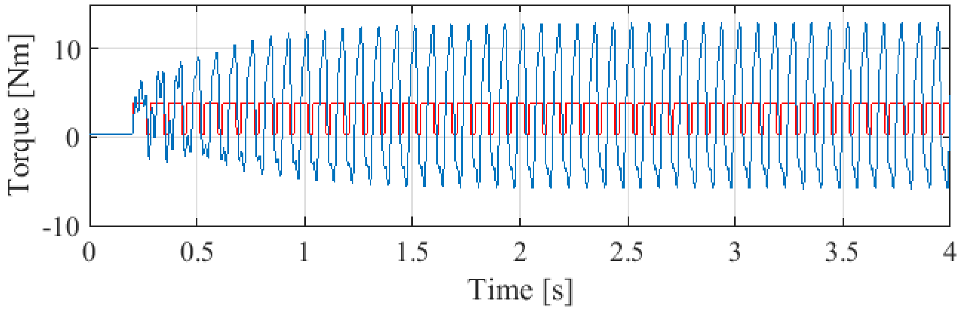

(c) f = 200Hz and D = 75%

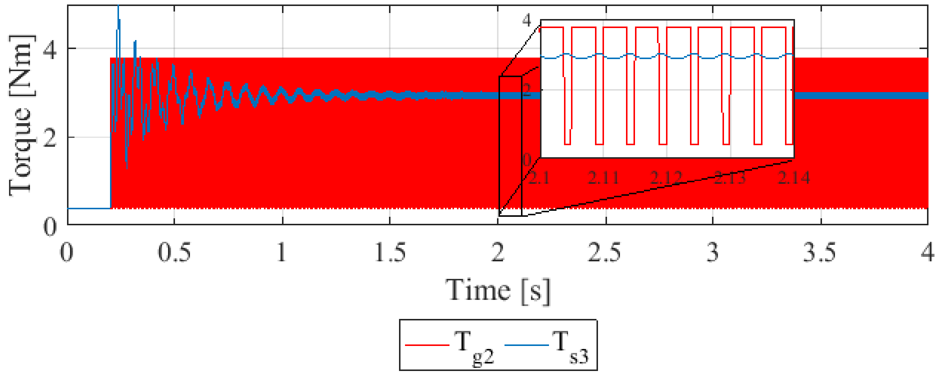

Figure 4.14. Generator 2 shaft torque versus time.

The effect of a broader frequency spectrum and different duty cycles is shown in Figure 4.15 and Figure 4.16. A sample of 200 frequencies distributed logarithmically from $f_1/100$ to $10f_1$ is used while keeping the mean value of torque constant at 2.928Nm. In the case of the duty cycle, 18 samples distributed linearly from 6 to 91% are analysed. The cases of duty cycle equal 0% and duty cycle equal 100% are not included since there is not pulsating connection in their operation. Likewise, duty cycle lower than 6% is not included because the maximum torque T_{max} needed to keep a mean value of 2.928Nm is too high and not realistic.

Figure 4.15 shows the peak torque value of the generator shaft torque T_{s_3} as a function of the duty cycle $D(\%)$ and the frequency rate between the frequency used f and the natural frequency f_1 of the system ($f/f_1 = f/11.9413\text{Hz}$). The peak amplitude is higher when the frequency analysed matches a natural frequency of the system, for example $f/f_1 = 1$ and for lower duty cycles. To observe this Figure 4.16 is presented, in which the peak torque value of the shaft torque T_{s_3} is plotted as a function of the frequency ratio for different duty cycles. The resonance effect is clearer when the duty cycle used is higher.

Higher peak values for lower duty cycles relates to equation (4.42), because for lower duty cycles, the maximum torque T_{max} must be higher to keep the mean torque T_{mean} constant. This effect disappears at high frequencies and it is strong at low ones, because as shown in Figure 4.14(a), for low frequencies each step connection has its own transient. Therefore, a high torque being connected has a high transient, making the peak torque value of the generator shaft higher. On the other hand, when high frequencies pulsating loads are connected, the mechanical system perceives only the mean torque, and thus the value of the duty cycle does not affect the system. This is also observed in Figure 4.16, in which for high frequencies the peak torque value of each curve is the same. Moreover, it is observed, that for duty cycles approximately higher than 30%, its effects for low frequencies decreases.

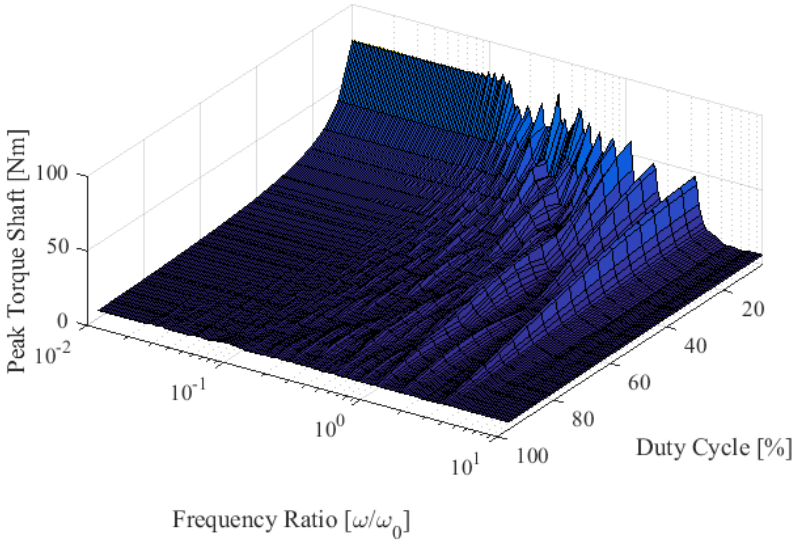

Figure 4.15: Peak shaft torque as a function of the frequency and duty cycle.

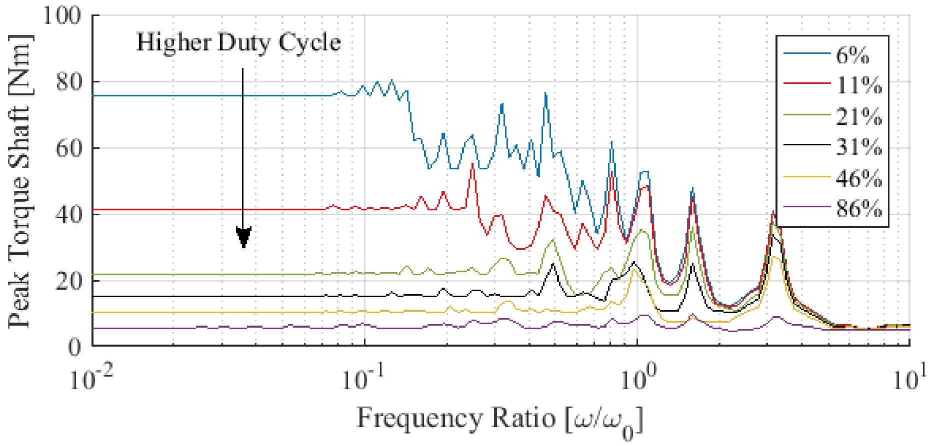

Figure 4.16: Peak shaft torque as a function of the frequency.

The effect on the mechanical system of each case is different, and thus the strategy taken to minimize the electromechanical interaction depends on the frequency of the pulsating signal. In summary, the following aspects must be considered when working with pulsating loads in order to maximize the lifespan of the shaft:

1. The natural frequencies must be avoided to avoid resonances.
2. For low frequencies:
    - Duty cycles must be roughly higher than 30% for constant power.
    - Each pulse must be considered as a step connection, and the strategies that are presented in chapter 5 must be applied in each pulse.
3. For high frequencies:
    - The losses in converter associated with the pulsating load must be considered. The losses that the system suffer from each switching depend on the converter used, but in general, higher the switching frequency has more power losses [108], [109]. These losses are detrimental because they made the devices work at higher temperatures that can affect the lifetime of the equipment. Therefore, the switching frequencies must minimize the losses of the switching device.

4.6 GCU Controller Effect

The previous section showed that an electrical load connection could have repercussions in the mechanical system, producing vibrations that decrease the shaft lifespan. However, as mentioned in chapter 3, the control systems can also be a source of electromechanical interaction. In [21] it is said that the electrical machine control can produce negative damping on the shaft. And in [63] it has been shown by simulation that the GCU produces an interaction on marine systems. To avoid these problems, the system must be designed appropriately.

Now, a case in which the Generator Control Unit (GCU) of the generator can produce instabilities in the mechanical system if its design is oversimplified is presented. For this reason, a GCU controller, which keeps the armature voltage v_a constant, is connected to the generator of the system modelled in section 4.3.

4.6.1 GCU Operation

As shown in Figure 4.17, a V/f open loop control is used to keep the armature voltage of the generator $v_a(t)$ constant at V_{nom} by regulating the field current $i_f(t)$.

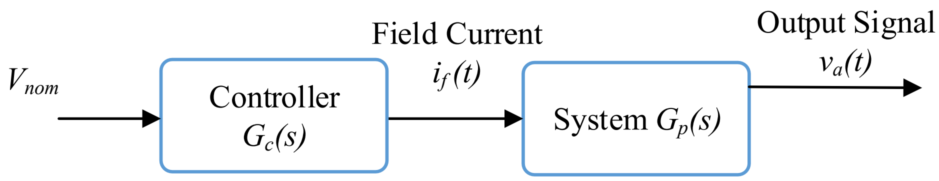

Figure 4.17: Simplified open loop GCU.

The field current i_f determines the back-EMF through equation (4.23), in which $E = ki_f\omega_{g_2}$. Then, as shown in equation (4.43) the field current applied to the machine depends on the speed of the system, which regulates the armature voltage. Replacing the value of the torque constant $k_t = ki_f$ in the electrical torque equation (4.26) and the back-EMF equation (4.23), the control values of these variables, given by equations (4.44) and (4.45) are found.

$$k_t = ki_f = \frac{V_{nom}}{\omega_{g_2}} \Rightarrow i_f = \frac{V_{nom}}{k\omega_{g_2}} \tag{4.43}$$

$$E = ki_f\omega_{g_2} = k_t\omega_{g_2} = V_{nom} \tag{4.44}$$

$$T_{g_2} = ki_fi_a = k_ti_a = \frac{V_{nom}}{\omega_{g_2}}i_a \tag{4.45}$$

The system is tested using the parameters of Table 4.1 and Table 4.2. To eliminate the change in power consumed in the windings $R_a = 0\Omega$. The nominal voltage V_{nom} is given by equation (4.46), in which V_0 is the voltage drop across the brushes (shown in Table 4.2), and $V_a^* = 40\text{V}$ the desired output voltage.

$$V_{nom} = V_a^* + V_0 \tag{4.46}$$

Figure 4.18 and Figure 4.19 show the results obtained for the electrical and mechanical systems after a step load connection. The protection resistance used is $R_P = 60\Omega$ and the load connected is $R_{L_1} = 5\Omega$. It is observed that with the exception of having a constant armature voltage (Figure 4.18 (b)), and thus, a higher power consumption and torque, the response of the rest of the system (electrical and mechanical) is equivalent to the one of a step connection with no GCU. The higher power and torque is due to the having a higher armature voltage since the GCU is keeping it constant. Figure 4.20 shows that when the torque is normalised, the behaviour of the system is the same with and without GCU.

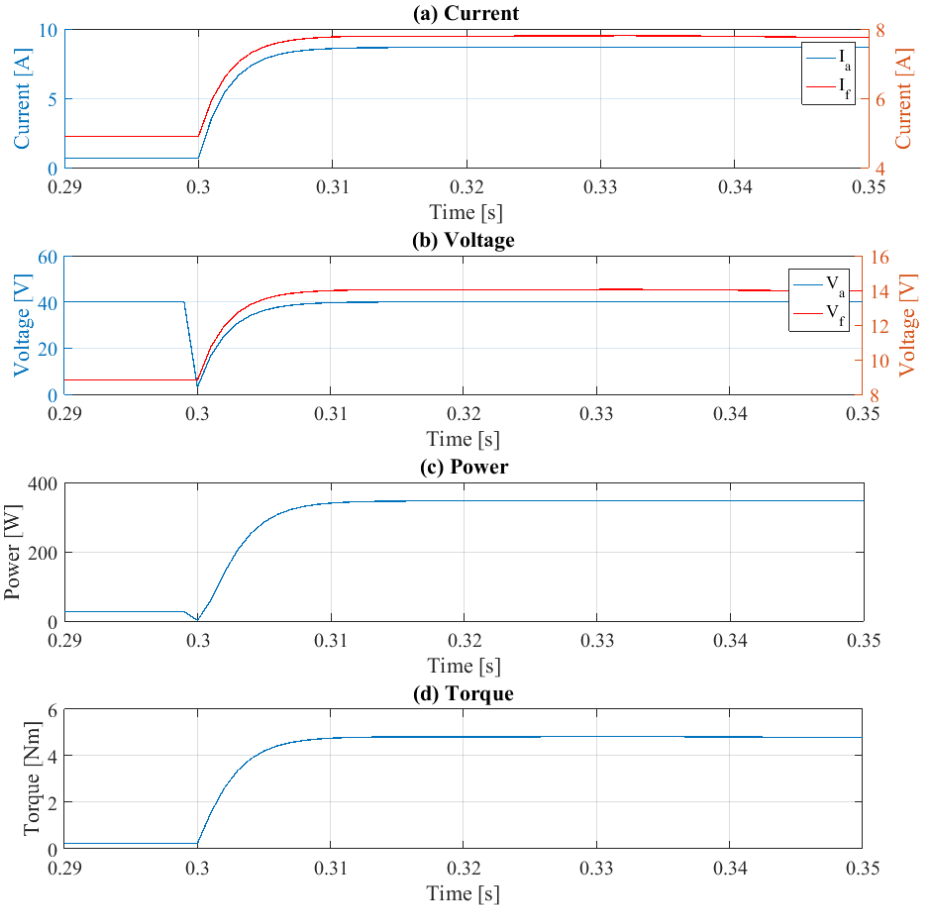

Figure 4.18: Electrical system with GCU.

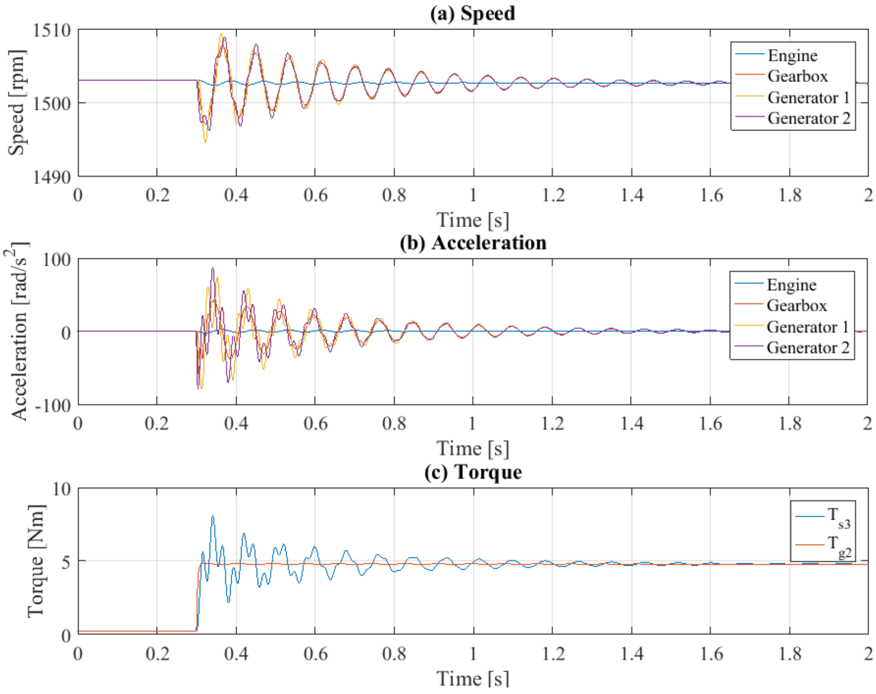

Figure 4.19: Mechanical system with GCU.

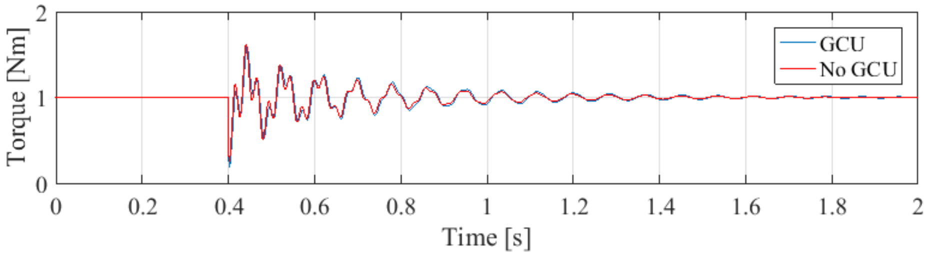

Figure 4.20: Normalised torque with and without GCU.

4.6.2 GCU Impact on Stability

To examine the stability of the GCU, two methods are considered: first, the stability of the electrical system is presented, and then the stability of the integrated electromechanical system is analysed.

4.6.2.1 Stability of the Electrical System

To study the stability of the electrical system, the transfer function in the Laplace domain is obtained. For this, the voltage equation (4.47) is linearized and converted to the Laplace frequency domain as shown in equation (4.48). I_{f_0} and ω_{g_20} are the steady state values of the field current and speed respectively.

$$k i_f \omega_{g_2} = \left(R_a + R_{eq}\right) i_a + L_a \frac{di_a}{dt} + V_0 \tag{4.47}$$

$$I_a(s) = \frac{\left(kI_{f_0}\omega_{g_2}(s) + k\omega_{g_20}I_f(s) - V_0\right)}{R_a + R_{eq} + sL_a} \tag{4.48}$$

The linearization of the controller given by equation (4.43), is obtained by differentiation and is shown in equation (4.49). Replacing the linearized controller given by equation (4.49) into equation (4.48), the transfer equation (4.50) is obtained. Replacing the state into $V_a = R_{eq}I_a$, the transfer function shown in equation (4.51) is found.

$$I_f(s) = \frac{V_{nom}}{\omega_{g_20}k} - \frac{I_{f_0}}{\omega_{g_20}}\omega_{g_2}(s) \tag{4.49}$$

$$I_a(s) = \frac{(V_{nom})}{R_a + R_{eq} + sL_a} \tag{4.50}$$

$$\frac{V_a(s)}{V_{nom}} = \frac{R_{eq}}{R_a + R_{eq} + sL_a} \tag{4.51}$$

From the transfer function (4.51), the pole of the electrical system $s = -(R_a + R_{eq})/L_a$ is obtained. As the resistances and inductances are always positive, the stability analysis of the electrical system shows that regardless of the GCU value, the system is stable.

4.6.2.2 Stability of the Electromechanical System

It has been demonstrated that when the electrical power system is analysed in isolation, the system is always stable. Now, the stability of the same system is studied, through state systems, including the mechanical drivetrain. For this, considering the electrical system in steady state, the stability is tested in the presence of a mechanical perturbation.

Equation (4.45) shows that when the GCU is connected, the electrical torque applied on the mechanical system depends on the armature current i_a and speed of the system ω_{g_2}. Because for a stable electrical system $i_a = constant$, since the armature current v_a and the power are constant, a new constant $K_g = V_{nom} i_a$ can be defined and replaced into (4.45) obtaining equation (4.52).

$$T_{g_2} = \frac{V_{nom}}{\omega_{g_2}} i_a = \frac{K_g}{\omega_{g_2}} \tag{4.52}$$

To obtain the state system, equation (4.52) must be linearized and equation (4.53) is obtained. The slope of the equation, given by $-K_g/\omega_{g_20}^2$ shows that GCU has a negative damping effect proportional to the nominal voltage V_{nom}. Therefore, there is a value in the system, in which the system becomes unstable.

$$T_{g_2} = -\frac{K_g}{\omega_{g_20}^2}\omega_{g_2} + \frac{2K_g}{\omega_{g_20}} \tag{4.53}$$

Equation (4.53) is replaced in the engine-drivetrain steady state system found in section 4.3.4 and given by equation (4.30), as shown in equation (4.54).

$$
\begin{aligned}
\begin{bmatrix}\dot{\theta}_R\\ \ddot{\theta}_R\end{bmatrix} &= A_{DE}\begin{bmatrix}\theta_R\\ \dot{\theta}_R\end{bmatrix} + B_{DE}\begin{bmatrix}B_{Engine}\\ 0\\ 0\\ -T_{g_2}\end{bmatrix}\\
&= A_{DE}\begin{bmatrix}\theta_R\\ \dot{\theta}_R\end{bmatrix} + B_{DE}\begin{bmatrix}B_{Engine}\\ 0\\ 0\\ \frac{K_g}{\omega_{g_2 0}}\dot{\theta}_{g_2} - \frac{2K_g}{\omega_{g_2 0}}\end{bmatrix}\\
&= \left(A_{DE} + B_{DE}\begin{bmatrix}0\\ 0\\ 0\\ \frac{K_g}{\omega_{g_2 0}^2}\end{bmatrix}\begin{bmatrix}0_{1x7} & 1\end{bmatrix}\right)\begin{bmatrix}\theta_R\\ \dot{\theta}_R\end{bmatrix} + B_{DE}\begin{bmatrix}B_{Engine}\\ 0\\ 0\\ -\frac{2K_g}{\omega_{g_2 0}}\end{bmatrix}\\
&= A_{GCU}\begin{bmatrix}\theta_R\\ \dot{\theta}_R\end{bmatrix} + B_{DE}\begin{bmatrix}B_{Engine}\\ 0\\ 0\\ -\frac{2K_g}{\omega_{g_2 0}}\end{bmatrix}
\end{aligned}
\tag{4.54}
$$

Rewriting the GCU constant as shown in equation (4.55), the nominal voltage value to be controlled is given by equation (4.56).

$$\widetilde{K} = \frac{K_g}{\omega_{g_2 0}^2} \tag{4.55}$$

$$V_{nom} = \frac{\widetilde{K}\omega_{g_2 0}^2}{I_{a0}} \tag{4.56}$$

For the system parameters of Table 4.1, Figure 4.21 shows the movement of the poles while $\widetilde{K}$ increases. Hence, when the stability of the whole system is analysed, there is a maximum V_{nom} that can be controlled by the GCU which turns the system unstable.

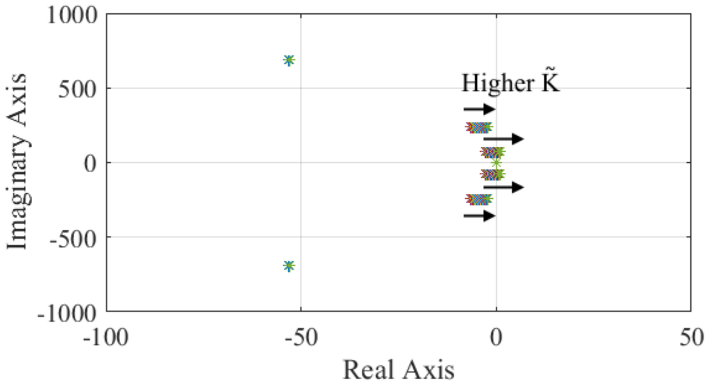

Figure 4.21: Poles movement of the electromechanical interaction system.

To analyse the stability limit and therefore the threshold value in which the GCU pole becomes positive, Routh-Hurwitz criteria is used [13], [14]. For the system in the study is obtained:

$$\widetilde{K} = \frac{K_g}{\omega_{g_2 0}^2} < 0.4680$$

Figure 4.22 shows the response of the electromechanical interaction system for three values of $\widetilde{K}$ in presence of a 1.5 rpm perturbation, which is applied to the generator speed operating in stability. In red is shown the electrical torque T_{g_2} and in blue the shaft torque T_{s_3}. It is observed that Figure 4.22 (a), operating with $\widetilde{K} = 0.4405$, returns to stability after the perturbation, while in (b) ($\widetilde{K} = 0.4435$ and (c) ($\widetilde{K} = 0.4441$), the system remains vibrating and gets unstable respectively. The error of the $\widetilde{K}$ obtained through simulation and out of state system analysis is 5.19%, and therefore is considered acceptable. This behaviour cannot be predicted from an analysis of the electrical system alone, making relevant the study of the electromechanical interaction in the design of GCU.

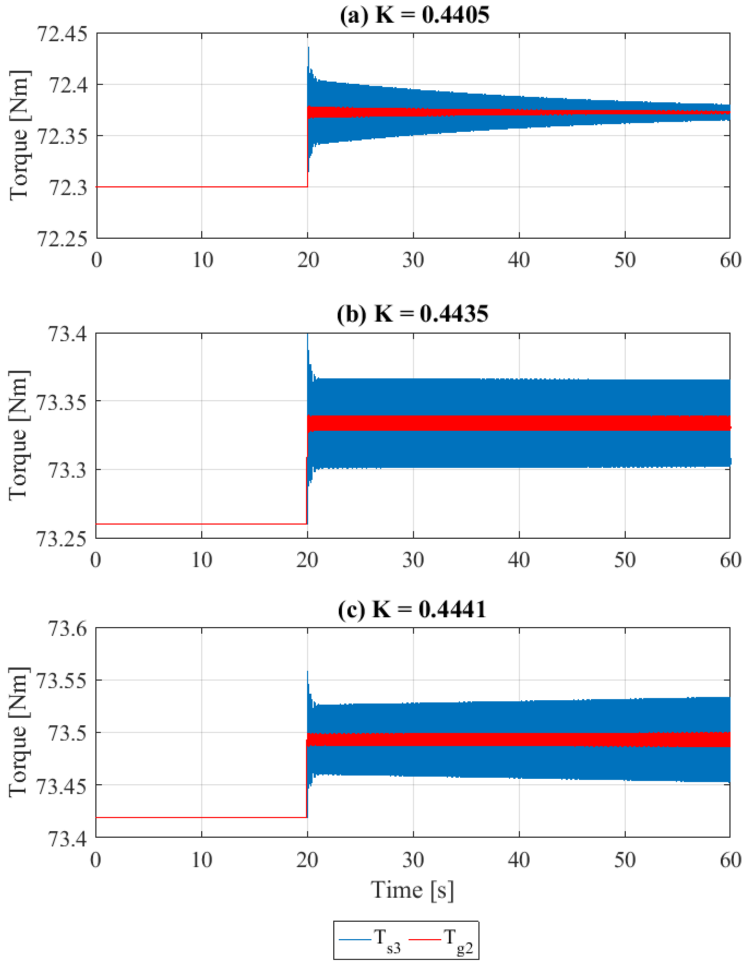

Figure 4.22: GCU stability.

4.7 Summary

In this chapter, the reduced electromechanical system representative of an aircraft drivetrain and electrical power system was presented and modelled. Its stability was studied, and its natural frequencies were analysed, proving that the model is representative of an aeroplane system since the main natural frequencies are found in a real plane.

Furthermore, the coupling between both systems (electrical and mechanical) was demonstrated through analysis of the effect of load connections and the GCU stability. These allowed the testing of the sources of electromechanical interaction presented in chapter 3: Control System, Step Load, and Pulsating Load. The effects of a Grid Fault are equivalent to the ones of a high step load, while the electromechanical interaction due to sub-synchronous currents is out of the scope of this thesis.

Moreover, the strategy to eliminate the vibrations due to electromechanical interaction depends on the reason for the torsional vibrations excitation. For example, to avoid instability due to the control system, the GCU needs to be designed considering the whole system. In the case of load connections, the strategy used to eliminate the transients depend on the load characteristics.

For pulsating loads, the operation at frequencies equal to the natural frequency is avoided. The transients produced due to each pulse connection at low frequencies are treated as a step connection, while for high frequencies, the overall torque applied over the mechanical shaft can be considered as a step.

To reduce the vibrations due to step connections, it was shown that the damping could be increased. However, as this is not desired in aircraft systems, the next chapter presents a power management system (PMS) that allows the suppression of the torsional vibrations due to electrical load connections.

Chapter 5

Power Management System

5.1 Introduction

In this chapter, a power management system (PMS) that reduces the excitation of torsional vibrations in the drivetrain due to electrical load connections is presented. Due to the different loads in an aircraft, in section 5.2 a classification of them is established: time non-critical, time critical, low frequency pulsating load, and high frequency pulsating load. Thus, the PMS must apply different strategies according to the electrical load connected, as shown in Figure 5.1. These strategies are based on the open loop Posicast method [110] and are called Single Level Multi-edge Switching (SLME), Multilevel Loading (MLL), and Multi-load Single Level Multi-edge Switching (MSLME). These strategies are presented in section 5.4 and 5.5.

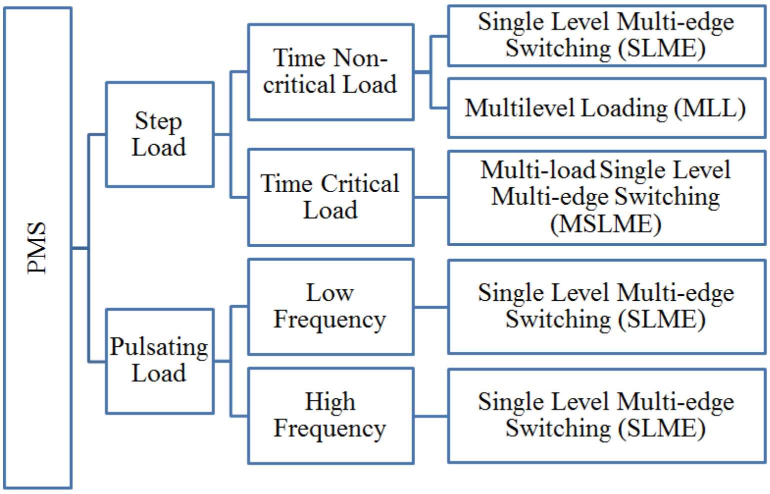

Figure 5.1: PMS layout.

Since this thesis studies the effect of resistive loads, the effects of inductance and capacitance are ignored in the strategies defined in this chapter. Thus, the torque steps applied by the generator are perfectly square. For this reason, the machine inductances of the system presented in chapter 4 are zero: $L_a = 0\mathrm{H}$. The effects of the inductances are shown in the experimental results presented in chapter 7 and studied in chapter 8.

The rest of the chapter is organised as follows. First, the classification of aircraft power loads is presented. Second, the relationship between the excitation of natural frequencies and the force applied is analysed. As a solution, the Posicast method is studied. Third, PMS strategies for step load connections are proposed and analysed. Later, the strategies to be applied in pulsating loads are introduced, and the requirements to apply the strategies in a real aircraft presented. Finally, the chapter summary is given.

5.2 Power Load Classification

Since not every load has the same requirements, the PMS applies different strategies according to the load connected to the system (shown in Figure 5.1). Table 5.1 classifies the MEA aircraft loads given in [9], into step loads with time critical and time non-critical requirements, and pulsating loads with low and high frequency.

Table 5.1: Classification of loads on aircraft system.

Step Load		Pulsating Load	
Time Critical	Time Non-critical	Low Frequency	High Frequency
• Flight Control Surfaces (2-35kW) • Fuel Pumps (10kW)	• De-Icing (20kW) • Cabin Air (4*70kW) • Landing Gear (5-70kW) • Engine starting (200kW)	• De-Icing (20kW)	• Radar

Step load connections can be either Time Critical or Time Non-critical. Time Critical Loads are those in which the connection time represents a crucial factor for its operation. For these loads, a precise connection time is essential. An example is the case of the flight control surfaces or the landing gear, which cannot have a delay in their connection.

On the other hand, Time Non-critical Loads are the ones for which an exact time connection is not a crucial factor for its operation. For example, the de-icing system and the air cabin can be connected and disconnected at any stage during the flight. In particular, it was stated in [111], that the de-icing system has a low-frequency pulsating behaviour. This characteristic is the one that makes the de-icing system the perfect load to use on the PMS strategies, as it is shown in section 5.4.

Pulsating loads can have high or low frequencies. In chapter 4 the low frequency pulsating loads were defined as those with frequencies below the natural frequencies of the mechanical system. By contrast, high frequencies pulsating loads are the ones with a switching over the resonance values.

Section 5.4 presents the strategies applied for step load connection and section 5.5 the ones for pulsating loads. Next, the relationship of the excitation of vibrations with the load applied is studied.

5.3 Vibration Analysis

The lumped mass system, presented in chapter 4, and modelled by equation (5.1) is a linear, time-invariant, viscously damped and multiple degrees of freedom system. In which, J is the inertia matrix, D the damping matrix, and K the stiffness matrix; x is the angle of each element in the system, and $f(t)$ is the excitation applied.

$$J\ddot{x} + D\dot{x} + Kx = f(t) \tag{5.1}$$

If the system (5.1) is initially at rest at its equilibrium position, the response of $x(t)$ to the external excitation $f(t)$ is given by the Duhamel integral as shown in equation (5.2). Here, $g(t)$ is the system impulse response function [49], [112]. Rewriting equation (5.2), to model a system in discrete time, equation (5.3) is obtained. Here, τ_D is the discrete time.

$$x(t) = \int_{\tau=0}^{\tau=t} f(\tau)g(t-\tau)d\tau \tag{5.2}$$

$$x(t) = \sum_{\tau_D=0}^{t} f(\tau_D)g(t-\tau_D) = \sum_{\tau_D=0}^{t} f(t-\tau_D)g(\tau_D) \tag{5.3}$$

If $f(t)$ is a unit step $b(t)$ at time T_k, the excitation can be modelled by equation (5.4). Defining the step response $h(t - T_k)$ to a system in steady state by equation (5.5), the response of the linear, time-invariant and viscously damped system $x(t)$ can be written as shown in equation (5.6).

$$b(t) = \begin{cases} 0 & t < T_k \\ 1 & t \geq T_k \end{cases} \tag{5.4}$$

$$h(t-T_k) := \sum_{\tau_D=T_k}^{t} g(t-\tau_D) \tag{5.5}$$

$$x(t) = h(t-T_K) \tag{5.6}$$

For a system that has been subjected to m steps with sizes $\{p_1, p_2, p_3, p_4, \ldots, p_m\}$ at the ordered time set $\{T_1, T_2, T_3, T_4, \ldots, T_m\}$, the excitation function $f(t)$ can be written by equation (5.7). Combining equation (5.6) and equation (5.7), the response of $x(t)$ is obtained as shown in equation (5.8).

$$f(t) = \sum\nolimits_{k=1}^{k=m} p_k b(t) \tag{5.7}$$

$$x(t) = \sum\nolimits_{k=1}^{k=m} p_k h(t-T_k) \tag{5.8}$$

The step response of equation (5.5) can be written as a function of system response modes, which is known as the modal approach [113]. Equation (5.9) is obtained, where λ_j represents the jth eigenvalue and h_j represents the corresponding coefficient.

$$h(t-T_k) = \sum_{j=0}^{n} h_j e^{\lambda_j(t-T_k)} \tag{5.9}$$

Since this thesis studies the undamped and underdamped cases, the eigenvalues λ_j are complex conjugate pairs as shown in equation (5.10). Each eigenvalue defines a mode of the system response, as was shown in chapter 4. For the undamped case ($D = 0$ or $\xi_j = 0$), ω_{nj} represents the frequency at which the system vibrates without the application of an external excitation. This frequency is called the natural frequency of the system [49].

$$\lambda_j = \omega_{nj}\left(-\xi_j \pm j\sqrt{1-\xi_j^2}\right) = -\xi_j\omega_{nj} \pm j\omega_{dj} \tag{5.10}$$

When the system is underdamped ($\xi_j < 1$), the vibrations of the system decay exponentially by $e^{-\xi_j\omega_{nj}}$. The vibration frequency of the damped model is defined by the imaginary part of the eigenvalue and is called the damped natural frequency ω_{dj}. The ratio between the real damping and the minimum damping required to stop the vibrations is represented by the damping ratio ξ_j. When the damping ratio is small, the damped natural frequency is comparable to the natural frequency [49].

To ensure that the response $h(t - T_k)$ is real, the coefficients h_j are also complex conjugate pairs in an undamped and underdamped system [49]. Also, a single step function excites all modes of the system, both vibrating modes and decay modes.

Substituting equation (5.9) into equation (5.8), the response of the system given by equation (5.11) is found [49]. Also, since the first natural frequency of mechanical system is the rigid mode $\lambda_0 = 0$, equation (5.11) can be rewritten by equation (5.12).

$$x(t) = \sum_{k=1}^{k=m} p_k \sum_{j=0}^{j=n} h_j\, e^{\lambda_j(t-T_k)} \tag{5.11}$$

$$x(t) = h_0 \sum_{k=1}^{k=m} p_k + \sum_{k=1}^{k=m} p_k \sum_{j=1}^{j=n} h_j\, e^{\lambda_j(t-T_k)} \tag{5.12}$$

Now, due to $\sum p_k$ not having an oscillatory component, it can be defined by equation (5.13). Then, the response of the linear system is given by equation (5.14), in which $h_0 p_0$ represent the steady state response of the system.

$$\sum\nolimits_{k=1}^{k=m} p_k = p_0 \tag{5.13}$$

$$x(t) = h_0 p_0 + \sum\nolimits_{j=1}^{j=n} h_j \sum\nolimits_{k=1}^{k=m} p_k e^{\lambda_j (t-T_k)} \tag{5.14}$$

Separating the eigenvalues and the step response in their conjugate terms, λ_j, λ_j^*, and h_j, h_j^* respectively:

$$x(t) = p_0 h_0 + \sum_{j=1}^{n} \left[h_j \sum_{k=1}^{k=m} p_k e^{\lambda_j (t-T_k)} + h_j^* \sum_{k=1}^{k=m} p_k e^{\lambda_j^* (t-T_k)} \right] \tag{5.15}$$

Separating the real and imaginary part of $h_j = h_{jr} + jh_{jc}$ and $\lambda_j = -\xi_j \omega_{nj} \pm j\omega_{nj}\sqrt{1-\xi_j^2} = -\xi_j \omega_{nj} \pm j\omega_{dj}$, equation (5.16) is obtained.

$$\begin{aligned} x(t) = p_0 h_0 + \sum_{j=1}^{n} \Bigg[& h_{jr} \sum_{k=1}^{m} p_k e^{(-\xi_j \omega_{nj} + j\omega_{dj})(t-T_k)} \\ & + jh_{jc} \sum_{k=1}^{m} p_k e^{(-\xi_j \omega_{nj} + j\omega_{dj})(t-T_k)} \\ & + h_{jr} \sum_{k=1}^{m} p_k e^{(-\xi_j \omega_{nj} - j\omega_{dj})(t-T_k)} \\ & - jh_{jc} \sum_{k=1}^{m} p_k e^{(-\xi_j \omega_{nj} - j\omega_{dj})(t-T_k)} \Bigg] \end{aligned} \tag{5.16}$$

Writing the complex factor of the exponential as a function of sine and cosine, and reordering the algebraic, the following equation (5.17) is found:

$$\begin{aligned} x(t) = p_0 h_0 + \sum_{j=1}^{n} \Bigg[& 2h_{jr} \sum_{k=1}^{m} p_k e^{-\xi_j \omega_{nj} (t-T_k)} \cos\left(\omega_{dj}(t-T_k)\right) \\ & + 2h_{jc} \sum_{k=1}^{m} p_k e^{-\xi_j \omega_{nj} (t-T_k)} \sin\left(\omega_{dj}(t-T_k)\right) \Bigg] \end{aligned} \tag{5.17}$$

The vibrations produced by the torsional mode associated with the natural frequency ω_{nj} are zero when the set of steps is orthogonal to the vibration mode. This condition is met when equations (5.18) are satisfied.

$$\left.\begin{aligned}\sum_{k=1}^{m} p_k e^{-\xi_j \omega_{nj} T_k} \cos(\omega_{dj} T_k) = 0 \\ \sum_{k=1}^{m} p_k e^{-\xi_j \omega_{nj} T_k} \sin(\omega_{dj} T_k) = 0\end{aligned}\right\} \forall\, \lambda_j \qquad (5.18)$$

This thesis proposes electrical load connection configurations that solve the equation system (5.18). The method that studies excitation function configurations is called Posicast or input shaping.

5.3.1 Posicast Method

The Posicast method was introduced in [110], [114] by Otto J. M. Smith. It is defined as an open loop compensator that connects an excitation $f(t)$ in segments. In most studies, systems with one frequency are analysed. In them, the load is split in two and the second half is connected half a period after the first one. The step size p_k and timing T_k of the load connection allows the elimination of the overshoot for systems with one or more natural frequencies, as given by equation (5.18).

Figure 5.2 shows the transient response of a system after a step response is shown. While, in Figure 5.2 (a), the load is applied as a step, in Figure 5.2 (b) the open loop Posicast compensator is used, which allows the elimination of the vibrations. By carefully choosing the excitation time and amplitude, the vibrations can be suppressed.

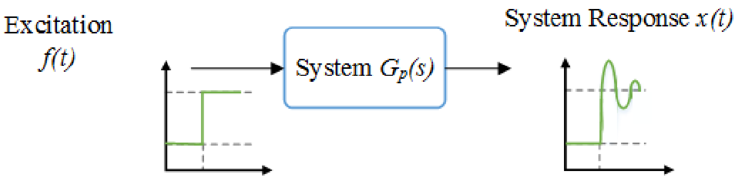

(a) Load Step Connection

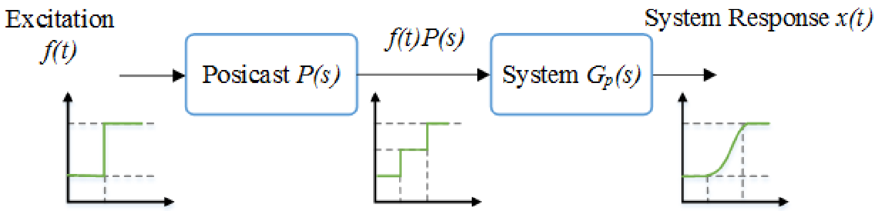

(b) Posicast Load Connection

Figure 5.2: System diagram with and without Posicast compensator.

The general expression of the Posicast compensator can be modelled in the Laplace domain as a series of delayed step connections, which is shown in equation (5.19) and Figure 5.3. p_k and T_k represent the k$^{\text{th}}$ step connection value and the time of it.

$$P(s) = p_1 e^{-sT_1} + \cdots + p_k e^{-sT_k} + \cdots + p_m e^{-sT_m} \tag{5.19}$$

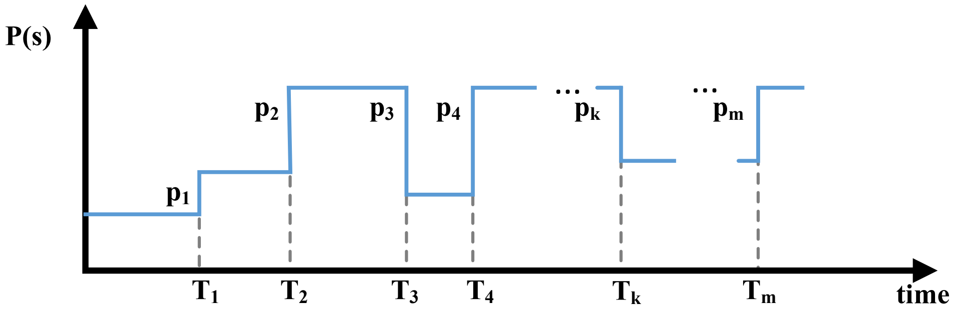

Figure 5.3: Posicast compensator steps.

In most cases, the Posicast compensator has been used to eliminate electrical transients in systems with one natural frequency, and a Posicast compensator of two steps has been applied. For example, in [115], [116] it was employed to eliminate power systems fluctuations in wind farms multi-machine systems, in [117] it was used to remove transients in IGBT drivers, and in [118] for the PWM in rectifiers. Furthermore, as the Posicast compensator depends on the knowledge of the natural frequencies of the system, to improve its response to perturbations, in [93], [119] a modified closed-loop Posicast is studied for second-order systems.

Also, when an optimal signal that eliminates the transient vibrations is analysed, the method is referred as input-shaping [120], [121]. In general, studies that eliminate transient vibrations for electrical systems speak about the Posicast method, while mechanical engineers call it input-shaping methods.

This chapter presents a PMS that applies open-loop strategies based on the Posicast method for the connection of step and pulsating loads.

5.4 Step Load

In this section, strategies to eliminate the torsional vibrations due to the connection of time non-critical and time-critical loads are developed using the theory presented.

5.4.1 Time Non-Critical Load Strategies

In section 5.2 time non-critical loads were described as those for which an exact time connection is not crucial, such as the de-icing system and the air cabin. For that reason, the PMS can apply the open loop Posicast compensator directly to the load connection.

To obtain the size of the steps p_k and connection times T_k the equation system from equation (5.18) is solved for each natural frequency in the system. For a system with n natural frequencies, the non-linear equation system (5.20) must be solved.

$$\begin{bmatrix} \sum_{k=1}^{m} p_k e^{-\xi_1 \omega_{n1} T_k} \cos(\omega_{d1} T_k) \\ \sum_{k=1}^{m} p_k e^{-\xi_1 \omega_{n1} T_k} \sin(\omega_{d1} T_k) \\ \sum_{k=1}^{m} p_k e^{-\xi_2 \omega_{n2} T_k} \cos(\omega_{d2} T_k) \\ \sum_{k=1}^{m} p_k e^{-\xi_2 \omega_{n2} T_k} \sin(\omega_{d2} T_k) \\ \vdots \\ \sum_{k=1}^{m} p_k e^{-\xi_n \omega_{nn} T_k} \cos(\omega_{dn} T_k) \\ \sum_{k=1}^{m} p_k e^{-\xi_n \omega_{nn} T_k} \sin(\omega_{dn} T_k) \end{bmatrix} = 0 \qquad (5.20)$$

The connection patterns used to connect electrical loads are based on the concepts of edges and levels. An edge refers to the number of pulses before arriving at the final value. Instead, the level denotes the number of consecutive additive steps taken before reaching the final value.

Based on the edges and levels, Figure 5.4 presents two different types of excitation pattern. Figure 5.4(a) shows a signal with two consecutive positive steps, corresponding to two levels. This excitation is called Multilevel Loading (MLL). Instead, Figure 5.4(b) shows a waveform in which there is a pulse composed of two edges and one level. This excitation is called Single Level Multi-edge Switching Loading (SLME). In both signals, MLL and SLME, the load goes from a load 1, L_1, to a load 2, L_2, but the connection pattern used is different. Next, the operation of the MLL and SLME is shown.

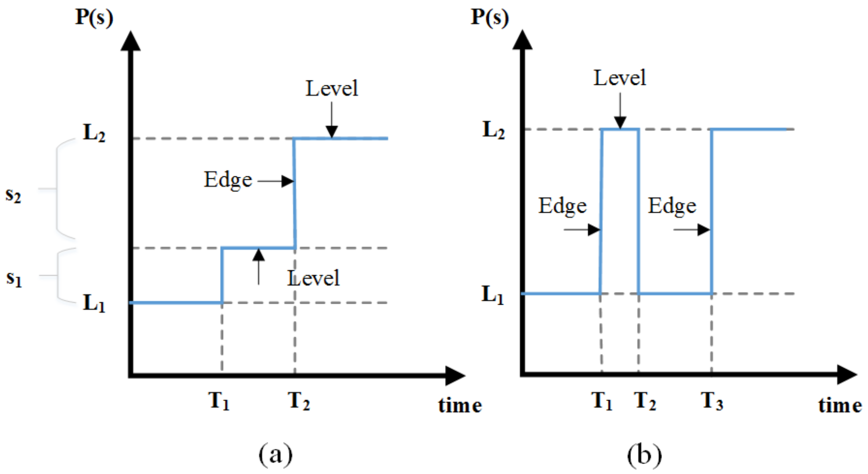

Figure 5.4: Time non-critical load strategies.

5.4.1.1 Multilevel Loading Switching

As shown in Figure 5.4(a), the Multilevel Loading Switching (MLL) strategy consists of connecting a load in consecutive steps, or multiple levels. Hence, it can be applied to time non-critical loads that do not need to be loaded to its full power at one single time instant.

To obtain the time and step values, the equation system (5.20) is solved. Equations (5.21) and (5.22) show the constraints applied to the signal. The initial time is zero, and the times are ascending. Moreover, the total steps are always positive, and the sum equals the total load being connected. This constraint is applied to a normalised load as shown in equation (5.22). Hence, for a system with n natural frequencies, the number of steps is given by $m = n + 1$.

$$\left.\begin{array}{c} T_1 = 0 \\ T_1 \leq T_2 \leq \cdots \leq T_k \leq \cdots \leq T_m \end{array}\right\} \tag{5.21}$$

$$\left.\begin{array}{c} p_1 + p_2 + \cdots + p_k + \cdots + p_m = 1 \\ p_k \geq 0 \end{array}\right\} \tag{5.22}$$

The solutions are first analysed for a one frequency system to study the behaviour of the MLL strategy. After, the method is applied to the electromechanical system presented in chapter 4.

For a one frequency system, $n = 1$ and $m = 2$. Thus, applying the equation system (5.20), the equation system (5.23) is obtained. From equation (5.21) and (5.22), $T_1 = 0$ and $p_2 = 1 - p_1$ respectively, hence the values of p_1 and T_2 must be found.

$$\begin{bmatrix} p_1 + p_2 e^{-\xi_1 \omega_{n1} T_2} \cos(\omega_{d1} T_2) \\ p_2 e^{-\xi_1 \omega_{n1} T_2} \sin(\omega_{d1} T_2) \end{bmatrix} = 0 \tag{5.23}$$

The frequencies are rewritten as a function of the period to analyse the response of the one frequency system as a function of the damping ratio. Equation (5.24) shows the period equation and (5.25) the transient response as a function of it. Now the connection times can be analysed as a function of the period T_p and the damping ratio $\xi \in [0,1]$.

$$T_p = \frac{2\pi}{\omega_n \sqrt{1 - \xi_n^2}} = \frac{2\pi}{\omega_d} \Rightarrow \begin{cases} \omega_d = \dfrac{2\pi}{T_p} \\ \omega_n = \dfrac{2\pi}{T_p \sqrt{1 - \xi^2}} \end{cases} \tag{5.24}$$

$$\begin{bmatrix} p_1 + p_2 e^{-2\pi \frac{\xi_1}{\sqrt{1-\xi_1^2}} \left(\frac{T_2}{T_p}\right)} \cos\left(2\pi \dfrac{T_2}{T_p}\right) \\ p_2 e^{-2\pi \frac{\xi_1}{\sqrt{1-\xi_1^2}} \left(\frac{T_2}{T_p}\right)} \sin\left(2\pi \dfrac{T_2}{T_p}\right) \end{bmatrix} = 0 \tag{5.25}$$

To simplify the notation, the following variable changes are defined: $\Gamma_2 := \mathrm{T}_2 / T_p$ and $\delta_1 := \xi_1 / \sqrt{1 - \xi_1^2}$. Replacing into equation (5.25), equation (5.26) is obtained.

$$\begin{bmatrix} p_1 + p_2 e^{-2\pi\delta\Gamma_2} \cos(2\pi\Gamma_2) \\ p_2 e^{-2\pi\delta\Gamma_2} \sin(2\pi\Gamma_2) \end{bmatrix} = 0 \tag{5.26}$$

Figure 5.5 shows the sine and cosine curves or residuals as a function of Γ_2 for ascending values of ξ ((a) $\xi = 0$, (b) $\xi = 0.1$, (c) $\xi = 0.3$, and (d) $\xi = 0.65$). The curves show that at higher values the oscillations of the sine and cosine decrease, proving that higher damping reduces the overshoot and settling time of a system. Additionally, for each damping ratio, the step p_1 has been chosen such that the sine (in blue) and cosine (in red) curves intersect at zero, obtaining the system's solution. It is observed than independently of the damping ratio, the curves intersect at $\Gamma_2 = 0.5$, and that for higher damping ratio the step p_1 tends to 1.

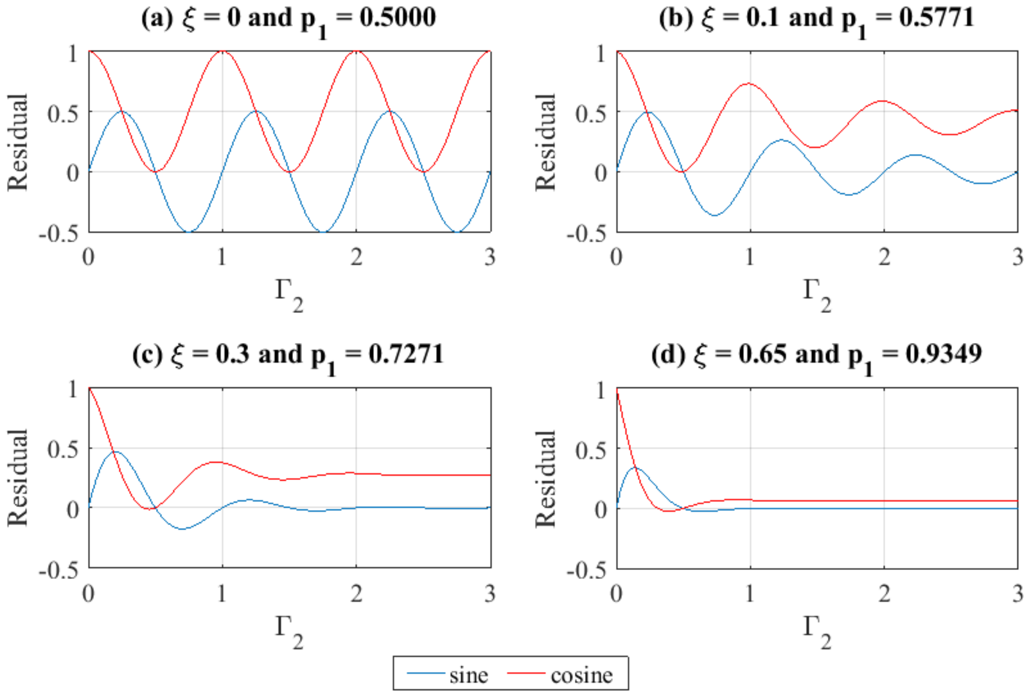

Figure 5.5: Residuals of MLL.

Further details on the solutions of the system are shown in Figure 5.6, in which the contour at zero of the sine and cosine curves is presented. The intersection of this curves, marked by *, represent the solutions of the system for $\Gamma_2 \in [0,3]$. The system has more than one solution, of which one is equal to half a period of the system, which is the solution presented in Figure 5.5. Moreover, the step connection tends to unity as the damping ratio increases, showing that when damping ratio reaches the critical value ($\xi = 1$) the compensator is not needed.

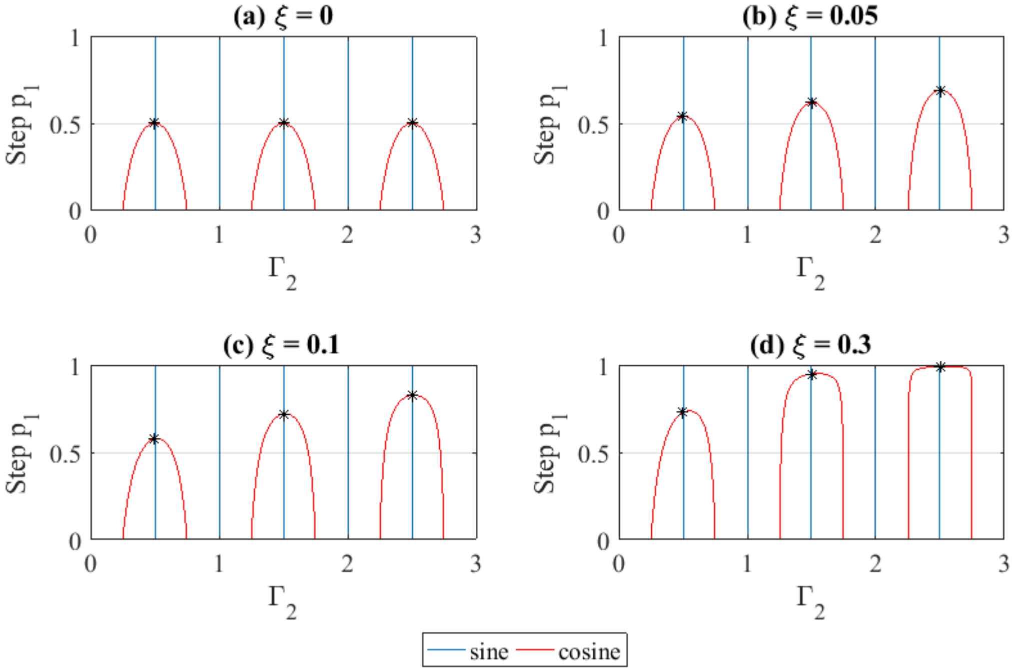

Figure 5.6: Solutions for MLL.

The solutions for the whole damping ratio spectrum in the one frequency system are presented in Figure 5.7. Again, it is observed that the connection time is 0.5 independent of the damping ratio value, while the step increases until the unity for a critically damped ($\xi = 1$) system. Hence, the MLL connection has always a solution inside half a period, and the step size tends to the unity for critically damped systems. This last statement confirms that the critical damping is the value at which the system stops vibrating.

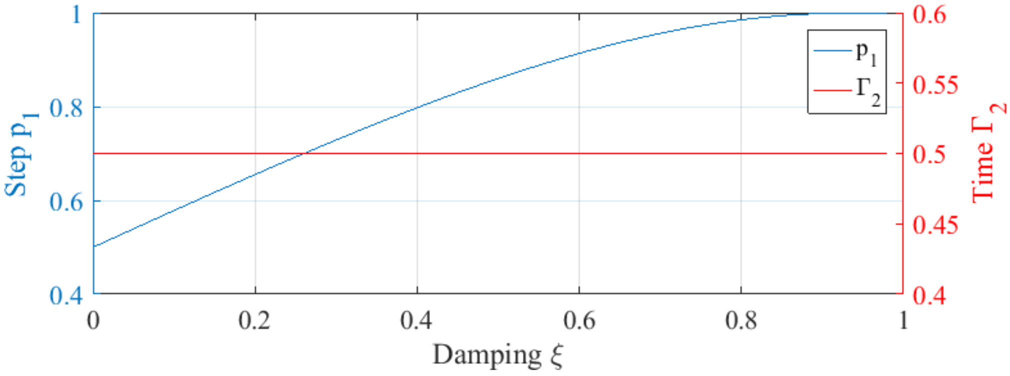

Figure 5.7: MLL time connection and pulse size as a function of ξ.

Since the MLL switching takes place in half a period of the system, for the natural frequencies of the aircraft drivetrain, the connection is made in milliseconds. Additionally, equation (5.24) shows that T_p increases for higher ξ. Thus the time connection T_2 also increases for higher ξ, while keeping the proportion Γ_2 constant.

For a simplified two inertia drivetrain with the parameters shown in Table 5.2, the frequency and damping ratio of the system are $f = 19.09\text{Hz}$ and $\xi = 0.0327$ respectively. Hence, $T_p = 52.4115\text{ ms}$, $p_1 = 0.5257$, and $\Gamma_2 = 0.5$ (or $T_2 = 26.2057\text{ms}$).

Table 5.2: Parameter of the two inertia system.

Parameter	**Value**
Engine Inertia	$J_m = 0.0965\text{ kgm}^2$
Generator Inertia	$J_g = 0.0376\text{ kgm}^2$
Shaft Stiffness	$k_s = 5.3995 * 10^2\text{ Nm/rad}$
Shaft Damping	$d_s = 0.125\text{ Nmrad/s}$

Figure 5.8 shows the shaft response for a torque connection equal to the one used for the step connection in chapter 4: from 0.3952Nm to 2.9282Nm, which is obtained by an electrical load connection of 5Ω when 60Ω are connected with a constant field of 6.2A. In red the generator torque T_{g_2} is shown, while in blue the shaft torque for the one frequency system is observed. The solution obtained, eliminates the torsional vibrations due to the torque connection. Furthermore, the switching occurs in half a period of the system ($T_p/2 = 26.2\text{ms}$), and as the damping ratio is higher than zero, the step size is greater than 0.5.

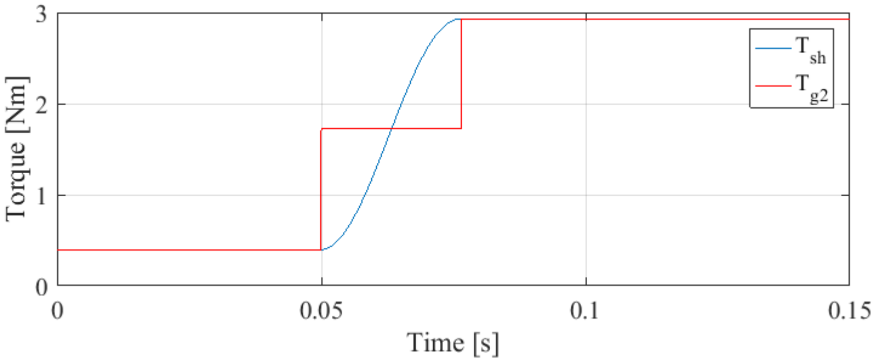

Figure 5.8: MLL torque response for a 1 natural frequency system.

Now that the MLL strategy has been demonstrated for a one frequency system, it can be applied to the system presented in chapter 4. The natural frequencies associated with the drivetrain in the study were:

- $f_1 = 11.9420\text{Hz}$ and $\xi_1 = 0.0369$
- $f_2 = 38.5929\text{Hz}$ and $\xi_2 = 0.0273$
- $f_3 = 109.7195\text{Hz}$ and $\xi_3 = 0.0774$

To eliminate the vibrations on a three natural frequency system ($n = 3$), a four-step connection must be made ($m = n + 1 = 4$). Replacing into equation (5.20), equation (5.27) is obtained, with $T_1 = 0$, and $p_1 + p_2 + p_3 + p_4 = 1$.

$$\begin{bmatrix} \sum_{k=1}^{4} p_k e^{-\xi_1 \omega_{n1} T_k} \cos(\omega_{d1} T_k) \\ \sum_{k=1}^{4} p_k e^{-\xi_1 \omega_{n1} T_k} \sin(\omega_{d1} T_k) \\ \sum_{k=1}^{4} p_k e^{-\xi_2 \omega_{n2} T_k} \cos(\omega_{d2} T_k) \\ \sum_{k=1}^{4} p_k e^{-\xi_2 \omega_{n2} T_k} \sin(\omega_{d2} T_k) \\ \sum_{k=1}^{4} p_k e^{-\xi_3 \omega_{n3} T_k} \cos(\omega_{d3} T_k) \\ \sum_{k=1}^{4} p_k e^{-\xi_3 \omega_{n3} T_k} \sin(\omega_{d3} T_k) \end{bmatrix} = 0 \tag{5.27}$$

Solving the non-linear equation systems (5.27) in MATLAB with Opti Toolbox [122], the following step values and times are obtained:

- $T_1 = 0\text{ms}$ and $p_1 = 0.3633$.
- $T_2 = 10.0190\text{ms}$ and $p_2 = 0.1529$.
- $T_3 = 41.1040\text{ms}$ and $p_3 = 0.3468$.
- $T_4 = 54.7240\text{ms}$ and $p_4 = 0.1370$.

The total period is $T_p = T_{p2} + T_{p3} + T_{p4} = 118.8579\text{ms}$, therefore as $T_4 < T_p/2 = 59.4303\text{ms}$ the solution is inside half a period. Applying the same step connection used before (from 0.3952Nm to 2.9282Nm) to the system modelled in Simulink in chapter 4, Figure 5.9 is obtained. In (a) a step connection is shown, and in (b) the MLL strategy is applied. The torque applied to the drivetrain by the generator T_{g_2} is shown in red. It is composed of the series of steps defined by the MLL strategy instead of a step connection. The shaft response T_{s_3} is observed in blue. Comparing with the step connection in (a), the Posicast compensator in (b) has eliminated the transient vibrations on the generator shaft. Hence, the use of the MLL allows suppression of the shaft vibrations due to electrical load connections.

(a) Step

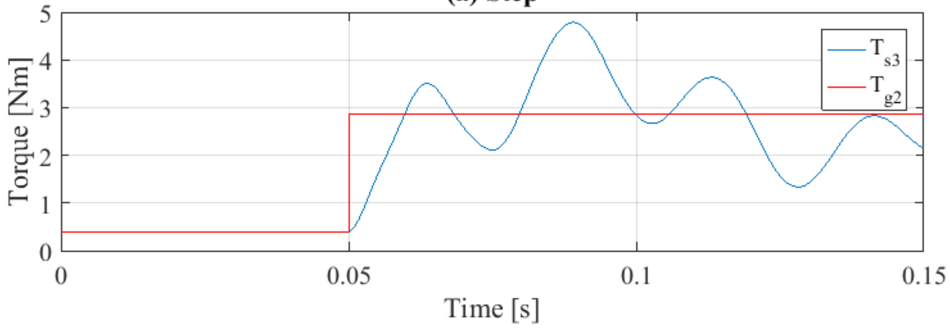

(b) MLL

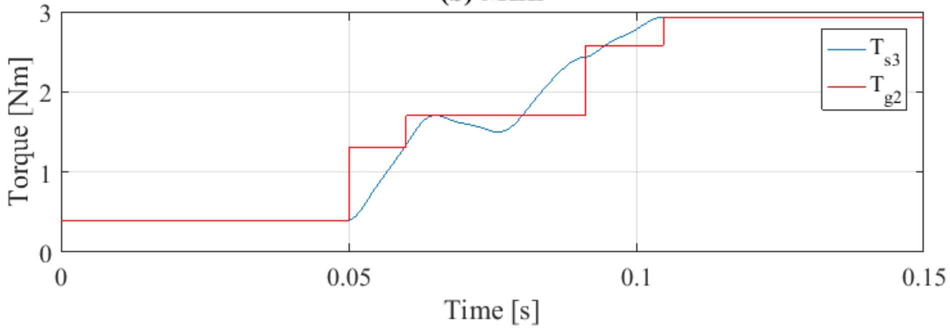

Figure 5.9: Torque shaft response with MLL signal.

In practice, this solution can be applied by using multilevel converters for loads that can be connected by steps, such as the ice protection systems. For loads that cannot be connected by multiple steps, the SLME connection strategy is proposed.

5.4.1.2 Single Level Multi-edge Switching Load

An alternative connection arrangement to eliminate the torsional vibrations due to electromechanical interaction is the Single Level Multi-edge Switching Loads (SLME) method showed in Figure 5.4(b). It consists of connecting the load as a series of on/off pulses. Therefore, the step applied to the system takes values ± 1

corresponding to the continuous connection and disconnection of the loads. This pulsating connection is comparable to the behaviour of a mechanical switch, which has a bounce in its connection. Time non-critical loads, such as radar and de-icing systems are examples of loads to which it can be applied.

Again the connection times are ascending and $T_1 = 0$. Equations (5.28) and (5.29) show the constraints used for the SLME strategy. The number of steps for a system with n frequencies is given by $m = 2n + 1$.

$$\left.\begin{array}{c} T_1 = 0 \\ T_1 \leq T_2 \leq \cdots \leq T_k \leq \cdots \leq T_m \end{array}\right\} \tag{5.28}$$

$$p_k = (-1)^{k+1} \tag{5.29}$$

Equally to the MLL connection, first the behaviour of the strategy for a one frequency system is studied, and after the strategy is applied to the aircraft system. For the one natural frequency system ($n = 1$), three pulses are applied ($m = 2n + 1 = 3$). Replacing n, m, and p_k into (5.20), the equation system (5.30) is obtained.

$$\begin{bmatrix} 1 + p_2 e^{-\xi_1 \omega_{n1} T_2} \cos(\omega_{d1} T_2) + p_3 e^{-\xi_1 \omega_{n1} T_3} \cos(\omega_{d1} T_3) \\ p_2 e^{-\xi_1 \omega_{n1} T_2} \sin(\omega_{d1} T_2) + p_3 e^{-\xi_1 \omega_{n1} T_3} \sin(\omega_{d1} T_3) \end{bmatrix} = 0 \tag{5.30}$$

Substituting the period of equation (5.24) into (5.30), the connection times of the system are modelled for a general period T_p in equation (5.31).

$$\begin{bmatrix} 1 + p_2 e^{-2\pi \frac{\xi_1}{\sqrt{1-\xi_1^2}} \frac{T_2}{T_p}} \cos\left(2\pi \frac{T_2}{T_p}\right) + p_3 e^{-2\pi \frac{\xi_1}{\sqrt{1-\xi_1^2}} \frac{T_3}{T_p}} \cos\left(2\pi \frac{T_3}{T_p}\right) \\ p_2 e^{-2\pi \frac{\xi_1}{\sqrt{1-\xi_1^2}} \frac{T_2}{T_p}} \sin\left(2\pi \frac{T_2}{T_p}\right) + p_3 e^{-2\pi \frac{\xi_1}{\sqrt{1-\xi_1^2}} \frac{T_3}{T_p}} \sin\left(2\pi \frac{T_3}{T_p}\right) \end{bmatrix} = 0 \tag{5.31}$$

As in the MLL case, to simplify the notation, the following variable changes are defined: $\Gamma_k := T_k/T_p$ and $\delta_1 := \xi_1/\sqrt{1-\xi_1^2}$. Replacing into equation (5.31), equation (5.32) is obtained.

$$\begin{bmatrix} 1 + p_2 e^{-2\pi\delta_1 \Gamma_2} \cos(2\pi\Gamma_2) + p_3 e^{-2\pi\delta_1 \Gamma_3} \cos(2\pi\Gamma_3) \\ p_2 e^{-2\pi\delta_1 \Gamma_2} \sin(2\pi\Gamma_2) + p_3 e^{-2\pi\delta_1 \Gamma_3} \sin(2\pi\Gamma_3) \end{bmatrix} = 0 \tag{5.32}$$

To analyse the connection times as a function of the period T_p and the damping ratio ($\xi \in [0,1]$), Figure 5.10, Figure 5.11, and Figure 5.12 are obtained. The sine and cosine curves as a function of Γ_3 are shown in Figure 5.10. At higher damping ratio, the vibrations decrease.

In Figure 5.11 the sine and cosine contour at zero for different damping ratio in a range of time $\Gamma_3 \in [0,3]$ are presented. Their intersections (marked by *) show that the system has multiple solutions, of which one is inside half a period of the system, independently of the damping value.

Lastly, Figure 5.12 illustrates the first solution of Γ_2 and Γ_3 that eliminates the vibrations for the underdamped spectrum. Like in the MLL solution, the time connections are inside half a period of the system. Moreover, while the damping ratio increases, the connection times Γ_2 and Γ_3 get closer. At the critical damping ($\xi = 1$) their values are the same, indicating again, that no compensator is needed for the connection of load in systems with high damping.

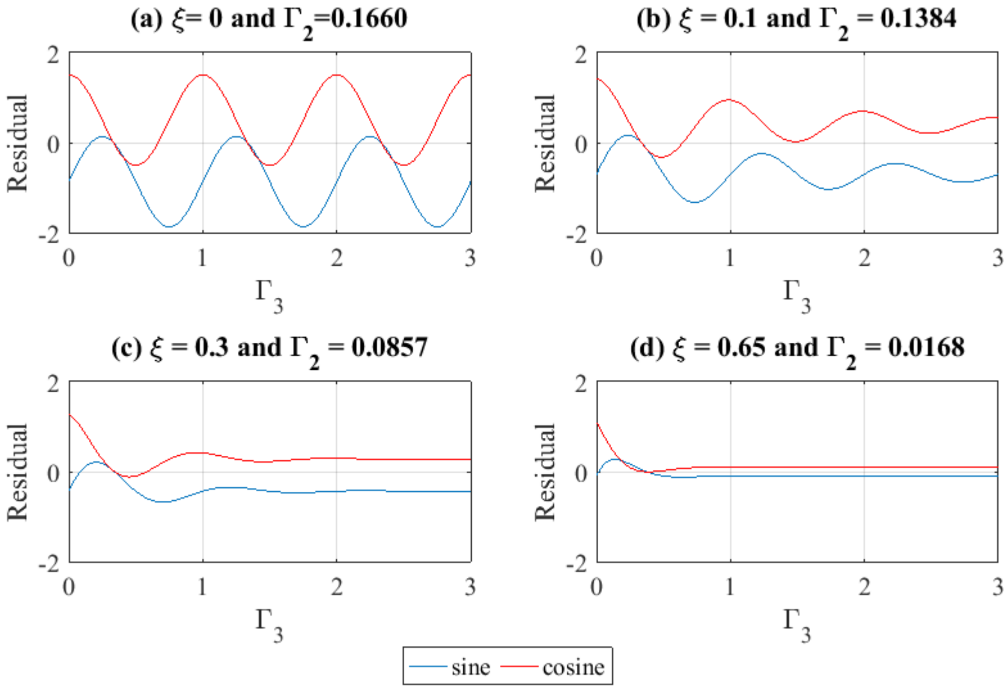

Figure 5.10: Residuals of SLME.

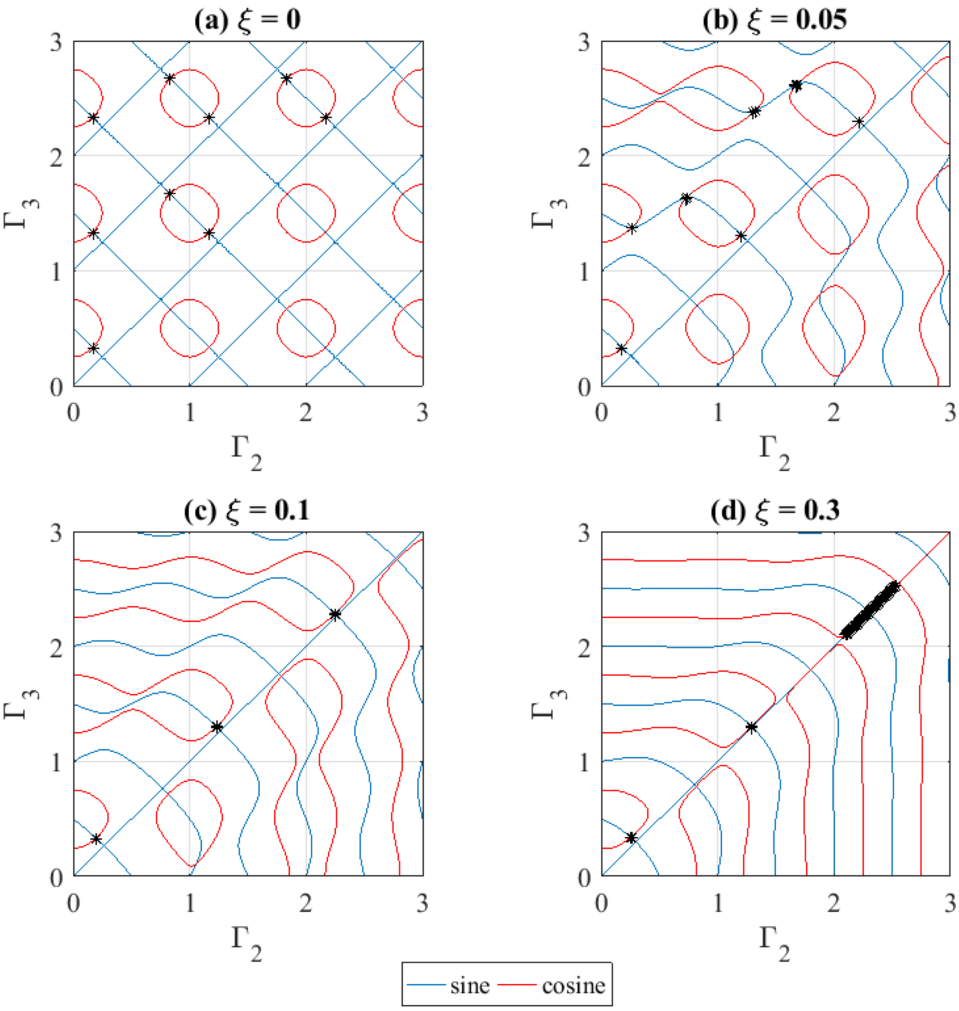

Figure 5.11: Solutions for SLME.

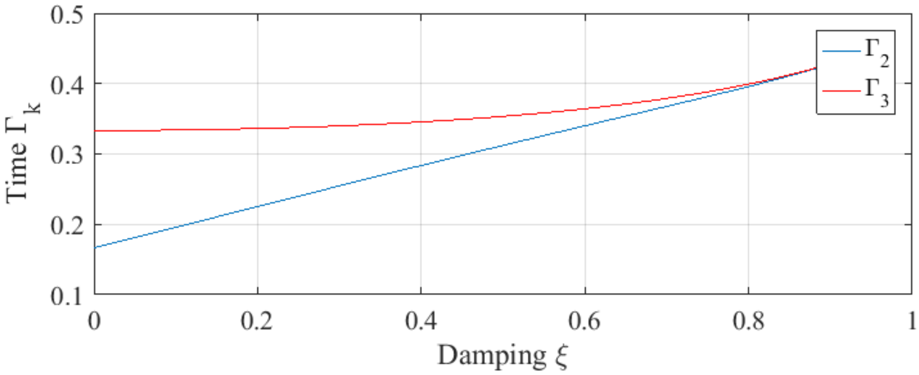

Figure 5.12: SLME time connection as a function of ξ.

Solving for the same one natural frequency system used in the MLL method and the same step connection from 0.3952Nm to 2.9282Nm, Figure 5.13 is obtained. In red, the pulsating generator torque applied to the mechanical system is shown, while in blue the system response is observed. Thus, SLME allows the elimination of the vibrations produced by electromechanical interaction. Since the connection times are $T_1 = 9.3508\text{ms}$ and $T_2 = 17.6990\text{ms}$, the pulsating connection takes place under half a period of the system ($T_p/2 = 59.4303\text{ms}$).

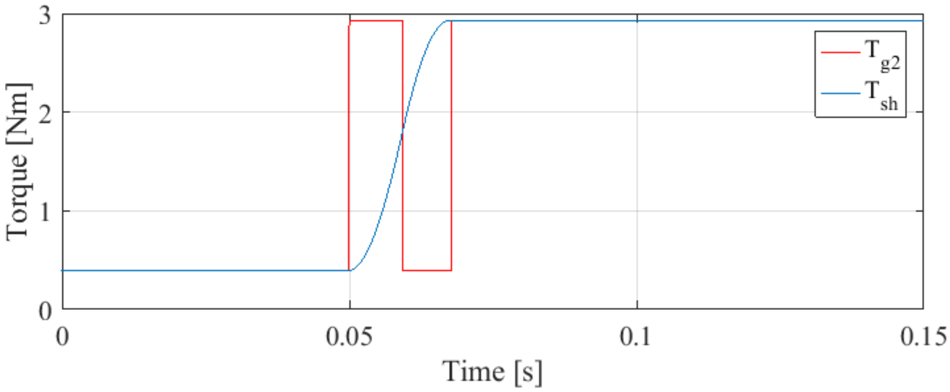

Figure 5.13: SLME torque response for a 1 natural frequency system.

Now, SLME is applied to the drivetrain described in chapter 4. For the three natural frequency system ($n = 3$), the SLME compensator applies seven pulses to the system ($m = 2n + 1 = 7$). The system from (5.33) must be solved for the connection times $T_2 - T_7$.

$$\begin{bmatrix} \sum_{k=1}^{7} (-1)^{k+1} e^{-\xi_1 \omega_{n1} T_k} \cos(\omega_{d1} T_k) \\ \sum_{k=1}^{7} (-1)^{k+1} e^{-\xi_1 \omega_{n1} T_k} \sin(\omega_{d1} T_k) \\ \sum_{k=1}^{7} (-1)^{k+1} e^{-\xi_2 \omega_{n2} T_k} \cos(\omega_{d2} T_k) \\ \sum_{k=1}^{7} (-1)^{k+1} e^{-\xi_2 \omega_{n2} T_k} \sin(\omega_{d2} T_k) \\ \sum_{k=1}^{7} (-1)^{k+1} e^{-\xi_3 \omega_{n3} T_k} \cos(\omega_{d3} T_k) \\ \sum_{k=1}^{7} (-1)^{k+1} e^{-\xi_3 \omega_{n3} T_k} \sin(\omega_{d3} T_k) \end{bmatrix} = 0 \tag{5.33}$$

Solving the non-linear system in Matlab with Opti Toolbox [122], the following connection values are obtained:

- $T_1 = 0\text{ms}$ and $p_1 = 1$.
- $T_2 = 5.7595\text{ms}$ and $p_2 = -1$.
- $T_3 = 8.6953\text{ms}$ and $p_3 = 1$.
- $T_4 = 14.1730\text{ms}$ and $p_4 = -1$.
- $T_5 = 20.3020\text{ms}$ and $p_5 = 1$.
- $T_6 = 26.8580\text{ms}$ and $p_6 = -1$.
- $T_7 = 33.7580\text{ms}$ and $p_7 = 1$.

Modelling the system in Simulink, Figure 5.14 is obtained. In (a) and (b) the step connection and the SLME strategy are respectively shown. The generator torque T_{g_2} applied is shown in red, while the shaft torque T_{s_3} is illustrated in blue. The parameters are the same that were used for the step connection in chapter 4 and the MLL strategy. Again, the vibrations produced by the connection have been eliminated.

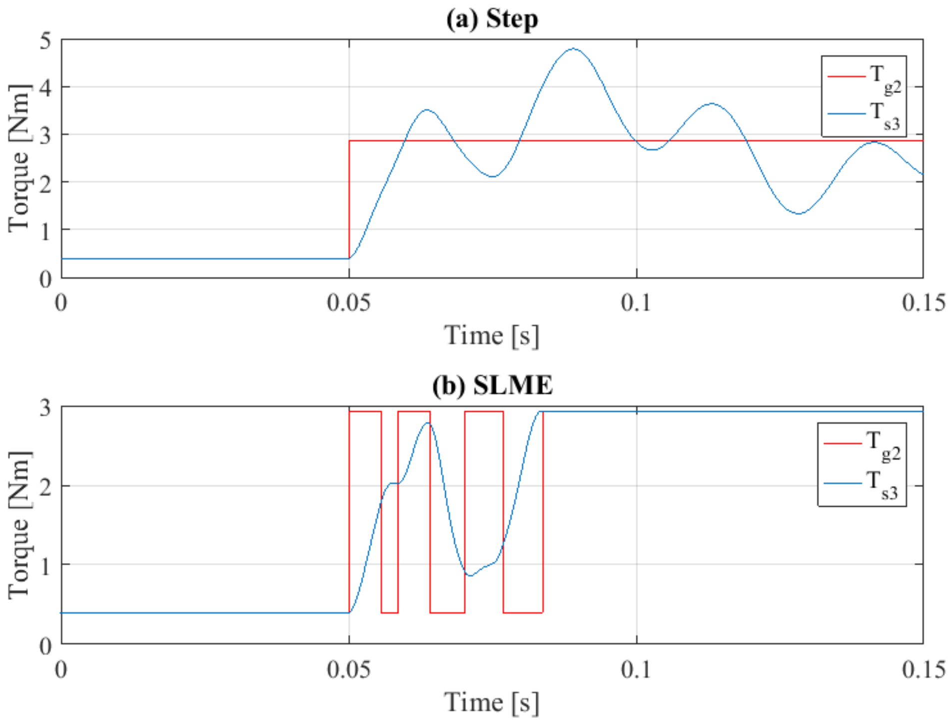

Figure 5.14: Torque shaft response with SLME signal.

Until now, two strategies to connect time non-critical loads have been shown. The MLL and SLME strategies can be applied to loads that allow the connection of multiple segments or under a pulsating pattern respectively. Moreover, the duration of the connection is in the order of milliseconds, which makes it faster than with other control strategies and virtually instantaneous for loads such as the de-icing system that remains connected for a longer time.

However, to find the timing and step values, the natural frequencies and damping ratio of the system must be known. In chapter 7, the identification of these parameters is studied, and in chapter 8, the robustness of the methods is analysed. Next, the case of time-critical loads is analysed.

5.4.2 Time Critical Load Strategy

So far strategies for time non-critical loads have been proposed. This section studies the case of time-critical loads, like flight control surfaces, to which a delay in their connection cannot be applied.

For this reason, to avoid the vibrations produced by a step connection the PMS uses an Auxiliary Load, while the time-critical load is connected as a step. Auxiliary loads are time non-critical loads already in the system (or that also need to be connected), to which a Posicast based strategy is applied. The electrical power of the time non-critical load must be higher than the one of the time-critical load being connected. An example of an auxiliary load is the ice protection system, which, as shown in [111], has an on/off/on operation pattern, making possible the connection and disconnection by short times.

It follows that the equation system that needs to be solved must include both loads, the auxiliary load L_{aux} and the critical load L_C. Thus, equation (5.18) has two components, one associated with the auxiliary load (p_{aux}, T_{aux}) and one to the critical load (p_c, T_c) as shown in (5.34). The step of the critical load is $p_c = 1$.

$$\left.\begin{aligned} p_c e^{-\xi_j \omega_{nj} T_k} \cos\left(\omega_{dj} T_c\right) + \sum_{k=1}^{m} p_{aux\,k} e^{-\xi_j \omega_{nj} T_k} \cos\left(\omega_{dj} T_{aux\,k}\right) = 0 \\ p_c e^{-\xi_j \omega_{nj} T_k} \sin\left(\omega_{dj} T_c\right) + \sum_{k=1}^{m} p_{aux\,k} e^{-\xi_j \omega_{nj} T_k} \sin\left(\omega_{dj} T_{aux\,k}\right) = 0 \end{aligned}\right\} \forall\, \lambda \quad (5.34)$$

The strategy used is presented in Figure 5.15. While the time-critical load (L_C in yellow line) is connected as a step, the auxiliary load (L_{aux} in purple line) is disconnected and reconnected using the SLME method. Thus, the total load applied to the generator ($L = L_C + L_{aux}$) is not a single step. This strategy is called Multi-load Single Level Multi-edge Switching Loads (MSLME).

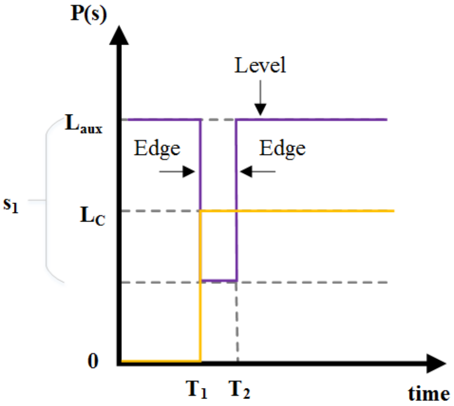

Figure 5.15: Time critical load.

For a system with n natural frequencies, the number of steps is given by $m = 2n$. Moreover, the equation's constraints are given by (5.35) and (5.36).

$$\left.\begin{aligned} T_1 = 0 \\ T_1 \le T_2 \le \cdots \le T_k \le \cdots \le T_m \end{aligned}\right\} \quad (5.35)$$

$$p_{aux\,k} = (-1)^k p \quad (5.36)$$

As was done for the time non-critical loads, the system is analysed for one frequency system first, and afterwards for the drivetrain in the study. It follows that the solution for the one frequency system, shown in equation (5.37), is obtained by substituting $n = 1$, and $m = 2n = 2$ into equation (5.34). The connection time T_2 and step value p that must be disconnected from the auxiliary load are the variables to obtain. In the case of one natural frequency, the MSLME strategy is equivalent to the MLL strategy since for a one natural frequency system the final excitation applied by the generator is the same.

$$\begin{bmatrix} 1 - p + pe^{-\xi_1 \omega_{n1} T_2} \cos(\omega_{d1} T_2) \\ pe^{-\xi_1 \omega_{n1} T_2} \sin(\omega_{d1} T_2) \end{bmatrix} = 0 \tag{5.37}$$

Writing the system as a function of the period T_p as shown in (5.24), and defining the variables $\Gamma_k := \mathrm{T_k}/T_p$ and $\delta_1 := \xi_1/\sqrt{1-\xi_1^2}$, equation (5.38) is obtained.

$$\begin{bmatrix} 1 - p + pe^{-2\pi\delta_1 \Gamma_2} \cos(2\pi\Gamma_2) \\ pe^{-2\pi\delta_1 \Gamma_2} \sin(2\pi\Gamma_2) \end{bmatrix} = 0 \tag{5.38}$$

The residuals for the sine and cosine equations are shown in Figure 5.16. The curves are equivalent to the ones obtained for the MLL strategy presented for time non-critical loads. However, for higher damping ratio, the step of the MSLME decreases until zero, while in the MLL case it increases. The difference originates from the step description: For MLL the step is connected and for MSLME is disconnected. The same is shown in Figure 5.17 in which the sine and cosine contours at zero are plotted. It is clear that the solutions of the MLL and MSLME are the same for a one frequency system.

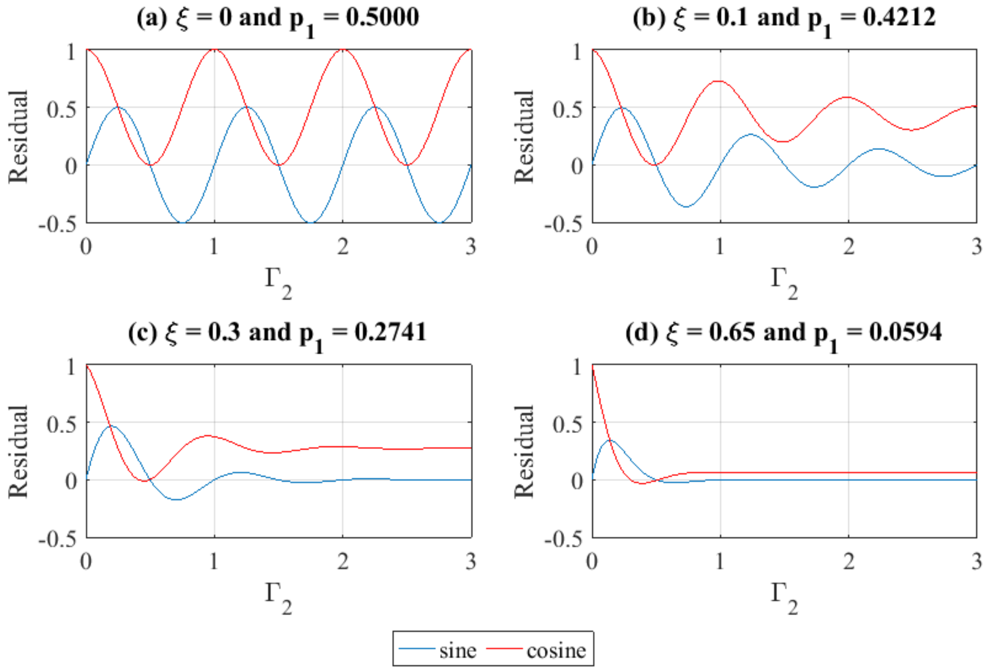

Figure 5.16: Residuals of MSLME.

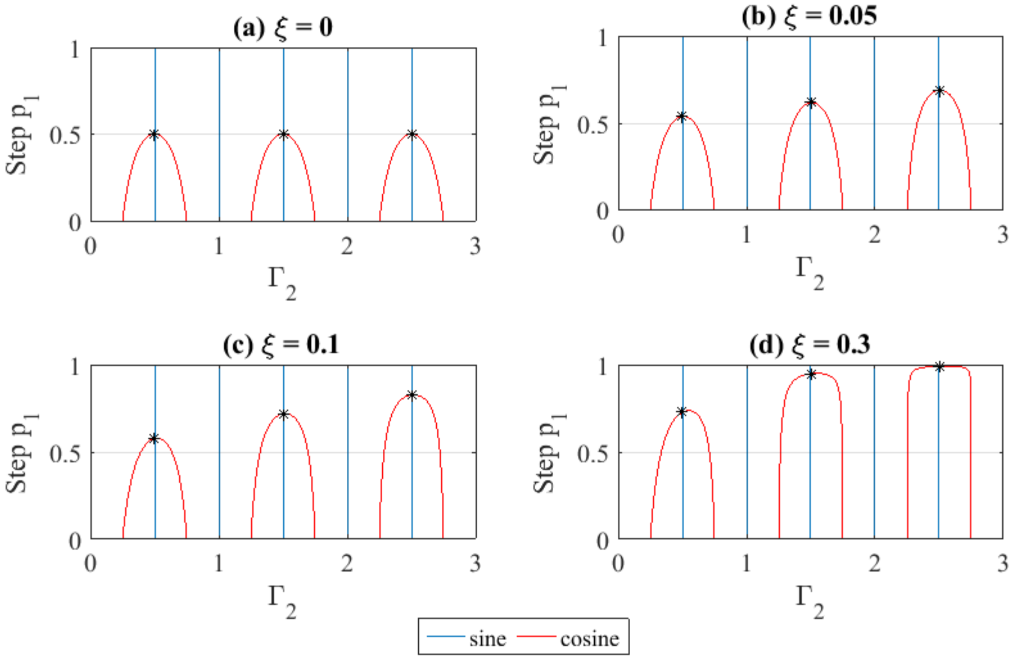

Figure 5.17: Solutions for MSLME.

In Figure 5.18 the solutions for the underdamped system are presented. While the time Γ_2 remains constant at half a period, the auxiliary load that must be disconnected decreases. When the damping ratio is high, there is no need to disconnect the auxiliary load.

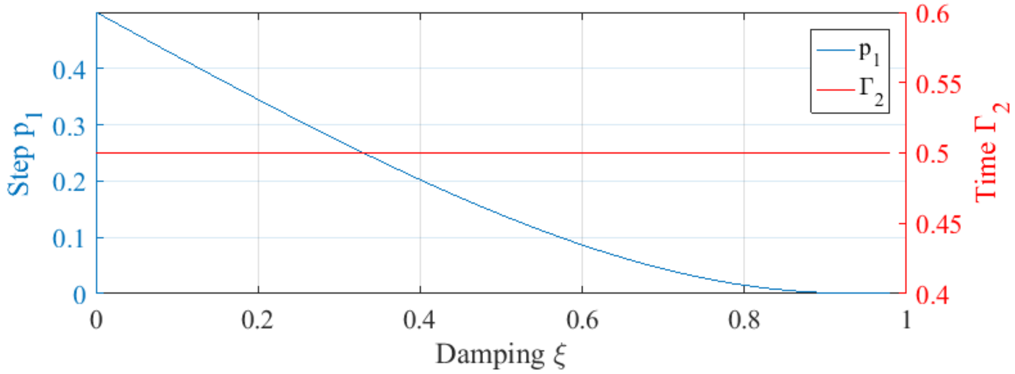

Figure 5.18: Solution spectrum for MSLME with $\xi \in [0,1]$.

Solving the one frequency system presented in section 5.4.1.1 Figure 5.19 is obtained. The initial torque is 0.3952Nm, the same initial torque of the other cases. Instead, the final torque is 1.0532Nm, the torque obtained when 30Ω are connected with a field current of 6.2A. The value of the load connected is lower than the one used for the MLL and SLME case because of the auxiliary load value, already connected to the system, is approximately half of the load being connected. In Figure 5.19(a) the auxiliary load (T_{aux} in purple), critical load (T_c in yellow), and total load (T_{g_2} in red) are shown. The resulting load T_{g_2} applied by the generator to the mechanical system is shown in Figure 5.19(b). As shown in the previous analysis for a one frequency system, the total torque is the same obtained for the MLL method. The torque shaft is shown in blue, and as expected the vibrations are eliminated after the final switching event.

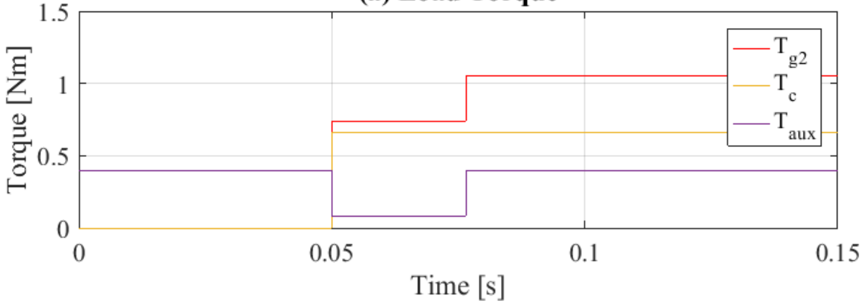
(a) Load Torque

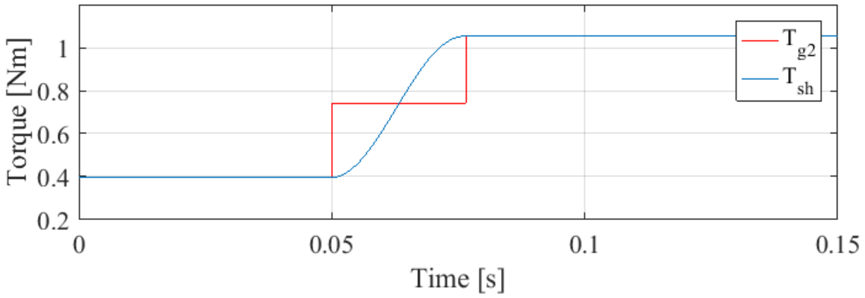
(b) Applied Torque

Figure 5.19: MSLME torque response for a 1 natural frequency system.

Now, the MSLME method is solved for the aircraft system composed of three natural frequencies. Replacing $n = 3$, the auxiliary load must be disconnected and connected six times ($m = 2n = 6$). The system from equation (5.39) must be solved.

$$\begin{bmatrix} 1+\sum_{k=1}^{6}(-1)^{k}pe^{-\xi_1\omega_{n1}T_k}\cos(\omega_{d1}T_k) \\ \sum_{k=1}^{6}(-1)^{k}pe^{-\xi_1\omega_{n1}T_k}\sin(\omega_{d1}T_k) \\ 1+\sum_{k-1}^{6}(-1)^{k}pe^{-\xi_2\omega_{n2}T_k}\cos(\omega_{d2}T_k) \\ \sum_{k=1}^{6}(-1)^{k}pe^{-\xi_2\omega_{n2}T_k}\sin(\omega_{d2}T_k) \\ 1+\sum_{k=1}^{6}(-1)^{k}pe^{-\xi_3\omega_{n3}T_k}\cos(\omega_{d3}T_k) \\ \sum_{k=1}^{6}(-1)^{k}pe^{-\xi_3\omega_{n3}T_k}\sin(\omega_{d3}T_k) \end{bmatrix} = 0 \tag{5.39}$$

The system is solved in MATLAB with Opti Toolbox [122], for the same time-critical load connection of 0.3952Nm to 1.0532Nm for the one natural frequency system. The connection and step values are:

- $T_1 = 0\text{ms}$, $p_c = 1$ and $p_{aux\,1} = -0.4936$.
- $T_2 = 37.3700\text{ms}$ and $p_{aux\,2} = 0.4936$.
- $T_3 = 40.9540\text{ms}$ and $p_{aux\,3} = -0.4936$.
- $T_4 = 44.4940\text{ms}$ and $p_{aux\,4} = 0.4936$.
- $T_5 = 56.0320\text{ms}$ and $p_{aux\,5} = -0.4936$.
- $T_6 = 57.7910\text{ms}$ and $p_{aux\,6} = 0.4936$.

Since $T_6 < T_p/2 = 59.4302$ ms , the connection takes places under half a period. Figure 5.20 shows the results obtained. In (a) the step connection is shown. In (b) the values of T_{aux} (yellow line), T_C (purple line), and the total load applied to the generator T_{g_2} (red line) are shown. It is observed that, even though the critical load is connected as a step connection, the total torque applied to the generator is not. In Figure 5.20(c) the total torque over the generator (red line) and the shaft torque (blue line) are presented. The total system transient shows the elimination of the vibrations, which demonstrated the effectiveness of this loading pattern.

(a) Step

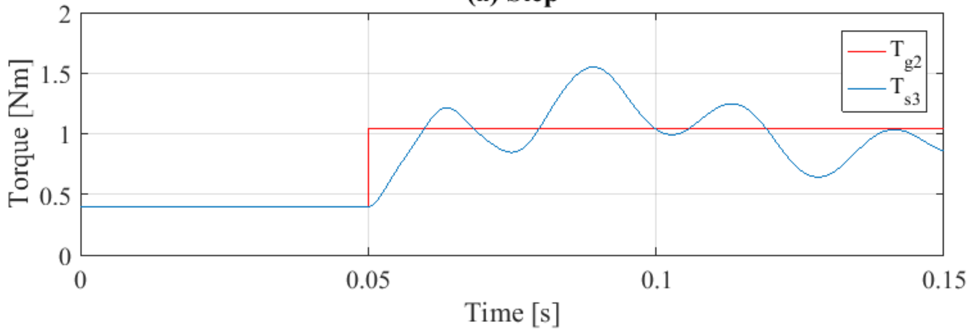

(b) MSLME Load Torque

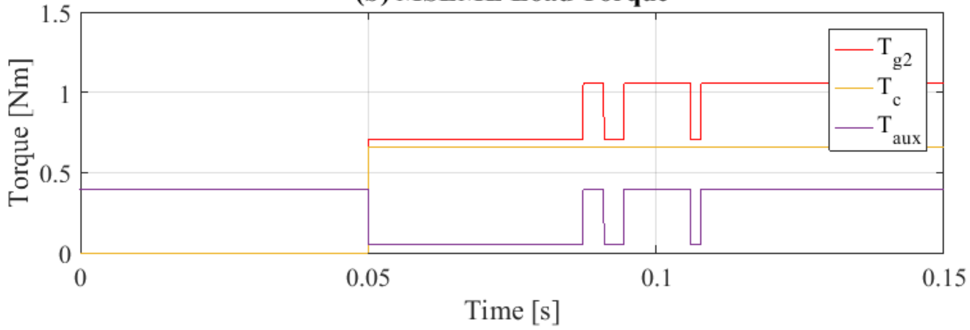

(c) Applied MSLME Torque

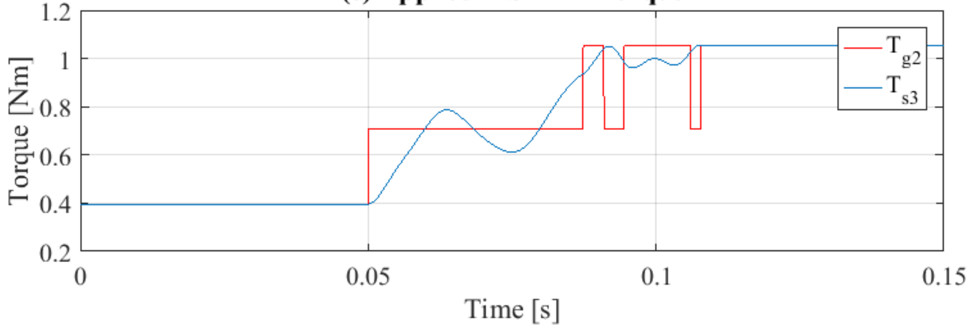

Figure 5.20: Torque shaft response with MSLME signal.

In summary, the torsional vibrations can be eliminated after the final switching event independently of the loads being connected. In the case of time non-critical loads, the Posicast based strategy can be applied directly to the resistance. Instead, for time-critical loads, an auxiliary load is needed.

Moreover, it has been shown that independently of the case, there is always a combination of steps inside half a period of the natural frequency. This guarantees that the strategy is applied in a short time interval. Hence, the operation of the aircraft is not disrupted by the PMS. To understand the performance of the strategies presented, next, the root locus and the Fourier analysis of the signal are studied.

5.4.3 Frequency Analysis

In this section, the effect of the Posicast based strategies is considered in terms of frequency. For this, the root locus analysis of the system and the Fourier analysis are studied.

5.4.3.1 Root Locus Analysis

To understand the effect of the strategies used by the PMS on the overall system, the zero-pole root locus technique is analysed for the system without and with the strategies MLL, SLME, and MSLME.

To analyse the root locus the transfer function of the system is calculated in the Laplace domain. For the base case (step connection), the transfer function $H_{plant}(s)$ is obtained from the drivetrain system presented in chapter 4 in equation (4.30)[2].

The transfer function of the system with the compensator is given by equation (5.40). In which, H_{plant} is the drivetrain transfer function used for the step connection, and $H_{Posicast}$ is the compensator applied to the system, MLL, SLME, or MSLME. The transfer function $H_{Posicast}$ is given by equation (5.19), in which p_k represents the height of the k^{th} step at a time T_k. Representing the time delays of the step connections by Padé approximation, the transfer function is obtained.

$$H_{System}(s) = H_{Posicast}(s)H_{Plant}(s) \tag{5.40}$$

Figure 5.21 shows the poles of the system with the zeros added by the PMS strategies. Figure 5.21(a) presents the poles (represented by x) of the drivetrain while Figure 5.21(b), (c) and (d) show the poles and zeros (represented by o) when the strategies are applied. In every case, the Posicast compensator adds zeros to the system at the poles values. For this reason, the poles cannot be excited by input signals, and the mechanical vibrations are suppressed. The extra poles added are due to the use of high order Padé approximations, which is a frequency domain expansion of a time domain delay.

---

[2] The command ss2tf from Matlab is used

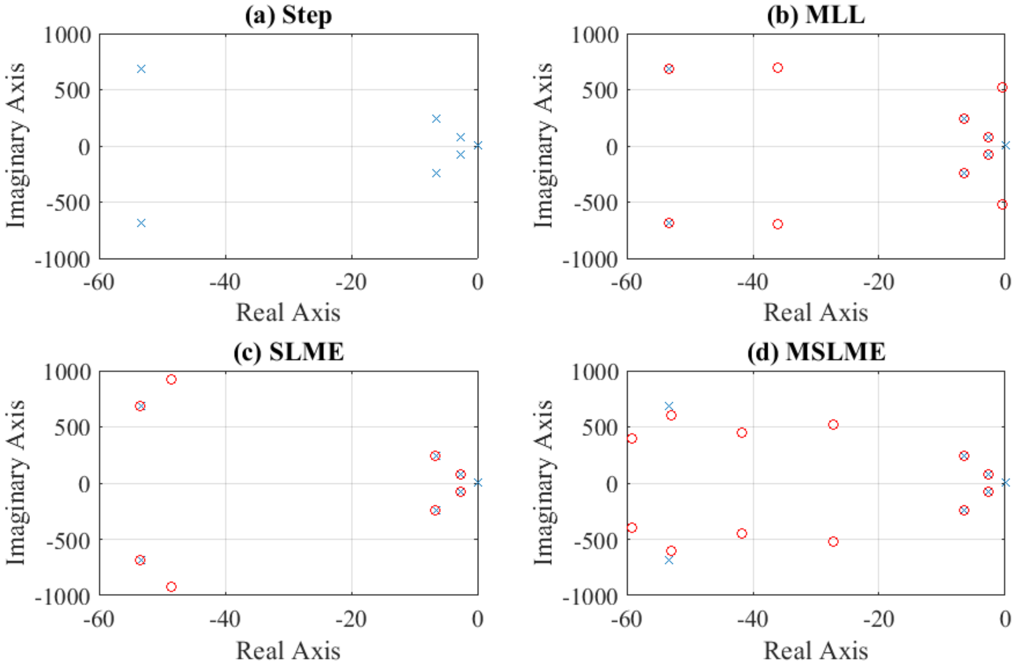

Figure 5.21: Poles (shown by x) and zeros (shown by o) of the system.

The cancellations of poles are similar to the use of a notch filter, in which the use of a filter cancels the resonant frequencies [123]. This method has been used for electromechanical systems as discussed in chapter 3.

5.4.3.2 Fourier Analysis

To analyse the frequencies excited by the load connection, the shaft torque T_{sh} is analysed through Fourier Transform. Figure 5.22 shows the frequency spectrum obtained for the loads connected as a step. In (a) the step connection presented in chapter 4 is shown, while in (b), (c), and (d) the results obtained with MLL, SMLE, and MSLME are analysed.

In the step case (a), the frequencies of the system are observed. This shows that after a step connection the torsional vibrations are excited. Instead when the strategies are applied no frequency is recognised, which corroborates that the Posicast methods do not excite the mechanical natural frequencies.

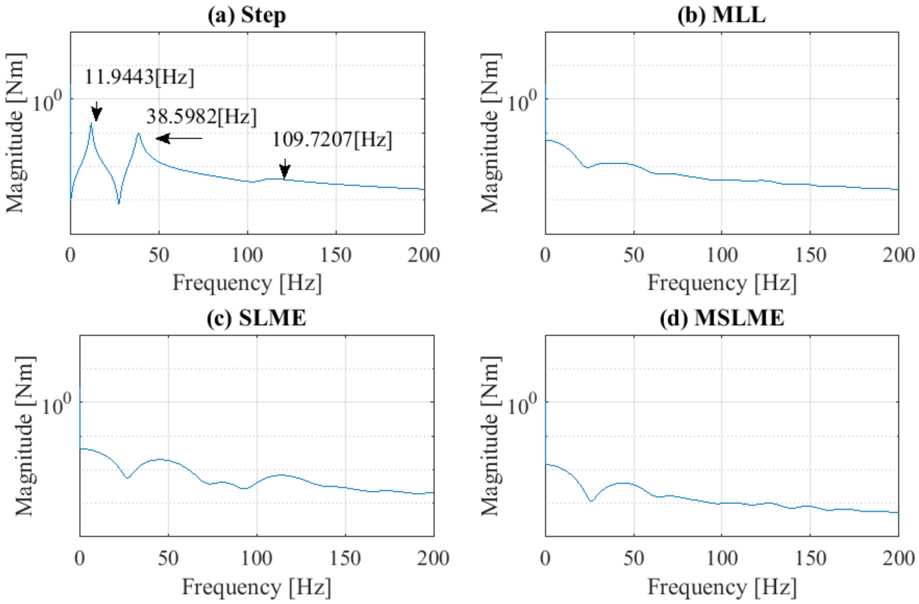

Figure 5.22: Fourier analysis of the system.

The Root Locus and Fourier analysis show that the PMS eliminates the vibrations of the system by cancelling the excitation of the mechanical system poles.

5.5 Pulsating Load

In section 5.4, the elimination of the torsional vibrations due to step loads was presented. Now, the case of pulsating loads is analysed. In chapter 4, three operation cases, based on its frequency were identified for pulsating trains: low frequency, a frequency equal to the mechanical vibration modes, and high frequencies. Low frequencies are defined as those under the natural frequencies of the mechanical system, and high frequencies the ones over.

For each situation, the following restrictions were proposed:

- The carrier frequencies equal to the torsional vibration modes must be avoided. For this reason, the vibration modes must be identified.
- Low frequencies must have duty cycles roughly higher than 30% for studies that keep the average power constant.
- High frequencies must be chosen to minimise the switching losses of the converter.

Now, the elimination of the transient vibrations due to the pulsating load's connection is analysed. Thus, strategies for the system operating at low and high frequencies are presented.

5.5.1 Low-Frequency Strategy

A pulsating load operating at a low frequency produces a complete transient response for each load pulse, as shown in Figure 5.23(a). In it, a pulsating load with an average torque equal to the load connected in the step connection (2.9282Nm), 60% duty cycle, and a frequency of 0.2Hz is applied to the system described in chapter 4.

The strategies presented in section 5.4 eliminate the system vibrations by applying a series of pulses in under half a period. Since the times between low-frequency pulses are higher than half a period of the mechanical system, to each pulse the Posicast compensator is applied. As well, low-frequency loads, such as the heating system, can act as an auxiliary load for the critical load connections. For the low frequencies pulsating train of Figure 5.23(a), the SLME strategy is implemented as shown in Figure 5.23(b). The transient vibrations are eliminated.

(a) Step Pulse

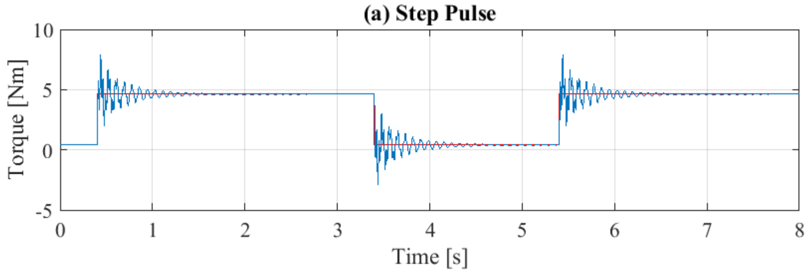

(b) SLME Pulse

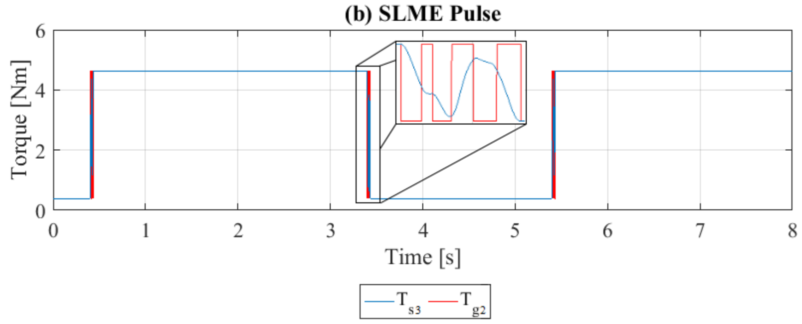

Figure 5.23: Low-frequency SLME.

5.5.2 High-Frequency Strategy

In the case of high frequencies, which switching time is higher than the natural frequencies of the drivetrain, the Posicast based strategies cannot be applied to each switching event. Moreover, Figure 5.24(a) shows that the connection of a high frequency pulsating load (T_{g_2} in red) is perceived as a step load connection by the mechanical system (T_{s_3} in blue). The signal applied T_{g_2} has a frequency of 2000Hz, 60% duty cycle and the same mean torque of the low frequency case and the step connection (2.9282Nm).

Therefore, the Posicast based strategies are applied at the beginning of the switching load connection as if it were a regular step connection. The final load applied T_{g_2} is obtained by convolution of the pulsating load T_{pl} and the Posicast method P as shown in equation (5.41).

$$T_{g_2}(t) = \sum_k T_{pl}(k)\, P(t-k+1) \tag{5.41}$$

Figure 5.24(b) shows the response of the system when the SLME strategy is applied to the pulsating load. As if the load was a step connection, the strategy eliminates the transient vibrations of the mechanical system.

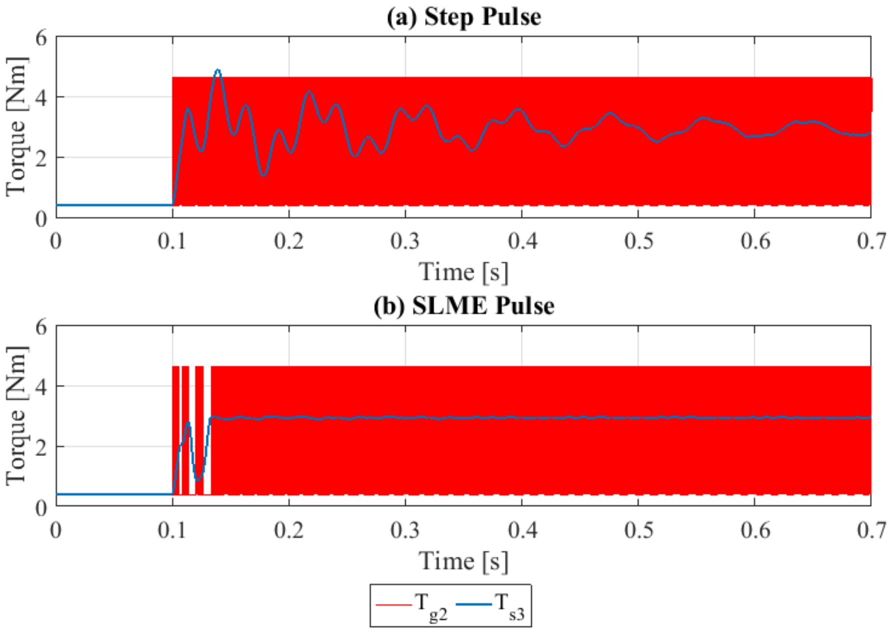

Figure 5.24: High-frequency SLME.

5.6 Real Application

In the last section a PMS for aircraft systems that allows the suppression of the excitation of torsional vibrations when electrical loads are connected has been presented. Now, the requirements of the electrical power system of the aircraft that allow the implementation of this PMS are presented:

- **Solid State switches to control the loads:** the electrical loads should be connected through solid state switches or converters to the grid. In present aircraft systems, electrical loads connected through mechanical switches can still be found. This switches have to be changed to be able to apply the connection patterns in study.
- **Ratio of load types:** to be able to apply the strategies for time critical loads, the time non-critical load installed on the system must be equal or higher than the time critical loads, $L_{Non\ Critical} \geq L_{Critical}$.
- **Minimum inner loop bandwidth in converter:** the control loop in which the current of the converter is given must be fast enough to allow the switching given by the PMS strategies. Therefore, the converters will operate with a minimum bandwidth for their control.
- **High bandwidth communication/sensing/control link:** for the application of the strategies for time critical loads, the signals must be sent simultaneously to both loads: critical and auxiliary. For this reason, the electrical power system must have a high bandwidth communication system, in order to avoid delays. Alternatively, high bandwidth communication control links between time critical and auxiliary loads or sensing strategies can be implemented.

5.7 Summary

This chapter introduced a PMS that allows the elimination of torsional shaft vibrations excited by the connection of electrical loads. The strategies, based on the Posicast compensator, can be applied to different purely resistive loads: time critical loads, time non-critical loads, and pulsating loads. The effect of inductance over the strategies implemented is shown in chapter 7 and analysed in chapter 8.

Moreover, the switching patterns defined by the PMS are applied inside half a period of the natural frequencies. Thus, for mechanical natural frequencies below 200Hz, the connection takes place in milliseconds, which is lower than the settling time of a step connection, and faster than the control strategies used in other applications.

Since the Posicast based strategies depend on the frequency and damping ratio of the system, in an experimental setup these values must be known. Chapter 7 presents a methodology for its identification and the experimental results, while in chapter 8 the robustness of the method for frequencies uncertainties is studied. In next chapter, the experimental setup to test the PMS is developed.

Chapter 6

Design of Test Rig

6.1 Introduction

In this chapter, the experimental rig used to study the electromechanical interaction on the system is designed. The aim of this test rig is to validate the electromechanical system model, verify the electromechanical interaction, and analyse the solutions presented in chapter 5.

The test rig design allows the testing of multiple aircraft systems: an in-line starter/generators, an air-riding seals, and the study of electromechanical interaction. The first two experiments were undertaken using the test rig aimed to minimise the transversal vibrations and analyse the fluid dynamic characteristics. Their study is out of the scope of this thesis, and more information can be found in [124]. This thesis considers the study of electromechanical interaction and the minimisation of the torsional vibrations due to electrical load connections. For this reason, in the rest of the chapter, only the components associated with the electromechanical interaction are discussed.

As presented in [18] and discussed in chapters 4 and 5, a reduced aircraft drivetrain can be used to study electromechanical interactions. As shown in Figure 6.1 the motor or prime mover is connected to a generator through a drivetrain. The drivetrain is composed of a shaft and a gearbox. The generator is coupled to a DC power system since from a control point of view the behaviour is the same. Only one generator is used in the test rig, instead of two. This simplification removes one torsional vibration mode of the system, while still allowing the analysis of the electromechanical interaction and the test of the power management system (PMS).

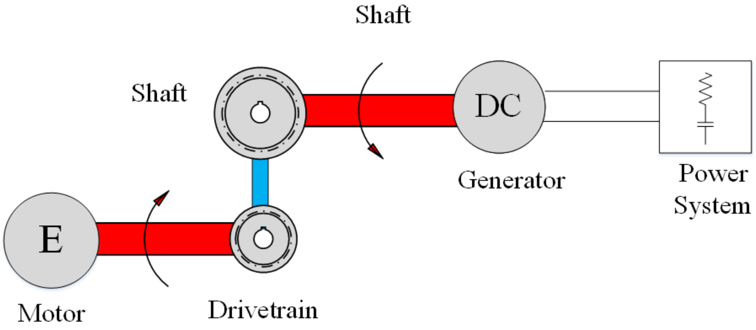

Figure 6.1: Rig schematic.

The following design considerations were used:

- Speed: the maximum speed of the system is 4500rpm a little lower than a real gas turbine with speeds between 5000 at 25000rpm. This limitation is due to the use of an industrial motor with a design speed of 1500rpm and a universal motor. Studies presented in [18], [19] have shown that the same torsional natural poles can be excited at lower speeds. Hence this limitation does not reduce the value of the experimental results.
- Torsional Vibration Modes: one generator instead of two are connected to the system. This simplification can be applied since regardless of the removal of one generator; the system has two torsional vibration mode under 100Hz. Therefore, the torsional frequencies of the system are still representative and allow testing the electromechanical interaction and the solutions in the study.
- Transmitted Power: the power of the machines are lower than the power of a real engine to be able to use industrial machines. The prime mover is a 2.2kW induction motor while the generator is a 1kW universal motor.
- Generator: a DC machine is used instead of synchronous generator because from a control point of view, they are the same and the operation of the DC machine is simpler. Moreover, this machine is a readapted universal motor, allowing the operation at higher speeds than are possible with an industrial synchronous generator.
- Electrical power system: the power system is a DC circuit with resistive load banks connected through IGBTs. The cables and machine windings are the only inductance on the system.

The rest of this chapter is organised as follows. First, the mechanical components are designed in section 6.2, and the torsional vibration modes are studied in section 6.3. In sections 6.4 and 6.5, the electrical system and control system are defined. In section 6.6 the sensors used are described, and finally, in section 6.7 and 6.8 the safety system and summary are introduced.

6.2 Mechanical System Components

Figure 6.2 shows the mechanical rig assembly. The system is composed of the motor, the generator, the drive train, and the air-riding seal. The drivetrain consists of three shafts rotating at different speeds, one connected to the prime mover, one to the seal, and one to the generator. The flywheels, depicted in blue, are used to obtain two torsional vibrations under 100Hz and hence obtain values close to the ones of an aircraft engine.

In other electromechanical interaction aircraft studies [18], [19], and in the studies presented in chapter 4 and 5 a flywheel is connected to the system to emulate the second generator connected to the engine. In this case, only one generator is used, and hence one vibration mode is removed. This does not affect the aim of the thesis because for the purpose of studying the electromechanical interaction and the Posicast solutions only one torsional mode is needed.

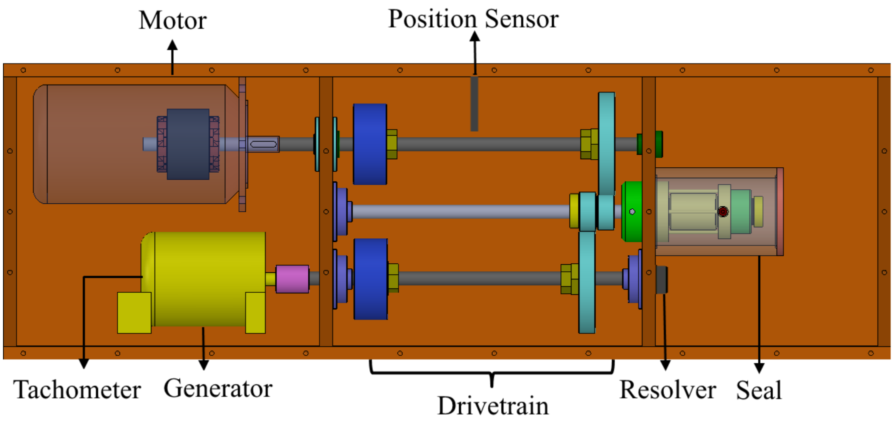

Figure 6.2: Mechanical rig assembly.

6.2.1 Generator

From a control point of view, a DC load and an AC load are equivalent. Therefore for simplification, a DC machine is used. Readily available Universal Motors can operate at speeds up to 15000rpm instead of 1500rpm for a typical industrial induction motor. For these reasons, the generator in the test rig is a washing machine universal motor, which windings have been reconnected to operate as a DC generator.

Figure 6.3 shows the winding connections and its terminals number for the machine working as Universal Motor in (a) and as DC generator in (b). The terminals 1, 2 and 5 are the field connectors, with 1 an alternative field connection; and terminals 3 and 4 are the armature connectors. A Universal Motor has the armature and field connected in series. To be able to use the machine as a generator, the windings must be disconnected. Then, the field is supplied by a DC power source instead of an AC one, and the output of the armature is connected to the loads on the system as shown in Figure 6.3 (b). The generator is coupled to a prime mover, which is used to apply a torque to the shaft.

(a) Universal Motor

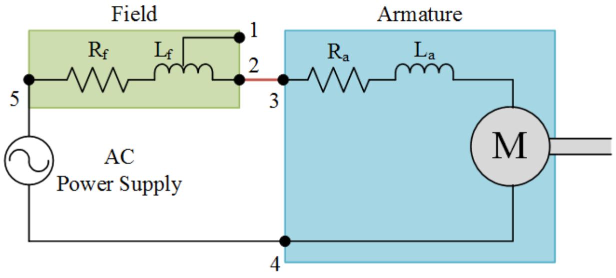

(b) DC Generator

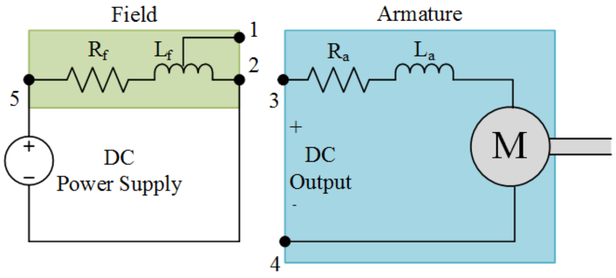

Figure 6.3: Universal motor circuit.

The machine used, shown in Figure 6.4, is a 1kW Nidec Universal Motor, which was supplied by Michele Degano and the Università degli studi di Trieste. The machine characteristics and parameters, shown in Table 6.1, were determined experimentally using the tests described in Appendix I.

Figure 6.4: Generator.

Table 6.1: Generator parameters.

Parameter	**Value**
Armature resistance	$R_a = 4.025\ \Omega$
Field resistance	$R_f = 2\ \Omega$
Armature Inductance	$L_a = 0.019\ \mathrm{H}$
Field Inductance	$L_f = 0.02\ \mathrm{H}$
Rotational inductance	$k_0 = 0.1274\ \mathrm{ln} - \mathrm{in/A}$
Rotational inductance constant	$b = 0.1271\ 1/\mathrm{A}$
Drop Voltage Brushes	$V_0 = 12.247\ \mathrm{V}$
Rotational inertia	$J_g = 0.0005\ \mathrm{kgm}^2$
Max speed	$\omega_{max} = 15000\ \mathrm{rpm}$
Max current continuous	$I_{max} = 6\ \mathrm{A}$
Max current / 5 min	$I_{max/5min} = 10\ \mathrm{A}$

As presented in Appendix I, the machine saturates at 3A. Because the saturation current is lower than the field current used in the rig, to model the rotational inductance equation (6.1), proposed in [125], is used. This equation has the advantage of modelling the basic features of saturation using one constant b and the magnetization value k_0 at the origin.

$$k = \frac{k_0}{1 + bi_f} \tag{6.1}$$

The power generated by the DC machine at different speeds and field currents is shown in Figure 6.5. The 1kW universal motor value is obtained at 5A and 4400rpm or at 6A and 3800rpm. Therefore, to be able to get a maximum power of 1kW the shaft is designed to operate up to 4500rpm.

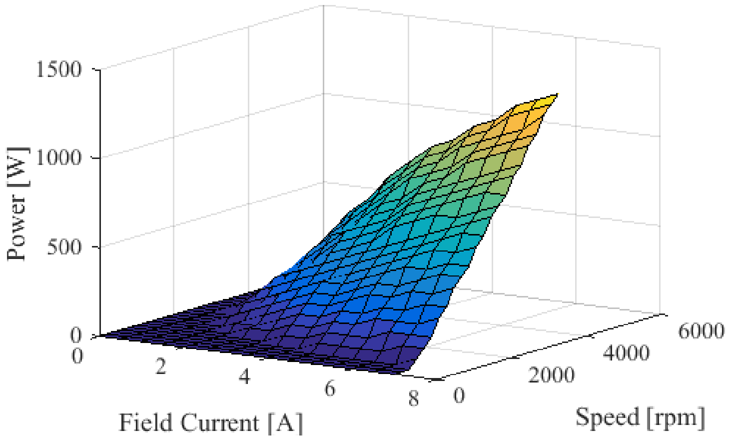

Figure 6.5: Generator curve. Power generated vs speed vs current.

6.2.2 Motor

An “off the shelf” industrial motor was chosen as the rig prime mover. The motor, model Marelli MAQ 100LA4, is a 2.2kW, two pole pair induction machine able to supply power to the generator and the drivetrain. Its nominal speed is 1445rpm and can get to 3000rpm when de-rated. The parameters of the motor are presented in Table 6.2.

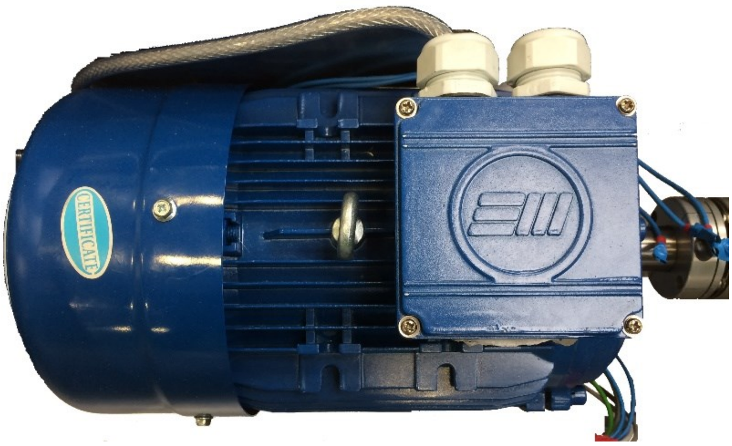

Figure 6.6: Motor.

Table 6.2: Motor parameters.

Parameter	Value	
Rated power	$P_n = 2.2$ kW	
Torque	$T_n = 14.5$ Nm	
Poles pair	$p = 2$	
Frequency	$f = 50$ Hz	
Voltage	V_{nom}	Y 400 V Δ 230 V
Current	I_{nom}	Y 4.65 A Δ 8.05 A
Maximum current	$I_{max} = 21$ A	
Speed	$\omega_n = 1445$ rpm	
De-rated max speed	$\omega_{max} = 3000$ rpm	
Efficiency (100% load)	$\eta = 84.4$	
Power factor	$\cos(\phi) = 0.81$	

6.2.3 Drivetrain

As shown in Figure 6.2, the drivetrain is formed by three shafts connected through a gearbox with two flywheels. The shafts have a diameter of 20mm and a length of 460mm.

The gearbox, shown in Figure 6.7, is designed to supply the generator with a speed of 4500rpm when the motor operates at 3000rpm. The speed of the seal shaft is three times the motor shaft one. The ratio between shafts is 1:3:1.5, with the prime mover shaft the slowest and the central shaft supplying the air-riding seal the fastest. The gears parameters are presented in Table 6.3. Finally, the flywheels have a diameter of 170mm and a length of 60mm. These flywheels allow torsional modes under 100Hz, as presented in the next section.

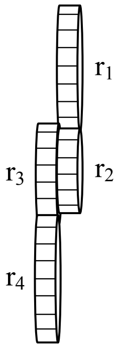

Figure 6.7: Gearbox connection.

Table 6.3: Gearbox parameters.

Gear	Model	Number of Teeth	Diameter [mm]
r_1	YG275	75	150
r_2	YG2 25	25	50
r_3	YG2 35	35	70
r_4	YG2 70	70	140

6.3 Torsional Vibrations Modes

In this section, the torsional vibrations modes of the rig are designed. These vibration modes allow the analysis of electromechanical interaction, and hence the selection of their value is fundamental for the objectives of this thesis. The torsional modes are determined by the flywheel connected next to the motor and generator as shown in Figure 6.2.

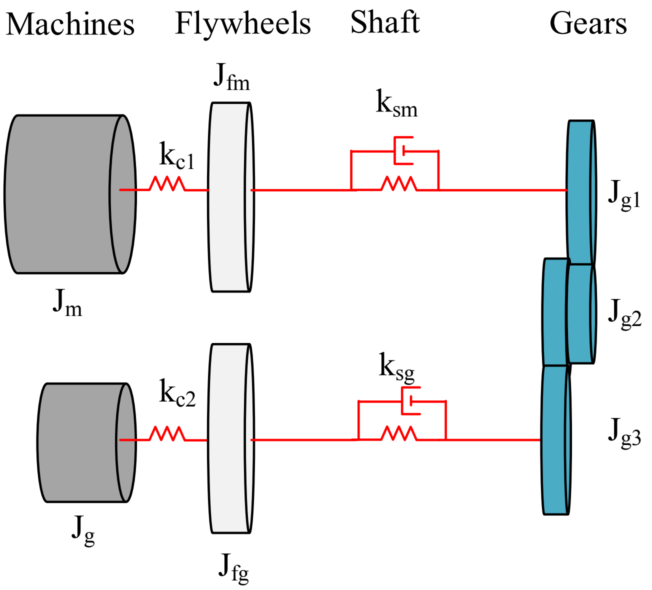

Figure 6.8: Mechanical layout.

Figure 4.4 illustrates the components of the mechanical system in terms of inertias, stiffness and damping, with J_m the inertia of the motor, J_{fm} the inertia of the flywheel connected to the motor shaft, J_{g1} the inertia of the motor shaft gear, J_{g2} the inertia of both gears in the central shaft, J_{g3}, the inertias of generator shaft gear, J_{fg} the inertia of the flywheel connected in the generator shaft, and J_g the generator inertia. k_{c1} and k_{c2} are the stiffness on the couplings of the motor and generator respectively, and k_{sm} and k_{sg} are the stiffness of the shaft.

The inertias and stiffness values are shown in Table 6.4. The flywheels and gears inertia in $\mathrm{kgm^2}$ were calculated using equation (6.2), with ρ the material density in $\mathrm{kg/m^3}$, L the length of the flywheel in m, and r_{ext} and r_{int} the external and internal flywheel radios in m. The motor inertia was given by the machine datasheet, and the generator inertia was obtained experimentally as shown in Appendix I. The shafts stiffness were calculated by equation (6.3), with G the shear modulus in GPa, r the shaft radios in m, and L the shaft length in m. The couplings stiffness was obtained from the datasheet.

$$J = \rho \pi L * \frac{(r_{ext}^4 - r_{int}^4)}{2} \tag{6.2}$$

$$k = \frac{G\pi r}{2L} \tag{6.3}$$

Table 6.4: Mechanical values.

Component	Value
Motor Inertia	$J_m = 0.0058\ \mathrm{kgm^2}$
Generator Inertia	$J_g = 0.0005\ \mathrm{kgm^2}$
Flywheel Inertia	$J_{fm} = 0.0386\ \mathrm{kgm^2}$ $J_{fg} = 0.0386\ \mathrm{kgm^2}$
Gears Inertia	$J_{gb1} = 0.0093\ \mathrm{kgm^2}$ $J_{gb2} = 4.7 * 10^{-3}\ \mathrm{kgm^2}$ $J_{gb3} = 0.0091\ \mathrm{kgm^2}$
Coupling Stiffness	$k_{c1} = 113406\ \mathrm{Nm/rad}$ $k_{c2} = 113406\ \mathrm{Nm/rad}$
Shaft Stiffness	$k_{sm} = 2.1598 * 10^3\ \mathrm{Nm/rad}$ $k_{sg} = 2.2398 * 10^3\ \mathrm{Nm/rad}$

The mechanical natural frequencies obtained are 0Hz, 35.99Hz, and 82.15Hz. The torsional vibration modes, obtained with TorTrans, a Matlab Toolbox written by Seamus Garvey, and associated with each natural frequency, are shown in Figure 6.9. The circles symbolise the inertias, the shafts are modelled in red, and the gearbox in blue. The vertical green lines represent the inertias referred angles in each operation mode. In the first mode or rigid mode, the system moves together.

In the second mode, the generator and motor are moving out of phase as was observed in chapter 4. In the third mode, the generator and motor move together while the gearbox moves in opposite direction. Comparing with the modes obtained in chapter 4, only the mode in which both generators move out of phase, and therefore, associated with the second generator has been eliminated. In chapter 7, mode 2 and 3 are suppressed through the strategies proposed in chapter 5.

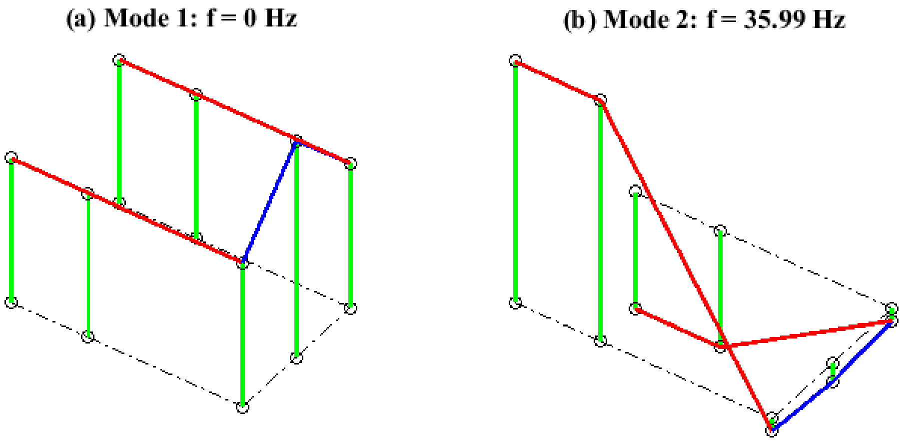

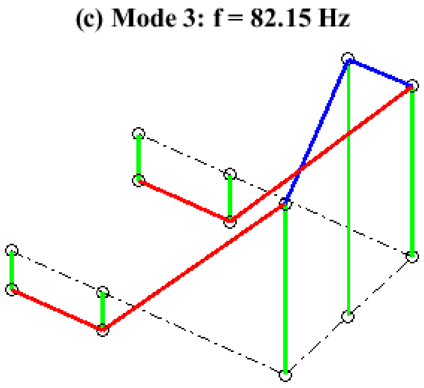

Figure 6.9: Mode shapes.

6.4 Electrical Power System Components

As already mentioned, the electrical power system is a DC system with three resistive loads R_L that can be switched on/off. As shown in Figure 6.10, the resistances are connected through an IGBT which allows its connection and disconnection. The resistances switching allows the application of the connection patterns in study: step connection, SLME connection, MLL connection, and MSLME connection.

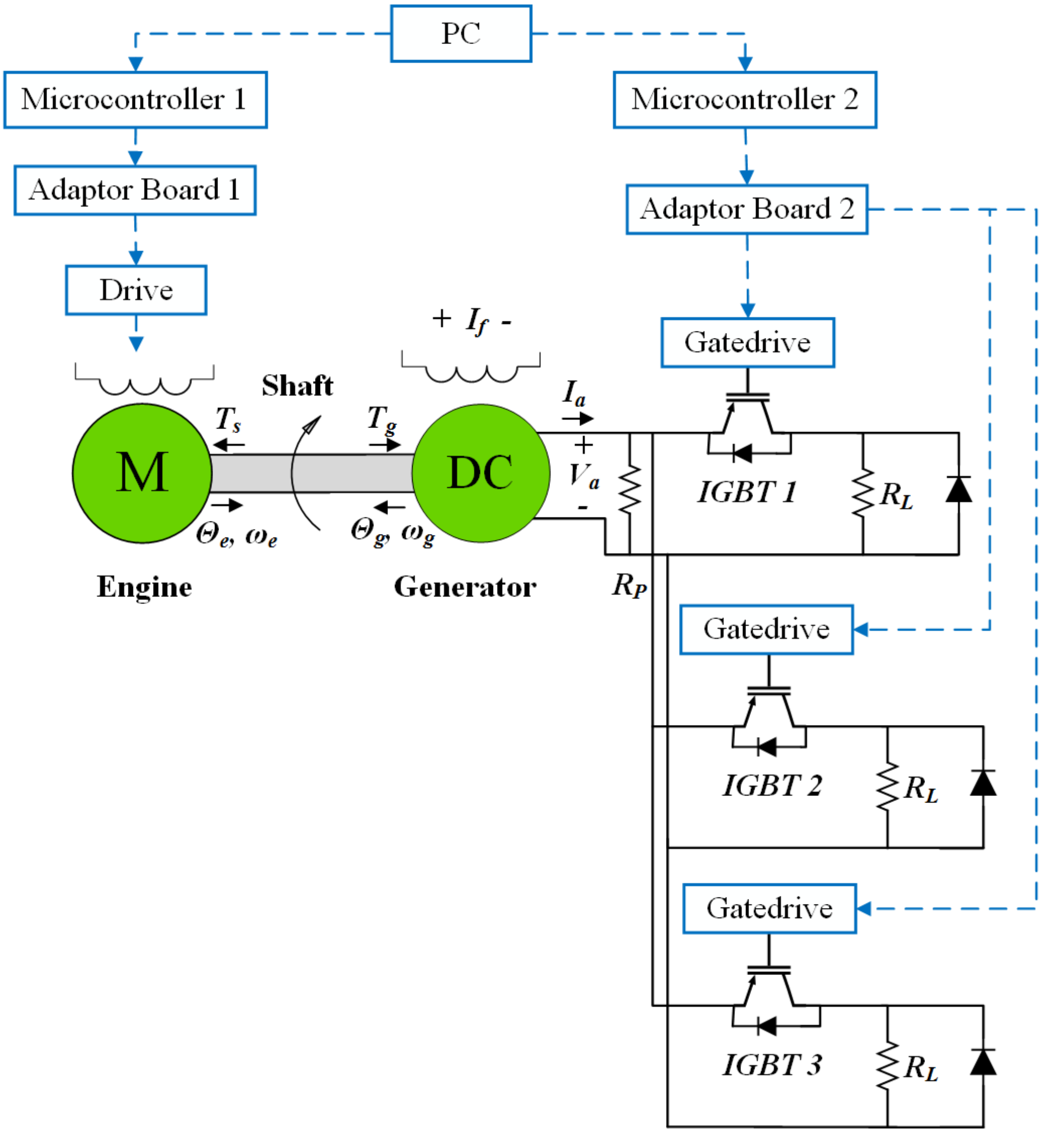

Figure 6.10: Electrical power system connection diagram.

As shown in Figure 6.10, the IGBT switching is controlled through the PC. The computer sends a signal to a microcontroller, which is connected to an adaptor board that sends a signal to the IGBT gate driver to open and close the switch. To control the speed of the motor, an industrial drive is used.

To guard the machines and IGBT of the currents produced by the inductances when the resistance is disconnected the following protections are used:

- To protect the generator and dissipate the current when the switches turn off, there is a high resistance R_P connected in parallel to the IGBT system.
- To protect the IGBT when the switches are off, a diode has been connected in parallel to each load.

In this section, the resistance, IGBT, microcontroller, drive, and power supplies are described. The control system, including the load connection and the motor drive, are presented in section 6.5.

6.4.1 Resistance Banks

The maximum current at which the generator can operate is 6A and 10A/15 min in overload. Thus, the resistances are chosen to stand these values.

The resistance R_P, used to protect the machine when the IGBT opens, is a fixed value resistance bank with enclosure, brand HVR Pentagon. It is composed by three resistance BX375 of 20Ω, each of a maximum of 1kW. Hence the total resistance connected in series is 60Ω and can stand a maximum of 3kW.

The load resistance R_L are three variable wire resistance, brand Arcol, model VRH320. One of the resistances can change its value between 1 and 10Ω, with a maximum current of 5.7A and $8\text{A}/15$ min in overload. While the other two resistance are 33Ω with a maximum current of 3.1A and $4.4\text{A}/15$ min in overload. Both operate at maximum 320V and $640\text{V}/15$ min in overload. For the cases in which higher resistances need to be connected, as in the MLL strategy, a spare resistance bank with the same characteristics of the resistance R_P is connected in series to the variable resistances.

6.4.2 IGBT and Gate driver

The IGBT used to connect the resistive loads are dual switch high power IGBT, model CM225DX-24S1 that can stand a maximum of 225A and 1200V. This IGBT model was chosen because of the existence of a gate driver designed to operate with it. The gate driver used with this IGBT is a Powerex VLA536-01R, which is fed by a 15V and maximum 1.58A power supply. To dissipate the heat produced by the IGBT a heatsink is used. Figure 6.11 shows the IGBT, and the gate driver connected.

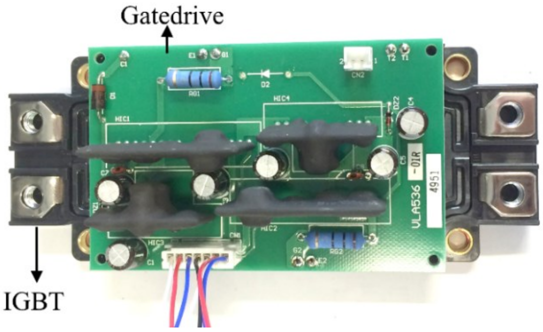

Figure 6.11: IGBT and gate driver.

The IGBT and gate driver are designed to operate with dual switches (half bridge), which are intended to be used in an inverter leg. In this experimental setup, only one IGBT is used for the switching and the second IGBT is kept open. Of the second IGBT, its diode is utilised for the protection of the system as shown in Figure 6.12. The diode permits the dissipation of the current stored in the resistance winding when the switch opens. For this operation, the two IGBT must operate independently, and thus the signals sent by the gate driver must be decoupled.

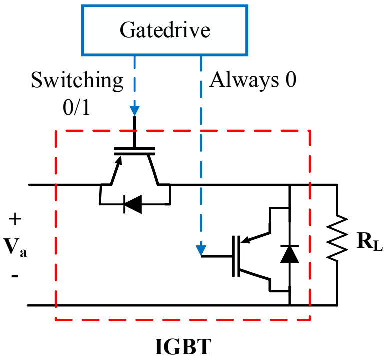

Figure 6.12: IGBT circuit.

To turn on the IGBT, the difference of voltage between the gate driver terminals Vin-IN1 must be 5V, while the current must be 13mA. Since the microcontroller cannot supply these values of current, an adaptor board is used. The control and adaptor board are presented in section 6.5.2. To keep the second IGBT open, and hence used only the protection diode, the terminals Vin-IN2 are directly connected, and its voltage is maintained in 0V.

6.4.3 Microcontroller

The microcontrollers used in the system are two Infineon Easy Kit XE164FM. This model was chosen due to the availability to control through the PC, and the compatibility with the software DAvE.exe that helps in its programming. Figure 6.13 shows the microcontroller. In red the main components of the board are highlighted: Pin Connectors, State Lights, USB Connection, and Power Supply.

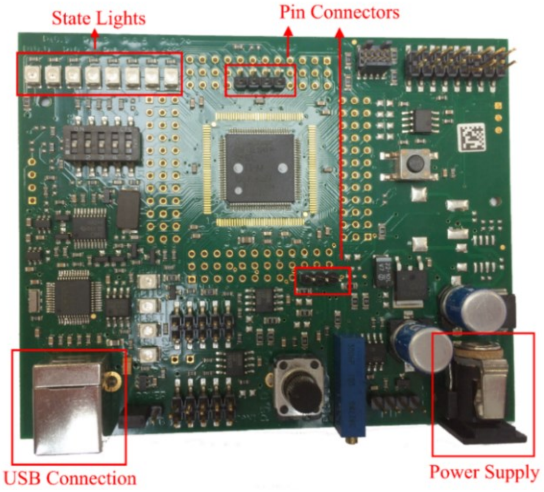

Figure 6.13: Microcontroller board.

The pin connectors allow the connection of the microcontroller and the adaptor board and have been soldered into the board to supply the requirements of this experimental rig. Each of them can generate a voltage difference of 5V. The state lights, internally connected to the board pin, can be programmed to turn on and off.

The USB connection can be used to supply the board electrically, to load the code, or/and to send signals from the PC. For this reason, the USB is a dual USB to UART/JTAG interface. To control the microcontroller from the PC, an RS232 serial interface is available via the USB port, which converts TTL-UART-signals to USB-signals using a virtual COM port. The power supply ($6-12\mathrm{V}$, max $400\mathrm{mA}$) is only needed when the power given through the USB is not enough.

6.4.4 Motor Drive

To keep the speed of the motor constant, the ACS150 ABB drive from Figure 6.14 is used. This drive has a single phase input that is connected to a 240Vrms, 8.8A power supply, and can operate in motors of up to 4kW and 5HP. To regulate the induction motor speed, the drive supplies the three-phase field current using a V/f control. The configuration and characteristics of the drive are presented in [126].

The motor must be connected in delta because the maximum voltage that the drive can supply is the value of the input voltage. Also, since the connectors are exposed, for safety the drive is controlled remotely through the PC. This configuration is presented in section 6.5.1. For the testing of the in-line starter/generator, the motor and its drive will be replaced by a different machine which will be controlled through dSpace.

Figure 6.14: Drive.

6.4.5 Power Supplies

Power Supplies are used to feed the generator field and the electronics of the system as shown in the following list:

- Generator Field: It is powered by a DC constant current power supply, like the one in Figure 6.15 (a). The current of the field can vary but the maximum value used is 6.5A.
- Current and Voltage Sensors: The sensors, described in section 6.6.1 use a $\pm 15\mathrm{V_{DC}},\ 0.5\mathrm{A}$ power supply like the one in Figure 6.15 (b).
- Gate driver: A $15\mathrm{V_{DC}}, 1.58\mathrm{A}$ supplies the gate driver, while a $5\mathrm{V_{DC}}, 1\mathrm{A}$ feeds the gate driver's adaptor board.
- Microcontroller: A $12\mathrm{V_{DC}}, 420\mathrm{mA}$ supplies the microcontroller used for the drive.
- Drive: A single phase 240Vrms, 8.8A power supply as the one in Figure 6.15 (c) is used.

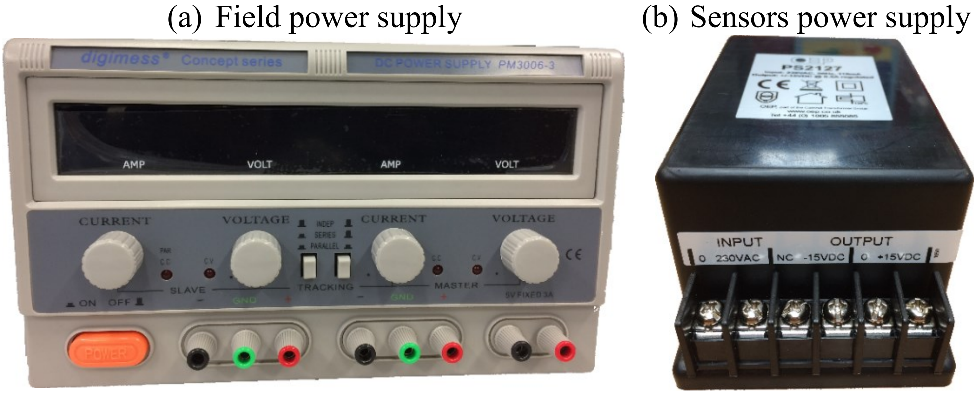

(a) Field power supply

(b) Sensors power supply

(c) Drive power supply

Figure 6.15: Power supplies.

6.5 Control System

As shown in Figure 6.10, there are two control systems in the rig: the motor drive control and the switching load control. The generator voltage is not controlled because the electromechanical interactions due to load connections are independent of the GCU.

The signals for the two separated control systems are sent by the computer and are controlled by the user. For this interaction, the microcontrollers are connected through an USB and any software that interacts with ports, such as MTTTY.exe or Docklight.exe can be used. In both cases, the microcontroller was programmed in C using the software Keil uVision and DAvE. DAvE is a software supplied with the Infineon board and provides a smoother programming of the board settings, such as the pin activation and clock used. A programming example of the microcontroller is presented in [127]. Next, the motor drive and the load control are described.

6.5.1 Drive Control

Due to the exposed connections of the drive presented in section 6.4.4, for safety, its control is done through the PC. Figure 6.16 shows the communication schematic for the drive control: the user, through the computer, sends the signal to the microcontroller, which is connected to the drive through an adaptor board.

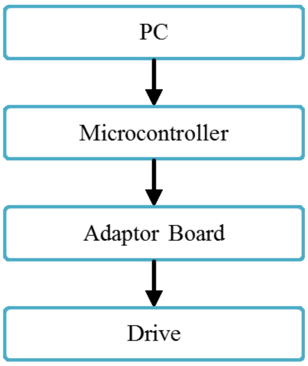

Figure 6.16: Drive communication diagram.

As shown in [126], five 24V signals are needed to control the drive remotely. These signals, that take binary values (0/1), control the turning on/off of the drive (DI1), the direction of rotation (DI2), the increase of the speed (DI3), the decrease of the speed (DI4), or the use of a fixed speed set on the drive for operation (DI5). Thus, to fix the operation speed of the drive two strategies can be taken: the designated fixed speed can be chosen turning on the pin DI5, or the speed can be controlled in a potentiometer basis using the signals DI3 and DI4. When DI3 and DI4 are simultaneously on or off the speed is constant, and when only one of them is on the value increases or decreases.

Since the microcontroller only generates 5V signals, to send the signals to the drive, an adaptor board is used. The schematic is shown in Figure 6.17. The board consists of five optocouplers connected to the drive 24V drive output, which turns on when the microcontroller sends the signals. The adaptor board is shown in Figure 6.18.

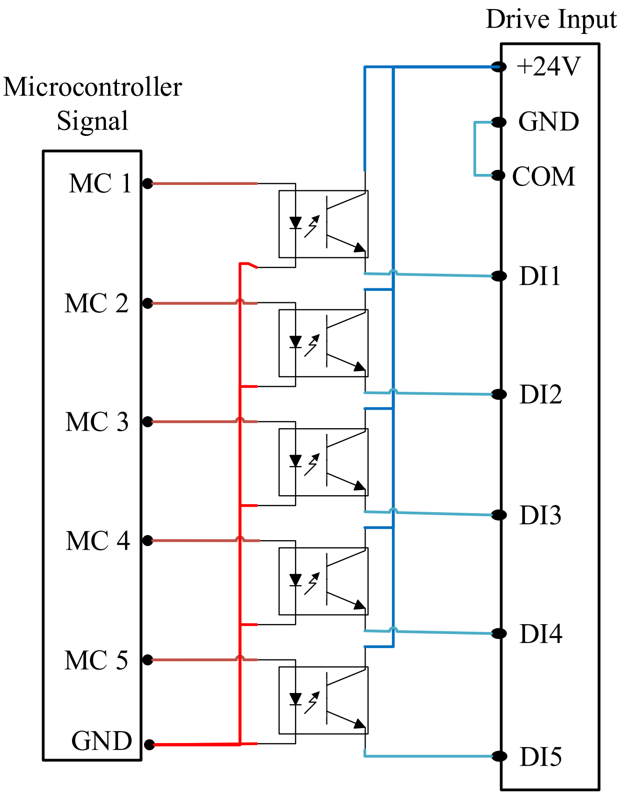

Figure 6.17: Drive adaptor board diagram.

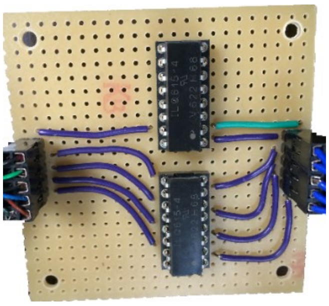

Figure 6.18: Real drive adaptor board.

6.5.2 Load Control

The connection and disconnection of loads in the system is done through the computer. As shown in Figure 6.19, the signal sent by the user through the PC is received by the microcontroller, which is connected to the three gate driver through an adaptor board.

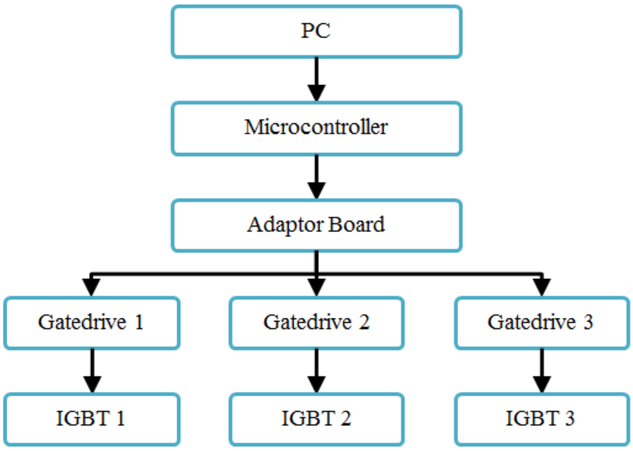

Figure 6.19: Load control communication diagram.

The adaptor board is used because the microcontroller cannot send a signal to the gate driver with enough power to turn them on. For this reason, as shown in Figure 6.20, the signal of the microcontroller (V_{MC}) is received by an inverter buffer which sends the signal to the gate driver. The adaptor board is shown in Figure 6.21.

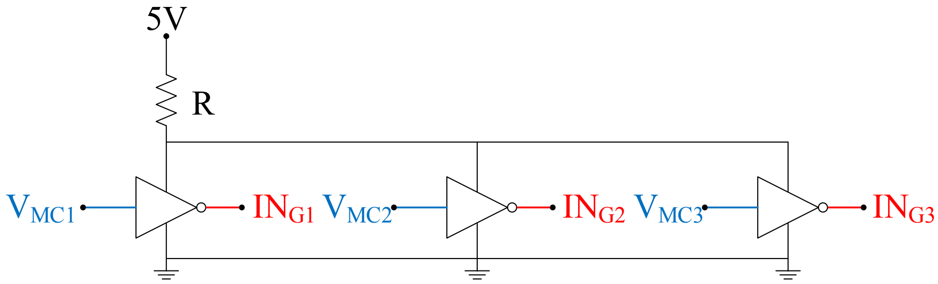

Figure 6.20: Load control adaptor board diagram.

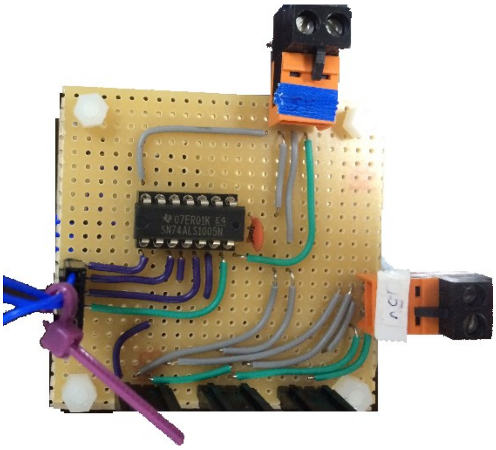

Figure 6.21: Load control adaptor board.

Finally, to switch on and off the loads using the different PMS strategies the user can choose between the following options which are given to the microcontroller trough MTTTY.exe or Docklight.exe:

- 0 – Disconnect the loads at the same time.
- 1 – Step connection of one resistance.
- 2 – SLME connection applied to one natural frequency.
- 3 – MLL and MSLME connection applied to one frequency.
- 4 – SLME connection applied to two natural frequencies.
- 5 – MLL connection applied to two natural frequencies.
- 6 – MSLME connection applied to two natural frequencies.

6.6 Sensors

To measure the electrical signals, the speed and the transversal position of the motor shaft, sensors are used. The electrical signals, armature current, armature voltage, and field current, are measured with LEM transducers. The speed is measured with a tachometer and a resolver connected at both ends of the generator shaft. The position of the motor shaft is measured with a position sensor. Figure 6.2 shows the position of the tachometer, resolver, and position sensor.

To visualise the sensor signals dSpace is used. dSpace is chosen for the control of the in-line starter/generator, out of the scope of this thesis, and the signals associated with this, such as the position sensor. To have the rest of the signals on the same platform, the tachometer, resolver, and LEM transducer are also connected to dSpace, using an acquisition frequency of 10kHz or 10^{-5}s. Next, the LEM transducer, tachometer, resolver, and position sensor are described.

6.6.1 LEM Transducer

To improve the resolution obtained with the probes available at the laboratory and to read the signals with dSpace, LEM transducers are used. Their operation is based on the Hall Effect, in which the current in a coil produces a magnetic field that induces a proportional voltage across an electrical conductor. In this thesis, two current LEM transducer and one voltage LEM transducer are used. Figure 6.22 shows the board with the LEM sensors. Next, the transducers used are described.

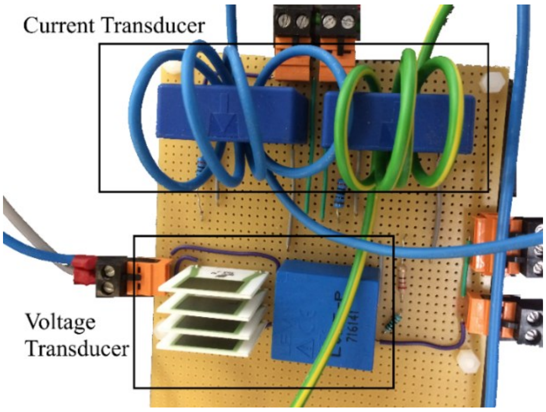

Figure 6.22: LEM sensors.

6.6.1.1 Current LEM

The current LEM transducer model LA100-P of Figure 6.23 is used to sense the armature and field current of the generator. To measure the current, the cable I_P must cross the transducer, which induces a secondary current I_S. To obtain the value of I_S, a measuring resistance R_M is connected at the output as shown in Figure 6.23. The parameters of the LEM LA100-P are given in Table 6.5.

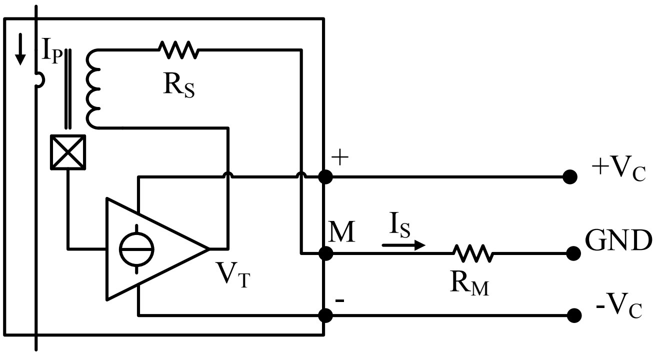

Figure 6.23: Current LEM circuit.

Table 6.5: Current LEM parameters.

Parameter	**Value**
Primary nominal current	$I_{PN} = 100$ A
Secondary nominal current	$I_{SN} = 100$ mA
Measuring resistance	$R_M = 40 \dots 95\ \Omega$
Conversion ratio	$N_P/N_S = 1/1000$
Supply voltage	$V_C = \pm 15$ V
Secondary coil resistance	$25\ \Omega$
Current consumption I_C	$R_S = 10 + I_s$ mA
Accuracy at I_{PN} and $25°C$	$\pm 0.45\%$
Linearity error	$< 0.15\%$

The nominal values of the transducer are significantly higher than the operational ones, in which the maximum current is 10A. For this reason, to increase the precision of the measurement, the number of turns of the measurement cable is increased to five ($N_P = 5$) and the measuring resistance R_M range is recalculated for these values.

The minimum value of the measuring resistance depends on V_C, and hence its value remains the same. Instead, the maximum value of the resistance can be obtained from the equations (6.4) and (6.5), in which V_T is the voltage before the coil resistance as shown in Figure 6.23.

$$N_P I_P = N_S I_S \tag{6.4}$$

$$V_T = (R_S + R_M) I_S \tag{6.5}$$

Using the LA100-P datasheet data, it is obtained that $V_T = 12\text{V}$. Designing the transducer for a nominal current $I_P = 6\text{A}$ and $N_P = 5$, it is obtained that $I_{SN} = 30\text{mA}$ and that the maximum measuring resistance value is $R_M = 375\Omega$. Finally, the value of R_M is chosen using equation (6.6). To have a nominal output voltage $V_M = 6\text{V}$ when the current is 6A, the measuring resistance is $R_M = 200\Omega$.

$$V_M = R_M I_S \tag{6.6}$$

6.6.1.2 Voltage LEM

A voltage transducer LV25-P is used to measure the armature voltage. As shown in Figure 6.24, the measured voltage is connected to the terminals +HV and –HV. For this reason, besides the measuring resistance R_M, the resistance R_1 used to obtain the current proportional to the measuring voltage, must be also calculated. Table 6.6 shows the main parameters of the voltage transducer.

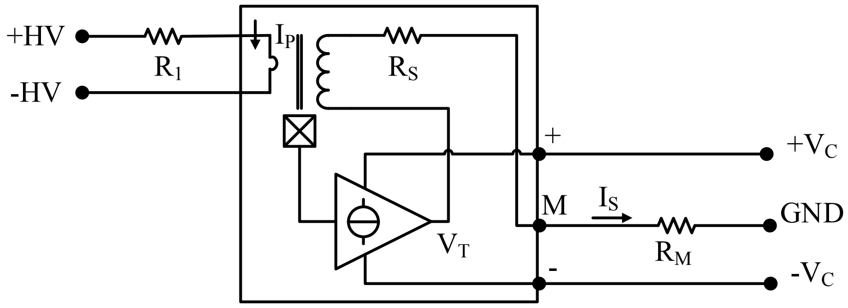

Figure 6.24: Voltage LEM circuit.

Table 6.6: Voltage LEM parameters.

Parameter	Value
Primary nominal current	$I_{PN} = 10$ mA
Primary current, measuring range	0 ... $\pm$ 14 mA
Secondary nominal current	$I_{SN} = 25$ mA
Measuring voltage range	$V_{PM} = 10 \ldots 500$ V
Measuring resistance	$R_M = 100 \ldots 350\ \Omega$
Conversion ratio	$N_P/N_S = 2500/1000$
Supply voltage	$V_C = \pm 15$ V
Secondary coil resistance	$R_S = 110\ \Omega$
Current consumption	$I_C = 10 + I_s$ mA
Accuracy at I_{PN} and $25°C$	$\pm 0.8\%$
Linearity error	$< 0.2\%$

To obtain the value of R_1, equation (6.7) is solved for a nominal voltage $V_{PN} = 160$V at which $I_{PN} = 10$mA, obtaining $R_1 = 16$kΩ.

$$V_{PM} = R_1 I_{PN} \tag{6.7}$$

To obtain the value of R_M, equation (6.8) is solved for a maximum measuring voltage $V_M = 10$V when working with $V_{PM} = 200$V, obtaining $R_m = 320\Omega$. The maximum output voltage is $V_M = 10$V because this is the maximum voltage that can be connected to dSpace.

$$V_M = R_M I_{SN} \tag{6.8}$$

6.6.2 Tachometer

The universal motor, reconnected as a DC generator, has an eight pole pairs ($p = 8$) tachometer embedded, which is shown in Figure 6.25. This tachometer is used to measure the speed of the system at one end of the generator shaft.

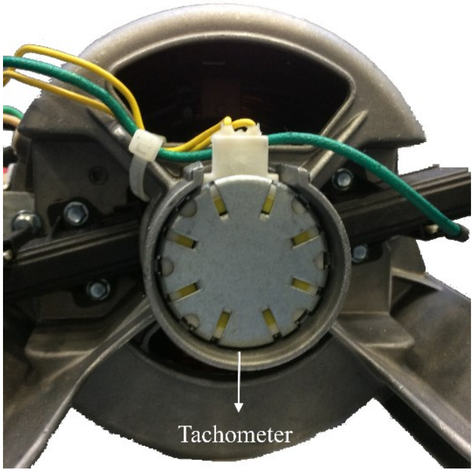

Figure 6.25: Tachometer.

The tachometer generates a sinusoidal voltage with frequency (f_V) proportional to the speed of the machine shaft (ω_{shaft}). To obtain the speed of the shaft in rpm, equation (6.9) is used.

$$\omega_{shaft}\ [\mathrm{rpm}] = f_V\ [\mathrm{Hz}] * \frac{60}{8} = f_V\ [\mathrm{Hz}] * 7.5 \tag{6.9}$$

6.6.3 Resolver

The resolver is connected opposite to the tachometer as shown in Figure 6.2. The aim is to provide higher resolution for the speed measurement than the one obtained with the tachometer. As presented in Figure 6.26, the operation of the resolver consists in inducing a sinusoidal current into two coils shifted by 90° (shown in blue), by exciting a rotating coil (shown in red).

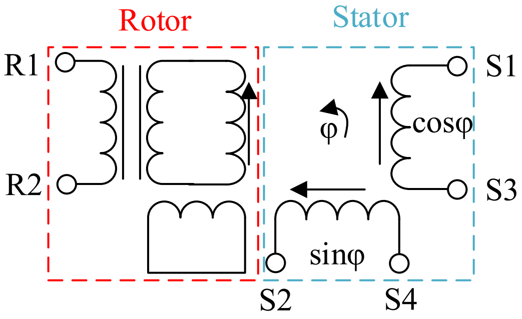

Figure 6.26: Resolver circuit.

The angle of the system is obtained from equation (6.10), in which ϕ is the rotational angle, E is the excitation voltage, K is the transformation ratio, and $R_1 - R_2$, $S_1 - S_3$, and $S_2 - S_4$ are the voltage difference between the resolver terminals.

$$\begin{aligned} E(S1 - S3) &= KE(R1 - R2)\cos(\phi) \\ E(S2 - S4) &= KE(R1 - R2)\sin(\phi) \end{aligned} \tag{6.10}$$

The resolver connected is a brushless frameless Harowe resolver, model 21BRX709 as the one in Figure 6.27. Table 6.7 presents the resolver parameters. The resolver is connected to the resolver input/output on dSpace, which sends the excitation field and measures the output angle.

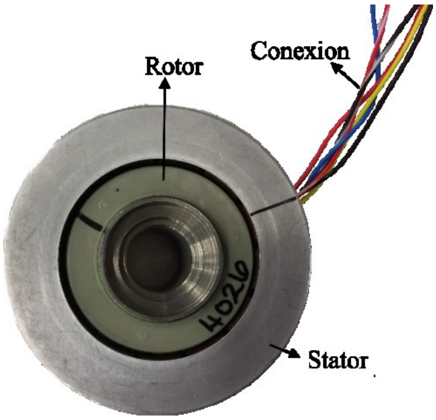

Figure 6.27: Resolver.

Table 6.7: Resolver parameters.

Parameter	Value
Excitation parameters	$f_E = 10$ kHz
Input voltage	$E_R = 7$ V
Input current	max 28 mA
Input power	0.065 W
Transformation ratio	$K = 0.31$
Inner shaft diameter	20 mm
Maximum continuous speed	20000 rpm

6.6.4 Position Sensor

The position sensor measures the motor shaft movements along the x and y-axis, which is fundamental for the in-line starter/generator as presented in [124]. In this thesis, the position sensor is only used to identify the critical speeds of the system.

The position sensor is a non-contact sensor, brand Lion Precision, and model U5C. Table 6.8 presents its parameters. The resolutions depend on the material being measured (ferrous and non-ferrous) and the frequency used (from 250Hz to 15kHz).

Table 6.8: Position sensor parameters.

Parameter	Value
Dimension	$X = 3.4$ mm
Dimension	$Y = 3.0$ mm
Dimension	$Z = 4.90\ +/-\ .025$ mm
Range	$0.25 - 1.5$ mm
Minimum resolution	75 nm
Maximum resolution	260 nm

6.7 Safety System

To protect the people working on the rig of unexpected hazards, the following safety precautions have been taken.

- Risk Assessment: A risk assessment, revised and certified by qualified university personnel has been carried out.
- Emergency button: A button as the one in Figure 6.28 allows the quick disconnection of all electric equipment.
- Remote operation: To avoid contact with electronics, the drive handling, and the connection and disconnection of loads is done through the PC.
- Covered rotating parts: As shown in Figure 6.29, the rotating shaft and machines of the rig are covered. They cannot be accessed while the system is in operation.
- Covered electronics: As shown in Figure 6.30(b), all the electronics are covered. The switches are covered by Plexiglas, while the drive is enclosed in a metal case.
- Isolated electronics: The electronics are isolated through the use of Paxolin.
- Grounded electronics: The electric components are grounded.

Figure 6.28: Emergency button.

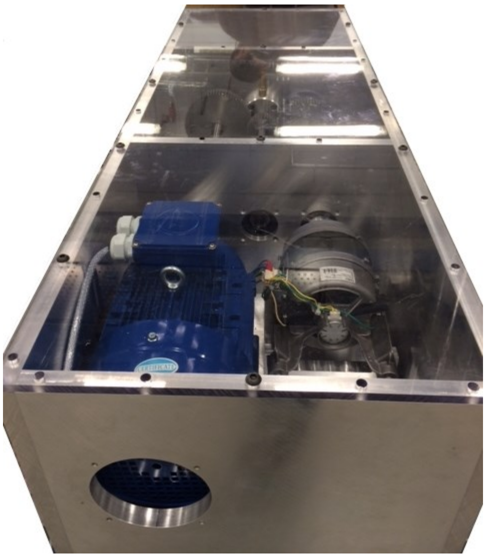

Figure 6.29: Rig protection.

6.8 Summary

The test rig developed is a multidisciplinary experiment that allows the analysis of different aircraft applications such as an air-riding seal, in-line starter/generator, and electromechanical interactions. In this chapter, the design of the electromechanical interaction capacity of the test rig has been presented. To test the electromechanical interaction, the system is equipped with IGBTs that switch on/off resistance banks and that are controlled through the PC with the use of Infineon microcontrollers. Figure 6.30 shows the whole rig, in (a) the mechanical components are shown while in (b) the electronics are presented. In the next chapter, the results obtained with the test rig are given.

(a) Mechanical components

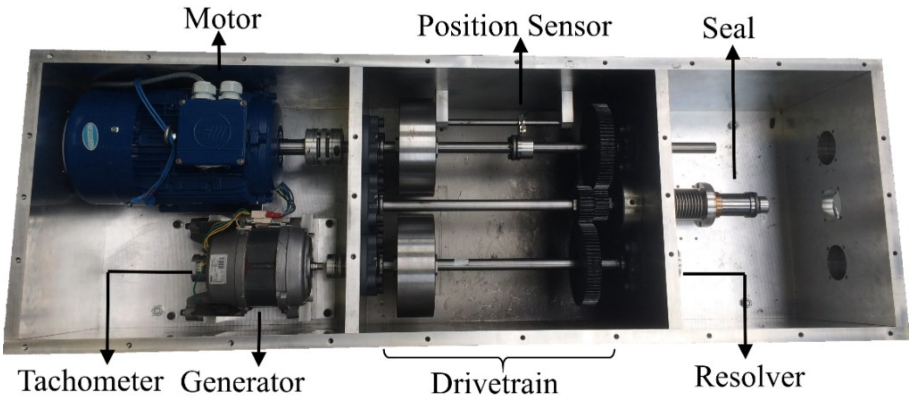

(b) Electrical components

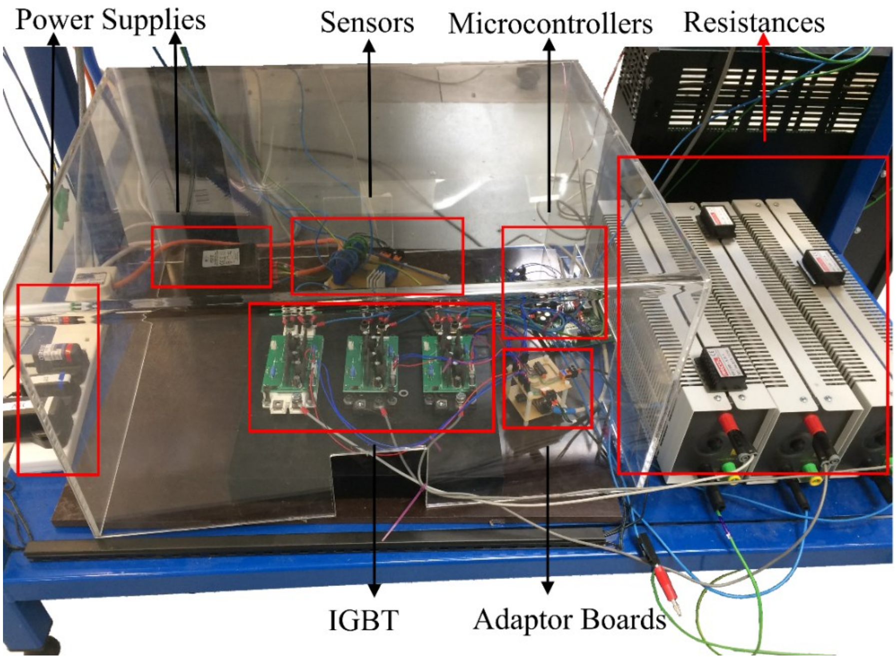

Figure 6.30: Whole rig picture.

Chapter 7

Results Experimental Test Rig

7.1 Introduction

In this chapter, the experimental system presented in chapter 6 is used to test the electromechanical interaction and the power management system (PMS) solutions presented in chapter 5. The rest of the chapter is organised as follows: First, the drivetrain is parametrised. After, the approach to obtain the vibrations of the system and the torque is defined. In section 7.4 the electromechanical interaction produced by an electrical load connection is shown. In section 7.5 Posicast strategies are experimentally tested. Finally, the chapter summary is given.

7.2 Drivetrain Characterisations

To apply the PMS strategies and avoid resonance with the mechanical system, the drivetrain is characterised in terms of its critical speeds or transversal frequencies and its torsional frequencies.

7.2.1 Critical Speeds

To prevent excessive vibration on the experimental rig, the critical speeds or transversal vibrations of the system are identified. For this purpose, the motor shaft displacement is measured for increasing speed. The movement of the shaft is measured through a position sensor as described in chapter 6, while the speed is obtained from the resolver. The resolver, connected to dSpace, gives the rotational angle of the shaft attached to the generator. Therefore, to get the motor shaft speed, the angle is differentiated and divided by 1.5, the speed factor between shafts. Both signals are recorded through dSpace.

Figure 7.1 shows the displacement of the shaft connected to the motor for ascending speed. Higher displacements show higher vibrations. Therefore, the critical speeds are those at which the vibrations are higher: 733rpm, 1497rpm, 1669rpm, 2170rpm, and 2631rpm. To avoid reducing the rig lifespan, the experimental system is not operated at these speeds.

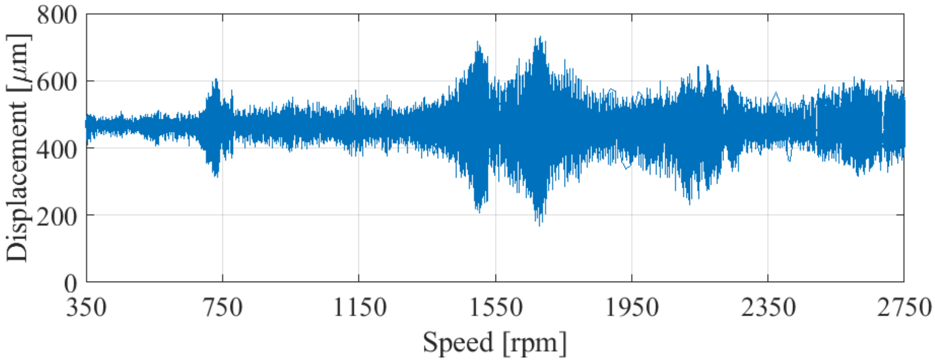

Figure 7.1: Critical speed identification.

7.2.2 Torsional Modes

To test the load connection strategies presented in chapter 5, the torsional modes of the rig must be determined. The natural frequencies are obtained using FFT analysis, while for the damping ratio a method based on the Hilbert Transform is employed.

7.2.2.1 Frequency Identification

The FFT is measured after applying a step connection to the system, which excites the torsional modes. The information recorded consists of 10 seconds of data with a sampling time $t_s = 10^{-5}\text{s}$. The FFT is applied to the armature current i_a, and the magnitude is normalised by the steady state value $i_a / i_{a_{steady}}$. Figure 7.2 shows the Fourier response of the system operating at 1500rpm and 2000rpm.

The frequencies $f_1 = 35\text{Hz}$ and $f_2 = 73.1\text{Hz}$ are shown in both plots encircled in red. However, in black, a second set of frequencies is marked. These frequencies are associated with the speed frequencies since $1500\text{rpm} = 25\text{Hz}$ and $2000\text{rpm} = 33\text{Hz}$. Likewise, 50Hz and 67Hz are the first speed harmonics, which are associated to the speeds in the middle shaft.

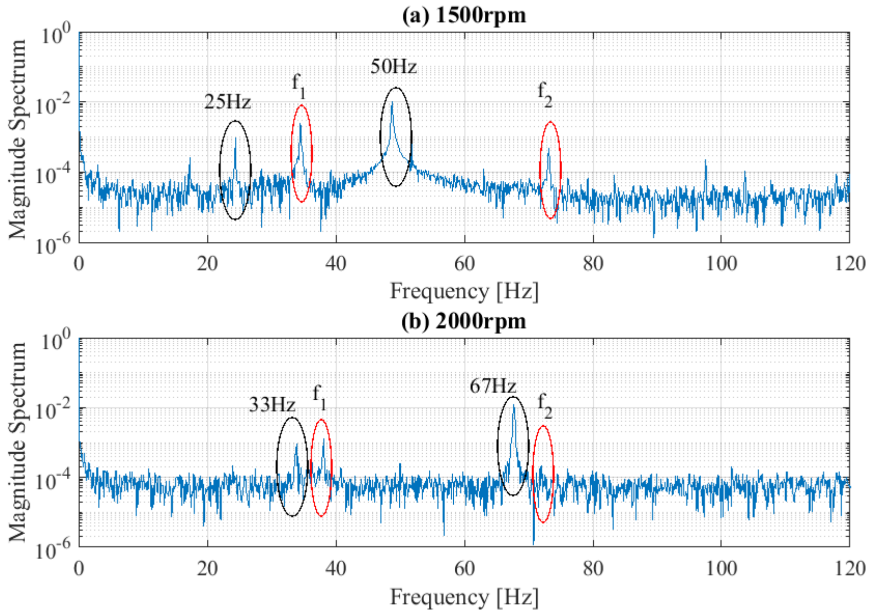

Figure 7.2: Fourier analysis at different speed.

Because the frequencies associated with the speed are not part of the torsional vibrations modes, they are filtered. Using a band stop IIR filter for each speed frequency, 25Hz and 50Hz, or 33Hz and 67Hz, with a bandwidth of 2Hz and 1Hz for the first and second frequency respectively, Figure 7.3 is obtained. Now, the frequencies obtained at both speeds are the same: 35Hz and 73.1Hz.

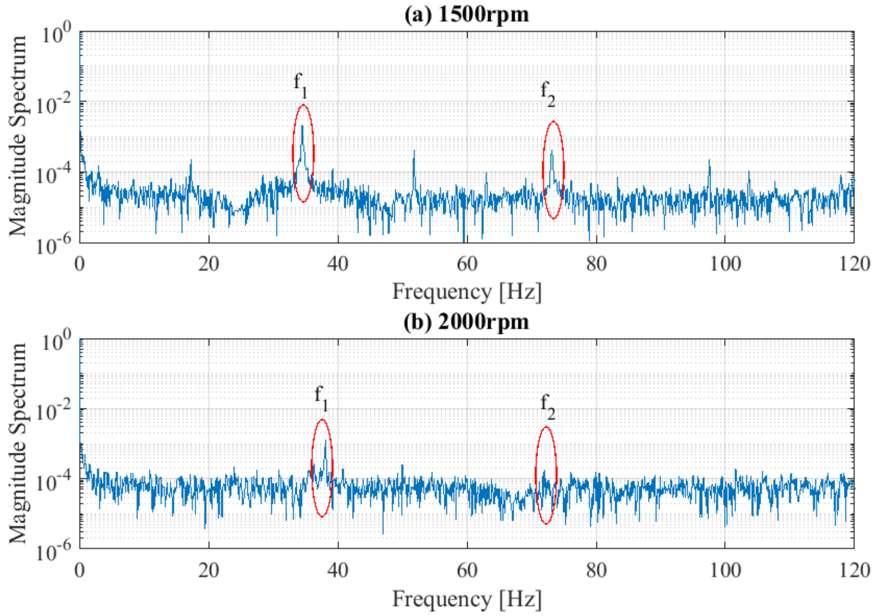

Figure 7.3: Filtered Fourier analysis.

Small frequency variations are detected between the two results. For example, the frequencies are less excited when the system is operating at 2000rpm. This is because the signal was taken when the system was closer to the steady-state than in the case of 1500rpm. Data closer to the load connection was not used, due to a high change in speed. This speed change generates many frequency peaks associated with the speed which difficults the FFT analysis.

Moreover, f_1 obtained at 2000rpm is higher than the one obtained at 1500rpm (37Hz instead of 35Hz). To understand this difference, further data sets have been used for the FFT recognition. Figure 7.4 shows the FFT obtained for a step load connection of the system operating at 1500rpm with 6.2A field current. Two seconds of data measured with an oscilloscope and a sampling time $t_s = 10^{-5}\text{s}$ was used. The frequencies obtained are $f_1 = 35.5\text{Hz}$ and $f_2 = 77.1\text{Hz}$. These frequencies are close to the ones presented in Figure 7.3 but not the same. The differences are due to small changes in the experimental rig between the measurements, such as movement of the flywheels and gears, and due to the noise of signals. The results obtained through different dataset show that the torsional frequencies of the system are in the following ranges:

- $f_1 \in [35 - 37]$ Hz
- $f_2 \in [73 - 77.1]$ Hz

Since the relative difference between the measurements is small (5.4% for f_1 and 5.1% for f_2), the values are considered acceptable. Also, the frequencies are close to the design values presented in chapter 6: 35.99Hz and 82.15Hz. Thus, the experimental system is close to its design.

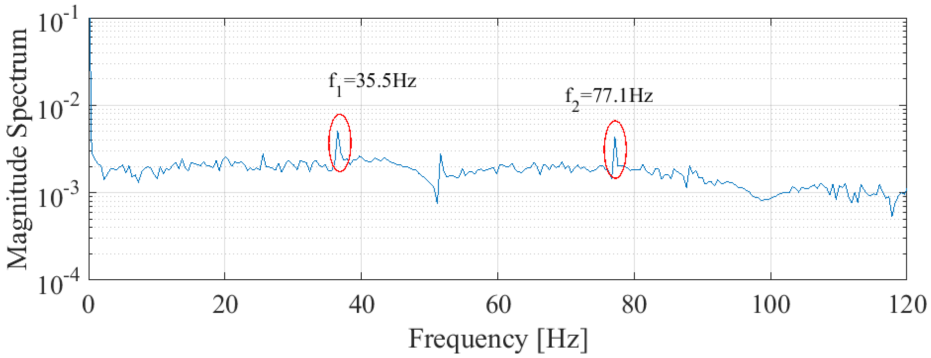

Figure 7.4: Filtered Fourier for different data.

Additionally, writing the frequencies in rpm is obtained that 35.5Hz equals 2130rpm. This value is one of the critical speeds found in section 7.2.1, showing that because of the gears the torsional vibrations produce transversal ones.

In this section, it has been demonstrated that the Fourier analysis allows the identification of torsional vibrations with an error of 5%. Since the difference is also affected by external changes, such as small movements of the components of the rig, the FFT method is a suitable identification method for torsional vibrations in real systems. However, for simulation cases, in which the system in the study can be symmetric, the FFT can fail to identify one or more natural frequencies due to the system acting as a vibration absorber configuration [49]. This is not a problem experimentally because small differences in the inertias and stiffness of the system are always present. The vibration absorber example is shown in Appendix II.

7.2.2.2 Damping Ratio Identification

In most cases, to determine the damping ratio associated with a frequency, the logarithmic decrement method is used. However, this approach presents high error in systems with high noise as this one [3]. For this reason, to identify the damping ratio, the Hilbert Transform Method combined with empirical mode decomposition (EMD) presented in [128], [129] is used.

The first step in this method is to separate the frequencies with EMD. For this, as shown in [128], the armature current signal is filtered using a passband filter around each frequency f_1 and f_2 with a bandwidth of 4Hz. To the filtered signals, the EMD method is applied to obtain the free response of a single mode. The central frequencies used for the filter are $f_1 = 35.5\text{Hz}$ and $f_2 = 77.1\text{Hz}$, since these are the frequencies that are used for the Posicast based methods in section 7.5. Figure 7.5 shows the vibration modes obtained.

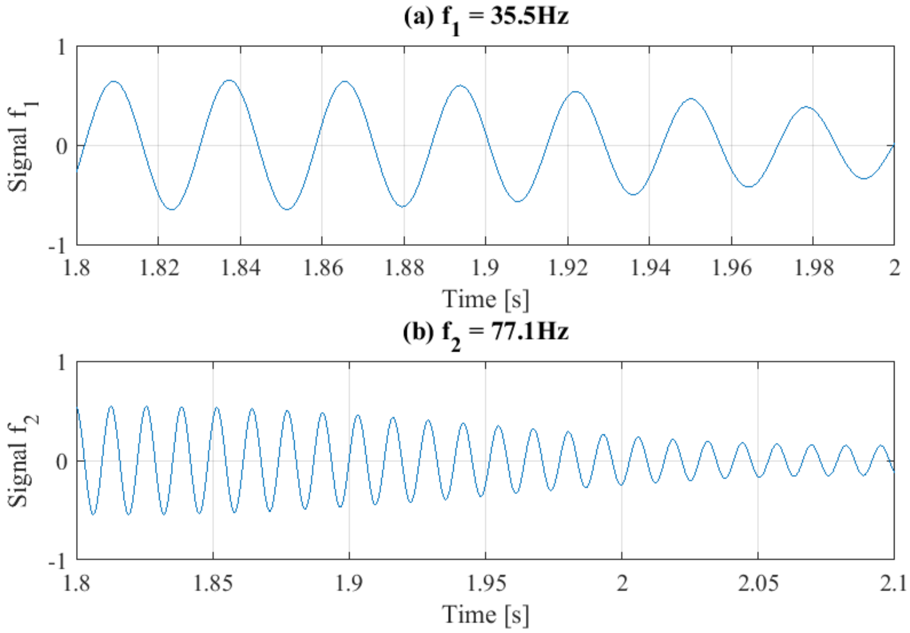

Figure 7.5: Mode decomposition.

After getting the response of the vibration modes, the Hilbert Transform is applied. The real and imaginary parts are expressed in terms of the amplitude and phase as shown in equations (7.1) and (7.2). Where ξ is damping ratio, $\omega(t)$ is the instantaneous frequency, ω_d and ω_n are the natural damped and natural frequencies, and A_0 and θ_0 are constants.

To obtain the damping ratio and the frequency associated with it, logarithm is applied to equation (7.1). The slope of this equation is $-\xi\omega_n$. The damped frequency is obtained by differentiating the angle as shown in equation (7.2).

$$A(t) = A_0 e^{-\xi\omega_n t} \rightarrow \log\big(A(t)\big) = \log(A_0) - \xi\omega_n t \tag{7.1}$$

$$\theta(t) = \omega_d t + \theta_0 \rightarrow \omega(t) = \omega_d = \omega_n\sqrt{1-\xi^2} \tag{7.2}$$

Figure 7.6 shows in blue, the data obtained by applying equations (7.1) and (7.2) to the data obtained by the Hilbert Transform. From the linear fit equations obtained, shown in Figure 7.6 in red, the value of the natural frequency and damping ratio can be identified.

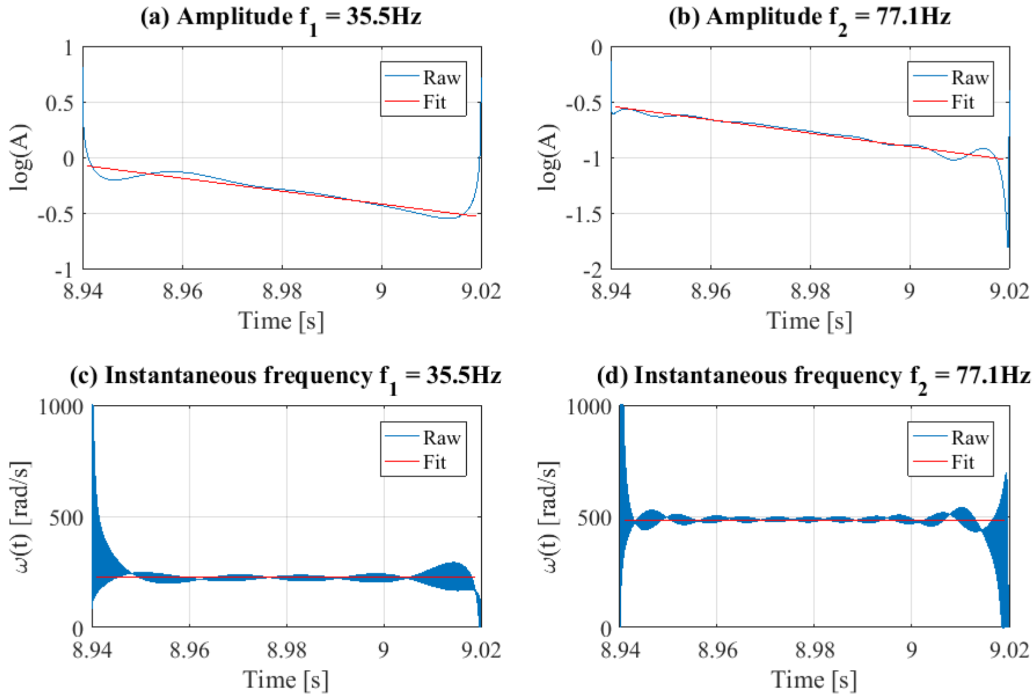

Figure 7.6: Hilbert curves.

Finally, the frequencies and its damping ratios are:

- $f_1 = 35.5\text{Hz}$ and $\xi_1 = 0.018$
- $f_2 = 77.1\text{Hz}$ and $\xi_2 = 0.012$

These values are used to solve the strategies in section 7.5.

7.3 Torque and Vibrations Measurement

As presented in chapter 6, the experimental setup measures the generator output voltage v_a (armature voltage), the generator output current i_a (armature current), the generator field current i_f, the generator shaft angle at the gear end using the resolver, and the generator speed using the tachometer connected to it. These measurements are recorded through dSpace with a sampling time of 10^{-5}s.

The torsional vibrations are analysed by obtaining the torque of the system. Since the torque is not being measured, its value is calculated by equation (7.3). The electrical torque T_g, gives the steady-state value and is obtained by equation (7.4), where P is the power generated by the machine and ω is the speed of it. Moreover, due to the use of a DC machine the electrical torque can also be obtained from $ki_f i_a$, in which k is the machine constant, i_f is the field current, and i_a is the armature current. This second method is used in this thesis. The transient torque T_{mec}, produces the vibrations of the system and is proportional to the acceleration $(d\omega/dt)$ as shown in equation (7.5). J is the inertia where the torque is being measured. In this case, since the higher torque is next to the flywheel J_{fg}, its inertia value is used. The value of T_g can be ignored to study the vibrations of the system if the steady-state value is not desired.

$$T_{sh} = T_{mec} + T_g \tag{7.3}$$

$$T_g = \frac{P}{\omega} = ki_f i_a \tag{7.4}$$

$$T_{mec} = J\frac{d\omega}{dt} \tag{7.5}$$

To obtain the torque of the system, the speed must be known. Two methods are going to be used to get the shaft speed: direct measurement and sensorless measurement. For the first one, the resolver and tachometer installed on the system are used. For the second, the speed and torque are obtained from the electrical signals: armature current, armature voltage, and field current.

To analyse the transient behaviour, the speed is analysed after an electrical load of 5Ω is connected to the system at 0.5s. The system operates at 1550rpm with a constant field current of 6.2A. The electrical parameters obtained are shown in Figure 7.7. In (a) the armature (in blue) and field (in red) current are presented and in (b) the armature voltage is shown. Plot (c) illustrates the consumed power P_{Load} given by equation (7.6). The resistance connected in the system $R_{Connected}$ can be obtained by equation (7.7), in which R_P and R_L are the protection resistance and the resistance of the load respectively.

$$P_{Load} = v_a i_a \tag{7.6}$$

$$R_{Connected} = \frac{R_P R_L}{R_p + R_L} = \frac{v_a}{i_a} \tag{7.7}$$

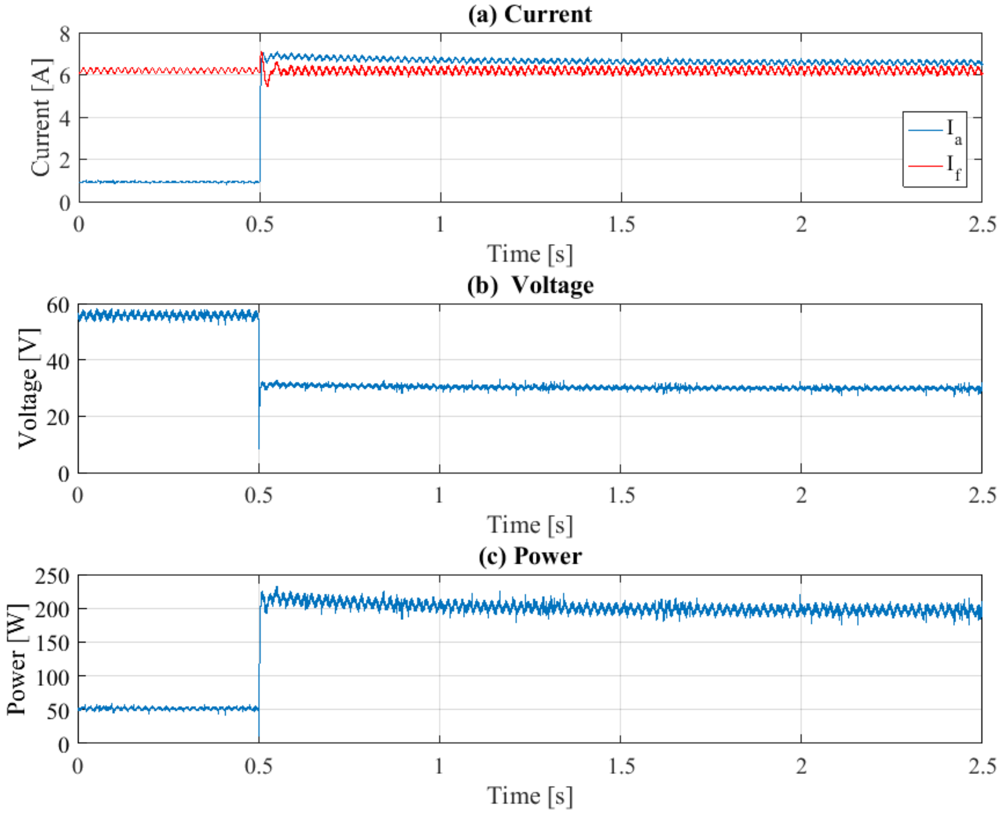

Figure 7.7: Electrical data for step connection.

7.3.1 Direct Speed Measurement

In this section, the steps to obtain the speed using the installed tachometer and resolver are shown.

7.3.1.1 Tachometer

As mentioned in chapter 6, the tachometer generates a sinusoidal voltage with frequency (f_V) proportional to the speed of the machine shaft measured by the tachometer v_t. To obtain the speed of the shaft in rpm, the frequency is detected through zero crossing, and its value is multiplied by 7.5 as shown in equation (6.9).

$$v_t[rpm] = f_V[Hz] * 7.5 \tag{7.8}$$

Figure 7.8(a) shows the voltage output of the tachometer (blue) and the speed (red) obtained by zero crossing after the electrical load is connected. The load connection produces a drop in the speed of the system. The drop shows that the speed is not entirely constant, which is due to the V/f open loop control in the motor. The time taken to reach the new steady state is given by the motor's driver constant.

As well, since the speed obtained shows high vibrations before and after the load connection, the transient vibrations produced by the step are not recognisable. The same problem is observed in Figure 7.8(b) in which the torque is shown. The torque is obtained by equations (7.3)-(7.5), but due to the high noise on the signals, the transient vibrations are not visible. The electrical component of the torque T_g is obtained using the steady-state values of the armature and field current. The constant k of the machine was obtained experimentally and is shown in Appendix I.

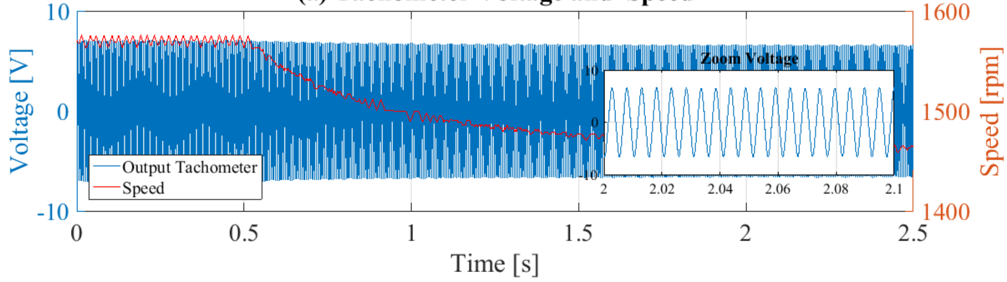
(a) Tachometer Voltage and Speed

(b) Tachometer Torque

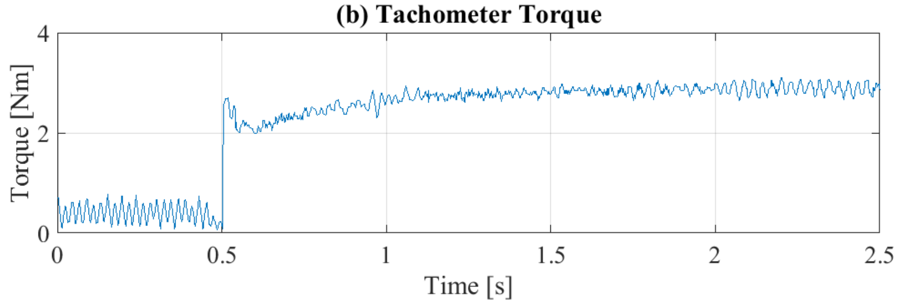

Figure 7.8: Tachometer voltage measure.

To improve the measurements obtained, the speed given by the tachometer is filtered using a moving average filter and a resonant filter. Since the torsional frequencies of the system are known (as shown in section 7.2), to remove the noise, the speed is filtered using the resonant filter of equation (7.9). f_0 is the filter frequency and q the quality factor given by equation (7.10). Here, ds is the bandwidth of the filter.

$$H(s) = \frac{2\pi \frac{f_0}{q} s}{s^2 + 2\pi \frac{f_0}{q} s + (2\pi f_0)^2} \tag{7.9}$$

$$q = \frac{f_0}{ds} \tag{7.10}$$

Using the resonant filter, the speed signal is filtered at the torsional frequencies value of f_1 and f_2. The middle values of the frequency ranges ($f_1 = 36.5\text{Hz}$ and $f_2 = 75\text{Hz}$) are chosen as the frequency f_0 of the resonant filter. A 2Hz bandwidth is used to cover the whole range of the torsional frequencies. Figure 7.9(a) shows the filtered speed at each frequency. In red, the system filtered at frequency 1, v_{tf_1}, is observed, while in blue, the system filtered at frequency 2, v_{tf_2}, is shown. At the moment of the load connection, the vibrations in both cases increase, which indicates that the step connection excites the torsional frequencies of the drivetrain. However, the vibrations in v_{tf_1} continue rising after the connection, which implies a negative damping on the system. As this behaviour opposes the expected one, the results are compared to the ones obtained by the resolver and the sensorless method in next sections.

To get the steady-state value of the speed, the dynamics of the V/f control are not taken into account since its value does not affect the vibrations on the system. Hence, the change in speed is assumed as a step, and the speed value before and after the step equals the mean value of the original signal. The total speed is obtained from equation (7.11). The components associated with f_1 and f_2, v_{tf_i}, are added to the steady state value of the speed, v_{tSS}. The total speed is shown in Figure 7.9(b). Due to the presence of v_{tf_1}, the speed vibrations do not decrease after the step connection.

$$v_T = v_{tSS} + \sum_{i=1}^{i=n} v_{tf_i} = v_{tSS} + v_{tf_1} + v_{tf_2} \tag{7.11}$$

(a) Speed Modes

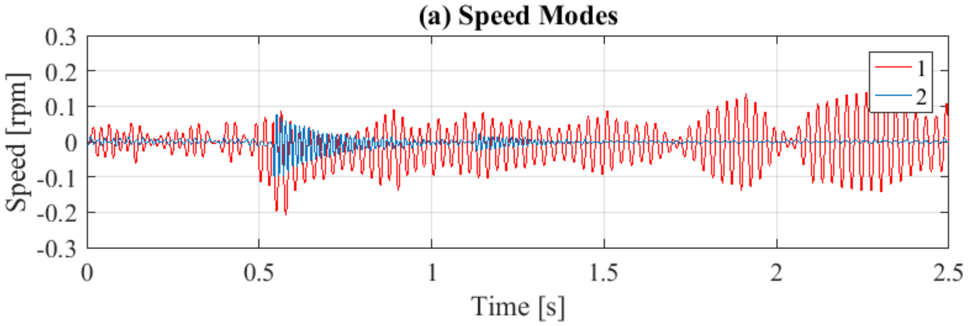

(b) Speed Filtered

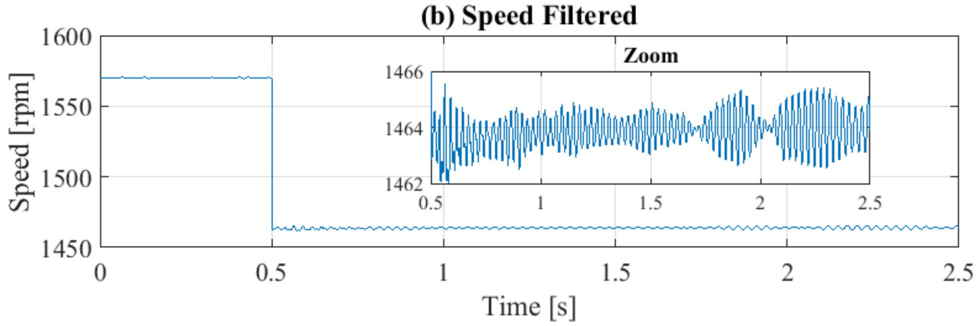

Figure 7.9: Tachometer filtered speed.

Finally, using equations (7.3)-(7.5) and the filtered speed v_T the torque is obtained and shown in Figure 7.10. The delay in the start of the vibrations is due to the use of the moving average filter. Comparing to the result obtained without the resonant filter, now the torsional vibrations excited by the electrical load connection are observed. However, since the vibrations associated with frequency f_1 do not decrease, the torque vibrations do not decay to zero. This can be due to noise in the system, unreliability on the sensor, or vibrations on the shaft system. To confirm the results, next the resolver and sensorless method are presented.

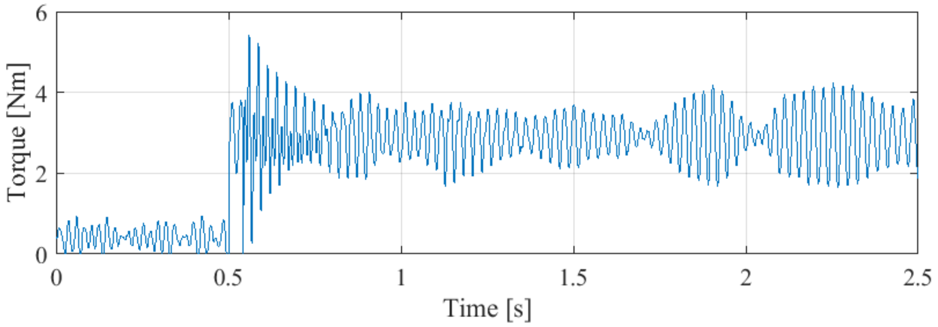

Figure 7.10: Tachometer torque.

7.3.1.2 Resolver

As presented in chapter 6, the output of the resolver connected to dSpace is the shaft angle. To obtain the speed, the angle must be differentiated. Since differentiating add high-frequency noise, a moving average filter is also used. Figure 7.11(a) shows resolver angle in rad and the speed obtained in rpm. The torque, obtained from equations (7.3)-(7.5) is shown in Figure 7.11(b). Like in the tachometer case, the speed and the torque show constant vibrations before and after the load connection. Therefore, the same filtering method presented for the tachometer signal is used for the resolver.

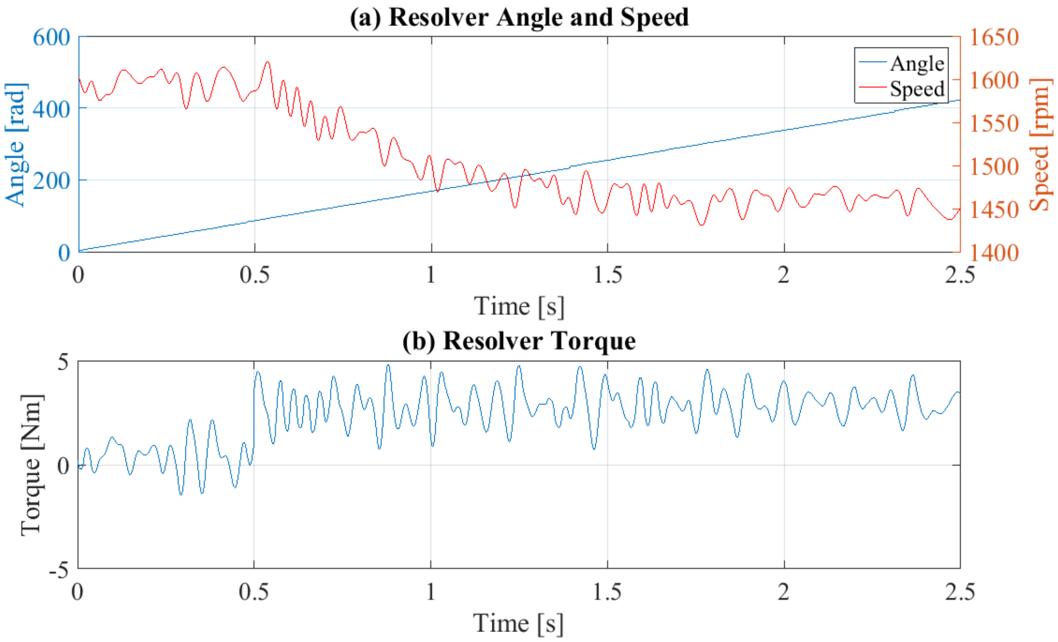

Figure 7.11: Resolver angle.

Using the same resonant filters that were described for the tachometer signal, the vibrations modes associated with each frequency v_{rf_1} and v_{rf_2} are obtained and shown in Figure 7.12(a). It is observed, that the speed vibrations rise for both frequencies f_1 and f_2 after the load connection. However, for f_1 the vibrations increase before the connection, while for f_2 the rise is after. The second case, as in the tachometer case is due to the moving average filter. Moreover, contrary to the tachometer case, the vibrations associated with both speed decrease with time. This shows that in the tachometer case, the increase in the frequency associated with f_1 is due to the sensor, and does not indicate that the vibrations in the system remain.

The total speed is obtained by equation (7.12). The steady state is the same of the tachometer. Figure 7.12(b) shows the total filtered speed.

$$v_R = v_{rSS} + \sum_{i=1}^{i=n} v_{rf_i} = v_{rSS} + v_{rf_1} + v_{rf_2} \tag{7.12}$$

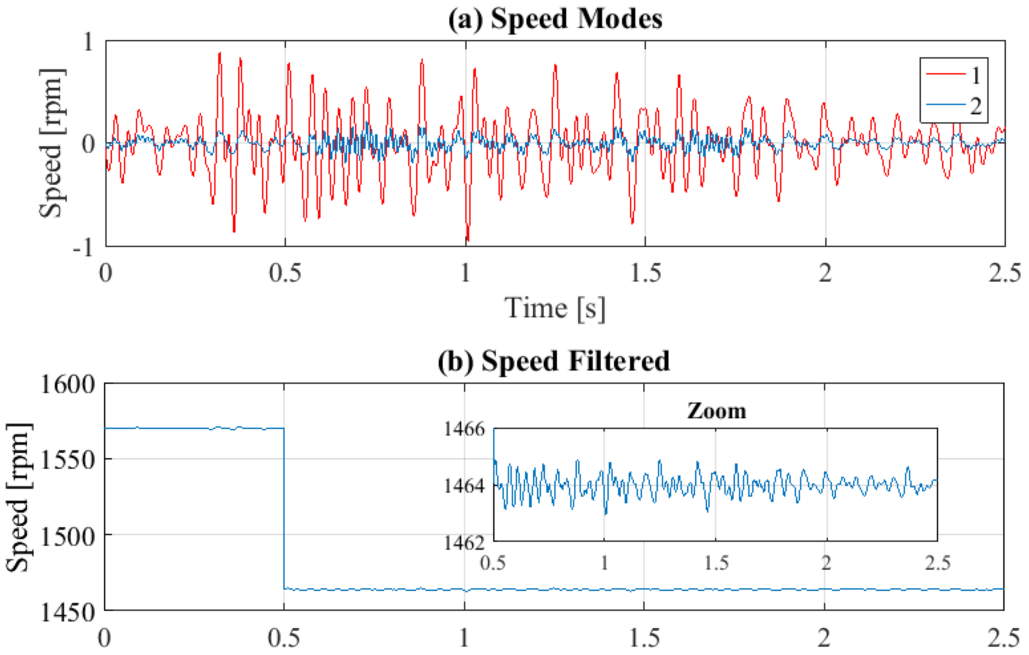

Figure 7.12: Resolver filtered speed.

Finally, the torque obtained is shown in Figure 7.13. Now it is observed that the load connection produces vibrations which decrease in time. However, the start of the vibrations before the load connection reduces the measurement reliability.

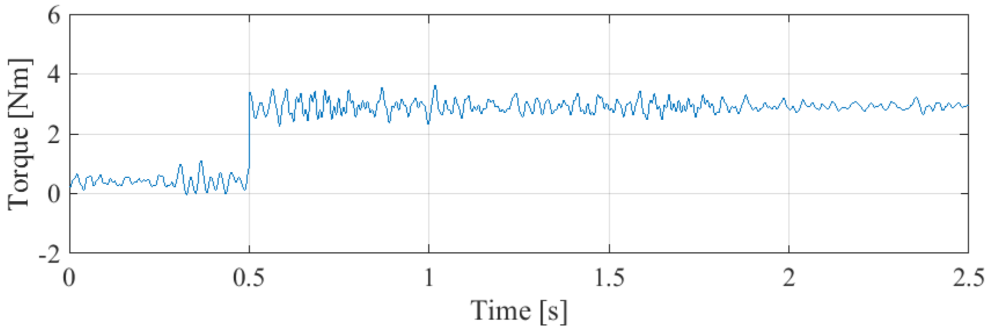

Figure 7.13: Resolver torque.

This section has shown that the torque of a system, and its transient value, can be obtained using speed measurements. However, since the torque vibrations are low, and the sensors have noise, if the signal is not filtered correctly, the transient response is not appreciated. Moreover, due to the high noise, the filters can recognise vibrations before the load has been connected as in the case of the resolver, or show higher vibrations after they have decreased as in the tachometer. For this reason, in next section, a sensorless torque measurement method is presented.

7.3.2 Sensorless Measurement

In most cases, it is possible but undesirable to install a torque sensor on a drivetrain. These sensors are expensive and require large installations [130]–[132]. Moreover, as shown in the tachometer and resolver analysis, sensors reduce the reliability because they are affected by vibrations and dust. Therefore the sensor can reduce transients and not show the electromechanical interaction response. The accuracy of the sensor is necessary for the transient analysis. The use of sensorless measurement overcomes these problems and allows the reduction of hardware complexity, cost and size [132].

The sensorless strategy depends on the machine used. In [19], methods for synchronous machines are presented, in [133], [134] DC machines are studied, and in [135] the induction case is investigated. Despite the use of diverse sensor strategies for different machines, in general, first sensorless measurements were open-loop. However, as parameters uncertainty and noise are not accounted for, the convergence of open-loop methods is low. For this reason, closed-loop strategies were introduced. Closed-loop estimators have better disturbance rejection and better robustness against parameters inaccuracy. An example is model reference adaptive system (MRAS) observers, which are used for speed estimation in cage induction machine [135].

Moreover, most sensorless measuring methods are based on estimation techniques or mathematical models. Mathematical model methods, such as the back-Electromotive Force (EMF) strategy are the standard industrial solution. They obtain the angle and speed of the system by estimating the back-EMF and are typically used for medium and high-speed systems [132], [136]. However, when operating at low speeds, the back-EMF presents large errors, because the voltage drop in the stator resistance is high compared to the EMF. For this reason, estimation methods are used for low-speed systems. Some studies estimate the resistance to reduce the errors. In [8], steady state and online methods to estimate the resistance are presented. In [132], [136], anisotropy-based techniques are studied. These strategies inject high-frequency signals into the machine to obtain the angle. However, this method can produce losses and larger torque ripple. Another angle estimation technique is presented in [135], in which a slip angle estimator for doubly fed induction generator is obtained from the stator inductance.

For DC machines, in [137] a method to improve the commutation performance of sensorless brushless dc motors is proposed. This method is robust to parameter variations, as well as to non-ideal back-EMF. In [134] a strategy based on the symmetrical characteristic of the phase back-EMF is suggested.

In general, it is not desired to work with systems that require high knowledge of its components. However, for the DC machine in the study, since the operation speed is high and its parameters are known, a model based back-EMF method is used. To eliminate the noise of the signals, the back-EMF method is combined with signal filtering.

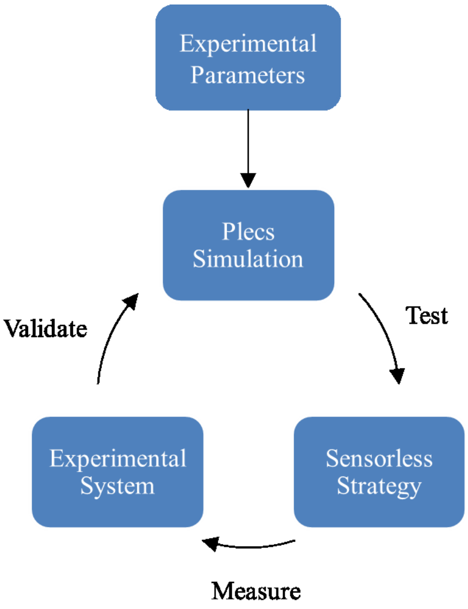

Figure 7.14: Sensorless strategy methodology.

Figure 7.14 shows the validation methodology used by the sensorless strategy in this chapter. First, the experimental system is simulated in PLECS using the electrical and mechanical parameters obtained empirically. Then, the sensorless strategy is tested using the simulation results. After confirming that the sensorless strategy allows the obtention of the same torque parameters, the strategy is used for measuring the torque in the experimental system. Finally, the experimental results are compared with the simulation ones and the system is validated.

Then, to test the sensorless system simulation data is used. To emulate the experimental data, noise is added to the electrical signals. The resulting noisy data is employed to test the proposed measurement strategy. These results are compared with the simulation torque to prove the reliability of the method. Figure 7.15 shows the simulation data in which the sensorless strategy is tested. The results were obtained by PLECS simulation of the experimental system described in chapter 6. The system speed is 1537rpm, and the field current is 6.2A. At 0.5s a load of 140.8W (from 47.56W to 188.4W) is connected, which is obtained by the connection of 4.7Ω.

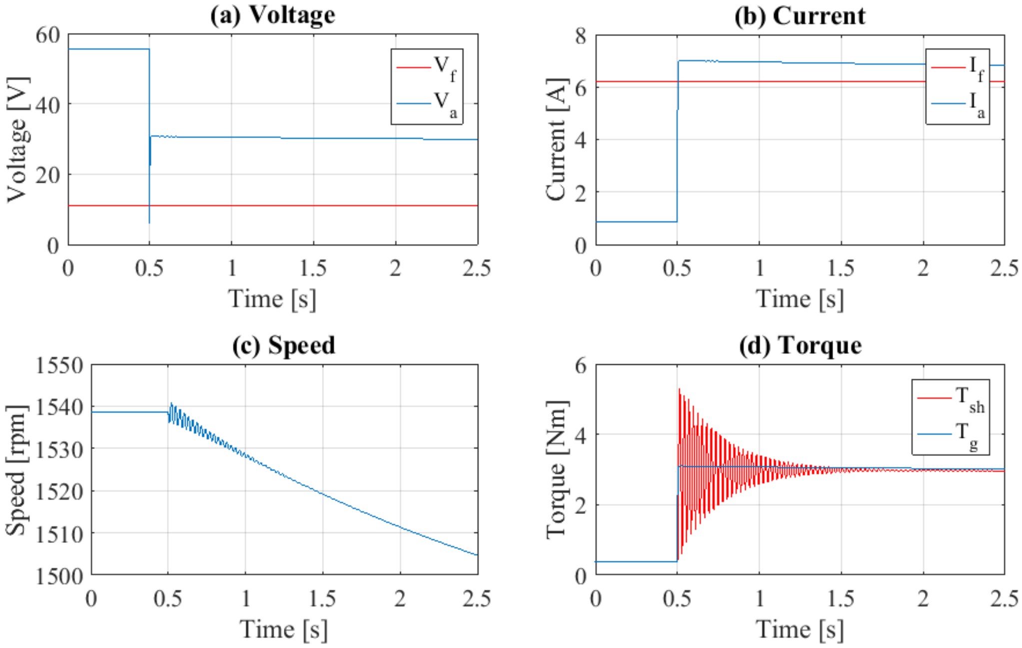

Figure 7.15: Original simulation data.

The rest of the section is organised as follows: First white noise is added to the simulation electrical signals to represent experimental data. Second, a filter is presented to eliminate the noise of the signals. Third, the speed of the system is calculated. Finally, the torque is obtained.

7.3.2.1 Noisy Data

It has been shown that a problem of the experimental data is the amount of noise, making it difficult to get torque measurements. Thus, to emulate the real results, white noise[3] is added to the armature voltage and current obtained by simulation. Since the field current is constant, noise is not needed to be added. Figure 7.16 shows a comparison of the signals before (in red) and after the noise has been added (in blue).

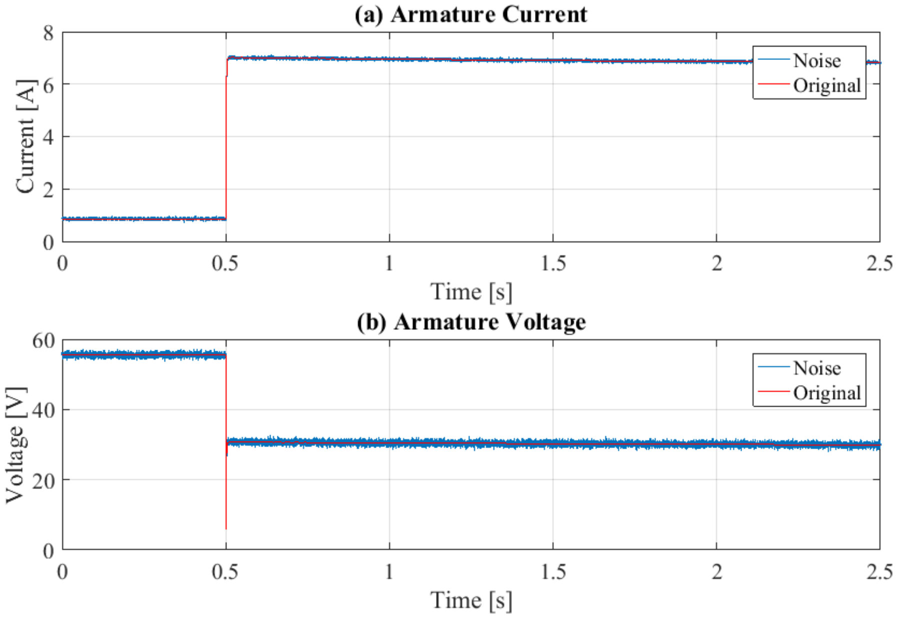

Figure 7.16: Noisy simulation signals.

7.3.2.2 Filtering of the Data

Like it was done with the resolver and tachometer data, to identify the vibrations associated with the torsional vibrations, the FFT of the armature current is obtained and shown in Figure 7.17. The magnitude is normalised by the steady-state value of the signal, and the natural frequencies at 36.73Hz and 83.67Hz are found.

---

[3] Matlab command: awgn(signal,40,’measured’)

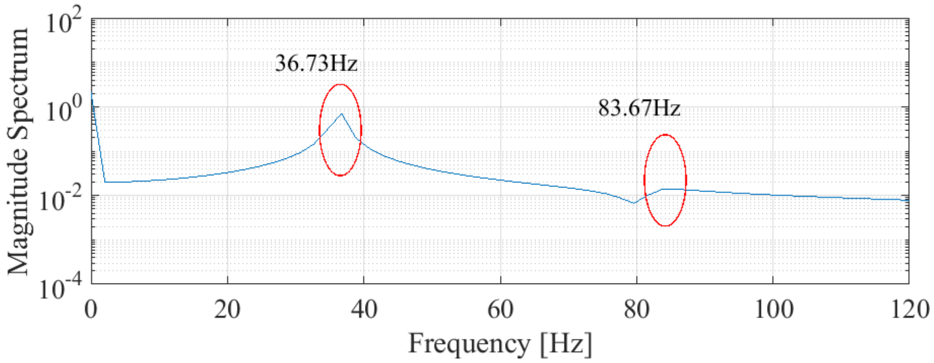

Figure 7.17: FFT Simulation system.

Once the torsional vibration modes have been identified, the current and voltage signals are filtered using resonant filters. The resonant filter used is equivalent to the one presented in the tachometer and resolver cases and the bandwidth used is $df = 1$Hz. Figure 7.18(a) and (b) show the modes associated with the frequencies f_1 and f_2 for the voltage and current respectively.

The noiseless reconstructed electrical signals v_E are given by equation (7.13). The signal v_E is formed by the sum of the steady-state value of the measured signal v_{ess} and the values of the signal at each natural frequency v_{ef_i}. Moreover, from Figure 7.18(a) and (b) it is observed that the values of the current and voltage modes are not proportional to the FFT magnitude at each frequency. For this reason, in the reconstructed noiseless signal, a participation g_i is added. This value is equal to the magnitude of the frequency of the normalised spectrum. Hence, from Figure 7.17 $g_1 = 0.3377$ and $g_2 = 0.0065$. The same factors are used independently of the strategy employed in the system.

$$v_E = v_{ess} + \sum_{i=1}^{i=n} g_i v_{ef_i} = v_{ess} + g_1 v_{ef_1} + g_2 v_{ef_2} \qquad (7.13)$$

The noiseless voltage and current compared to the original simulation signal (before the noise is added) are shown in Figure 7.18(c) and (d). The frequency of the filtered signals is the same of the original voltage and current. However, the magnitude is higher. The higher magnitude is due to the resonant filter response to the step connection.

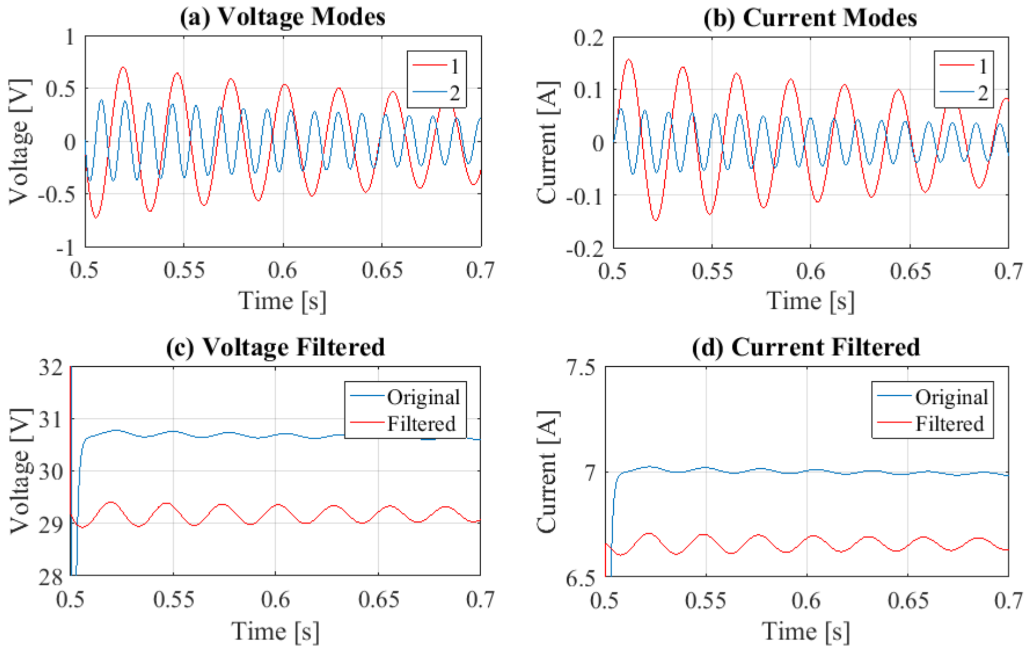

Figure 7.18: Filtered simulation data

For this reason, the step connection (with no transient response) of the voltage and current is filtered with the same resonant filter used for the noisy signals. Figure 7.19 shows the results obtained. It can be observed, that even though the system has no frequencies present, the resonant filter produces vibrations, and therefore the voltage and current filtered have a transient response while the step does not.

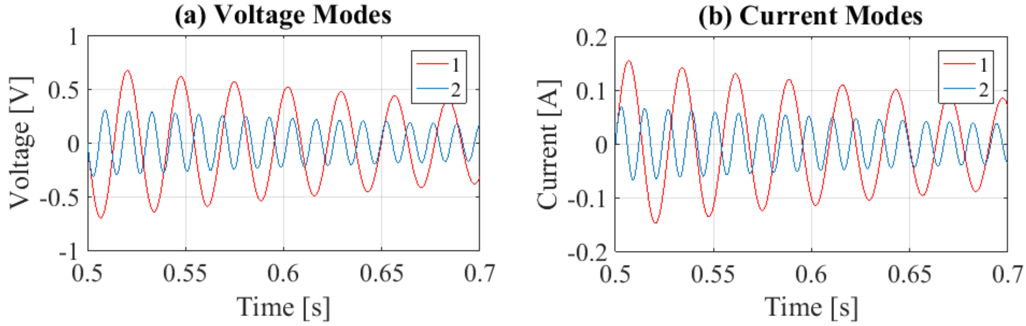

Figure 7.19: Step resonant filter response.

To eliminate the resonant filter response and obtain only the voltage and current vibrations of the signal, the filter response shown in Figure 7.19 is subtracted to the results presented in Figure 7.18. In the case of the resolver and tachometer, the reaction of the resonant filter does not need to be removed from the filtered speed, because the signal does not present a sharp step as in the case of the current and voltage. The resulting modes and results are shown in Figure 7.20. It is observed that after removing the filter response, the values of voltage and current obtained after the noise signal has been filtered are equal to the ones obtained initially by simulation. The difference in the voltage and current mean value are due to neglecting the motor drive dynamics. This approximation is applied since in this study only the vibrations are relevant.

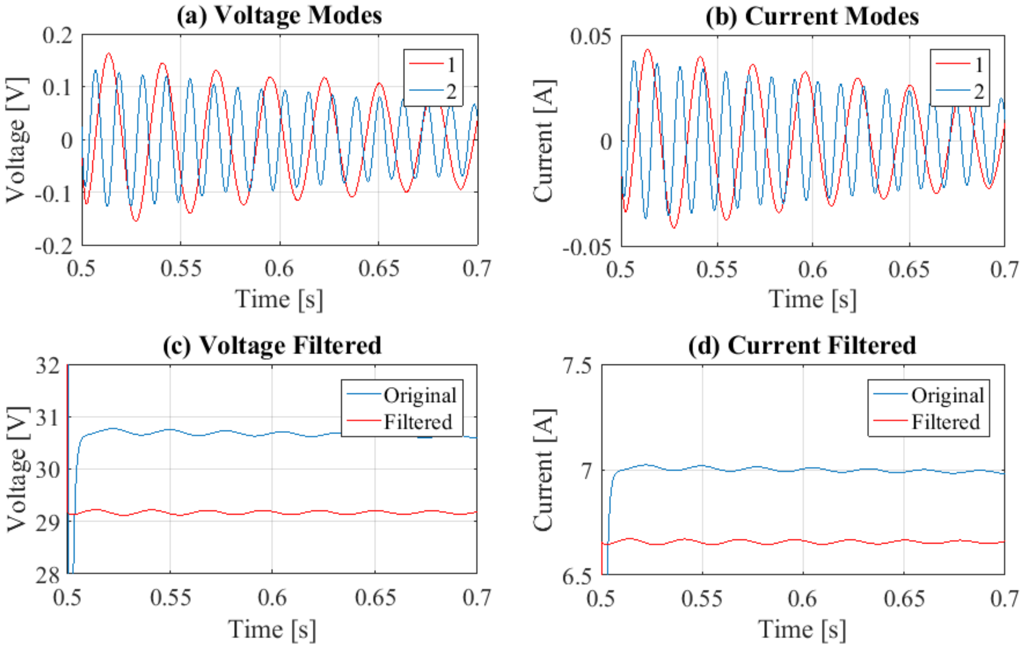

Figure 7.20: Final simulation filtered data.

7.3.2.3 Speed Determination

To get the torque, the speed must be found. For a single phase DC machine, its value in $\mathrm{rad/s}$ can be obtained using equation (7.14), which is based on the back-EMF method. The values of k and i_f are constant and the induced voltage (or back-EMF) E, depends on the filtered armature voltage and current as given by equation (7.15). The effect of the inductance has been simplified. The values of R_a, V_0, and k have been determined experimentally for the DC machine as presented in Appendix I. In the case of working with a synchronous generator, as in most aircraft, the steps are equivalent. The speed is proportional to the machine frequency, and the electrical torque can be obtained as a function of the electrical power and the speed.

$$\omega_g = \frac{E}{k i_f} \tag{7.14}$$

$$E = R_a i_a + v_a + V_0 \tag{7.15}$$

Figure 7.21 shows the speed obtained in the simulation (in blue) and sensorless (in red). It is observed that the frequency and amplitude of the vibrations are the same. However, like for the voltage and current, the average value of the estimated signal is lower than the original one. As already explained, this is due to the simplification of the motor dynamics.

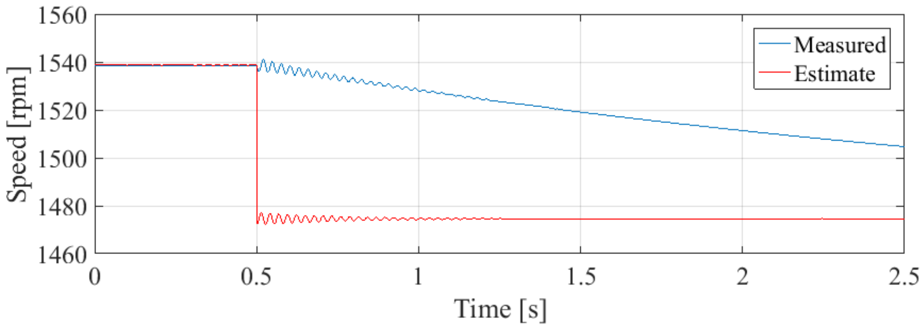

Figure 7.21: Speed of the system by simulation.

7.3.2.4 Torque Determination

After finding the speed, the torque can be obtained following the same equations (7.3)-(7.5) used for the resolver and tachometer sensors. Figure 7.22 shows the torque obtained from the simulation software PLECS (in blue), and the torque obtained with the described sensorless procedure (in red). The results reached are the same for the transient response, and therefore the estimated torque is not affected by the simplification of the motor dynamics.

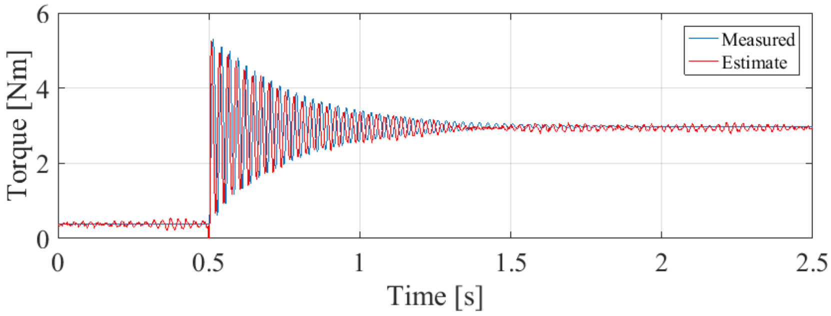

Figure 7.22: Sensorless simulation torque measurement.

For the analysis of the steady-state response, the sensorless measurement presents low vibrations around the steady-state value. These vibrations are due to the high-frequency noise added by the resonant filters. To show this, in Figure 7.23 the FFT of the original and filtered signals are presented. The low frequencies and the torsional frequencies are the same. However, the estimated signal has high-frequency noise added, which is consistent with the noise observed in Figure 7.22 for the steady-state value. Calculating the relative error of the estimated signal respect to the simulation value, 0.0799% is obtained. This value demonstrates that the sensorless measurement presented is accurate despite the noise added to the system by the resonant filter.

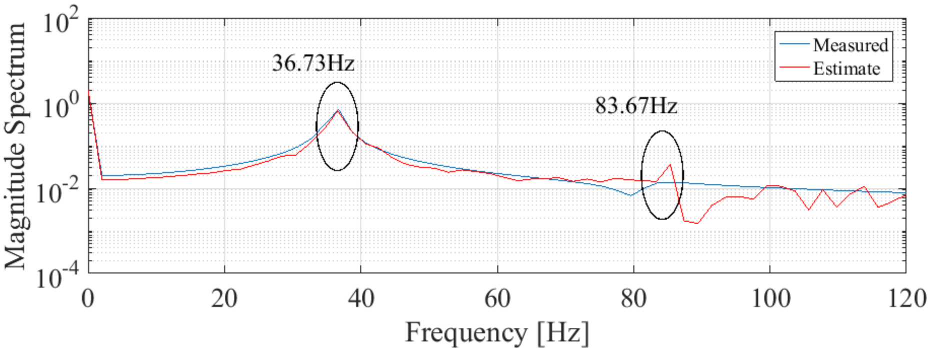

Figure 7.23: FFT sensorless simulation data.

After proving the sensorless method by simulation, the strategy is applied to the electrical signal obtained experimentally presented in Figure 7.7. Figure 7.24 shows the speed and torque obtained sensorless. The signals were filtrated at 36.5Hz and 75Hz using resonant filters with a bandwidth of 2Hz as in tachometer and resolver cases. These two frequencies correspond to the middle frequency of the ranges determined in section 7.2.2. The participation factors used from now and in the rest of the thesis are $g_1 = 0.06796$ and $g_2 = 0.04703$. It is observed that the step connection excites the voltage and current modes associated with the frequencies. However, contrary to the tachometer and resolver results, both signal decay with time, reaching a steady state. The same is observed for the torque, in which the vibrations are observed much clearer than for the other measuring methods. Furthermore, the signals obtained with the sensorless method have less noise than the ones obtained with the tachometer and resolver, allowing a clear view of the torque step produced by the load connection. Moreover, the results are close to the ones obtained through simulation and shown in Figure 7.22 in which the same system was modelled. This indicates that the simulation is accurate and that the results obtained experimentally are reliable.

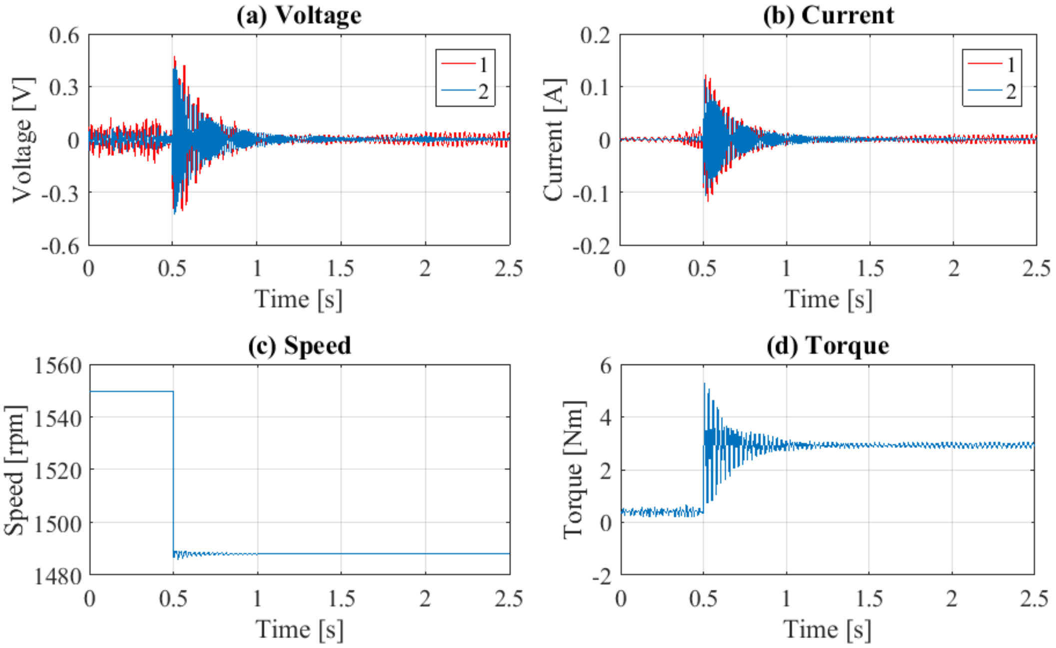

Figure 7.24: Sensorless speed and torque.

In next sections, the electromechanical interaction due to load step connection and the application of the PMS strategies is shown. The resolver, tachometer and sensorless method are used and compared.

7.4 Electromechanical Interaction

In sections 7.2 and 7.3 the electromechanical interaction due to electrical load connections has been indirectly shown. In this section, the results obtained are analysed. The electrical signals of the step connection (current and voltage) and the calculated power and resistance are shown in section 7.3 in Figure 7.7. The system operates with a field current of 6.2A and at a speed of 1550rpm approximately. After the load is connected, the speed decreases to under 1500rpm. The load initially attached to the system is 50.82W, given by the protection resistance of

60Ω. The final load in the system is 210W. The same parameters are used to test the PMS strategies in section 7.5.

The filtered speed and torque were shown in the sensor analysis, and it is summarised in Figure 7.25. The torsional vibrations due to the load connection can be observed. This shows the electromechanical interaction due to the connection of electrical loads. Moreover, as mentioned in the last section, the result obtained by the resolver and tachometer sensor strategies have a higher presence of noise than the sensorless method. This noise produces problems in the visualization of the results when the PMS strategies are applied, as shown in the next section.

The steady state torque obtained is 2.92Nm. The peak torque obtained by the resolver, tachometer and sensorless method are 3.5Nm, 5.4Nm, and 5.3Nm respectively. The results obtained with the Posicast compensators are compared with these values in next section.

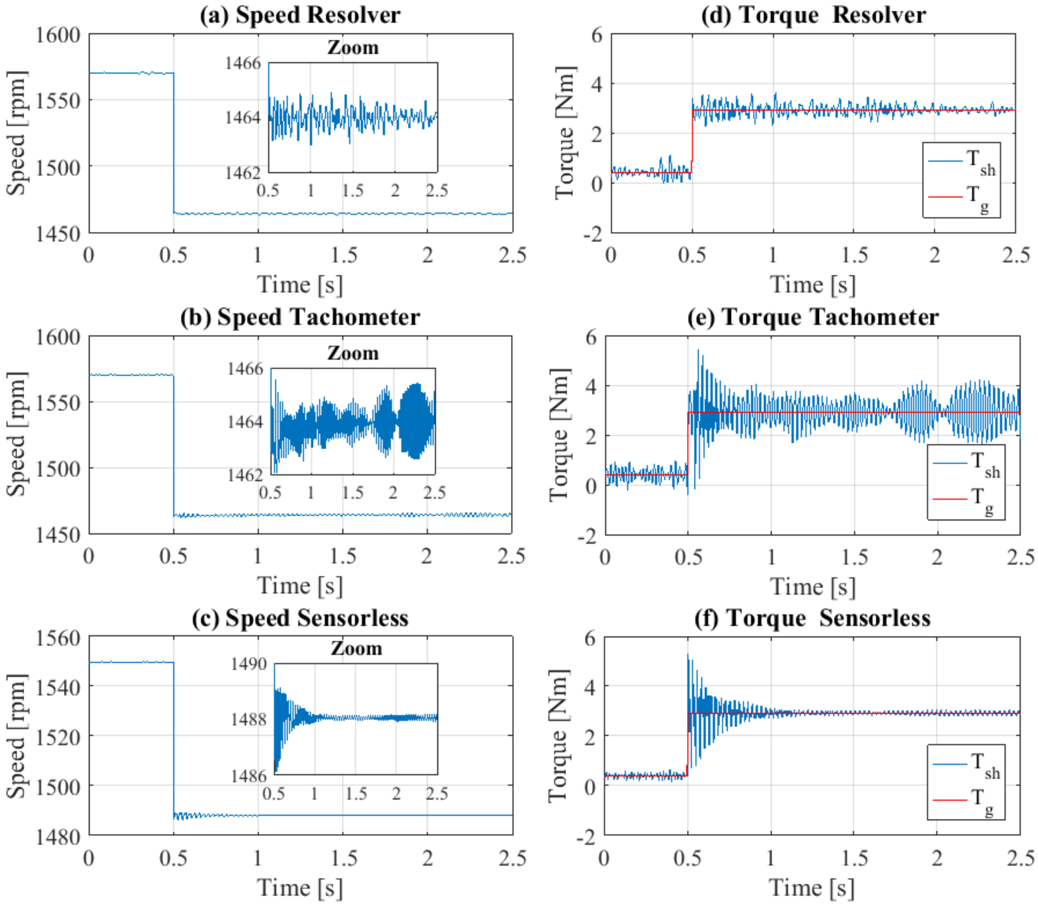

Figure 7.25: Speed and torque for step connection.

The FFT analysis of the armature current uses 10 seconds of data after the load is connected. Figure 7.26 shows the results obtained. The presence of the peak at f_1 and f_2 shows the excitation of the vibrations. Thus, the torque results can be confirmed.

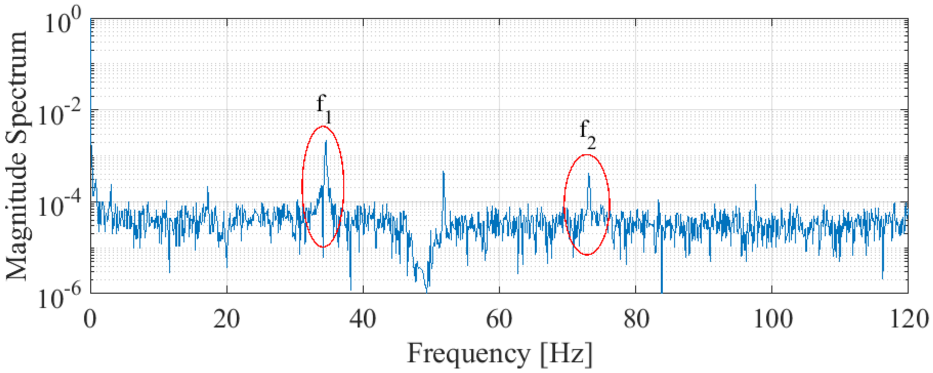

Figure 7.26: FFT for step connection.

In the next section, the results obtained by the Posicast based strategies are presented. In each case, the torque found by the tachometer, resolver, and sensorless method are analysed.

7.5 Power Management System Operation

Until now, the electromechanical interaction due to electrical step connection has been tested experimentally. In this section, the PMS strategies, based on the Posicast compensator are verified.

The strategies for time non-critical loads (MLL and SLME) and time-critical loads (MSLME) described in chapter 5 are solved for the two frequency system found in section 7.2:

- $f_1 = 35.5\text{Hz}$ and $\xi_1 = 0.018$
- $f_2 = 77.1\text{Hz}$ and $\xi_2 = 0.012$

The vibrations of the system are measured using the methods presented in section 7.3. For the sensorless measuring method, the participation factors are the same used in the step connection: $g_1 = 0.06796$, and $g_2 = 0.04703$.

The loads switching is executed by the three IGBT connected in parallel as shown in Figure 6.12 in chapter 6. Moreover, in the three cases, the initial and final operation parameters are the same used for the step connection. The generator field current is 6.2A, and the speed is 1550rpm. The protection resistance is 60Ω, and the initial power and torque are 50.82W and 0.41Nm respectively. The final load connected is approximately 210.52W and 2.93Nm.

7.5.1 Single Level Multi-edge Switching Load

The first strategy to be tested is the Single Level Multi-edge Switching Load or SLME. For a two natural frequency system ($n = 2$), the SLME method consists of five pulses ($m = 2n + 1 = 5$). Solving the equation system (5.33) in Matlab with Opti Toolbox [122], the following switching times are obtained:

- $T_1 = 0\text{s}$
- $T_2 = 2.5\text{ms}$
- $T_3 = 6.7\text{ms}$
- $T_4 = 11.1\text{ms}$
- $T_5 = 13.4\text{ms}$

$$\begin{bmatrix} \sum_{k=1}^{5} (-1)^{k+1} e^{-\xi_1 \omega_{n1} T_k} \cos(\omega_{d1} T_k) \\ \sum_{k=1}^{5} (-1)^{k+1} e^{-\xi_1 \omega_{n1} T_k} \sin(\omega_{d1} T_k) \\ \sum_{k=1}^{5} (-1)^{k+1} e^{-\xi_2 \omega_{n2} T_k} \cos(\omega_{d2} T_k) \\ \sum_{k=1}^{5} (-1)^{k+1} e^{-\xi_2 \omega_{n2} T_k} \sin(\omega_{d2} T_k) \end{bmatrix} = 0 \qquad (7.16)$$

Figure 7.27 shows the switching signals sent by the microcontroller to IGBT 1. The resistance being connected and disconnected by the IGBT is 4.95Ω.

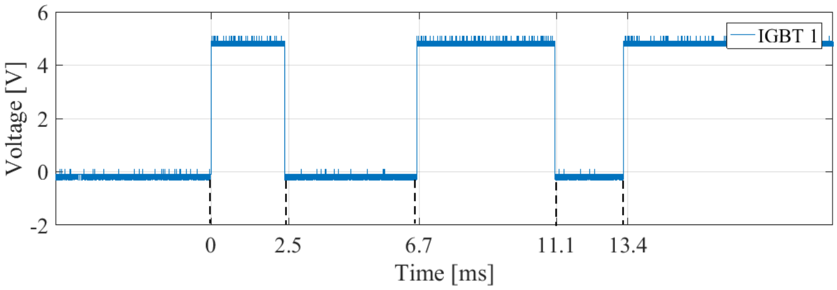

Figure 7.27: Switching SLME.

Figure 7.28 shows the measured current and voltage of the system, along with the power obtained. From (c) is observed that the final power is close to 210.51W, which makes the results comparable with ones obtained for the step connection. Moreover, from the zoom presented in each subplot, the switching of the load is appreciated. Observing the current in Figure 7.28(a), it is appreciated that the step has an exponential component which stops the whole load from being applied at once in each connection. This delay is due to the inductance of the system, which is mostly given by the DC machine.

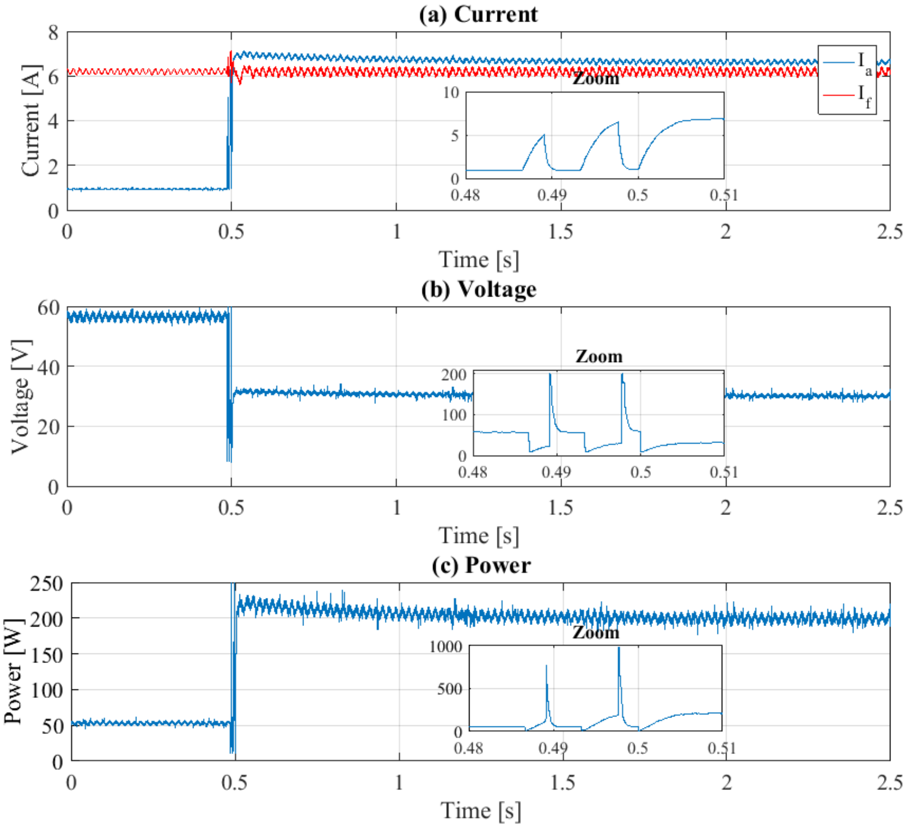

Figure 7.28: Electrical data for SLME connection.

Figure 7.29(b) shows the speed obtained from the resolver and tachometer before the application of the resonant filter. Comparing with the results obtained by a step connection, presented in Figure 7.29(a), the system is operating at the same speed.

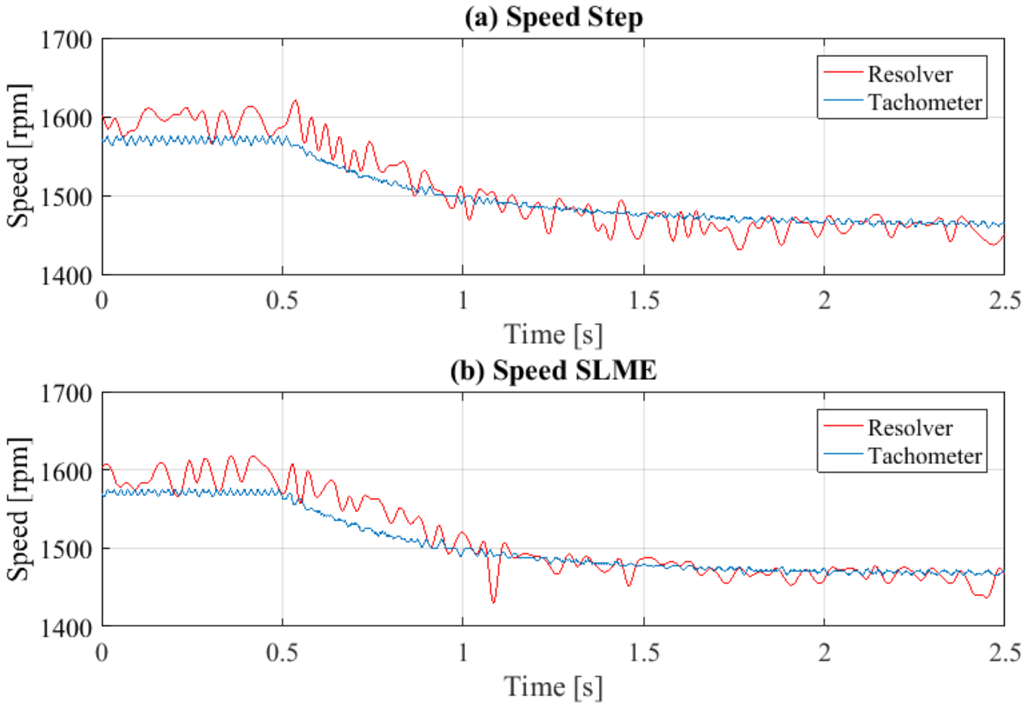

Figure 7.29: Resolver and tachometer speed for SLME connection.

The filtered speed and torque obtained through the sensors and sensorless method are shown in Figure 7.30. In (d), (e), and (f) the torque obtained through the resolver, tachometer and sensorless method is shown. In red the electrical torque connection, in blue the resulting shaft torque, and in yellow the shaft torque in the step case are shown. The steady state value of the SLME connection torque is the same of the step connection: 2.93Nm. Comparing the transient response with the step connection results, the measurements given by the tachometer and sensorless method show considerably lower peak torque vibrations. In both cases, for the step connection, the peak vibration was 5.5Nm and 5.3Nm respectively. With the SLME connection, the peaks are 3.9Nm and 3.8Nm respectively. This shows that the SLME strategy reduces the vibrations comparing with the step connection. However, the vibrations are not completely eliminated after the load switching as was presented by simulation. This difference is because the steps applied to the mechanical system are not perfect square step, but exponential. Moreover, the frequencies for which the strategy was solved is not precise since in section 7.2.2 a range for each torsional frequency was identified instead of a single value. Since the strategy was solved for a specific value, a level of uncertainty is present in the response. This situation and the robustness of the strategies is analysed in chapter 8.

On the other hand, since the resolver results are similar to the step connection, and the tachometer has high vibrations after the steady state has been reached, the sensors are not reliable for the transient analysis of the system. For further analysis of the resolver and tachometer performances, the results obtained through the MLL and MSLME are analysed in the next section.

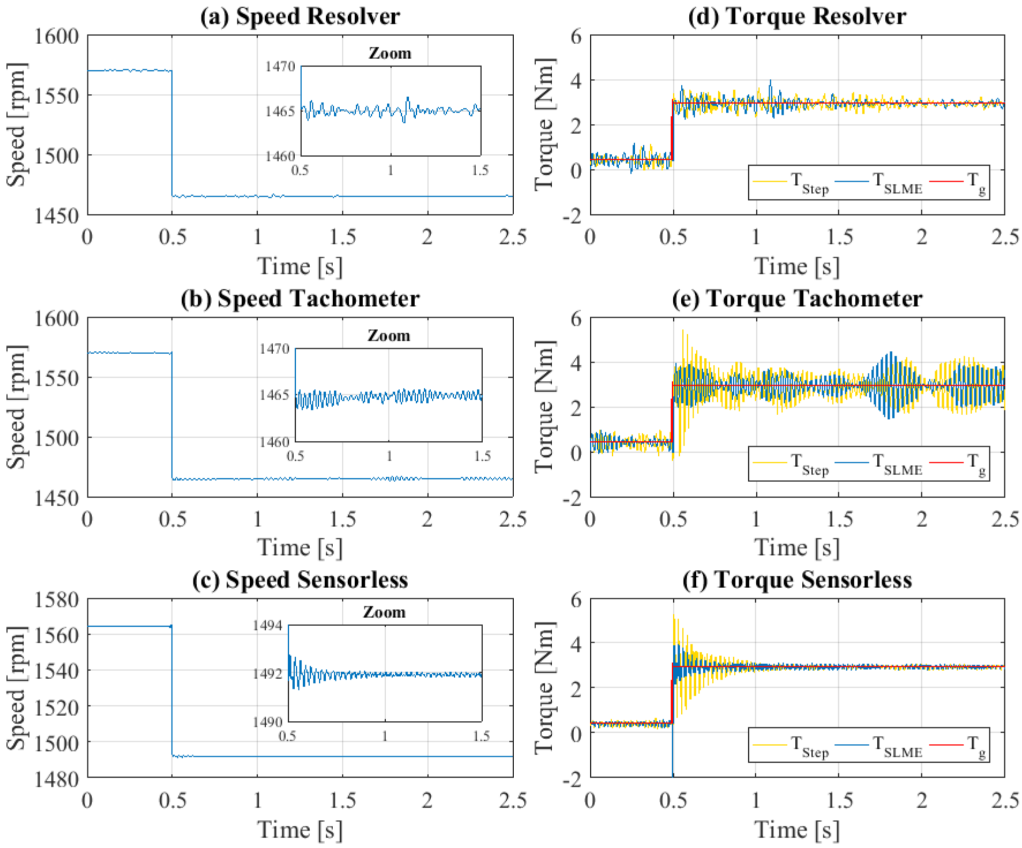

Figure 7.30: Speed and torque for the SLME connection.

The FFT of the step and SLME connection, calculated for 10s of armature current data after the load connection are shown in Figure 7.31(a) and (b) respectively. Comparing the SLME results with the results obtained for the step connection, it is observed that the vibrations are slightly reduced. This confirms the torque performance.

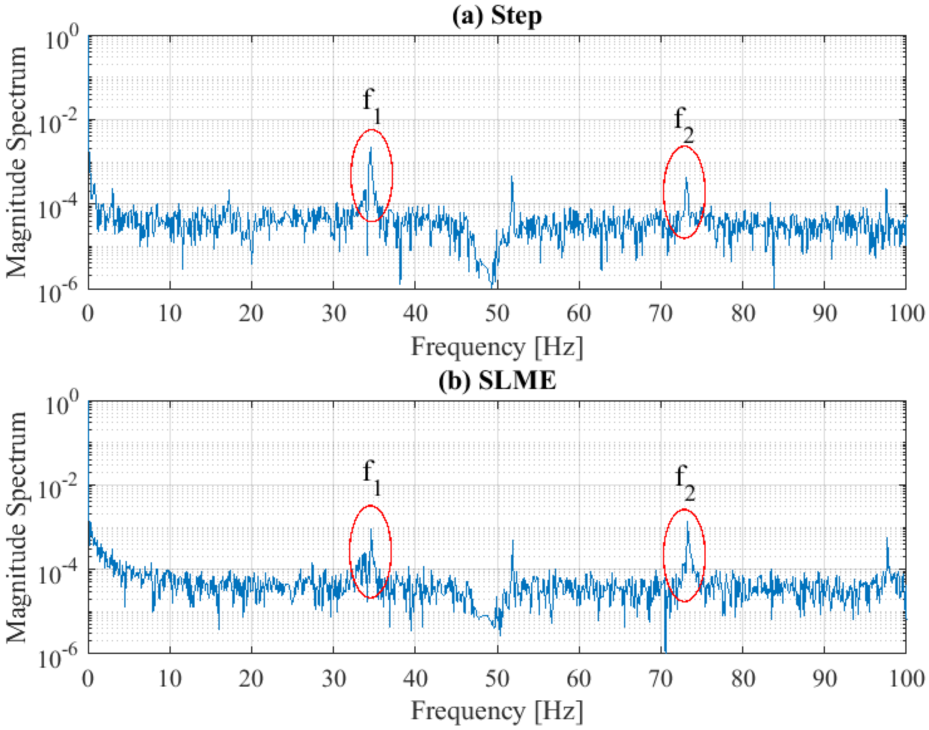

Figure 7.31: FFT SLME connection.

7.5.2 Multilevel Loading Switching

Now, the Multilevel Loading Switching (MLL) is tested. For a two natural frequency system ($n = 2$), the MLL method is formed by three steps ($m = n + 1 = 3$). Thus, the three IGBT connected on the system are used. Each IGBT is connected to a load, which value and connection time is given by equation system (7.17). Solving in Matlab with Opti Toolbox [122], the following switching times and step values are obtained:

- $T_1 = 0\text{s}$ and $p_1 = 0.37$
- $T_2 = 8.9\text{ms}$ and $p_2 = 0.29$
- $T_3 = 17.7\text{ms}$ and $p_3 = 0.33$

$$\begin{bmatrix} \sum_{k=1}^{3} p_k e^{-\xi_1 \omega_{n1} T_k} \cos(\omega_{d1} T_k) \\ \sum_{k=1}^{3} p_k e^{-\xi_1 \omega_{n1} T_k} \sin(\omega_{d1} T_k) \\ \sum_{k=1}^{3} p_k e^{-\xi_2 \omega_{n2} T_k} \cos(\omega_{d2} T_k) \\ \sum_{k=1}^{3} p_k e^{-\xi_2 \omega_{n2} T_k} \sin(\omega_{d2} T_k) \end{bmatrix} = 0 \tag{7.17}$$

Figure 7.32 shows the switching signals sent by the microcontroller to IGBT 1, IGBT 2 and IGBT 3. Each IGBT is turned on, at the times obtained. The resistances connected to each of them that allow having the torque step sizes required are $R_{L1} = 30.53\Omega$, $R_{L2} = 18.29\Omega$, and $R_{L3} = 10.23\Omega$.

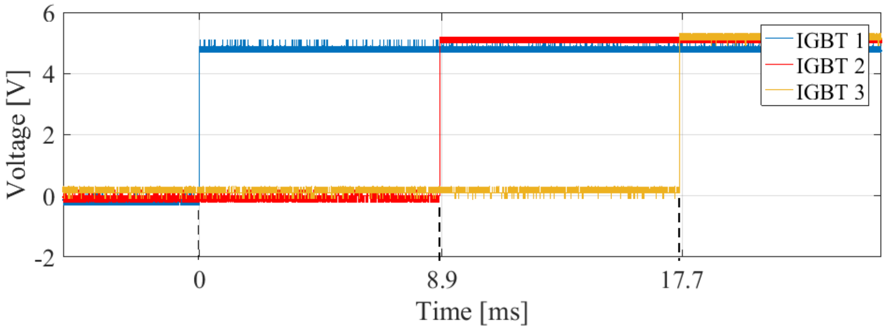

Figure 7.32: Switching MLL.

The electrical signals obtained are shown in Figure 7.33. From (c), it can be seen that the final load connected to the system is close to 210W. Therefore the data can be compared to the step connection. Moreover, the current signal in (a) shows the effect of the machine inductances, which produces exponential load connections instead of step load connections. However, contrary to the SLME connection, in this case, the loads are completely connected before the next IGBT is switched on, making the connection closer to the theory.

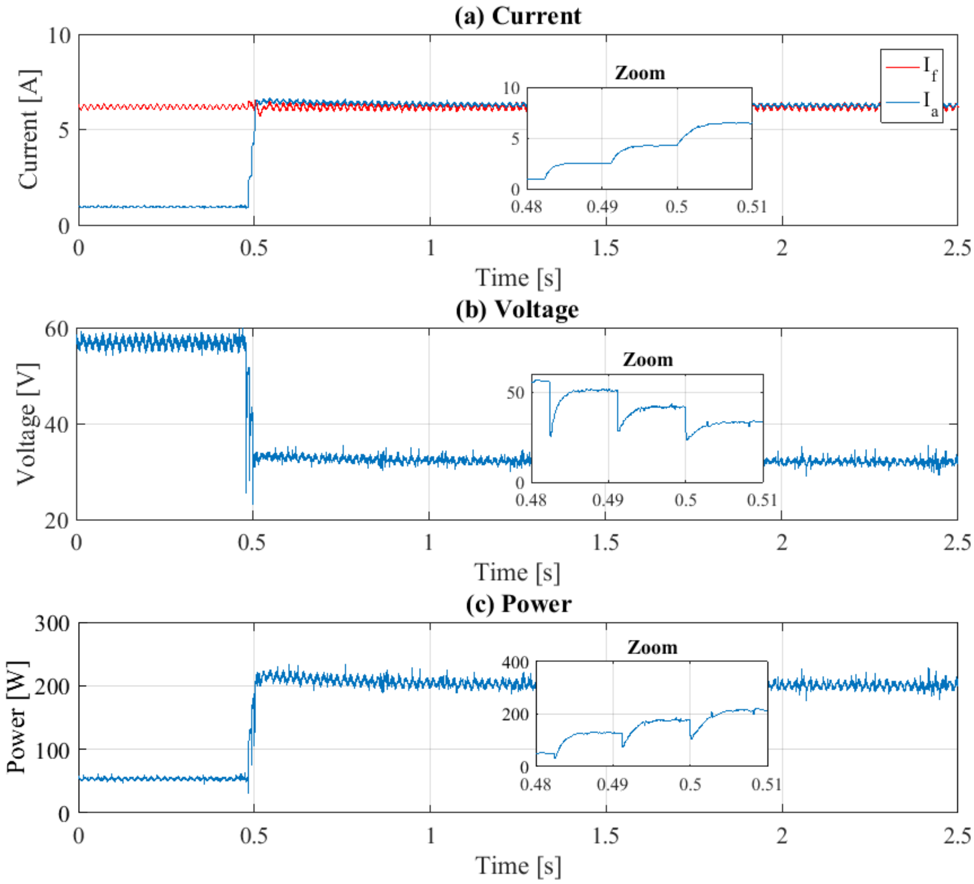

Figure 7.33: Electrical data for MLL connection.

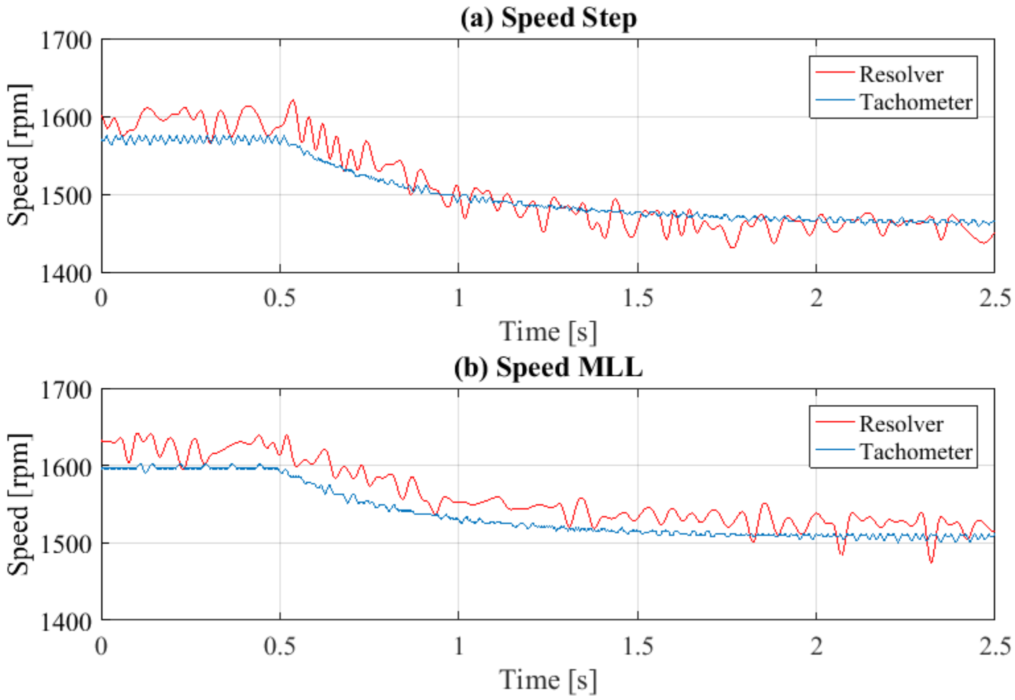

Figure 7.34: Resolver and tachometer speed for MLL connection.

Figure 7.34(b) shows the speed obtained from the resolver and tachometer before the filter has been applied. The system speed is higher than the one of the step case shown in Figure 7.34(a) by 50rpm. The relative difference is 3.18%, and hence it is considered inside the margin error, making the comparison feasible.

The filtered speed and torque are shown in Figure 7.35. In red, the torque applied is shown, while in blue the shaft torque response is shown. In yellow the torque obtained in the case connection case is depicted. As in the step and SLME cases, the results given by the resolver are similar, decreasing from 3.5Nm to 3.1Nm. On the other hand, the torque obtained by the tachometer and sensorless method are considerably lower than the ones obtained in the other two cases. The results shown by the tachometer and sensorless indicate that the vibrations have been almost entirely eliminated with the MLL strategy. The peak values are 3.3Nm and 3.1Nm, instead of 5.5Nm and 5.3Nm as in the step connection. The steady state torque value is 2.77Nm which is 5% lower than in the other two cases. This difference is inside the comparable range.

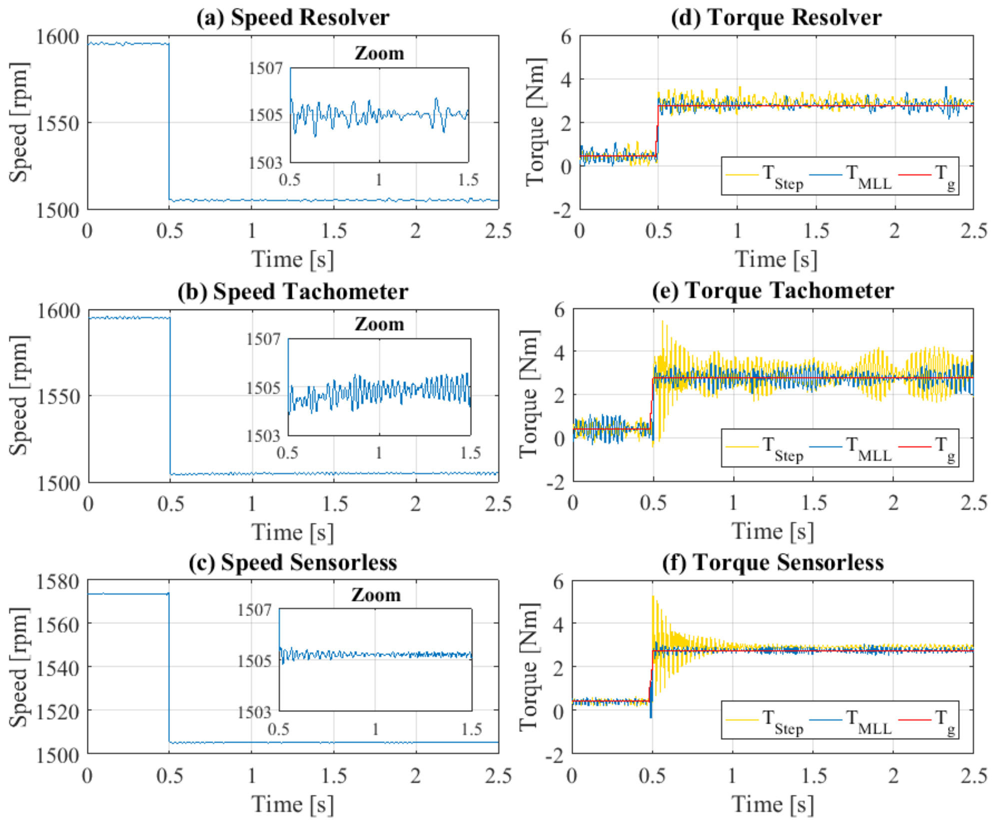

Figure 7.35: Speed and torque for MLL connection.

The same behaviour is confirmed by the FFT analysis of Figure 7.36. In (a) the frequencies excited by the step connection are shown, while in (b) it can be seen that for the MLL connection, the frequencies associated with the torsional modes are not excited. Therefore, the MLL method tested allows almost the complete elimination of the vibrations after the switching event, although the load applied is exponential and the frequency used has a level of uncertainty. This result implies that the main reason for the remaining vibrations in the SLME connection are the inductances.

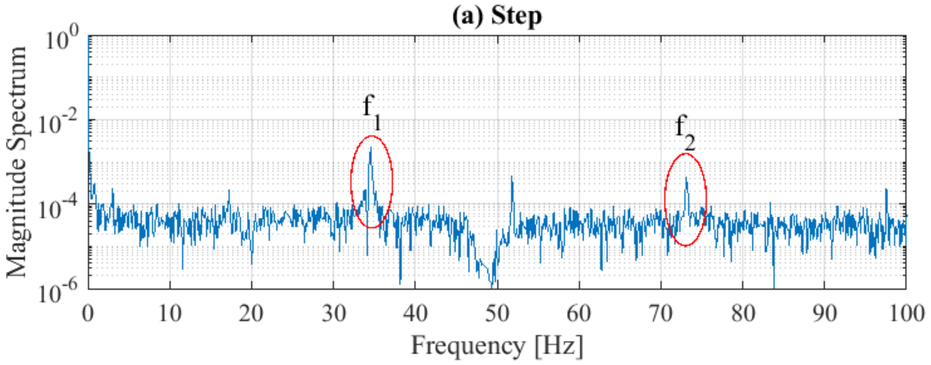
(a) Step

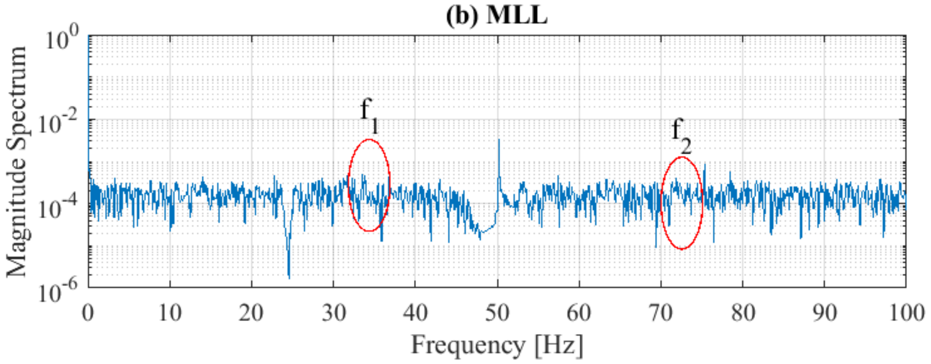
(b) MLL

Figure 7.36: FFT for MLL connection.

Moreover, the low change in the resolver measurements, and the remaining noise in the tachometer support that these sensors are reliable for the torque measurement in this experimental setup.

7.5.3 Multi-load Single Level Multi-edge Switching Loads

Finally, for the case of working with Time Critical loads, the strategy Multi-load Single Level Multi-edge Switching Load (MSLME) was presented in chapter 5. It consisted in connecting the time-critical load as a step connection, and apply a pulsating pattern to a time non-critical load. In chapter 5, the time non-critical load was disconnected and connected following the desired pattern. In this case, to work with the same final load of the other three connection strategies, the auxiliary load is a secondary load being connected as shown in red in Figure 7.37. The equations to solve are the same of the disconnection case since the overall effect in the drivetrain is equal. Then, for a two natural frequency system ($n = 2$), the MSLME method is formed by four load connections ($m = 2n = 4$). Solving the equation system (7.18) in Matlab with Opti Toolbox [122], the following switching times are obtained:

- $T_1 = 0\text{s}$
- $T_2 = 10.7\text{ms}$
- $T_3 = 13.2\text{ms}$
- $T_4 = 16.3\text{ms}$

The auxiliary load value is 60% of the time-critical load connected.

$$\begin{bmatrix} 1 + \sum_{k=1}^{4} (-1)^k p e^{-\xi_1 \omega_{n1} T_k} \cos(\omega_{d1} T_k) \\ \sum_{k=1}^{4} (-1)^k p e^{-\xi_1 \omega_{n1} T_k} \sin(\omega_{d1} T_k) \\ 1 + \sum_{k-1}^{4} (-1)^k p e^{-\xi_2 \omega_{n2} T_k} \cos(\omega_{d2} T_k) \\ \sum_{k=1}^{4} (-1)^k p e^{-\xi_2 \omega_{n2} T_k} \sin(\omega_{d2} T_k) \end{bmatrix} = 0 \tag{7.18}$$

Figure 7.37 shows the switching signals sent by the microcontroller to IGBT 1 and IGBT 2. The critical load, connected to IGBT 1, and which value is 13.34Ω is connected as a step. The auxiliary load, coupled to IGBT 2 is connected as a pulse at time T_2. Its value is 9.07Ω.

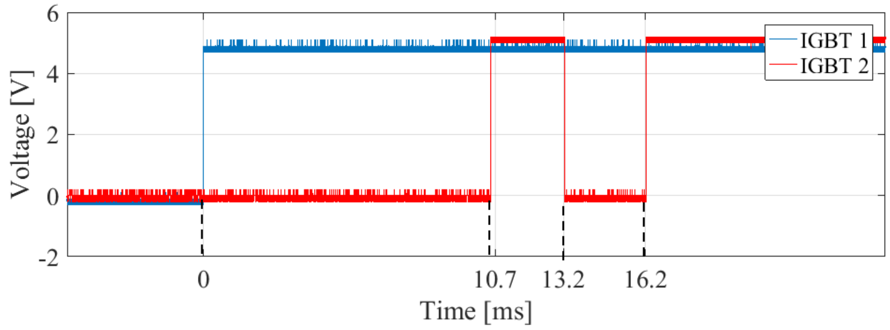

Figure 7.37: Switching MSLME.

Figure 7.38 shows the electrical data obtained. In (c), the final electrical load connected to the system is 207W, which is close to the values presented in the other three cases. From the current in (a) is observed that due to the closeness between steps, the inductance has a high effect on the connections. Therefore, as in the SLME case, some transient vibrations are obtained.

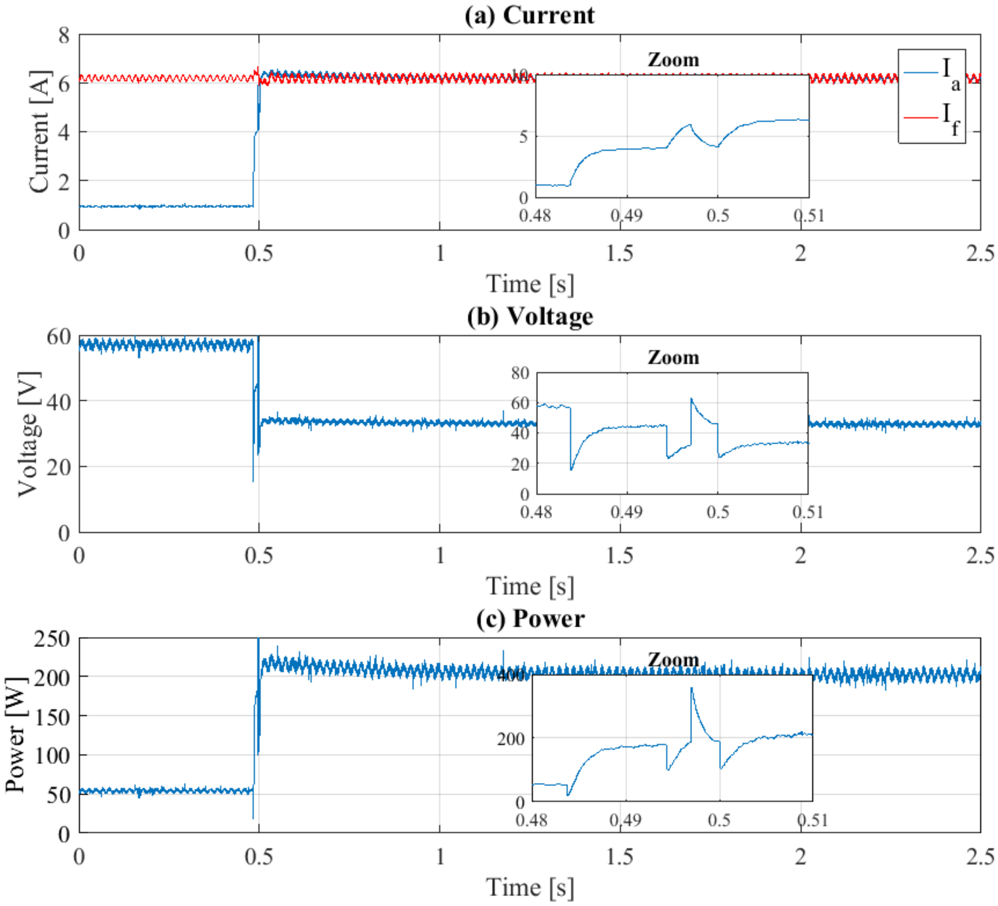

Figure 7.38: Electrical data for MSLME connection.

From Figure 7.39(b) it is observed that as in the MLL case, the speed of the system is 50rpm higher than in the step case shown in Figure 7.39(a). Since the values are close, the results obtained are comparable.

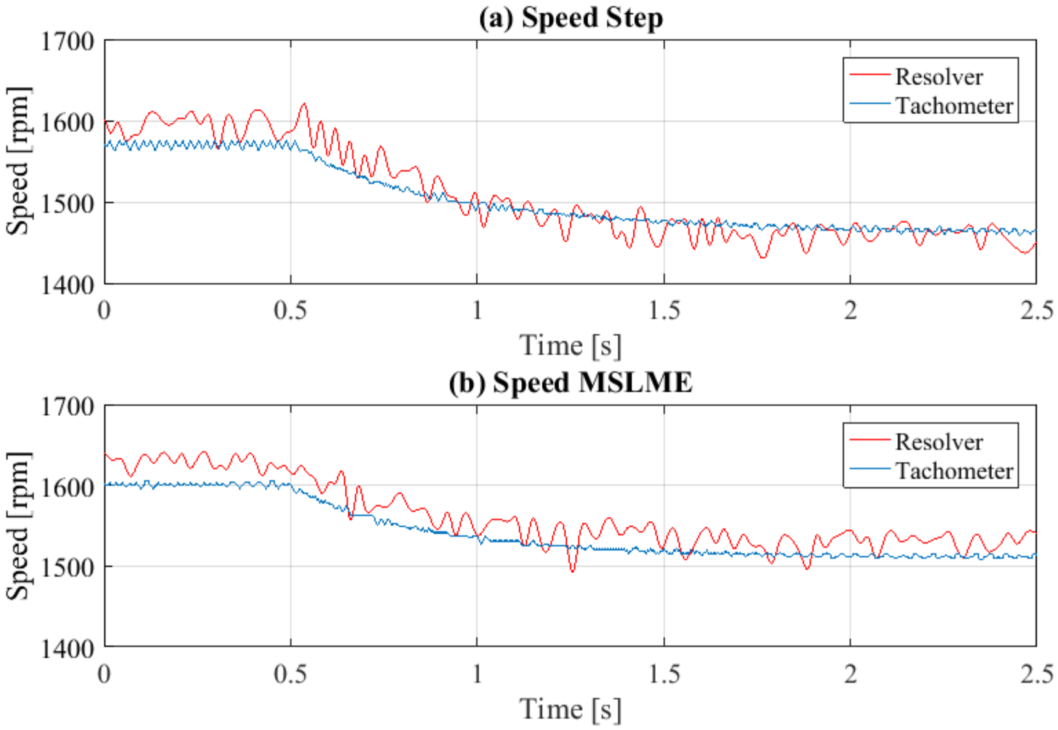

Figure 7.39: Resolver and tachometer speed for MSLME connection.

The filtered speed and torque obtained through the different methods are shown in Figure 7.40. In red, the torque applied is shown, while in blue the shaft torque response is shown. In yellow the torque obtained in the case connection case is depicted. The steady state torque is 2.723Nm which is close to the one in the step connection, and thus comparable with the ones of the other cases. The vibrations obtained by the sensorless method are lower than in the SLME and step cases, but higher than the MLL. This was expectable since the steps are affected by the system inductance less than in the SLME connection but more than in the MLL. This shows the correlation between the time between steps and the inductance in the system. Further analysis is presented in chapter 8.

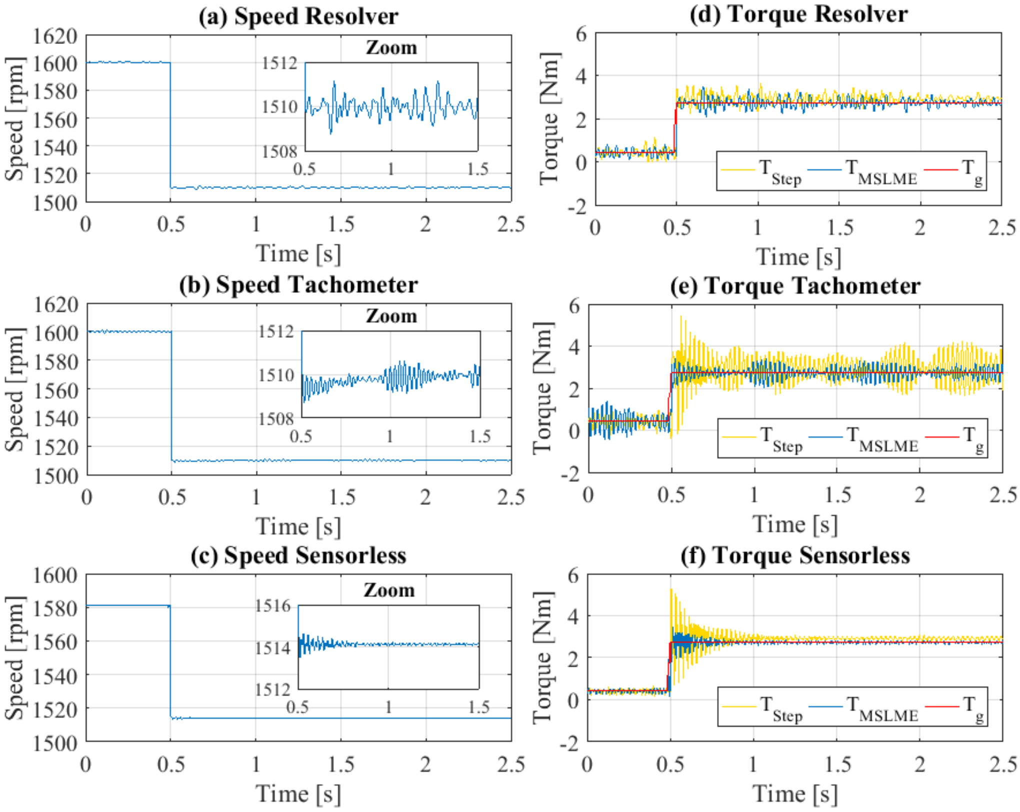

Figure 7.40: Speed and torque for MSLME connection.

The FFT of the system analysed is shown in Figure 7.41. In (a) the results obtained for the step connection are shown, while in (b) the results obtained using the MSLME strategy are presented. Using the MSLME strategy, the excitation of f_1 has almost entirely been cancelled, while f_2 is not. This can be explained by the connection curve. The steps associated with higher frequencies are closer. From Figure 7.38(a), the closer the steps, the higher the effect of the inductance in the system. Therefore, the inductances in the system are mostly affecting the cancellation of the second frequency.

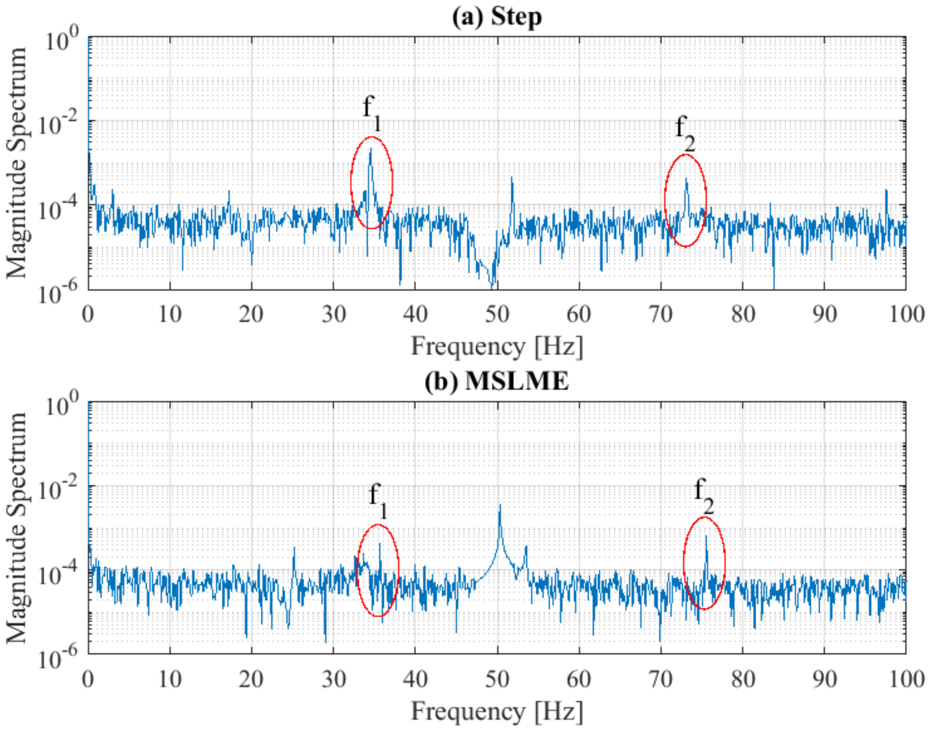

Figure 7.41: FFT for MSLME connection.

Moreover, the results obtained by the tachometer and resolver show, again, that the sensorless method is less affected by the noise. The resolver shows slightly lower vibrations than the ones obtained in the step connection, and higher than the MLL case. However, the delay in the start of the vibrations could be due to the filter used, or because the vibrations have noise. Similarly, the results obtained by the tachometer show lower vibrations than the ones achieved by the MLL strategy. These vibration increase after. Both situations are contrary to what is expected by theory and obtained with the sensorless method. Therefore, the results obtained by the tachometer and resolver, are highly affected by the noise and not reliable. On the other hand, the sensorless method has shown results close to the theory and the Fourier analysis of the armature current. For this reason, from now, only the results obtained by the sensorless method are studied.

7.5.4 Summary

The results obtained in each case, Step, MLL, SLME, and MSLME connections with the sensorless torque measuring are shown in Figure 7.42. In red the load applied is shown, while in blue and yellow the shaft torque vibrations obtained experimentally and in theory respectively are presented. As explained in each case, the Posicast based strategies reduced the vibrations on the shaft produced by the electromechanical interaction in load connection cases.

However, due to the effect of the inductances in the step connection and the uncertainty in the frequency, some vibrations remain after the switching. In particular, due to the higher relevance of the inductance in SLME and MSLME, in these cases, the vibration reduction is lower. These strategies are more affected than MLL, due to the closeness between the steps being connected.

(a) Step

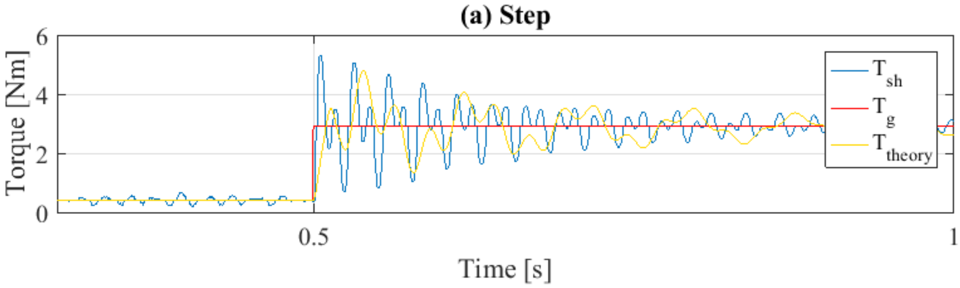

(b) MLL

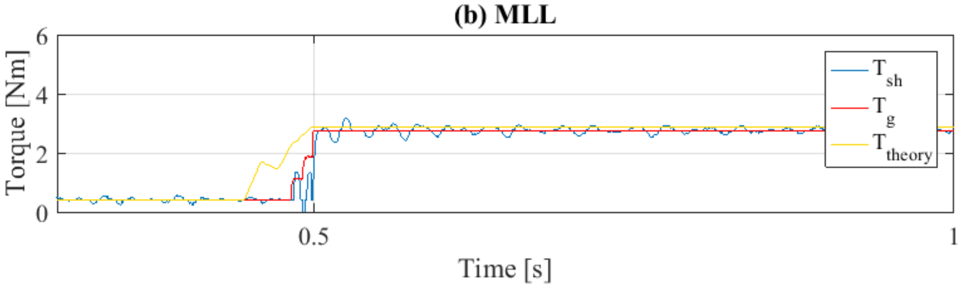

(c) SLME

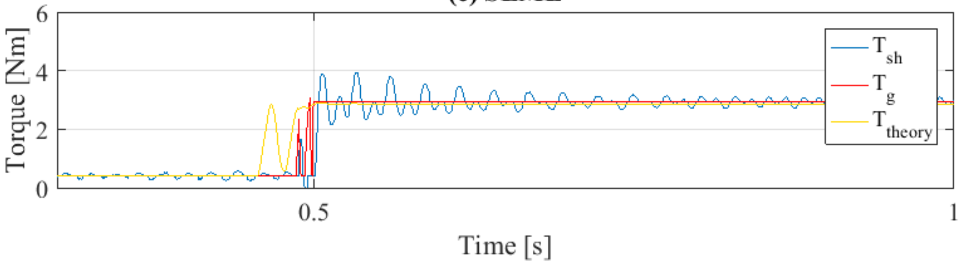

(d) MSLME

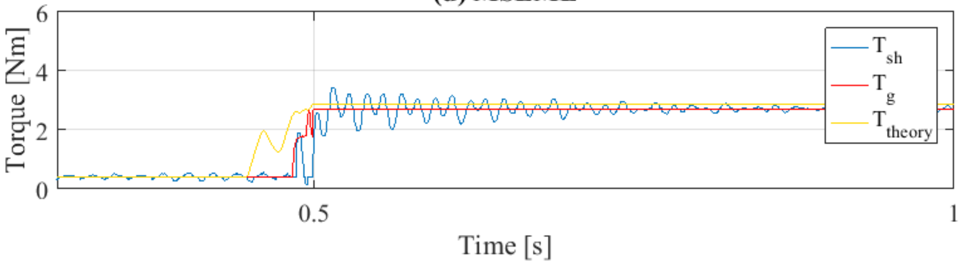

Figure 7.42: Summary PMS strategies.

Analysing the strategies in terms of the overshoot and the settling time of the transient, the same behaviour is observed. Table 7.1 shows the results. The settling time was calculated for a torque value of 5% of the steady-state value, while the overshoot was obtained with equation (4.40) presented in chapter 4. The overshoot and settling time of every strategy is lower than the one in the step connection case. Even in the SLME and MSLME cases, which are highly affected by the inductance, the performance has improved in 50%. These results show that the Posicast strategies allow the reduction of the torsional vibrations produced by the connection of electrical loads. Chapter 8, presents the robust analysis of the strategy.

Table 7.1. PMS strategies performance.

Connection	Overshoot [%]	Settling Time [s]
Step	80.85	0.64
SLME	33.90	0.44
MLL	13.63	0.39
MSLME	26.22	0.49

7.6 Summary

In this chapter, the electromechanical interaction due to electrical loads connection presented in chapter 4 has been experimentally tested. The case of a pulsating load has not been studied because as shown in chapter 4 and 5, its behaviour is equal to a step load.

The analysis of the experimental system has identified a range of frequencies close to the design ones presented in chapter 6. To find these parameters the method of Fourier analysis combined with Hilbert Transform and EMD has been used. This has allowed the verification of the designed system.

Moreover, three torque measuring methods have been compared: tachometer sensor, resolver sensor, and sensorless. The results obtained in each strategy applied have shown that the sensor-based methods are highly affected by the system noise for low power systems. The same does not happen for the sensorless strategy. A methodology to validate the experimental results using the back-EMF and resonant filter sensorless method has been presented. This method has shown results that are validated by the FFT analysis and the simulation results.

Likewise, the PMS based on the Posicast method presented in chapter 5 has been experimentally tested. The results have shown that the strategies allow the reduction of the torsional vibrations due to electrical load connections. However, due to the machine inductances and the uncertainty in the torsional frequencies values the vibrations are not completely eliminated after the load switching. Respect the first aspect; the load connections applied are not perfect steps, which reduces the efficacy of the strategies. The inductances affect mostly the SLME and MSLME due to the closeness of their pulses.

Regarding the frequency uncertainty, a range of the torsional values has been identified. Therefore, the Posicast based strategies have not been solved for the exact value. FFT post analysis shows that at the moment of the test the frequencies of the system were 35Hz and 73Hz instead of 35.5Hz and 77.1Hz. The changes in frequency may be due to movements of the gears and flywheels. This difference is responsible for the remaining vibrations.

Nonetheless, even in the connection strategies most affected by the uncertainty and inductances, the overshoot has been reduced by more than 50%. Even more, for the MLL connection, in which the effect of the inductance is lower, the overshoot has been reduced to an eighth of the step connection. For this reason, despite the uncertainties, the strategies are able to reduce of vibrations. Chapter 8 presents a robust analysis to approach the uncertainty in the system parameters and the effect of the inductance.

Chapter 8

Power Management System Robustness Analysis

8.1 Introduction

In chapter 7 the power management system (PMS) was experimentally tested. It was shown that the strategies presented in chapter 5 allow the reduction of the torsional vibrations. However, due to the uncertainty in the natural frequencies values and the presence of inductance in the system, the vibrations were not fully suppressed after the electrical load switching. Additionally, the MLL strategy proved to be more robust to uncertainty and the presence of inductances. To further analyse the sensitivity of the three methods (SLME, MLL, and MSLME), in this chapter the PMS robustness and the effect of the inductances are studied.

The rest of the chapter is organised as follow. First, the sensitivity of the system is studied, and the effects of uncertainty in frequency and damping ratio for each method are established. After, strategies to minimise the effect of the inductance in the system are studied. Later, the strategies presented are compared with alternative methods used in the literature. Finally, the summary is presented.

8.2 Sensitivity Analysis

Two approaches are taken to study the sensitivity of the system. First, experimental results obtained for the strategies with different connection values are shown. Second, a theoretical analysis of the strategies robustness for frequency and damping ratio uncertainty is carried out. Finally, a summary is presented.

8.2.1 Experimental Results

In this section, the experimental system was tested for SLME, MLL, and MSLME connections solved for three different natural frequencies and damping ratio. Three cases are compared: The first case or base case are the results presented in chapter 7 and is solved for the frequencies $f_{1B} = 35.5\text{Hz}$ and $f_{2B} = 77.1\text{Hz}$ and the respective damping ratio $\xi_{1B} = 0.018$ and $\xi_{2B} = 0.012$. The second case is solved for different natural frequencies and damping ratio than the ones used in chapter 7. This case is solved for $f_{1C} = 36.4\text{Hz}$ and $f_{2C} = 77\text{Hz}$ and the respective damping ratio $\xi_{1C} = 0.0219$ and $\xi_{2C} = 0.0096$. These frequencies are inside the frequency range defined in chapter 7 ($f_1 \in [35 - 37]\text{Hz}$ and $f_2 \in [73 - 77.1]\text{Hz}$). Lastly, the third case, consists in solving the strategies for one natural frequency instead of two. The natural frequency and damping ratio used, corresponds to the lower natural frequency of the base case $f_{1B} = 35.5\text{Hz}$ and $\xi_{1B} = 0.018$, omitting the value of f_{2B} and ξ_{2B}. The results obtained by each strategy and case are compared in terms of overshoot and settling time. The connection times and step values of each case studied are shown in Table 8.1.

Table 8.1: Connection times.

Case	SLME		MLL		MSLME	
	Time [ms]	Step Size	Time [ms]	Step Size	Time [ms]	Step Size
f_{1B} f_{2B}	$T_1 = 0$ $T_2 = 2.5$ $T_3 = 6.7$ $T_4 = 11.1$ $T_5 = 13.4$	$p_1 = 1$ $p_2 = -1$ $p_3 = 1$ $p_4 = -1$ $p_5 = 1$	$T_1 = 0$ $T_2 = 8.9$ $T_3 = 17.7$	$p_1 = 0.37$ $p_2 = 0.29$ $p_3 = 0.33$	$T_1 = 0$ $T_2 = 10.7$ $T_3 = 13.2$ $T_4 = 16.3$	$p_1 = 0.40$ $p_2 = 0.60$ $p_3 = -0.60$ $p_4 = 0.60$
f_{1C} f_{2C}	$T_1 = 0$ $T_2 = 2.4$ $T_3 = 6.6$ $T_4 = 11.1$ $T_5 = 13.3$	$p_1 = 1$ $p_2 = -1$ $p_3 = 1$ $p_4 = -1$ $p_5 = 1$	$T_1 = 0$ $T_2 = 8.8$ $T_3 = 17.6$	$p_1 = 0.37$ $p_2 = 0.29$ $p_3 = 0.33$	$T_1 = 0$ $T_2 = 10.5$ $T_3 = 13.2$ $T_4 = 16.2$	$p_1 = 0.39$ $p_2 = 0.61$ $p_3 = -0.61$ $p_4 = 0.61$
f_{1B}	$T_1 = 0$ $T_2 = 4.8$ $T_3 = 9.4$	$p_1 = 1$ $p_2 = -1$ $p_3 = 1$	$T_1 = 0$ $T_2 = 14.1$	$p_1 = 0.51$ $p_2 = 0.49$	$T_1 = 0$ $T_2 = 14.1$	$p_1 = 0.51$ $p_2 = 0.49$

The base case results obtained in chapter 7 are shown in blue in Figure 8.1, while the results of the case f_{1C} and f_{2C} are shown in yellow. Comparing with the base case, the vibrations obtained for f_{1C} and f_{2C} are slightly higher: The overshoot increases from 33.9% to 38.37% in the SLME connection, from 13.63% to 16.15% in the MLL, and from 26.22% to 27.01% in the MSLME. Instead, the settling times are similar. Since the variations of natural frequency and damping ratio are small, it was expectable to obtain similar results. Moreover, because the vibrations are lower for the base case $f_{1B} = 35.5\text{Hz}$ and $f_{2B} = 77.1\text{Hz}$ these frequencies are closer to the real value of the system.

(a) Step

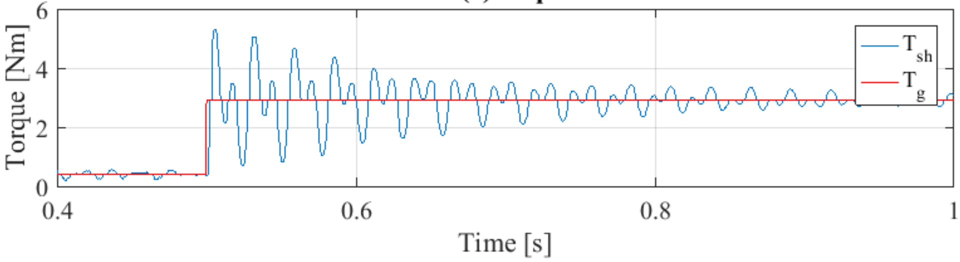

(b) MLL

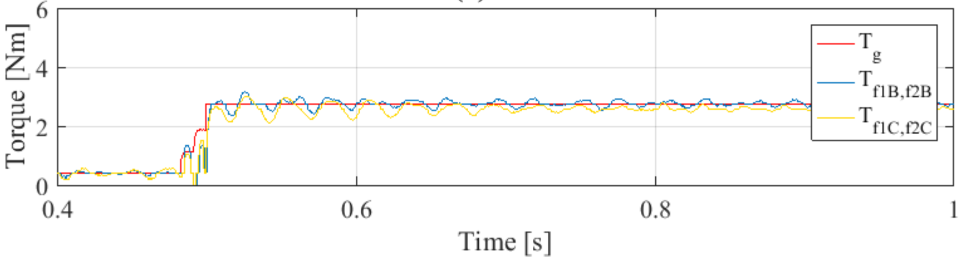

(c) SLME

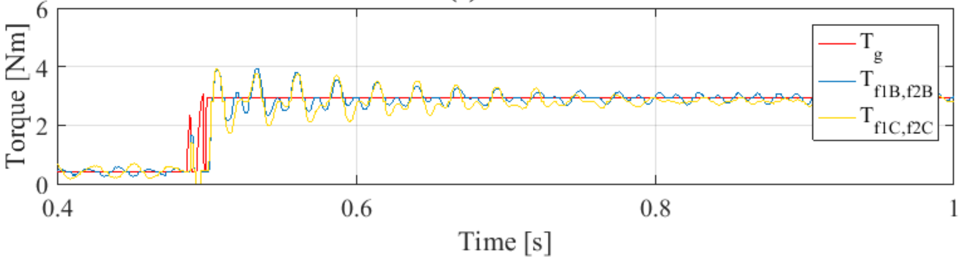

(d) MSLME

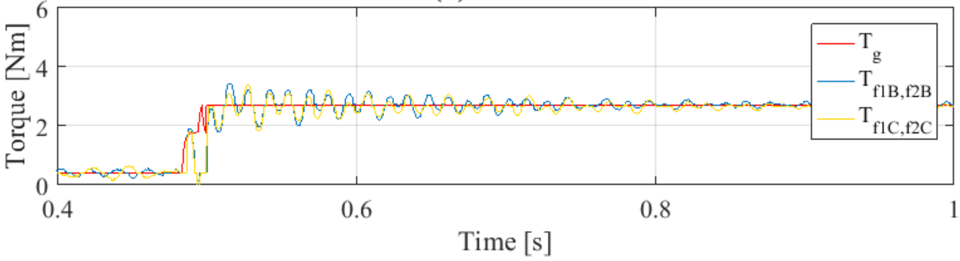

Figure 8.1: Torque with different natural frequencies.

To study the importance of the proper identification of the number of torsional frequencies, Figure 8.2, shows in yellow the results obtained when the system is solved for one natural frequency f_{1B}. In blue, the base case is shown. The results show that in every strategy the vibrations are higher than for the base case. However, plot (b) and (d), shows that despite the omission, the strategies MLL and MSLME reduce the vibrations in comparison to the step connection. On the other hand, the SLME strategies increases the torsional vibrations on the system. This result shows that SLME is more susceptible to changes and the importance of studying the system in which the strategies are being applied to not obtain higher vibrations.

(a) Step

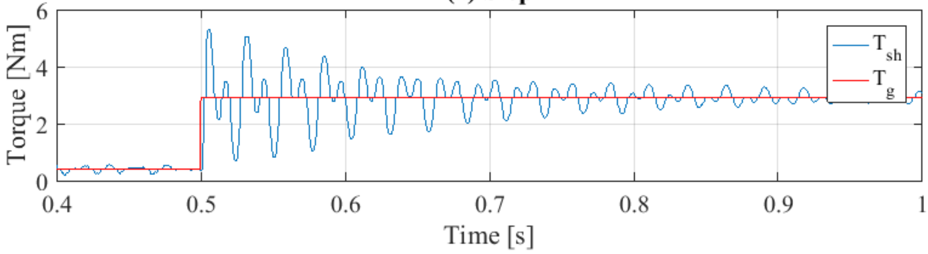

(b) MLL

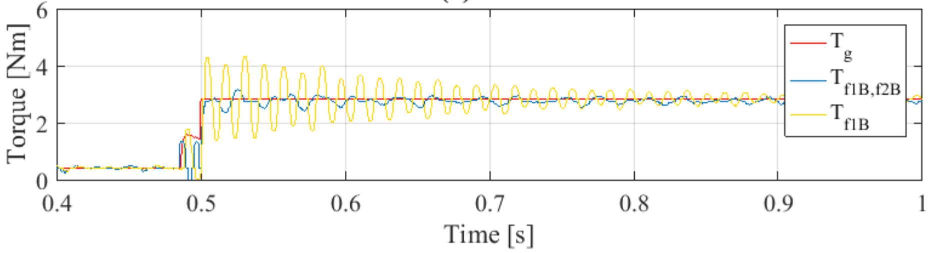

(c) SLME

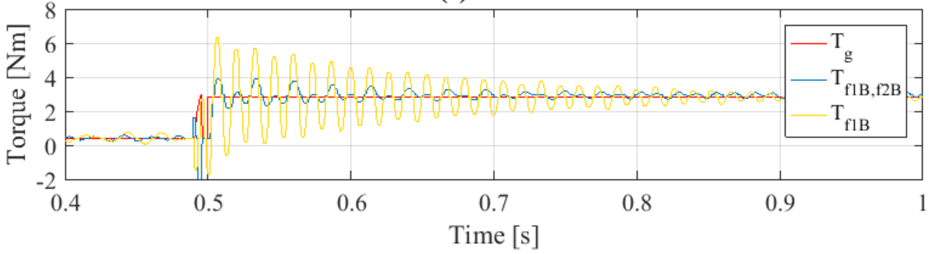

(d) MSLME

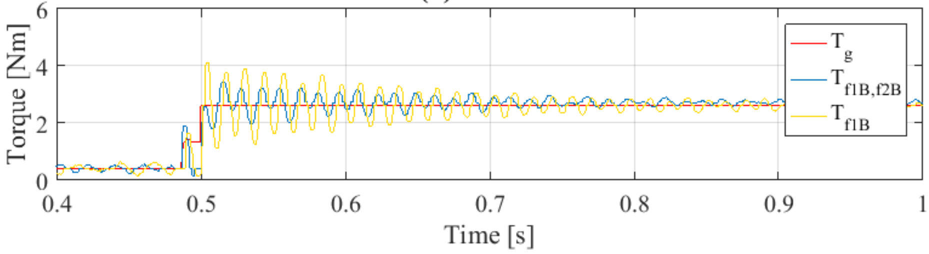

Figure 8.2: Torque with 1 natural frequency.

A comparison of the results obtained by the three strategies solved for the different frequencies is presented in Table 7.1. As observed in Figure 8.1 and Figure 8.2, the higher overshoot of the torsional vibrations is obtained for the load connection SLME f_{1B}, while the lower is obtained for MLL f_{1B}, f_{2B}. Moreover, the overshoot obtained by each strategy when the system is solved for the frequencies f_{1C} and f_{2C} are only slightly higher than for the base case. In terms of settling time, the results are equivalent: Higher settling times are obtained for f_{1B}, while f_{1C} and f_{2C} only increases slightly the settling time compare to f_{1B} and f_{2B}.

Table 8.2. PMS strategies performance.

Strategy	Frequencies	Overshoot [%]	Settling Time [s]
Step	-	80.85	0.643
SLME	f_{1B} f_{2B}	33.90	0.44
SLME	f_{1C} f_{2C}	38.37	0.571
SLME	f_{1B}	130.90	0.636
MLL	f_{1B} f_{2B}	13.63	0.39
MLL	f_{1C} f_{2C}	16.15	0.39
MLL	f_{1B}	51.99	0.44
MSLME	f_{1B} f_{2B}	26.22	0.48
MSLME	f_{1C} f_{2C}	27.01	0.50
MSLME	f_{1B}	56.84	0.43

In this section, the PMS strategies have been solved for different values of frequency and damping ratio. It has been shown that small variations in frequency and damping ratio can increase the torsional vibrations slightly. However, the use of only one of the natural frequencies of the system produces higher vibrations, which can be higher than the ones obtained in the step connection. For this reason, the identification of the number of the torsional frequencies and their value is significant. To determine the ranges of frequencies and damping ratio uncertainty, in which the strategies are beneficial to the system, a theoretical sensibility analysis is presented next.

8.2.2 Operation Limits

To establish the operating limits at which the Posicast strategies are beneficial for the system in the study, a theoretical sensitivity analysis is carried out. The study analyses the step response of the experimental system transfer function using the Matlab function "*stepinfo*". The transfer function of the experimental system is obtained in the same manner than in chapter 5: The transfer function of the state system is found using the Matlab command "*ss2tf*". Then the load connection, written in the Laplace domain, is modelled using the Padé approximation.

For the step connection, the settling time for a 5% of the steady-state value is $t_s = 0.56\text{s}$ and the overshoot is 79.7%. These values are close to the ones obtained experimentally (80.85% of overshoot and $t_s = 0.643\text{s}$) and presented in last section. Therefore, the theoretical analysis is representative of the system.

Now, to test the sensitivity to frequency and damping ratio variations, the step response of the system is calculated for the SLME, MLL, and MSLME strategies solved with different frequencies and damping ratio values. Figure 8.3 shows the results obtained when the frequency f_1 is different from the real values, while keeping ξ_1, f_2 and ξ_2 constant. In (a) and (b) the settling time and overshoot are shown. In each plot, the response of the SLME strategy is presented in blue, MLL in red, and MSLME in black.

The strategies were tested for frequency values from 10% of f_1 to 200% of it. From (b) it is observed that under-measuring the frequency produces higher vibrations than detecting a value higher than the real one. In terms of settling time, the same behaviour is obtained, but the differences are smaller. Moreover, any value of frequency higher than the real one (in the range of up to 200%), allows the reduction of the vibrations comparing to the step case. This makes the strategies good for the system even if the value of the frequency is not known exactly. Even more, in a range of $\pm 5\text{Hz}$, like the one obtained for the experimental system in chapter 7, the overshoot increase is small. This confirms, that most of the vibrations obtained in last section and chapter 7 are due to the presence of inductances and not the uncertainty in the frequency value. If the behaviour of the three strategies is compared, the experimental results are confirmed. SLME is less robust to frequency variations than MLL and MSLME, with MLL the most. This confirms the experimental results in which the MLL method generated a lower overshoot.

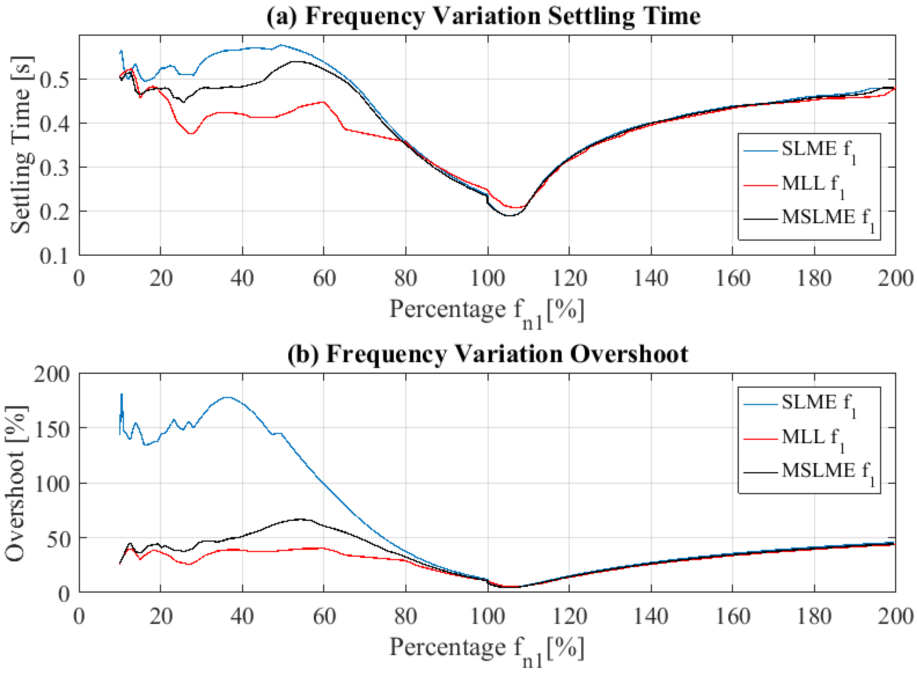

Figure 8.3: Sensitivity to changes in f_1.

A clearer view of the sensibility of the SLME strategy is shown in Figure 8.4. In it, the shaft torque obtained for a step connection and the SLME strategy solved for different values of frequency f_1 is presented. As shown before, it is clear that the use of higher frequencies affects less the system than the use of lower ones.

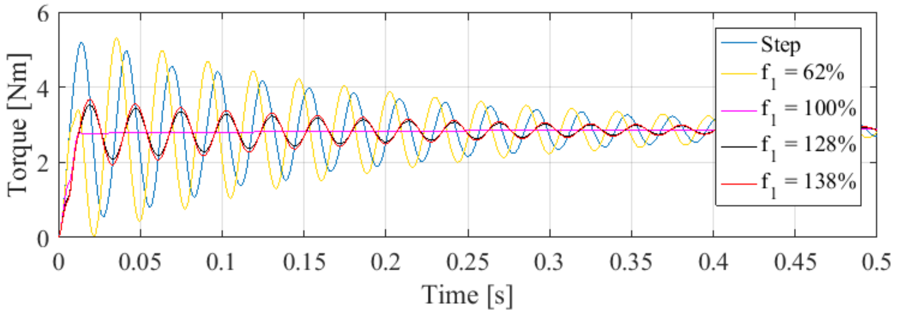

Figure 8.4: SLME response sensitivity in f_1.

The sensitivity of the system to changes in ξ_1, while keeping f_1, f_2, and ξ_2 is shown in Figure 8.5. The system was tested for damping ratios between 0 and 1, which are logarithmically distributed. In (b) it is observed that for ξ_1 values below 0.04

the overshoot is zero. For the same range, in (a) it is seen that the settling time remains below 0.1s, though the time increases for damping ratio different than the one associated with the system. Since the damping ratio of the system is inside this range, it is consider that the damping ratio does not affect the Posicast strategies in study. The same is shown in Figure 8.6, in which the effect of solving the SLME strategy for different damping is shown. Damping below 0.05 produce no difference, while damping below 0.1 produce only small vibrations.

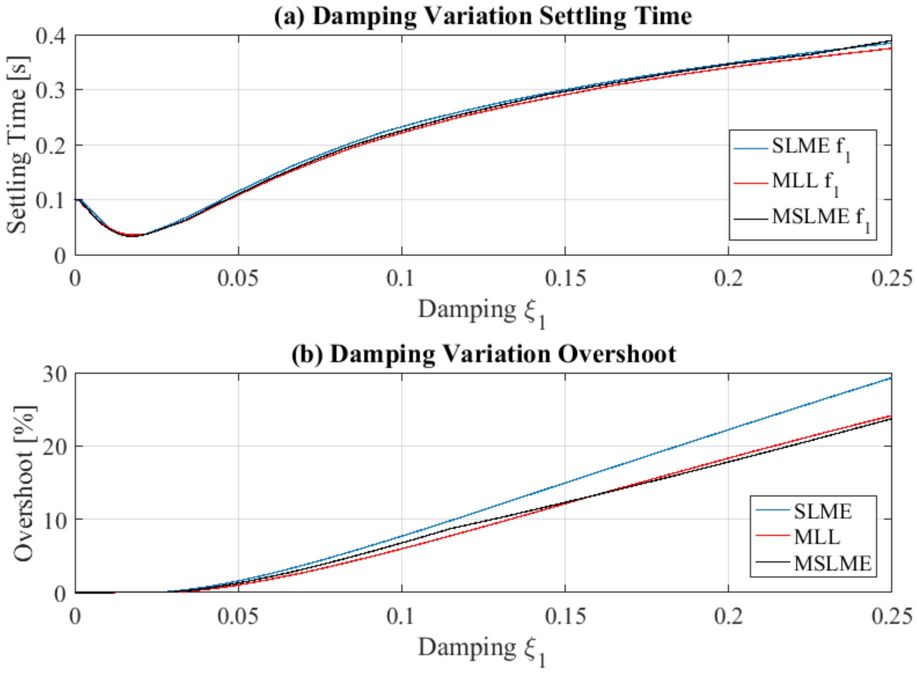

Figure 8.5: Sensitivity to changes in ξ_1.

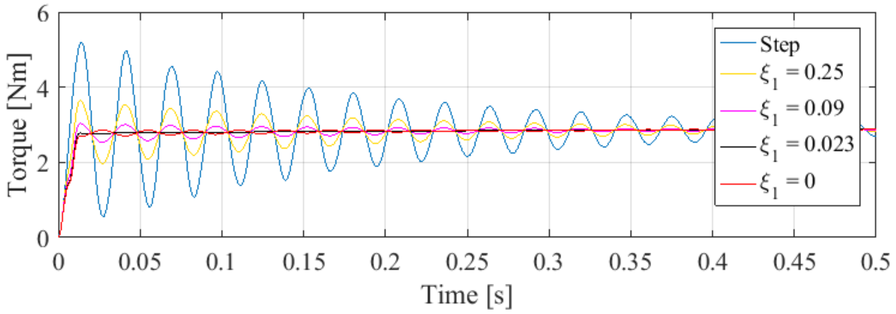

Figure 8.6: SLME response sensitivity in ξ_1.

Examining the robustness of the methods to variation in f_2, while keeping f_1, ξ_1, and ξ_2 constant, Figure 8.7 is obtained. The results are equivalent in terms of strategy robustness to the ones obtained for changes in f_1. SLME is more affected by the uncertainty in frequency, followed by MSLME, and finally by MLL. However, the variations of the frequency used in the strategy generate lower overshoot and settling times than the equivalent cases for f_1. Moreover, SLME is the only strategy that produces overshoots higher than 10%, and merely for frequencies equivalent to 10% of f_2. This behaviour implies that the Posicast strategies are more robust to the secondary or tertiary frequencies of the system, making the identification of the first frequency fundamental. The torque vibrations obtained solving the SLME for different values of f_2 are shown in Figure 8.8. It is clear that the system is robust respect this variable.

(a) Frequency Variation Settling Time

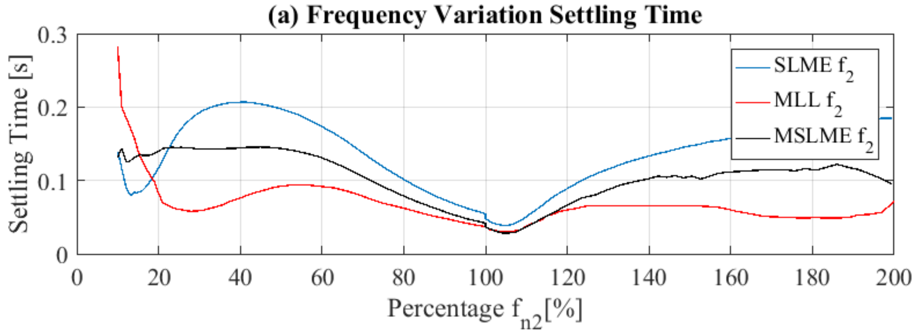

(b) Frequency Variation Overshoot

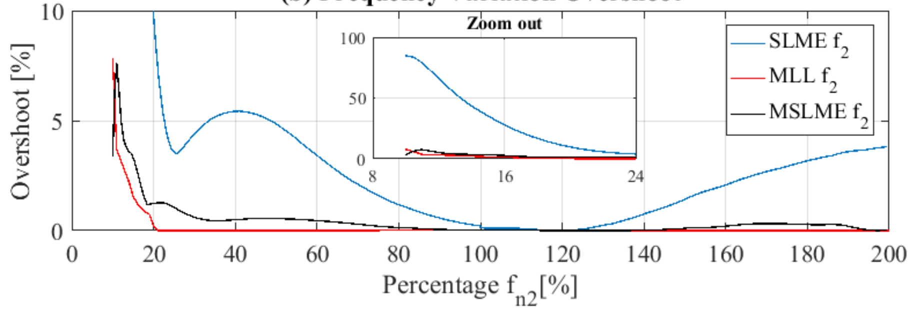

Figure 8.7: Sensitivity to changes in f_2.

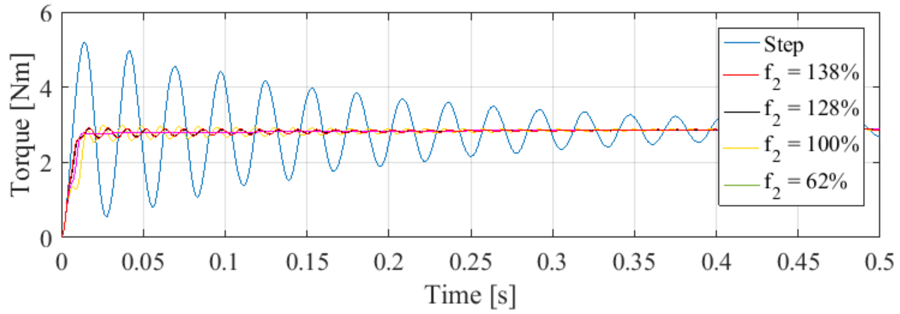

Figure 8.8: SLME response sensitivity in f_2.

The robustness of the strategies to variations in the damping ratio ξ_2, while keeping the frequencies and the damping ratio ξ_1 constant, is shown in Figure 8.9. It is observed that for damping ratio values below 0.1, the overshoot is 0.1%, while the settling time remains constant for values below 0.04. This shows that as in the case of variations in ξ_1, the strategies are robust to changes in the damping ratio of the second natural frequency. The same is shown in Figure 8.10, where the vibrations obtained when solving the SLME strategy for different values of ξ_2 are presented. Therefore, the studies must be focused in the frequency identification and not in the identification of the damping ratio.

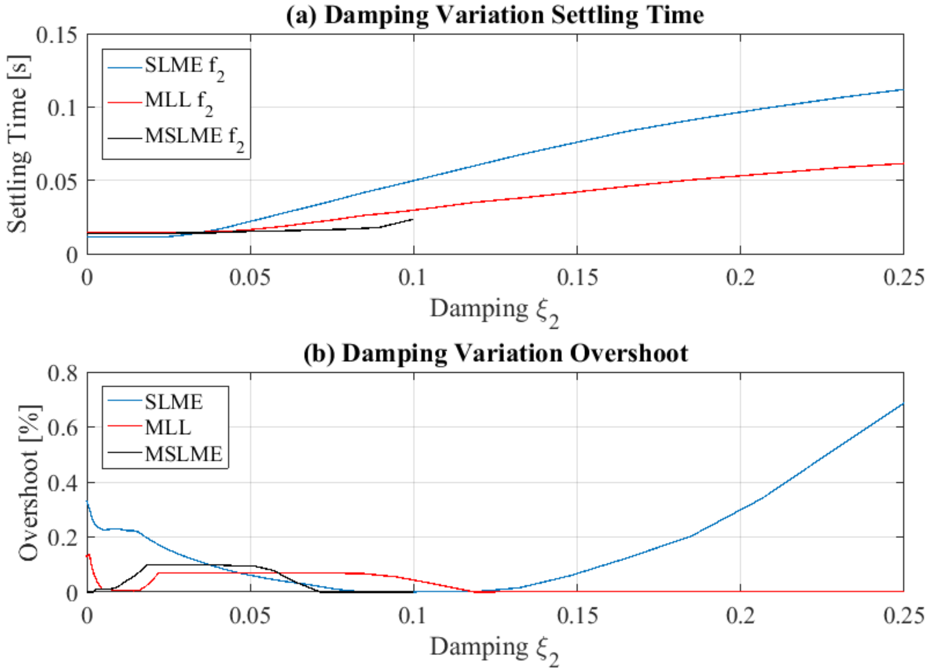

Figure 8.9: Sensitivity to changes in ξ_2.

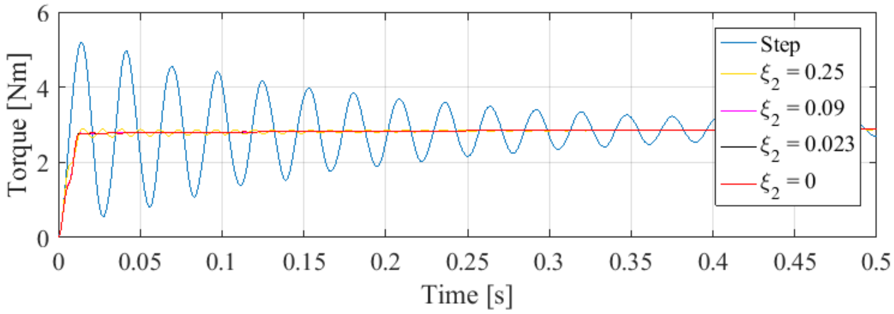

Figure 8.10: SLME response sensitivity in ξ_2.

The robustness of the strategies for errors in the identification of f_1 and ξ_1, while f_2 has been omitted are shown in Figure 8.13 and Figure 8.11 respectively. Since the system is solved for one frequency, the results obtained by MLL and MSLME are the same, as it was explained in chapter 5.

In terms of damping ratio, the results obtained in Figure 8.11 are equivalent to the ones obtained in the other cases. This shows, again, that the damping ratio identification is not as important as the frequency identification. Figure 8.12 shows the torque vibrations obtained for different values of damping.

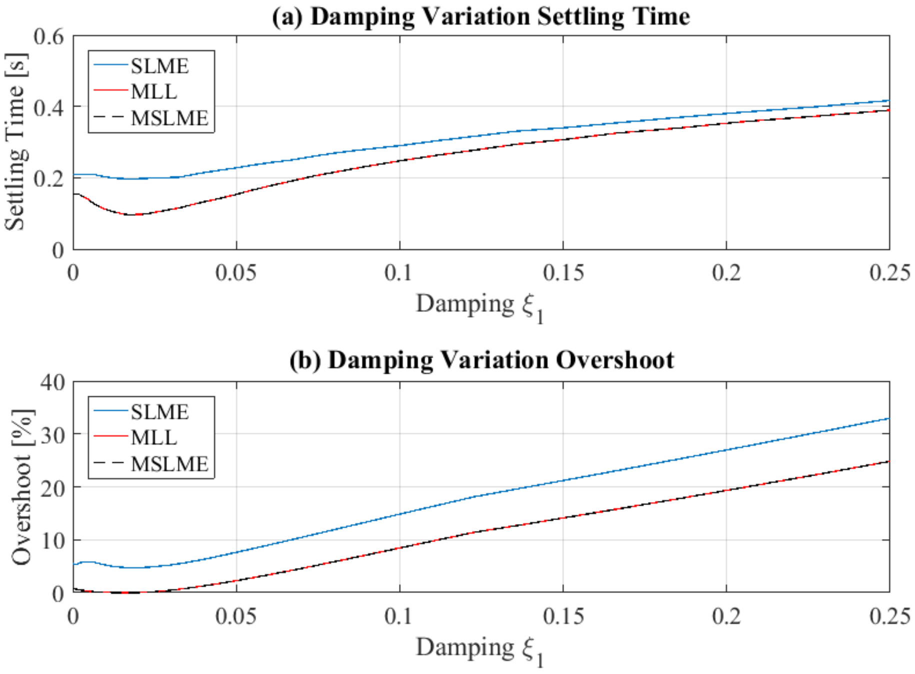

Figure 8.11: Sensitivity to changes in ξ_1 and missing one frequency.

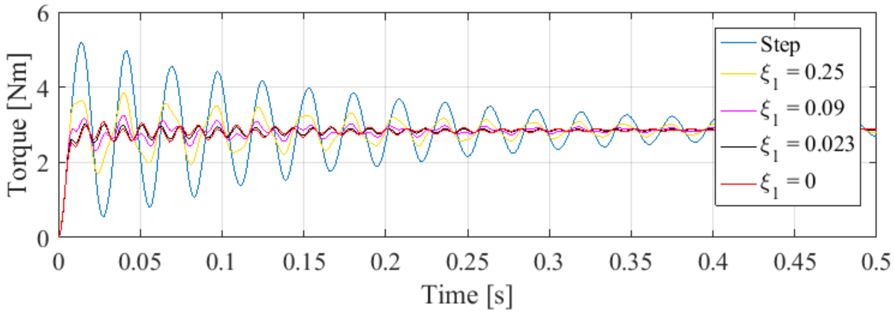

Figure 8.12: SLME response sensitivity in ξ_1 and missing one frequency.

On the other hand, regarding the frequency, as expected from the experimental results shown in section 8.2.1, the overshoot of the system is higher when one frequency is missing, especially for the SLME connection. In the experimental SLME solved for one frequency, the overshoot was 130%, which is higher than the 80% obtained for the step connection. Comparing with the results of Figure 8.13(b), SLME has 130% of overshoot when the system has been solved for a frequency equal to 50% of the real value. The same is observed from Figure 8.14 where the torque obtained after applying the SLME solved for different values of f_1 is shown. Since the frequencies of the experimental system have a ±2Hz of uncertainty, the higher overshoot obtained experimentally is associated with the presence of inductances. For this reason, in section 8.3, strategies that include the inductances are presented.

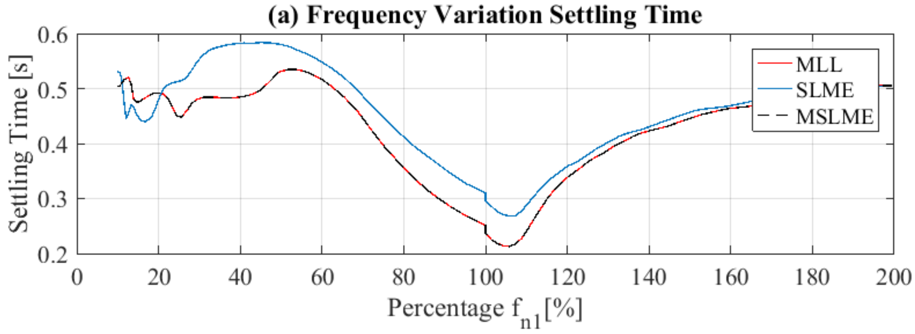
(a) Frequency Variation Settling Time

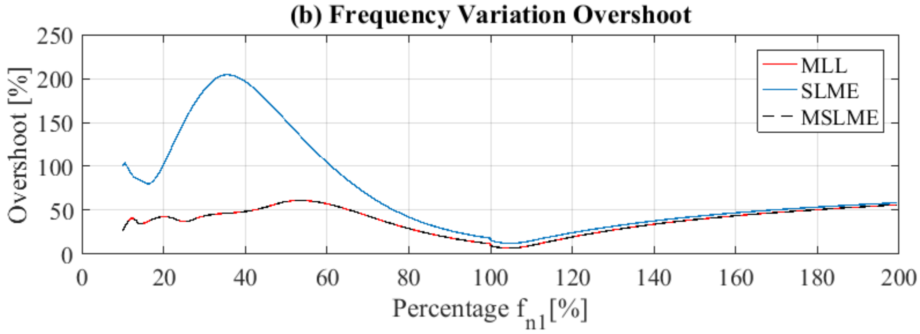
(b) Frequency Variation Overshoot

Figure 8.13: Sensitivity to changes in f_1 missing one frequency.

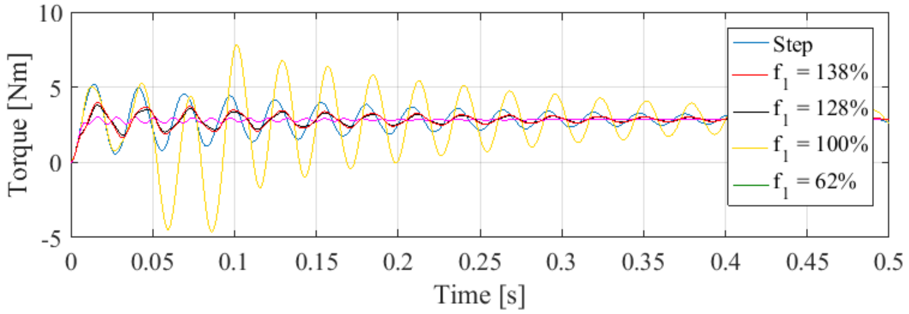

Figure 8.14: SLME response sensitivity in f_1 and missing one frequency.

8.2.3 Summary

In this section, the robustness of the Posicast based methods has been studied. From the experimental and theoretical results, it has been obtained that the strategy SLME is less robust than MLL and MSLME. This behaviour is associated with the longer time of the MLL and MSLME switching. Moreover, it was shown that the system is robust to damping ratio below 0.05, which is an acceptable value for the system in the study. Likewise, the frequency can have an uncertainty of ± 5 Hz and produce vibrations close to zero. Again, since the uncertainty of the experimental data is ± 2Hz, the robustness of the method is acceptable. Also, for higher variations in frequency, the strategies MLL and MSLME always produce better or equal results than the step connection, making the strategies right to apply also in systems with uncertainty. In the case of the SLME connection, high-frequency uncertainty can produce higher vibration than the step connection, which was shown experimentally.

Additionally, the effect of the inductances is higher in the SLME case, since the connection can not be completed before the next step is applied. For this reason, in next section strategies to minimise the effect of the inductances are presented.

8.3 Electrical Load with Inductance

In chapter 7 was shown that the experimental system has inductances, which produce a delay in the load connection. Since the strategies presented in chapter 5 are designed to eliminate the vibrations by the application of perfect steps, when there is inductance in the system some vibrations remain, as was shown in chapter 7. For this reason, in this section, modified Posicast strategies that include the inductances in the system are introduced. The analysis is carried out for the SLME strategy since the effect of the inductance is higher in this method. The methodology for MLL and MSLME is equivalent.

The study is carried out using the simulation system presented in chapter 4, in which the value of L_a is 0.019H. Figure 5.9 shows the results obtained when a step connection and the SLME connection presented in chapter 5 are applied to the system. In red the electrical torque applied over the drivetrain is shown, in blue the shaft response is depicted, and in black, the desired rectangular step is presented. It is observed that now the steps applied are not rectangular and that the SLME strategy does not eliminate the vibrations but reduced them. Moreover, the delay in the step does not allow the connection of the whole switching event in the SLME strategy before the next step has been applied. Therefore, the time delay should be at least smaller than the time between steps connections. This problem is accentuated for systems with higher frequencies in which the steps are closer in time. The results for the two inertia system used to analyse the strategies in chapter 5 are equivalent and shown in Figure 8.16.

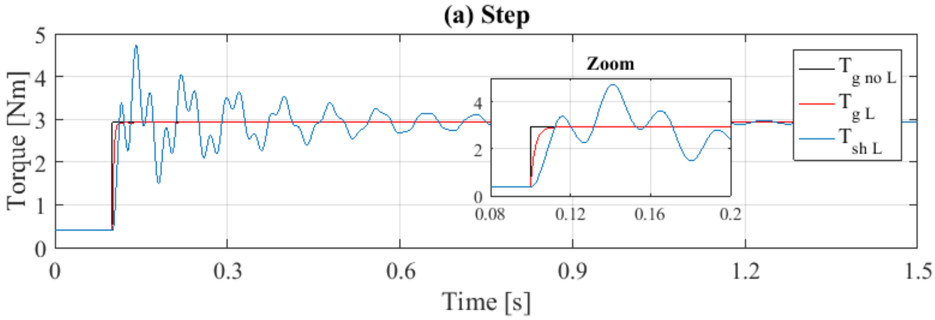

(b) SLME

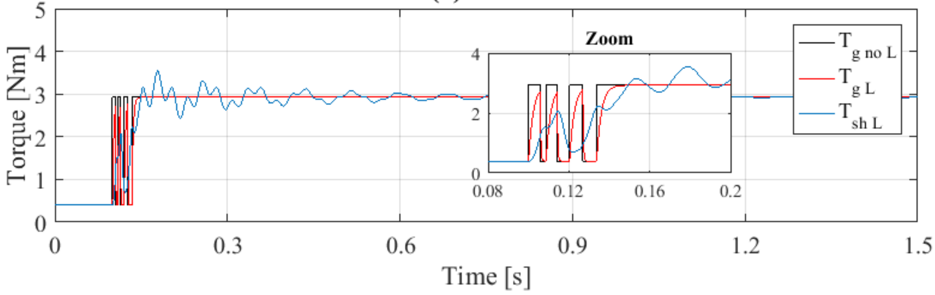

Figure 8.15: Torque shaft response with Step and SLME.

(a) Step

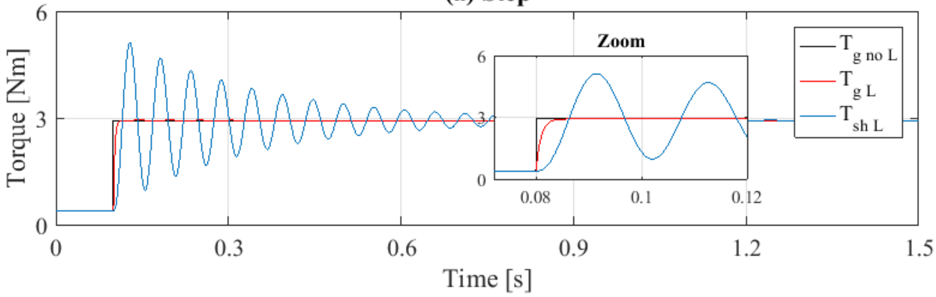

(b) SLME

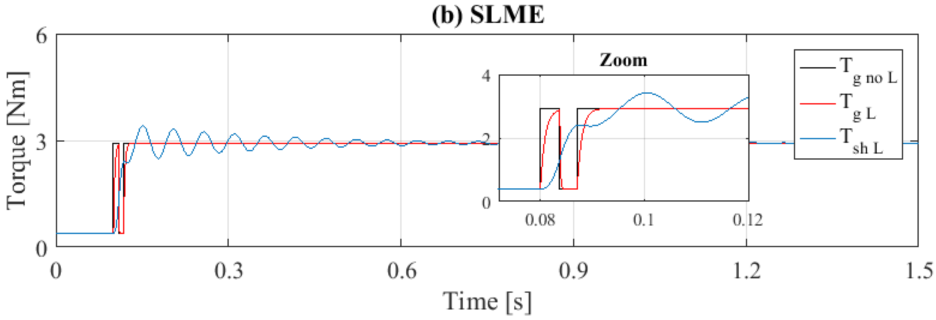

Figure 8.16: Torque shaft response in a 2 inertia system with Step and SLME.

The delay of the system is given by equation (8.1) in which L is the inductance and R is the resistance. Replacing the armature inductance $L_a = 0.019\text{H}$ and the resistances connected to the system $R_{eq1} = 4.55\Omega$ when the electrical load is connected, and $R_{eq2} = 60.5\Omega$ when the electrical load is disconnected, the delays are:

- $\tau_1 = 4.1\text{ms}$
- $\tau_2 = 0.3\text{ms}$

The same results can be obtained from Figure 5.9 (b).

$$\tau = \frac{L}{R} \tag{8.1}$$

Next, three methodologies to minimise the effect of the inductance in the Posicast strategies are presented. First the time constant value is studied, second, the delay of the connection is included in the SLME solver, and thirdly, the real step is modelled in the SLME solver.

8.3.1 Change of Time Constant

The most straightforward strategy to minimise the effect of the inductance is to reduce the time delay in the system. In equation (8.1) was shown that the delay in the step connection depends on the inductance and the resistance. Therefore, for systems in which the inductance is fixed, working with high resistances which can reduce the delay in the connection considerably, allows the elimination of the vibrations.

However, this method is not feasible for every system. For example, in the experimental setup, the resistances needed to reduce the time delay would not allow the analysis of the electromechanical interaction, since the load connected would be too small. Therefore, two strategies that include the delay in the solver are studied next.

8.3.2 Delay SLME

A solution to decrease the effect of the delay in the step connection due to the inductances in the electrical system is its inclusion in the solver. For this reason, in the equations presented in chapter 5 to solve the SLME connection, the term T_k is replaced by $(T_k + \tau_k)$ as shown in the equation system (5.20). τ_k represents the delay for the kth step. For the SLME connection in study, $\tau_k = \tau_1$ for odd connections and $\tau_k = \tau_2$ for even connections. Moreover, as presented in chapter 5, $p_k = (-1)^{k+1}$. This method is applied in the same manner to the strategies MLL and MSLME.

$$\begin{bmatrix} \sum_{k=1}^{m} p_k e^{-\xi_1 \omega_{n1}(T_k+\tau_k)} \cos\big(\omega_{d1}(T_k+\tau_k)\big) \\ \sum_{k=1}^{m} p_k e^{-\xi_1 \omega_{n1}(T_k+\tau_k)} \sin\big(\omega_{d1}(T_k+\tau_k)\big) \\ \sum_{k=1}^{m} p_k e^{-\xi_2 \omega_{n2}(T_k+\tau_k)} \cos\big(\omega_{d2}(T_k+\tau_k)\big) \\ \sum_{k=1}^{m} p_k e^{-\xi_2 \omega_{n2}(T_k+\tau_k)} \sin\big(\omega_{d2}(T_k+\tau_k)\big) \\ \vdots \\ \sum_{k=1}^{m} p_k e^{-\xi_n \omega_{nn}(T_k+\tau_k)} \cos\big(\omega_{dn}(T_k+\tau_k)\big) \\ \sum_{k=1}^{m} p_k e^{-\xi_n \omega_{nn}(T_k+\tau_k)} \sin\big(\omega_{dn}(T_k+\tau_k)\big) \end{bmatrix} = 0 \tag{8.2}$$

Following the steps of chapter 5, first the solutions for the 2 inertia system with one natural frequency $f_{n1} = 19.09\text{Hz}$ and $\xi_1 = 0.0327$ are presented. Solving the system with the time delays τ_1 and τ_2 calculated before, the times of the step connections are $T_1 = 0\text{ms}$, $T_2 = 11.4\text{ms}$, $T_3 = 17.7\text{ms}$. The load connected is the same that has been used in the other cases, from 0.3952Nm to 2.9282Nm, corresponding to the connection of a resistance of 5Ω. The simulation results are shown in Figure 8.17. It is observed that the vibrations have been almost completely eliminated, showing that the strategy works.

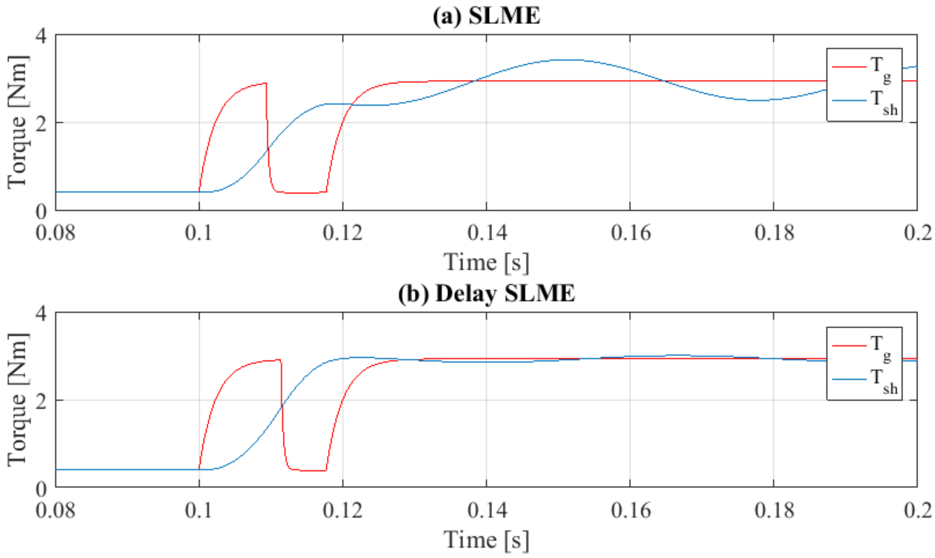

Figure 8.17: Torque shaft response in a 2 inertia system for delay SLME.

Now, the system is solved for the 3 natural frequency system in the study. The parameters were presented in chapter 4 and used in chapter 5 ($f_1 = 11.9443$Hz, $\xi_1 = 0.0362$, $f_2 = 38.5982$Hz, $\xi_2 = 0.0276$, $f_3 = 109.7207$Hz, $\xi_3 = 0.0774$). The time delays are $\tau_1 = 4.1$ms and $\tau_2 = 0.3$ms. The connection times and step values are:

- $T_1 = 0$ms and $p_1 = 1$.
- $T_2 = 7.7578$ms and $p_2 = -1$.
- $T_3 = 8.6957$ms and $p_3 = 1$.
- $T_4 = 16.1720$ms and $p_4 = -1$.
- $T_5 = 20.3030$ms and $p_5 = 1$.
- $T_6 = 28.5560$ms and $p_6 = -1$.
- $T_7 = 33.7590$ms and $p_7 = 1$.

The results obtained are shown in Figure 8.18. It is observed, that like for the two inertia system, comparing with the normal SLME case in (a), the vibrations have been reduced almost to zero.

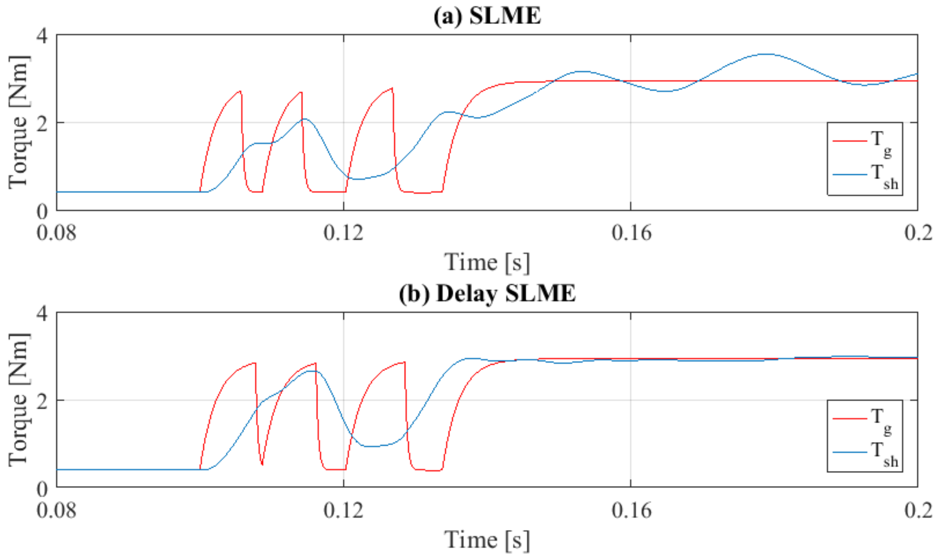

Figure 8.18: Torque shaft response for delay SLME.

To further study strategies that allow the elimination of the torsional vibrations after the switching event in systems with inductances, next section presents an Exponential SLME strategy.

8.3.3 Exponential SLME

It has been presented that including the delay in the solver allows further reductions of the vibrations when the system has inductances. In this section, another strategy to achieve the same aim is presented.

The exponential SLME consists in modelling the real step connection in the equation system that allows the elimination of the vibration after the switching connection. For this reason, the load connection p_k is modelled as a series of infinite steps in time $p_{kt}(t_p)$ as shown in equation (8.3). The value of each step is given by equation (8.4), in which t_p is the time of the step, τ_k is the delay produced by the inductance, $p_{k(t-1)}$ is the value of the step in the previous instant, and T_K is the connection time of each exponential step. By subtracting $p_{k(t-1)}$, the equation system takes into account that the step connection may not have finished before the next step is applied. Replacing into the standard SLME equation, the equation system to solve is given by (8.5).

$$p_k = \sum_{t_p=0}^{T_{k+1}} p_{kt}(t_p) \tag{8.3}$$

$$p_{kt} = (-1)^k + (-1)^{k+1} e^{-\frac{t_p}{\tau_k}} - p_{k(t-1)} \tag{8.4}$$

$$\begin{bmatrix} \sum_{k=1}^{m} \sum_{t_p=0}^{T_{k+1}} p_{kt} e^{-\xi_1 \omega_{n1}(T_k+t_p)} \cos\left(\omega_{d1}(T_k+t_p)\right) \\ \sum_{k=1}^{m} \sum_{t_p=0}^{T_{k+1}} p_{kt} e^{-\xi_1 \omega_{n1}(T_k+t_p)} \sin\left(\omega_{d1}(T_k+t_p)\right) \\ \sum_{k=1}^{m} \sum_{t_p=0}^{T_{k+1}} p_{kt} e^{-\xi_2 \omega_{n2}(T_k+t_p)} \cos\left(\omega_{d2}(T_k+t_p)\right) \\ \sum_{k=1}^{m} \sum_{t_p=0}^{T_{k+1}} p_{kt} e^{-\xi_2 \omega_{n2}(T_k+t_p)} \sin\left(\omega_{d2}(T_k+t_p)\right) \\ \vdots \\ \sum_{k=1}^{m} \sum_{t_p=0}^{T_{k+1}} p_{kt} e^{-\xi_n \omega_{nn}(T_k+t_p)} \cos\left(\omega_{dn}(T_k+t_p)\right) \\ \sum_{k=1}^{m} \sum_{t_p=0}^{T_{k+1}} p_{kt} e^{-\xi_n \omega_{nn}(T_k+t_p)} \sin\left(\omega_{dn}(T_k+t_p)\right) \end{bmatrix} = 0 \tag{8.5}$$

Solving the equation system for the one natural frequency system used in the other cases (with $n = 1$ and $m = 3$), Figure 8.19 is obtained. The times of the connections are: $T_1 = 0\text{ms}$, $T_1 = 11.0\text{ms}$ and $T_3 = 17.3\text{ms}$. Comparing to the results given by the methods SLME and Delay SLME, the vibrations have been completely eliminated after the switching load connection. This shows that the modelling of the load connections as a series of steps allows the elimination of the vibrations.

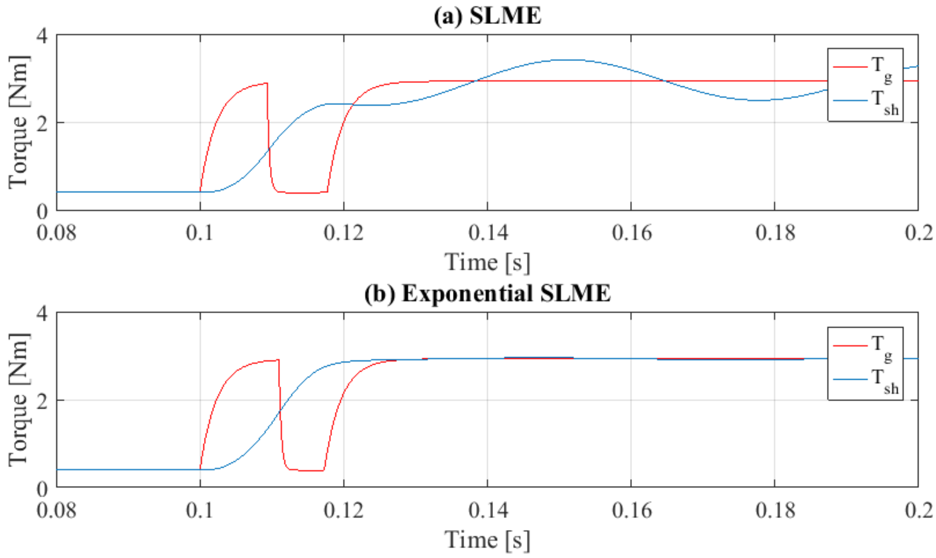
(a) SLME

(b) Exponential SLME

Figure 8.19: Torque shaft response in a 2 inertia system for exponential SLME.

Solving the equations for the 3 natural frequencies system in the study, with $n = 3$ and $m = 7$, the following connection times are obtained:

- $T_1 = 0\text{ms}$ and $p_1 = 1$.
- $T_2 = 7.4696\text{ms}$ and $p_2 = -1$.
- $T_3 = 13.8950\text{ms}$ and $p_3 = 1$.
- $T_4 = 23.2620\text{ms}$ and $p_4 = -1$.
- $T_5 = 30.3730\text{ms}$ and $p_5 = 1$.
- $T_6 = 40.4690\text{ms}$ and $p_6 = -1$.
- $T_7 = 41.5040\text{ms}$ and $p_7 = 1$.

Figure 8.20 shows the torque obtained when the same load connection of the past cases is applied. Contrary to what was expected, the remaining vibrations are slightly higher than the ones obtained by the Delay SLME strategy. This behaviour is due to solver inaccuracies since the system is more complicated than the one from the past cases. Since the addition of infinite steps adds a new level of difficulty to the solver, the accuracy required to obtain the result has to be decreased. This was not a problem for the one natural frequency system since the solution was obtained graphically, through the sine and cosine residual curves.

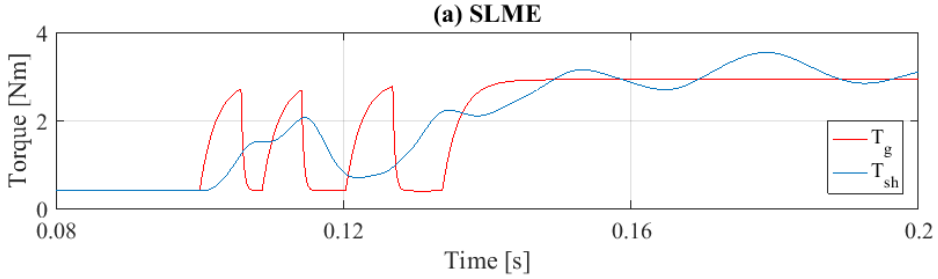
(a) SLME

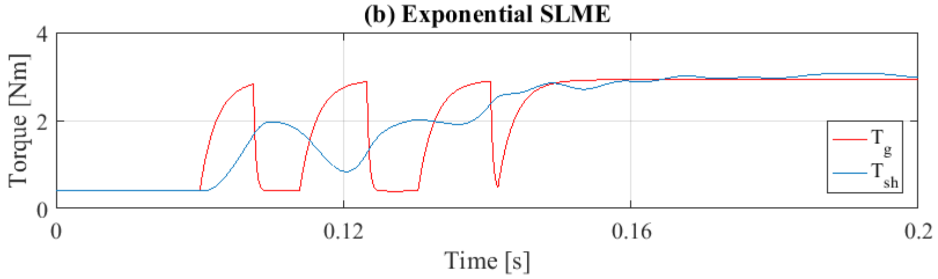
(b) Exponential SLME

Figure 8.20: Torque shaft response for exponential SLME.

Therefore, the exponential SLME allows the elimination of the torsional vibrations in systems with inductances, but the complexity of the equation system implies that new solver strategies must be used. Next, the advantages and disadvantages of each method are discussed.

8.3.4 Summary

In this section strategies that take into account the effect of the inductance in the system were presented. Now, comparisons between the SLME, Delay SLME, and Exponential SLME methods are discussed. The change in the time constant by increasing the resistance is not further analysed since its application is not applied to the system in the study.

To compare the strategies, first, the sine and cosine residual curves for the 2 inertia system are presented in Figure 8.21. The curves, like in chapter 5, were obtained as a function of the period $\Gamma_k = T_k/T_p$, and hence their values are normalised. The delay values used are the one used in the past sections. In (a), (c), and (e) the solutions for a system with no damping ratio are shown, while in (b), (d), and (f), the case in which the damping ratio is $\xi = 0.3$ is presented. From the zero damping ratio situations is observed that the curves obtained by delay SLME and exponential SLME are almost the same, which shows the similitude between the results obtained. Likewise, it can be seen that the effect of the delay changes considerably the curves associated with the cosine. From the plots obtained for $\xi = 0.3$, it is observed that for higher damping ratio the curves and results tend to the same value. However, in the case of the exponential SLME, only the first solution of the system remains, since the rest of the curves do not cross.

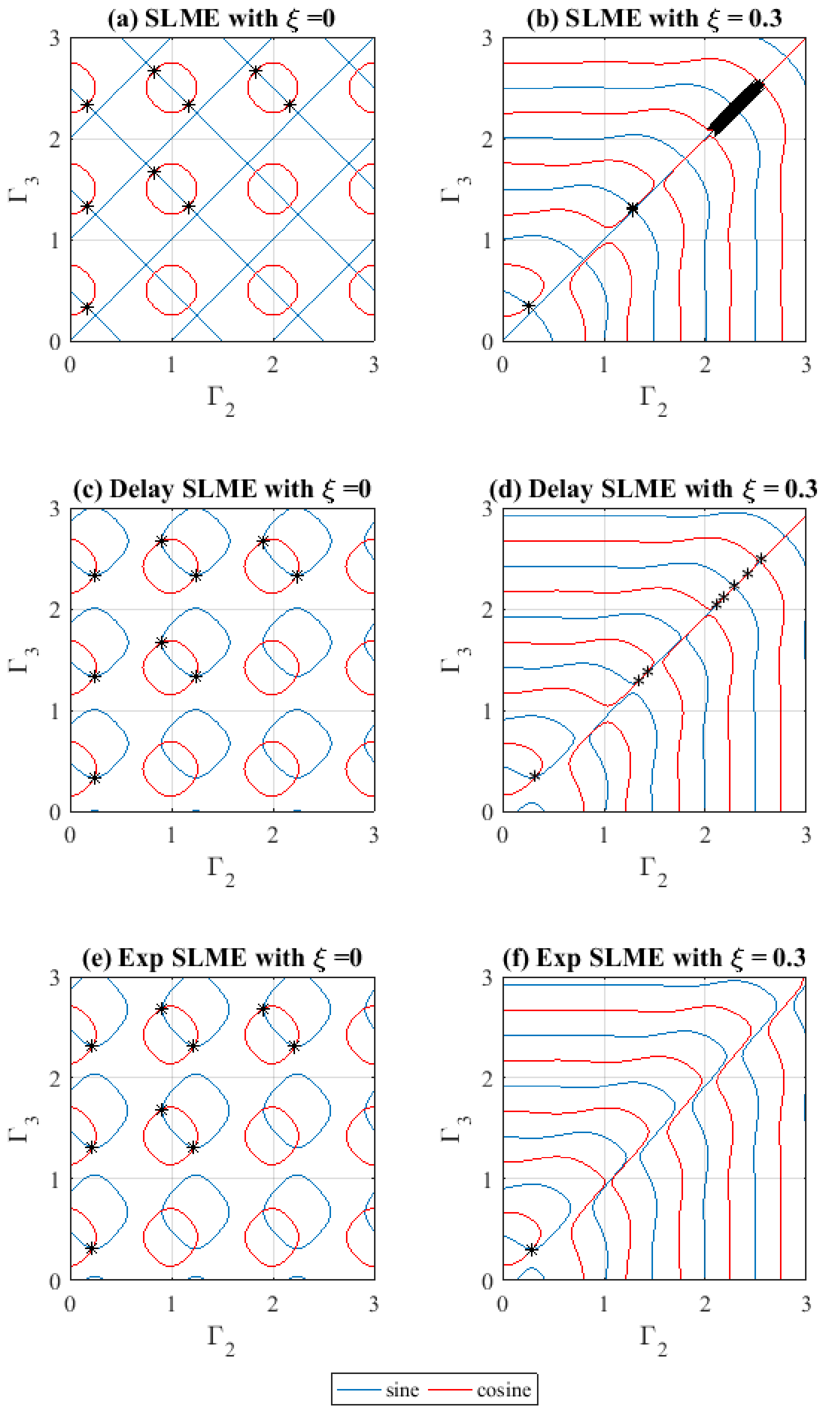

Figure 8.21: Summary solutions of system with inductance.

A summary of the results obtained for the 3 natural frequencies system is shown in Figure 8.22. As previously described, the presence of inductance reduces the effectivity of the SLME connection. While SLME method still reduces the vibrations considerably, as was shown experimentally in chapter 7, some vibrations remain after the switching connection. From (c) and (d) the response of the systems solved with delay SLME and exponential SLME are presented. While in theory, exponential SLME should produce better results, eliminating all the vibrations after the switching, the complexity in its solving makes delay SLME an easy method to apply in practice.

(a) Step

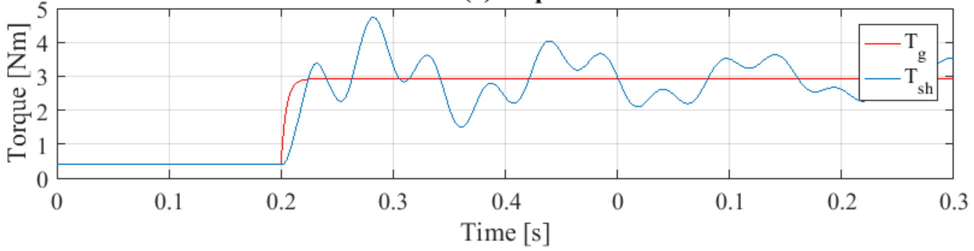

(b) SLME

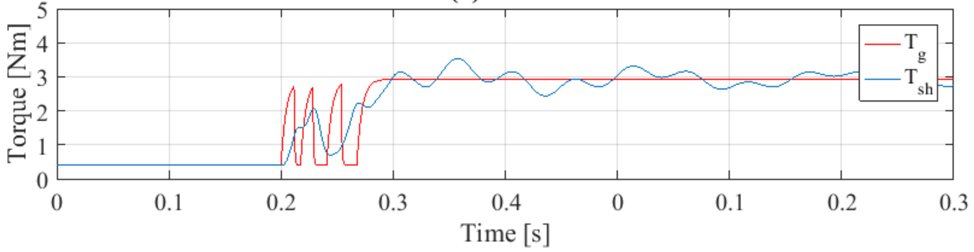

(c) Delay SLME

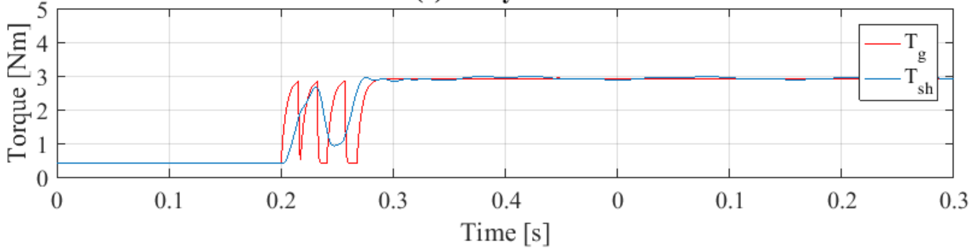

(d) Exponential SLME

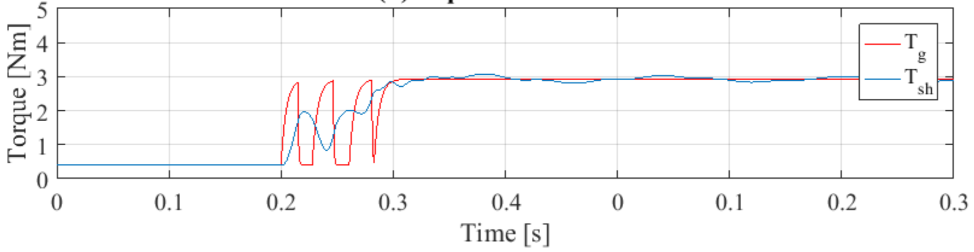

Figure 8.22: Summary torque in system with inductance.

The advantage of exponential SLME is that by modelling the load connection as a series of steps, the methodology can be expanded to any curve shape. For example, a ramp connection, presented as a solution in chapter 3, eliminates the vibrations because an adequate slope solves the Posicast equation system, which can be shown by the modelling of the connection as a series of infinite steps.

Moreover, the results presented by the delay SLME and exponential SLME show that the inductance in a system is not an impediment to eliminate the vibrations produced by electromechanical interaction. In future work these methodologies can be expanded for different loads (capacitive for example) and for the MLL and MSLME strategies.

8.4 Comparison with Alternative Methods

In this section the strategies proposed in this thesis are compared with the methods used in the literature and which have been presented in chapter 3. A summary of them is shown in Figure 8.23. The strategies can be divided in three approaches. System analysis, which consists in analysing the natural frequencies or vibration modes of the mechanical system to avoid the operation of the electrical system at those values. System design, which designs the mechanical system with higher damping or stiffness to reduce the vibrations. And finally, controller design, in which different control methods are used. One method is to control the torque applied by the machine and apply a ramp. The ramp reduces the vibrations since the torque applied at a given time is lower. Otherwise, torque strategies with closed-loop torque are used. When using this system, the torque applied by the machine is controlled by the value of the torsional torque vibrations. Finally, anti-resonant filters which cancel the excitation of frequencies can be used to avoid reduce the torsional vibrations. In addition, all the strategies found in the literature have been applied to the machine connected to the mechanical system.

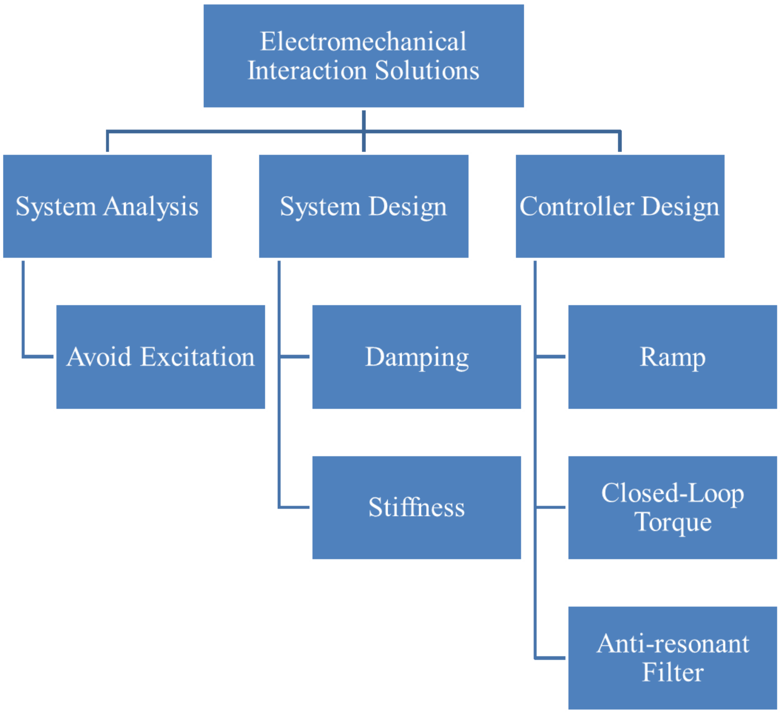

Figure 8.23: Torsional vibration solutions for electromechanical systems.

Of the strategies presented, the system analysis does not reduce the vibrations when electrical loads are being connected. On the other hand, the design of the system with higher damping or stiffness, makes the system heavier and larger. For this reason, the solutions for the reduction of the torsional vibrations excited by the connection of electrical loads are based in controller design.

In general, the controller design strategies used consist in slowing down the system. For example, the ramp and the closed-loop torque strategies are effective but slow. Moreover, these strategies reduce the vibration but do not consider the reason for their excitation. For this reason, in this thesis, strategies based on the Posicast Compensator, a filter that stops the excitation of the resonance frequencies was studied. This method allows the elimination of the torsional vibrations in a time lower than half the period of the torsional frequency, making it much faster than the other methods commonly used.

However, the Posicast compensator and the methods used in the literature review are not independent, but complementary. First, it was mentioned that the Posicast compensator is part of the Anti-resonant filter subsection, since it consists in eliminating the excitation of the torsional vibrations. Second, as was shown in the last section, the step connection of loads can be used to model any load shape. For this reason, the use of a ramp connection can be a solution of the same problem. The difference with the ramp connection used nowadays would be the time of the connection. There is one ramp slope that allows the elimination of the vibrations in half a period. Finally, the use of closed-loop torque feedback can be integrated in the strategies presented to increase the robustness of the system.

The main difference between the strategies typically used and the ones presented in this work is where they are being applied. Most studies apply the strategies directly on the machine since the studies on machines and electrical power system are independent. However, in this thesis the control to reduce the torsional vibrations is applied to the electrical loads. The main reason for this is to reduce the effect on the stability of the electrical power system, since in current aircraft electrical power system, the loads are already being connected in a pulsing pattern by the use of mechanical switches.

Still, as presented in chapter 5 to be able to apply the control in the electrical power system, the following requirements must be fulfilled:

- Solid State switches to control the loads.
- A given ratio of load types.
- Minimum inner loop bandwidth in converter.
- High bandwidth communication/sensing/control link.

If the requirements cannot be satisfied, a combination between the traditional methods and the methods presented in this thesis can be used. The strategies presented in this thesis have been applied on the loads but they can be applied in the machine too. For example, for the connection of loads in which solid state switches are not available yet, the strategy can be applied directly to the machine. The same can done if the amount of critical loads connected is higher than the quantity of non-critical loads.

8.5 Summary

This chapter presented a robust analysis of the Posicast based strategies and modifications to include the effect of the inductances in the system. The study of the sensitivity of the strategies allowed the identification of the parameters that affect the robustness of the methods. It was obtained, that for damping ratio below 0.05, which are the normal values obtained, its identification is not critical. Likewise, it was obtained that the identification of the correct number of torsional frequencies in the system is essential, since solving the strategies for fewer frequencies reduce the effectivity and can produce vibrations higher than for the step connection. Also, it was shown that the identification of a correct first frequency is more important than the second. Finally, for uncertainties of $\pm 5\text{Hz}$, the results of the strategies are similar.

Regarding the inductances of the system, it was shown that their value must be considered in the strategies because the delay produced by them affects the strategy as much as the frequency uncertainty. The combined effect of inductance and frequency uncertainty can produce vibrations higher than the ones obtained for the step connection. For this reason, two strategies that remove the effect of the inductances were presented: delay SLME and exponential SLME. It was shown that while delay SLME has some vibrations after the switching event, exponential SLME allows the elimination of them. However, exponential SLME has high computational requirements which reduce the solver effectivity. For this reason, if the complete elimination of the vibrations is desired, new solver strategies for the non-linear equation system must be studied.

Summing up, this chapter has shown the importance of identifying the overall system parameters. In an aircraft system, the drivetrain torsional vibrations are given by the machine and gears inertias and the shaft stiffness. Since these values do not present considerable variations during its operation, a first identification through the FFT method is enough for the application of the strategies. Moreover, since the torsional frequencies must be known regardless of the Posicast strategies, to avoid resonance between the drivetrain and the generator control, the PMS presented is a feasible solution to reduce the torsional vibrations.

Chapter 9

Conclusions and Future Work

9.1 Summary

This thesis presented a study of the electromechanical interaction in aircraft systems. The importance of studying the excitation of the drivetrain torsional vibration modes by the connection of electrical loads has been shown. For this, a reduced aircraft drivetrain has been analysed.

To reduce the vibrations produced by the excitation of the drivetrain natural frequencies, a power management system (PMS) has been developed. The PMS proposes the use of strategies based on the Posicast compensator to suppress the excitation of vibrations when different electrical loads are connected.

In the ideal case (known frequency and no inductance or capacitance), the torsional vibrations can be eliminated after the switching connection by the application of a switching event. Experimentally, the system parameters are not known, and thus they must be estimated. Therefore, the frequencies used have an error respect to the real system values. Likewise, the experimental system has inductance, which was omitted by simulation, and which generates logarithmic load connections instead of steps. For these two reasons, experimentally the PMS strategies reduce the torsional vibrations to values close to zero instead of eliminating them. To study these effects a sensitivity analysis was carried on, and strategies based on logarithmic load connections were proposed to improve the system response. Therefore, the presence of inductance in the system does not affect the elimination of the torsional vibrations produced by electromechanical interaction.

In chapter 2 and 3, the literature review was presented. Chapter 2 described the evolution of aircraft systems, while chapter 3 presented a review of the electromechanical interaction across diverse electrical applications. The study shows the importance this subject has gained in every area that involves interchange of electrical and mechanical power. Sources and solutions applied in each field of study have been presented.

In chapter 4, the electromechanical interaction in aircraft systems has been studied. Simulation results have been presented to show the effect of the connection of step and pulsating electrical loads on the mechanical drivetrain. Furthermore, the importance of designing the machine control system considering the electrical and mechanical system has been shown.

In chapter 5, a PMS that eliminates the torsional vibrations due to the connection of electrical loads has been designed. The PMS can be applied to pulsating loads and step electrical loads with or without a critical time connection. Each of the strategies is based on the Posicast method, which cancels the vibrations by the connection of a series of switching events. The switching is determined as a function of the natural frequencies and damping ratio of the drivetrain. Further understanding of the strategies has been given by studying the solution range as a function of the system's damping ratio. Graphically, it has been shown that the Posicast strategies eliminate the vibrations by adding zeros at the poles value.

To experimentally test the PMS, in chapter 6 the experimental setup was designed. The rig presented allows the testing of different aircraft related studies, such as an in-line starter/generator, an air-riding seal, and the electromechanical interactions. Of them, this thesis only studies the electromechanical interactions. Furthermore, it was shown that a domestic appliance universal motor could be readapted to operate as a generator in the experimental setup. The use of this machine allows the simplification of the system and the reduction of the cost.

In chapter 7 the PMS strategies have been tested experimentally. To prove the strategies SLME, MLL and MSLME, the frequencies were identified and torque measuring strategies presented. For the frequency and damping ratio identification, a method based on the FFT, the empirical mode decomposition and Hilbert Transform were used. To measure the shaft torque, sensor and sensorless methods were presented. It was shown, that for the low load and high noise application the sensorless method provides the best results. The sensorless torque measurement methodology can be expanded to synchronous generators like the ones used in aircraft. Moreover, the results of the PMS have demonstrated that the torsional vibrations are reduced when the strategies are applied. The effect of the inductance and the frequency uncertainty over the SLME, MLL, and MSLME strategies have been shown. For closer steps, such as the steps associated with 77.1Hz in the SLME connection, the inductances affect the step shape, reducing the effectivity of the method.

Finally, in chapter 8 the robustness of the Posicast strategies was studied, and future enhancements to the method presented. Regarding the robustness, a comparison of the three strategies presented (SLME, MLL, and MSLME) show that MLL is less affected by the uncertainty of the system and by the presence of inductance. The reason behind this behaviour is that the MLL strategy is slower than the other two. A slower strategy allows the step connection to finish, regardless of the inductance, before the next switching takes place, and at the same time makes the system more robust to frequency uncertainty. To include a wider range of loads, the modelling of any connection pattern as a series of steps has been proposed. In particular, for the case of inductive and resistive loads, the solving of the equation system for load connections has been introduced.

9.2 Conclusions

This thesis showed that the electromechanical interaction is a relevant problem for aircraft systems since it reduced the life of the mechanical drivetrain and creates instability. For the case in which the interaction is due to the connection of electrical loads, the solutions in the literature review are not optimal. Since the behaviour of the vibrations is not considered, the time it takes to eliminate the torsional vibrations is high. For this reason, this thesis presented strategies to cancel the excitation of torsional vibrations which are based on the characteristics of the mechanical system. The connection is carried out in half a period of the drivetrain natural frequency, which is in the order of milliseconds.

The method presented is not necessarily independent from the ones already in use but can be complementary. In this study, the Posicast compensator has been applied to the electrical loads being connected to the system, but it can also be applied to the machine control and can be expanded to ramp connections and closed loop.

Moreover, the strategies were demonstrated by simulation and experimentally. It was also shown that the methods are robust respect to the damping and the second (or higher) frequencies and that its response depends more on the shape of the connection than the frequency identification. Therefore, the robust studies should focus on the identification of the lower natural frequency and the shape of the connection.

Finally, it is concluded that the PMS presented in this thesis is a valid alternative to the suppression of torsional vibrations in aircraft electromechanical systems. The strategies presented can be applied as presented here or partially, and they can also be adapted to systems with similar problems, like the interconnection of electrical power system and wind turbines applications.

9.3 Future Work

Future works that can be developed from the work presented in this thesis are listed below:

- **Posicast with uncertainty and non-linear loads:** In this thesis open-loop Posicast strategies have been applied to systems with known frequencies and damping ratio and operating with resistive loads. To extend the method to a wider range of systems, the effect of uncertainty and non-linear loads must be studied.
    - Respect to the system uncertainty, Posicast strategies with closed-loop can be developed. For example, a PI can improve the results for systems in which the value of the frequencies is not exact. These results can be further extended to comprise systems in which the

    frequencies are unknown or change in time by the use of adaptive controllers.
  - In consideration of systems with non-resistive loads, chapter 7 show that the presence of inductance can affect the Posicast method. For this problem, chapter 8 proposed the solving of the Posicast strategies for inductive loads. By the modelling of any connection pattern as a series of infinite steps, the strategy can be adapted to different loads. Therefore, further work can include inductive and capacitive loads, which are common in aircraft systems. The same strategy can also be used to obtain the optimal ramp which allows the connection of the load in half a period of the drivetrain natural frequency. Moreover, combining the connection patterns with closed-loop methods, the Posicast based method can be extended to non-linear loads with frequencies uncertainty.
- **Implementation of the Posicast strategies in other applications**: The Posicast strategies can be applied to cancel the vibrations produced on other electrical and mechanical systems. For example, in wind turbines in which there is electromechanical interaction due to changes in the turbine rotation speed. Alternatively, the Posicast methods can be applied on the synchronisation of systems, such as microgrids, which can see their interconnection stopped due to the presence of high transients. Furthermore, the use of Posicast compensator can be beneficial for the interconnection of electrical systems. For example, in aircraft systems, when one generator fails, the two power networks are connected. This connection can be seen as the connection of a high load and therefore it will produce torsional vibrations on the shaft of the remaining generator. To avoid these vibration the Posicast compensator can be used.

  Moreover, the Posicast strategies can be studied to reduce the transients in electrical systems. In general, the use of these strategies to reduce transient vibrations in electrical systems require high switching, since the connection is made in half a period. However in chapter 5 was shown that each equation system has more than one solution. Therefore, to avoid the use of high switching devices, to apply the Posicast strategies to electrical systems, connection times greater than half a period are desired. This work can also be combined with closed-loop Posicast strategies, allowing the reduction of the vibrations in a system with uncertainty.

- **Experimental rig integration with in-line starter/generator:** In chapter 6 was mentioned that the experimental rig allows the testing of three aircraft aspects: the electromechanical interaction presented in this thesis, an in-line starter/generator, and an air-riding seal. The starter/generator allows the reduction of the transversal vibrations, while the seal is benefited by the decrease. Since the PMS strategies reduce the torsional vibrations produced by electromechanical interaction, further analysis can be done by integrating these strategies into the starter/generator. This will allow the presentation of a system that reduces transversal and torsional vibrations simultaneously.
- **Study of electrical power system requirements:** In chapter 5, the requirement of the electrical power system for the application of the proposed PMS were stated. Future work should study:
    - The implementation of the strategies on the power electronics of the system.
    - The effect of the communication system on the strategy presented. For example, the delay in the communication should be considered and strategies to minimise its effect proposed.
    - The power quality of the electrical power system after applying the proposed PMS.

9.4 Publications

- C. Ahumada, S. Garvey, T. Yang, P. Wheeler, "Electromechanical Interaction Analysis through Sensorless Torque Measurement," 2017 IEEE

Southern Power Electronics Conference (SPEC), Puerto Varas, Chile, 2017, pp. 1-6., doi: 10.1109/SPEC.2017.8333597.

- C. Ahumada, S. Garvey, T. Yang, P. Kulsangcharoen, P. Wheeler and H. Morvan, "Minimization of electro-mechanical interaction with posicast strategies for more-electric aircraft applications*," IECON 2016 - 42nd Annual Conference of the IEEE Industrial Electronics Society*, Florence, 2016, pp. 4423-4428, doi: 10.1109/IECON.2016.7794134.
- Ahumada Sanhueza, C., Bristot, A., Kumar, S., Schneider, N. et al., "An Integrated System's Approach Towards Aero Engine Subsystems Design," SAE Technical Paper 2016-01-2020, 2016, doi:10.4271/2016-01-2020.
- S. C. Ahumada, S. Garvey, T. Yang, P. Wheeler and H. Morvan, "The importance of load pulse timing in aircraft generation," *2015 18th International Conference on Electrical Machines and Systems (ICEMS),* Pattaya, 2015, pp. 1339-1345, doi: 10.1109/ICEMS.2015.7385247.
- Ahumada S., C., Garvey, S., Yang, T., Wheeler, P. et al., "Impact of Electric Loads on Engine Shaft Dynamics within More Electric Aircraft," SAE Technical Paper 2015-01-2409, 2015, doi:10.4271/2015-01-2409.

Appendix I - Universal Motor

This appendix presents the universal motor parameters and its connection to operate as a single phase DC generator. The plate characteristics of the machine are presented in Table A I - 1. Figure AI - 1 shows the winding connection for its operation as a universal motor (in (a)) and as a DC generator (in (b)).

Table A I - 1: Machine plate parameters.

Characteristic	Value
Brand	Nidec
Speed	$480 - 15000$ rpm
Frequency	$50 - 60$ Hz
Voltage	$230 - 240$ V

(a) Universal Motor

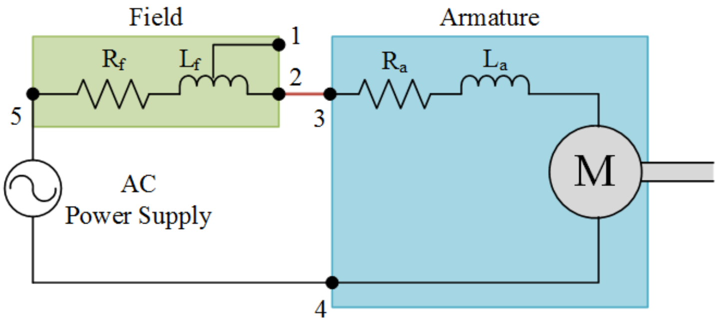

(b) DC Generator

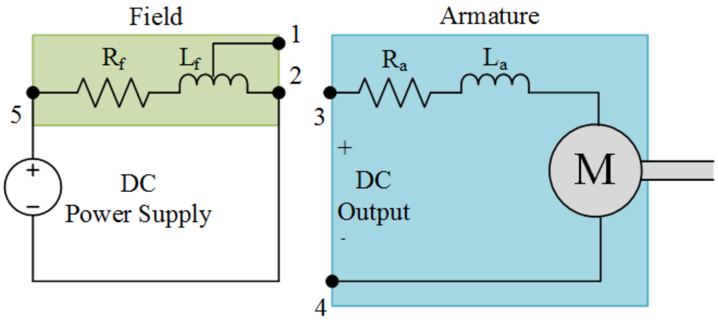

Figure AI - 1: Universal motor circuit.

In the following sections, the resistance of the windings, the rotational inductance, the maximum operating current, and the inertia are determined. The values of the armature and field inductance are $L_a = 0.19$H and $L_f = 0.2$H respectively and they have been determined by Michele Degano at the Università degli studi di Trieste.

A I -1 Windings Resistance

To determine the resistance of the armature and field windings, each of them is connected to a power source (not simultaneously) when the machine is cold, as shown in Figure AI - 2. Measuring the voltage and current on the windings, the resistance is obtained as given by equation (A I - 1). Table A I - 2 show the parameters obtained.

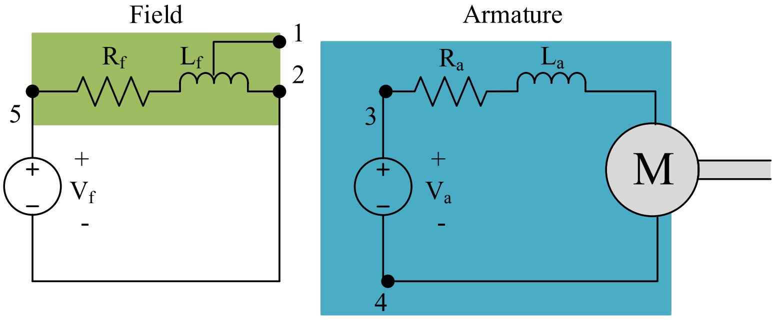

Figure AI - 2: Connection diagram for winding determination.

$$R = \frac{V}{I} \qquad \text{(A I - 1)}$$

Table A I - 2: Field and armature resistance determination.

Winding	Voltage [V]	Current [A]	Resistance [Ω]
Field	10.1	4.93	2.0487
Armature	17.8	4.42	4.025

A I -2 Generator Magnetization Curve

The generator magnetisation curve is studied to determine the rotational inductance and to analyse the machine saturation. To obtain it, the machine is connected as shown in Figure AI - 1(b). With no load connected, the armature voltage is measured for different values of field current, while keeping the speed constant. The test is repeated increasing the current, and decreasing it for two different speed values. Figure AI - 3 show the results obtained. In blue, the magnetisation curve for an increasing field current is shown, while in red the curve obtained when the current decrease is depicted.

(a) Speed 1436rpm

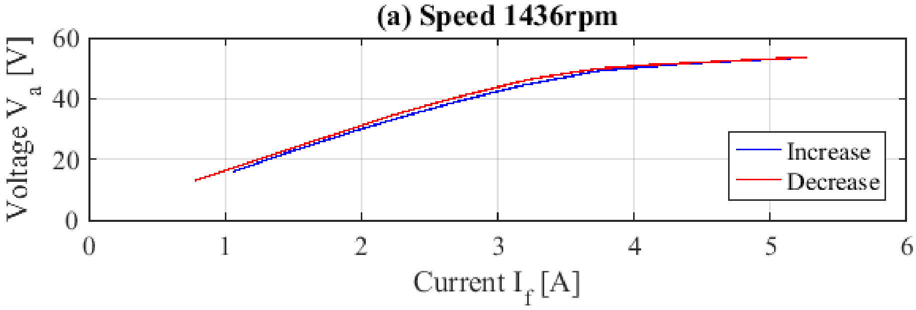

(b) Speed 1353rpm

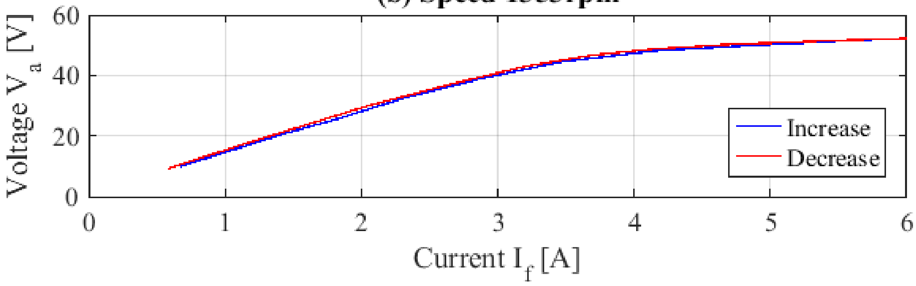

(c) Increase Speed

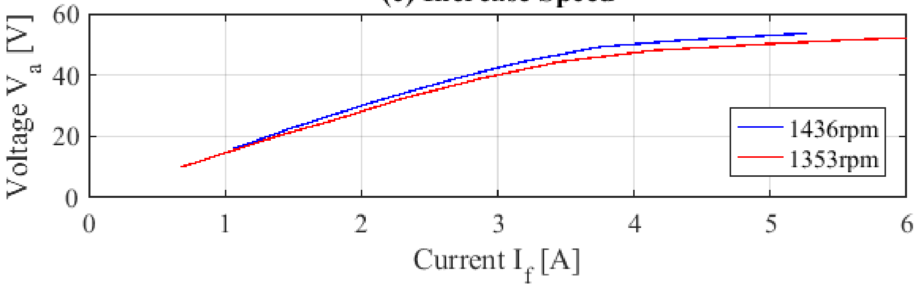

Figure AI - 3: Results magnetization curve of the generator.

It is observed that the machine saturates slightly after 3A. Because the saturation current is lower than the field current that is used in the rig, to model the rotational inductance $k(i_f)$ equation (A I - 2), proposed in [125], is used. This equation has the advantage of modelling the basic features of saturation using one constant b and the magnetization value k_0 at the origin, with i_f the field current. The value of the rotational inductance as a function of i_f is found from equation (A I - 3).

$$k(i_f) = \frac{k_0}{1 + bi_f} \qquad \text{(A I - 2)}$$

$$v_a = E = k(i_f) i_f \omega \qquad \text{(A I - 3)}$$

Fitting the data from the figures the following values are obtained:

$$k_0 = 0.1274$$
$$b = 0.1221$$

A I -3 Maximum Current Test

In last section was shown that the machine starts saturating at 3A. This section studies the maximum current at which the machine can operate. For this test, the machine is connected as a generator with no load and no speed. Then, the field voltage was measured during 5 minutes (or 300 seconds) while supplying a constant current. The test was repeated for currents from 4A to 10A. Between each test, the machine must cool down to obtain correct results. Figure AI - 4(a) shows the results obtained. It is observed that for lower currents the voltage changes less than at higher values.

The change in voltage is associated with a rise in the field resistance as shown in Figure AI - 4(b). The field resistance was obtained from equation (A I - 1). The results show that the generator can run up to a current of 6A without increasing the machine resistance considerably. Also, it is observed that for a field current of 4, 6, and 9A, the resistance at the start of the measurement R_0 has the same value of 1.8Ω, while in the other two cases the resistance is higher. This behaviour shows that the two measurements at 8 and 10A were done when the machine was warm, while for the other three, the measurements started with the machine cold.

(a) Voltage

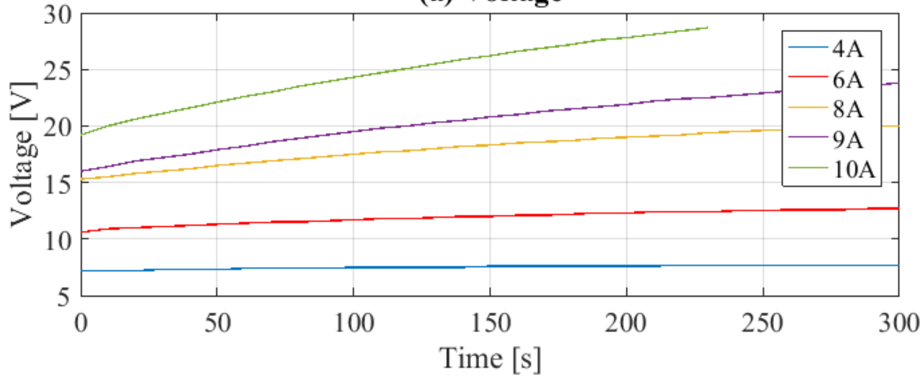

(b) Resistance

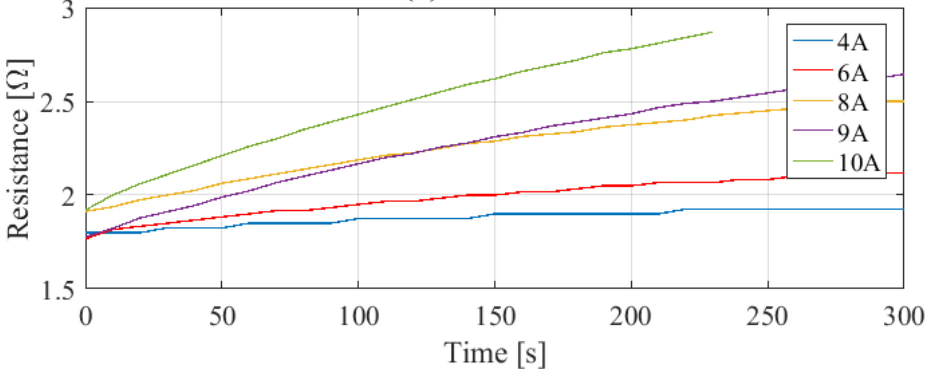

Figure AI - 4: Maximum machine current.

Now that the field resistance has been obtained, its behaviour can be modelled as a function of the field current and the time. The resistance has a common initial value R_0, which changes exponentially with the time. Therefore, it can be modelled by an exponential curve as shown in equation (A I - 4). With, R_0 the resistance at the origin, R_t, the resistance variation, and τ the time constant of the resistance change.

$$R(t, i_f) = R_0 + R_t\left(1 - \exp\left(-\frac{1}{\tau}t\right)\right) \qquad \text{(A I - 4)}$$

Fitting the five resistance curves of Figure AI - 4(b), the parameters from Table A I - 3 are obtained for each current. As mentioned before, the value of R_0 is the same for currents of 4, 6 and 9A, while in the other two cases higher results are obtained. Since the higher values of R_0 indicate that the machine was warm when the test was done, from now on, the value of $R_0 = 1.79\Omega$ is assumed real.

Table A I - 3: Resistance parametrization constant.

Current i_f $[A]$	R_0 $[\Omega]$	R_t $[\Omega]$	τ $[s]$
4	1.792	0.1702	176.3
6	1.788	0.435	215.1
8	1.908	0.8905	268.4
9	1.783	1.385	312.1
10	1.937	1.675	284.4

On the other hand, the parameters R_t and τ are not constant, and therefore an approximation must be found. Since R_t and τ depend on the current of the system, applying curve fitting is obtained that their behaviour can me modelled by equations (A I - 5) and (A I - 6), with $R_{t0} = 0.01599\Omega/\mathrm{A}^2$, $\tau_0 = 103.5\mathrm{s}$, and $\tau_1 = 18.91\mathrm{s/A}$.

$$R_t(i_f) = R_{t0} i_f^2 \tag{A I - 5}$$

$$\tau(i_f) = \tau_0 + \tau_1 i_f \tag{A I - 6}$$

Replacing the values of R_0, and equations (A I - 5) and (A I - 6) into equation (A I - 4), the following equation to represent the field resistance as a function of current and time is obtained:

$$R(t,i) = 1.79 + 0.01599 i^2 \left(1 - \exp\left(-\frac{1}{103.5 + 18.91 i} t\right)\right) \tag{A I - 7}$$

The resistance values found by equation (A I - 7) are compared with the real values in Figure AI - 5. It is obtained that the model is representative of the system. Therefore, calculating the field resistance as a function of time and current Figure AI - 6 is obtained. From here it is gotten that the maximum current at which the machine can operate is 6A continuous or 10A for 5min, which warranties that the resistance has not increased to the double of its value. Moreover, since the machine operates for periods longer than 5 minutes, the field resistance is assumed as $R_f = 2\Omega$, which is the value obtained in section A I -1.

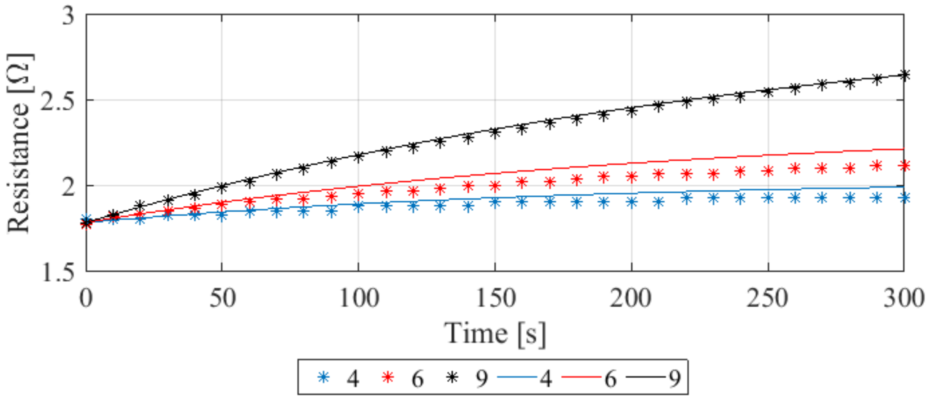

Figure AI - 5: Comparison of estimation and real field resistance.

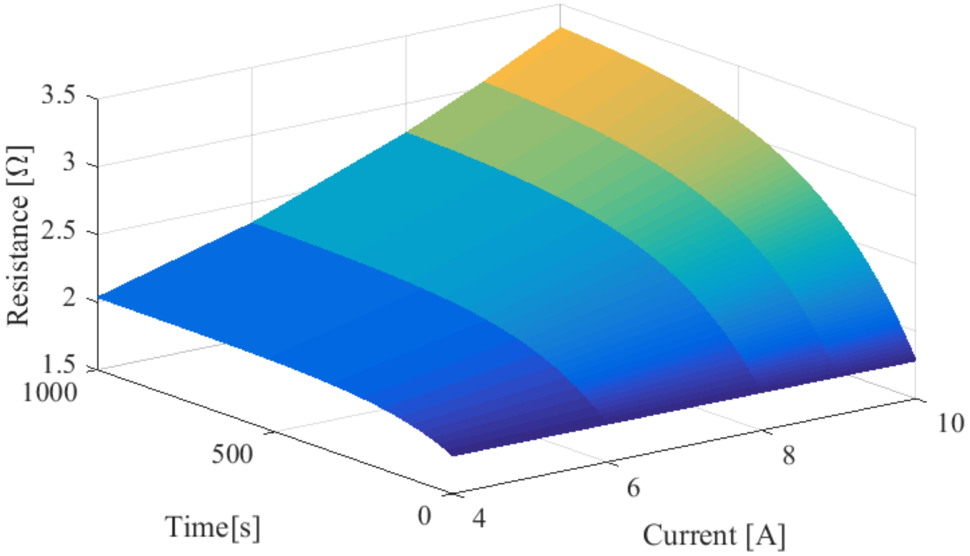

Figure AI - 6: Estimated field resistance as a function of time and field current.

A I -4 Brush Voltage Drop

As mentioned in [96] there is a voltage drop in the brushes of the universal motor. To determine its value equations (A I - 8) and (A I - 9) are used. With E the back-EMF in V, R_a the armature resistance in Ω, L_a the armature inductance in H, i_a and i_f the armature and field current in A, v_a the armature voltage in V, V_0 the voltage drop in the brushes in V, k the rotational inductance obtained in section A I -2, and ω the speed in rad/s.

$$E = R_a i_a + L_a \frac{di_a}{dt} + v_a + V_0 \qquad \text{(A I - 8)}$$

$$E = k i_f \omega \qquad \text{(A I - 9)}$$

When the system is in steady state $di_a/dt = 0$. Replacing its value and (A I - 9) into (A I - 8), equation (A I - 10) is obtained.

$$V_0 = k i_f \omega - R_a i_a - v_a \qquad \text{(A I - 10)}$$

To find the value of the brushes voltage drop, the steady state date of Figure AI - 7 is used.

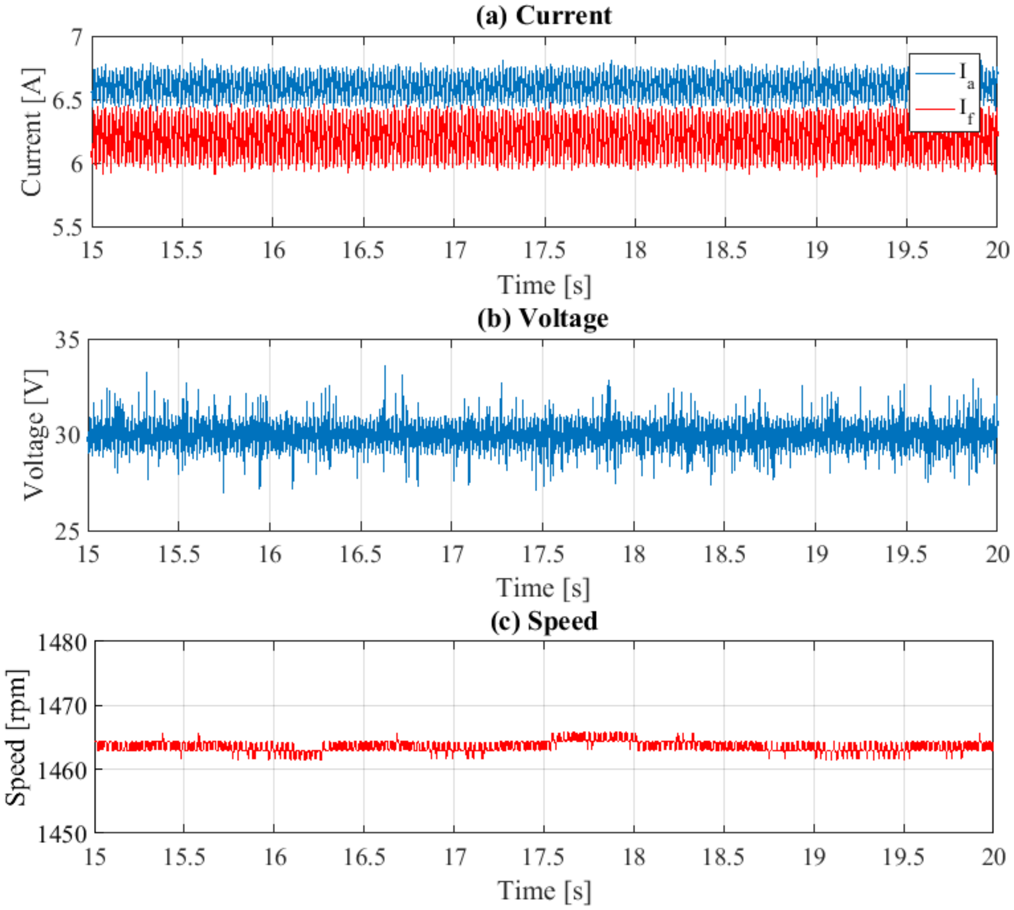

Figure AI - 7: Experimental steady state data.

Finally it is obtained that the voltage drop in the brushes is:

$$V_0 = 12.247 \text{ V}$$

A I -5 Inertia Determination

To determine the inertia of the machine the acceleration must be measured. For this test, the machine is connected as an independent field motor, as shown in Figure AI - 8. Connecting a resistance in parallel to the armature voltage, the speed is measured after the armature voltage has been disconnected while keeping the field current constant. The test is repeated for three initial armature currents (20, 25, and 30V) and two values of R_L, 30 and 59Ω, and for the case in which no resistance is connected. Figure AI - 9 shows the speed obtained in each case. Differentiating the speed, the results of Figure AI - 10 are obtained.

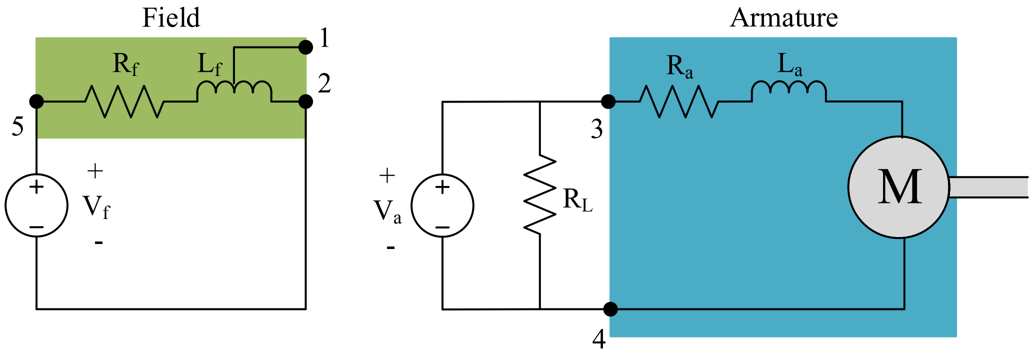

Figure AI - 8: Diagram for J determination.

(a) Without R_L connected

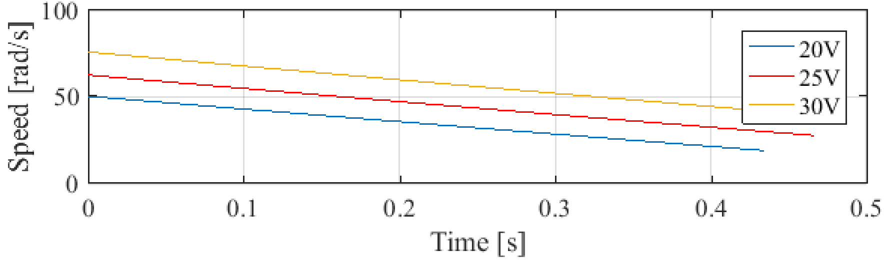

(b) R_L = 30 [Ω]

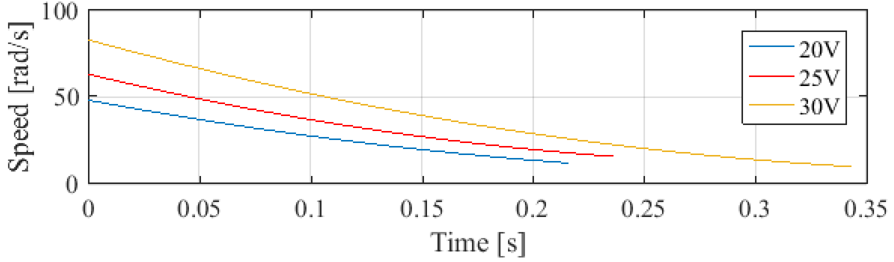

(c) R_L = 59 [Ω]

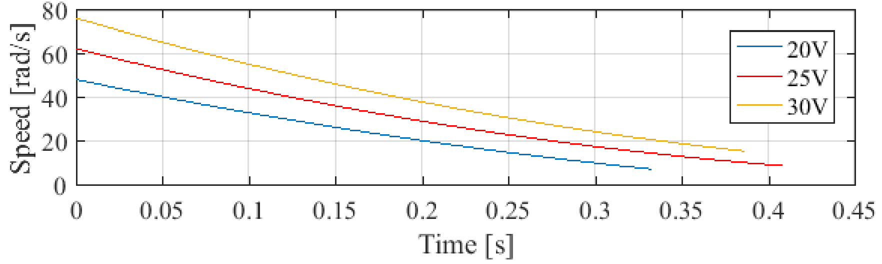

Figure AI - 9: Speed of the machine.

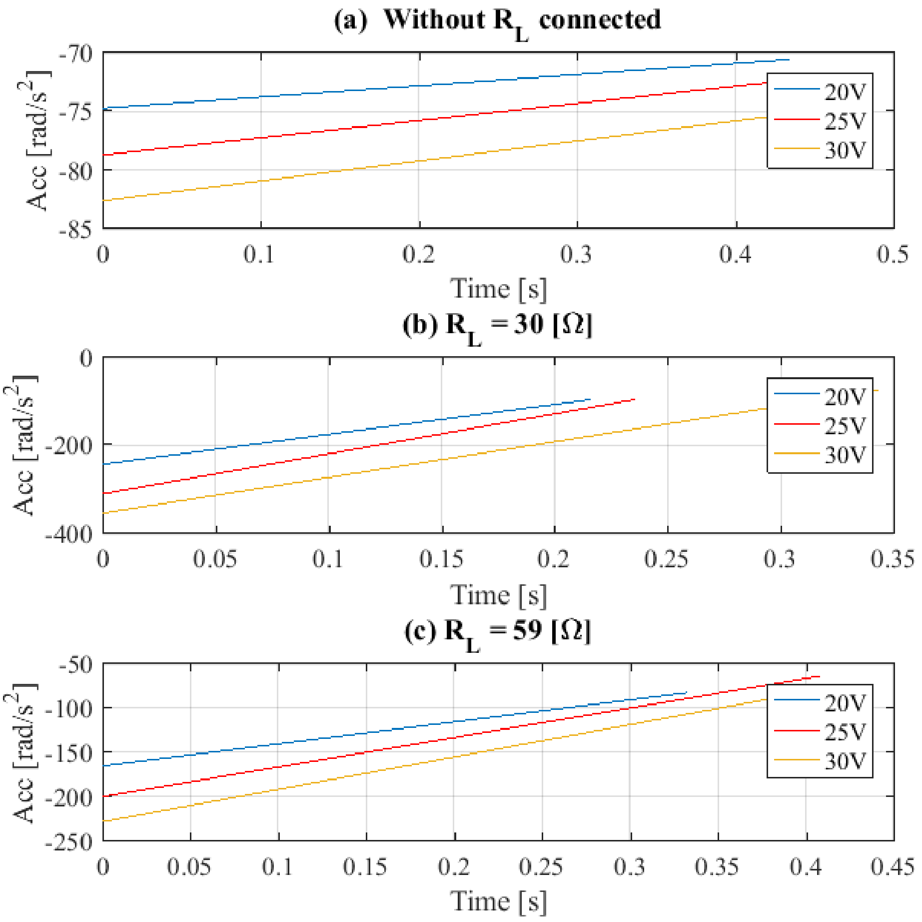

Figure AI - 10: Acceleration of the machine.

Now that the acceleration has been found, the inertia can be calculated. Equation (A I - 11) represent the relationship between the acceleration of the machine $\dot{\omega}$, the electrical torque produced T_e, the torque associated with the load connected to the machine T_L, and the torque consumed by the losses $T_{windage}$ and $T_{friction}$.

$$J\dot{\omega} = T_e - T_L - T_{windage} - T_{friction} \qquad \text{(A I - 11)}$$

Since the machine is operating as a motor, disconnected from any other machine, the value of the load torque is $T_L = 0$. The torque used by the friction can be represented by equation (A I - 12), while the torque consumed by the windage, $T_{windage}$, is proportional to the square of the speed, as shown in equation (A I - 13).

$$T_{friction} = D\omega \qquad \text{(A I - 12)}$$

$$T_{windage} \propto \omega^2 \quad \text{(A I - 13)}$$

The value of the electrical torque T_e produced by the machine depends on the connection of the resistance R_L. Each case is explained next.

Case with resistance R_L

When there is a resistance R_L connected parallel to the armature voltage, the armature current and therefore the airgap torque of the machine does not become automatically zero after disconnecting the voltage. Therefore, there is a torque T_e which for a given load is proportional to the speed, as shown in equation (A I - 14) [96].

$$T_e = f(\omega) = A\omega \quad \text{(A I - 14)}$$

Replacing the values of T_e, $T_{friction}$, and $T_{windage}$ into equation (A I - 11), equation (A I - 15) is obtained. Since the data can be fitted by equation (A I - 16), the relationships from equations (A I - 17) and (A I - 18) are found.

$$\dot{\omega} = \frac{A\omega - D\omega - T_{windage}}{J} \quad \text{(A I - 15)}$$

$$\dot{\omega} = k_1\omega^2 + k_2\omega + k_3 \quad \text{(A I - 16)}$$

$$A - D = Jk_2 \quad \text{(A I - 17)}$$

$$-\frac{T_{windage}}{J} = k_1\omega^2 + k_3 \quad \text{(A I - 18)}$$

Case without resistance R_L

When there is not a resistance R_L connected to the system, the armature current and therefore the electrical torque T_e become automatically zero after disconnecting the voltage. Consequently, the equation that describes the system can be modelled by (A I - 19), while the data of the system can be fitted using equation (A I - 20). From these two equations, the relationships from equations (A I - 21) and (A I - 22) are found.

$$\dot{\omega} = \frac{-D\omega - T_{windage}}{J} \tag{A I - 19}$$

$$\dot{\omega} = k'_1\omega^2 + k'_2\omega + k'_3 \tag{A I - 20}$$

$$D = -Jk'_2 \tag{A I - 21}$$

$$-\frac{T_{windage}}{J} = k'_1\omega^2 + k'_3 \tag{A I - 22}$$

Then, fitting the experimental data with the equations described, the parameters presented in Table A I - 4 and Table A I - 5 are obtained for each case.

Table A I - 4: Parametrization variables for data with load.

Voltage V_a [V]	Load Resistance R_L [Ω]	k_1	k_2	k_3
20	59	0.0159	-2.8510	-63.1070
25	59	0.0230	-4.0452	-33.4146
30	59	0.0164	-3.7411	-35.2987
20	30	0.0464	-6.6667	-26.0642
25	30	0.0474	-7.9945	11.8159
30	30	0.0310	-6.3704	-28.9132

Table A I - 5: Parametrization variables for data with no load.

Voltage V_a [V]	k'_1	k'_2	k'_3
20	1.1958e-4	-0.1401	-67.9584
25	2.5081e-4	-0.2170	-66.0593
30	2.9762e-4	-0.2506	-65.2397

Now, the equation system given by (A I - 17), (A I - 18), (A I - 21), and (A I - 22) is solved for the resistance $R_L = 30\Omega$ and $R_L = 59\Omega$ compared to the no resistance case. The inertias J and damping D obtained in each case are shown in Table A I - 6. It is observed that the values obtained are relatively constant, and from now on, the inertia of the machine is approximated by $J = 5e - 4\text{kgm}^2$.

Table A I - 6: Inertia and damping.

Voltage V_a [V]	Load Resistance R_L [Ω]	Inertia $J[Kgm^2]$	Damping $D\left[\frac{Nms}{rad}\right]$
20	30	5.2095e-4	7.2985e-5
25	30	4.3716e-4	9.4864e-5
30	30	5.5557e-4	1.3923e-4
20	59	6.6399e-4	9.3025e-5
25	59	4.7019e-4	1.0203e-4
30	59	5.1569e-4	1.2923e-4

A I -6 Summary

The parameters of the universal motor used as a generator are shown in Table A I - 7.

Table A I - 7: Generator parameters.

Parameter	**Value**
Armature resistance	$R_a = 4.025\ \Omega$
Field resistance	$R_f = 2\ \Omega$
Armature Inductance	$L_a = 0.019$ H
Field Inductance	$L_f = 0.02$ H
Rotational inductance	$k_0 = 0.1274\ \text{ln} - \text{in/A}$
Rotational inductance constant	$b = 0.1271\ 1/\text{A}$
Rotational inertia	$J_g = 0.0005\ \text{kgm}^2$
Max speed	$\omega_{max} = 15000$ rpm
Max current continuous	$I_{max} = 6$ A
Max current / 5 min	$I_{max/5min} = 10$ A
Brush Voltage Drop	$V_0 = 12.247$ V

Appendix II - Vibration absorber

The vibration absorber happens when the values of inertias and stiffness of the system are symmetrical and the gears take the same torque. In this case, some torsional modes are not excited. The results change if the FFT is measured from a non-symmetrical point. In practice, the machines and inertias connected to a system always have differences on their values, and therefore the vibration absorber case does not occur.

Table AII- 1: Vibration absorber parameters.

Parameter	**Normal Case**	**Vibration Absorber**
Engine Inertia	$J_m = 0.0965\ \text{kgm}^2$	$J_m = 0.0965\ \text{kgm}^2$
Gear 1 Inertia	$J_{gb1} = 0.002325\ \text{kgm}^2$	$J_{gb1} = 0.002325\ \text{kgm}^2$
Gear 2 Inertia	$J_{gb2} = 0.00047\ \text{kgm}^2$	$J_{gb2} = 0.00047\ \text{kgm}^2$
Gear 3 Inertia	$J_{gb3} = 0.0091\ \text{kgm}^2$	$J_{gb3} = 0.00047\ \text{kgm}^2$
Generator 1 Inertia	$J_{g1} = 0.0386\ \text{kgm}^2$	$J_{g1} = 0.0386\ \text{kgm}^2$
Generator 2 Inertia	$J_{g2} = 0.0376\ \text{kgm}^2$	$J_{g1} = 0.0386\ \text{kgm}^2$
Shaft 1 Stiffness	$k_{s1} = 5.3995 * 10^2\ \frac{Nm}{rad}$	$k_{s1} = 5.3995 * 10^2\ \frac{Nm}{rad}$
Gearshaft 1 Stiffness	$k_{gs1} = 3 * 10^9\ \frac{Nm}{rad}$	$k_{gs1} = 3 * 10^9\ \frac{Nm}{rad}$
Gearshaft 2 Stiffness	$k_{gs2} = 3 * 10^9\ \frac{Nm}{rad}$	$k_{gs2} = 3 * 10^9\ \frac{Nm}{rad}$
Shaft 2 Stiffness	$k_{s2} = 2.2398 * 10^3\ \frac{Nm}{rad}$	$k_{s2} = 2.2398 * 10^3\ \frac{Nm}{rad}$
Shaft 3 Stiffness	$k_{s3} = 2.2398 * 10^3\ \frac{Nm}{rad}$	$k_{s3} = 2.2398 * 10^3\ \frac{Nm}{rad}$

To show its effects, the aircraft model presented in chapter 4 and the data from Table AII- 1 are used. Table AII- 1 presents two cases: symmetrical and non-symmetrical parameters. To both data cases, a step torque connection is applied in generator 2. Measuring the torque in the second generator shaft, and calculating the FFT, Figure AII- 1 is obtained. Comparing (a) and (b), it is observed that in the case of applying a step connection to a system with symmetrical parameters, the third vibration mode is not excited. For this reason, it is important to not use symmetrical parameters in simulation analysis.

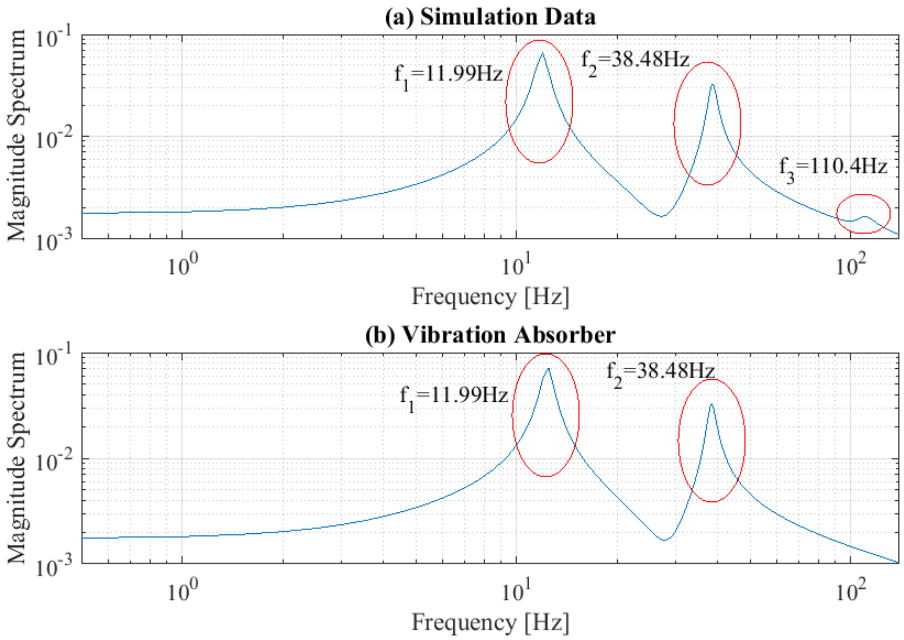

Figure AII- 1: Vibration absorber FFT.

References

[1] R. Seresinhe and C. Lawson, “Electrical load-sizing methodology to aid conceptual and preliminary design of large commercial aircraft,” *Proc. Inst. Mech. Eng. Part G J. Aerosp. Eng.*, vol. 229, no. 3, pp. 445–466, Mar. 2015.

[2] A. Boglietti, A. Cavagnino, A. Tenconi, S. Vaschetto, and P. di Torino, “The safety critical electric machines and drives in the more electric aircraft: A survey,” in *2009 35th Annual Conference of IEEE Industrial Electronics*, 2009, pp. 2587–2594.

[3] M. J. Provost, “The More Electric Aero-engine: a general overview from an engine manufacturer,” in *International Conference on Power Electronics Machines and Drives*, 2002, vol. 2002, pp. 246–251.

[4] Acare, “Strategic Research & Innovation Agenda,” Brussels, Belgium, 2017.

[5] J. Chen, C. Wang, and J. Chen, “Investigation on the Selection of Electric Power System Architecture for Future More Electric Aircraft,” *IEEE Trans. Transp. Electrif.*, vol. PP, no. 99, p. 1, 2018.

[6] J. A. Rosero, J. A. Ortega, E. Aldabas, and L. Romeral, “Moving towards a more electric aircraft,” *IEEE Aerosp. Electron. Syst. Mag.*, vol. 22, no. 3, pp. 3–9, Mar. 2007.

[7] J. A. Weimer, “Electrical power technology for the more electric aircraft,” in *[1993 Proceedings] AIAA/IEEE Digital Avionics Systems Conference*, 1993, pp. 445–450.

[8] R. I. Jones, “The More Electric Aircraft: the past and the future?,” in *IEE Colloquium. Electrical Machines and Systems for the More Electric Aircraft*, 1999, vol. 1999, pp. 1–1.

[9] P. W. Wheeler, J. C. Clare, A. Trentin, and S. Bozhko, “An overview of the more electrical aircraft,” *Proc. Inst. Mech. Eng. Part G J. Aerosp. Eng.*, vol. 227, no. 4, pp. 578–585, Apr. 2013.

[10] M. J. J. Cronin, “The all-electric aircraft,” *IEE Rev.*, vol. 36, no. 8, p. 309, 1990.

[11] R. T. Naayagi, “A review of more electric aircraft technology,” *Energy Efficient Technologies for Sustainability (ICEETS), 2013 International Conference on*. pp. 750–753, 2013.

[12] I. Moir, “The all-electric aircraft - major challenges,” in *IEE Colloquium on All Electric Aircraft*, 1998, vol. 1998, pp. 2–2.

[13] L. J. Feiner, “Power-by-wire aircraft secondary power systems,” in *[1993 Proceedings] AIAA/IEEE Digital Avionics Systems Conference*, 1993, pp. 439–444.

[14] T. Yang, “Development of Dynamic Phasors for the Modelling of Aircraft Electrical Power Systems By,” Phd Thesis University of Nottingham, 2013.

[15] B. Sarlioglu and C. T. Morris, “More Electric Aircraft: Review, Challenges, and Opportunities for Commercial Transport Aircraft,” *IEEE Trans. Transp. Electrif.*, vol. 1, no. 1, pp. 54–64, Jun. 2015.

[16] P. J. Norman, S. J. Galloway, G. M. Burt, D. R. Trainer, and M. Hirst, “Transient analysis of the more-electric engine electrical power distribution network,” *Power Electronics, Machines and Drives, 2008. PEMD 2008. 4th IET Conference on*. pp. 681–685, 2008.

[17] P. J. J. Norman, S. J. J. Galloway, G. M. M. Burt, J. E. E. Hill, and D. R. R. Trainer, *Evaluation of the dynamic interactions between aircraft gas turbine engine and electrical system*. York: IET, 2008, pp. 671–675.

[18] T. Feehally, I. E. Damian, and J. M. Apsley, “Analysis of Electromechanical Interaction in Aircraft Generator Systems,” *IEEE Trans. Ind. Appl.*, vol. 52, no. 5, pp. 4327–4336, Sep. 2016.

[19] G. Moore, “Electro-Mechanical Interactions in Aerospace Gas Turbines,” University of Nottingham, 2012.

[20] M. A. Valenzuela, J. M. Bentley, and R. D. Lorenz, “Evaluation of Torsional Oscillations in Paper Machine Sections,” *IEEE Trans. Ind. Appl.*, vol. 41, no. 2, pp. 493–501, Mar. 2005.

[21] Li Ran, Dawei Xiang, and J. L. Kirtley, “Analysis of Electromechanical Interactions in a Flywheel System With a Doubly Fed Induction Machine,” *IEEE Trans. Ind. Appl.*, vol. 47, no. 3, pp. 1498–1506, May 2011.

[22] M. Yang, C. Wang, D. Xu, W. Zheng, and X. Lang, “Shaft Torque Limiting Control Using Shaft Torque Compensator for Two-Inertia Elastic System With Backlash,” *IEEE/ASME Trans. Mechatronics*, vol. 21, no. 6, pp. 2902–2911, Dec. 2016.

[23] W. C. Carter, “Mechanical Factors Affecting Electrical Drive Performance,” *IEEE Trans. Ind. Gen. Appl.*, vol. IGA-5, no. 3, pp. 282–290, May 1969.

[24] M. A. Valenzuela, J. M. Bentley, and R. D. Lorenz, “Evaluation of torsional oscillations in paper machine sections,” in *Conference Record of 2004 Annual Pulp and Paper Industry Technical Conference (IEEE Cat. No.04CH37523)*, 2004, pp. 15–22.

[25] R. Muller, D. Schmitt, and J. Kimber, “Create - Creating innovative air transport technologies for Europe,” Brussels, Belgium, 2010.

[26] M. Bailey, “Distributed electrical power management architecture,” in *IEE Colloquium. Electrical Machines and Systems for the More Electric Aircraft*, 1999, vol. 1999, pp. 7–7.

[27] I. Moir and A. Seabridge, *Aircraft Systems*. Chichester, UK: John Wiley & Sons, Ltd, 2008.

[28] Wenping Cao, B. C. Mecrow, G. J. Atkinson, J. W. Bennett, and D. J. Atkinson, “Overview of Electric Motor Technologies Used for More Electric Aircraft (MEA),” *IEEE Trans. Ind. Electron.*, vol. 59, no. 9, pp. 3523–3531, Sep. 2012.

[29] M. E. Elbuluk and M. D. Kankam, “Potential starter/generator technologies for future aerospace applications,” *IEEE Aerosp. Electron. Syst. Mag.*, vol. 12, no. 5, pp. 24–31, May 1997.

[30] Jie Chang and Anhua Wang, “New VF-power system architecture and evaluation for future aircraft,” *IEEE Trans. Aerosp. Electron. Syst.*, vol. 42,

no. 2, pp. 527–539, Apr. 2006.

[31] K. Emadi and M. Ehsani, “Aircraft power systems: technology, state of the art, and future trends,” *IEEE Aerosp. Electron. Syst. Mag.*, vol. 15, no. 1, pp. 28–32, 2000.

[32] A. Garcia, J. Cusido, J. A. Rosero, J. A. Ortega, and L. Romeral, “Reliable electro-mechanical actuators in aircraft,” *IEEE Aerosp. Electron. Syst. Mag.*, vol. 23, no. 8, pp. 19–25, Aug. 2008.

[33] L. Han, J. Wang, and D. Howe, “Stability assessment of distributed Dc power systems for ‘more- electric’ aircraft,” in *4th IET International Conference on Power Electronics, Machines and Drives (PEMD 2008)*, 2008, pp. 661–665.

[34] B. MacIsaac and R. Langton, *Gas Turbine Propulsion Systems*. Chichester, UK: John Wiley & Sons, Ltd, 2011.

[35] S. J. Khalid, “Mitigating Impact of Bleed and Power Extraction with More Electric Architectures,” in *SAE Technical Paper*, 2016.

[36] R. Newman, “The more electric engine concept,” *SAE Tech. Pap.*, no. 2004–013128.

[37] T. Feehally, “Electro-mechanical Interaction in Gas Turbine-generator Systems for More-electric Aircraft,” PhD Thesis University of Manchester, 2012.

[38] A. Griffo and J. Wang, “Stability assessment of electric power systems for more electric aircraft,” *Power Electronics and Applications, 2009. EPE ’09. 13th European Conference on*. pp. 1–10, 2009.

[39] L. Han, J. Wang, and D. Howe, “Small-signal stability studies of a 270V DC more-electric aircraft power system,” in *IET Internation Conference on Power Electronics Machines and Drives*, 2006, pp. 162–166.

[40] I. Chakraborty, D. N. Mavris, M. Emeneth, and A. Schneegans, “A methodology for vehicle and mission level comparison of More Electric

Aircraft subsystem solutions: Application to the flight control actuation system," *Proc. Inst. Mech. Eng. Part G J. Aerosp. Eng.*, vol. 229, no. 6, pp. 1088–1102, May 2015.

[41] P. Kundur, *Power System Stability and Control*, 1st ed. New York: McGraw-Hill Professional Publishing, 1994.

[42] L. Han, J. Wang, A. Griffo, and D. Howe, "Stability assessment of AC hybrid power systems for more electric aircraft," in *2008 IEEE Vehicle Power and Propulsion Conference*, 2008, pp. 1–6.

[43] F. Barruel, N. Retiere, and J. L. Schanen, "Stability analysis for aircraft on-board system," in *3rd IET International Conference on Power Electronics, Machines and Drives (PEMD 2006)*, 2006, vol. 2006, no. 33, pp. 361–367.

[44] K.-N. Areerak, T. Wu, S. V. Bozhko, G. M. Asher, and D. W. P. Thomas, "Aircraft Power System Stability Study Including Effect of Voltage Control and Actuators Dynamic," *IEEE Trans. Aerosp. Electron. Syst.*, vol. 47, no. 4, pp. 2574–2589, 2011.

[45] L. C. Herrera and B.-H. Tsao, "Analysis and Control of Energy Storage in Aircraft Power Systems with Pulsed Power Loads," *SAE Int. J. Aerosp.*, vol. 9, no. 1, pp. 2016-01–1981, Sep. 2016.

[46] F. Gao, S. Bozhko, and P. Wheeler, "An Enhanced Secondary Control Approach for Voltage Restoration in the DC Distribution System," in *SAE Technical Papers*, 2016.

[47] T. Wu, "Integrative System Modelling of Aircraft Electrical Power Systems," Phd Thesis University of Nottingham, 2010.

[48] H. Cohen and G. Rogers, *Gas turbine theory*, 4th ed. Essex, 1996.

[49] M. I. Friswell, J. E. T. Penny, S. D. Garvey, and A. W. Lees, *Dynamics of Rotating Machines*. Cambridge University Press, 2010.

[50] D. J. Sheppard, "Torsional vibration resulting from adjustable-frequency AC drives," *IEEE Trans. Ind. Appl.*, vol. 24, no. 5, pp. 812–817, 1988.

[51] IEEE, “Proposed Terms and Definitions for Subsynchronous Oscillations,” *IEEE Trans. Power Appar. Syst.*, vol. PAS-99, no. 2, pp. 506–511, 1980.

[52] D. N. Walker, C. E. J. Bowler, R. L. Jackson, and D. A. Hodges, “Results of subsynchronous resonance test at Mohave,” *IEEE Trans. Power Appar. Syst.*, vol. 94, no. 5, pp. 1878–1889, Sep. 1975.

[53] J. H. Holdrege, W. Subler, and W. E. Frasier, “AC Induction Motor Torsional Vibration Consideration - A Case Study,” *IEEE Trans. Ind. Appl.*, vol. IA-19, no. 1, pp. 68–73, Jan. 1983.

[54] J. Song-Manguelle, J.-M. Nyobe-Yome, and G. Ekemb, “Pulsating Torques in PWM Multi-Megawatt Drives for Torsional Analysis of Large Shafts,” *IEEE Trans. Ind. Appl.*, vol. 46, no. 1, pp. 130–138, 2010.

[55] S. N. Vukosavic and M. R. Stojic, “Suppression of torsional oscillations in a high-performance speed servo drive,” *IEEE Trans. Ind. Electron.*, vol. 45, no. 1, pp. 108–117, 1998.

[56] G. W. Buckley, “The effects of torsional elements on the transient performance of large induction motor drives,” *Electr. Mach. Power Syst.*, vol. 5, no. 1, pp. 53–64, Jan. 1980.

[57] D. Ramey, A. Sismour, and G. Kung, “Important Parameters in Considering Transient Torques on Turbine-Generator Shaft Systems,” *IEEE Trans. Power Appar. Syst.*, vol. PAS-99, no. 1, pp. 311–317, Jan. 1980.

[58] A. Gaikwad and P. Rajarapollu, “Analysis of mechanical stresses developed on T-G shaft during faults,” *Information and Communication Technology in Electrical Sciences (ICTES 2007), 2007. ICTES. IET-UK International Conference on*. pp. 126–131, 2007.

[59] D. N. Walker, S. L. Adams, and R. J. Placek, “Torsional Vibration and Fatigue of Turbine-Generator shafts,” *IEEE Trans. Power Appar. Syst.*, vol. PAS-100, no. 11, pp. 4373–4380, Nov. 1981.

[60] P. Pourbeik, D. G. Ramey, N. Abi-Samra, D. Brooks, and A. Gaikwad, “Vulnerability of Large Steam Turbine Generators to Torsional Interactions

During Electrical Grid Disturbances," *Power Systems, IEEE Transactions on*, vol. 22, no. 3. pp. 1250–1258, 2007.

[61] R. L. Steigerwald, G. W. Ludwig, and R. Kollman, "Investigation of power distribution architectures for distributed avionics loads," in *Proceedings of PESC '95 - Power Electronics Specialist Conference*, 1995, vol. 1, pp. 231–237.

[62] A. A. Shaltout, "Analysis of torsional torques in starting of large squirrel cage induction motors," *IEEE Trans. Energy Convers.*, vol. 9, no. 1, pp. 135–142, Mar. 1994.

[63] I. M. Elders, P. J. Norman, J. D. Schuddebeurs, C. D. Booth, G. M. Burt, J. R. McDonald, J. Apsley, M. Barnes, A. Smith, S. Williamson, S. Loddick, and I. Myers, "Modelling and Analysis of Electro-Mechanical Interactions between Prime-Mover and Load in a Marine IFEP System," in *2007 IEEE Electric Ship Technologies Symposium*, 2007, pp. 77–84.

[64] S. Higuchi, M. Ishida, and T. Hori, "Reduction of mechanical vibration of an induction motor with pulsating torque load by feedforward control utilizing an acceleration sensor and a timing sensor," in *Proceedings of 4th IEEE International Workshop on Advanced Motion Control - AMC '96 - MIE*, vol. 1, pp. 316–320.

[65] J. K. Kambrath, A. A. Ayu, Y. Wang, Y.-J. Yoon, X. Liu, C. J. Gajanayake, and A. K. Gupta, "Dynamic study of electromechanical interaction in marine propulsion," in *2016 IEEE Energy Conversion Congress and Exposition (ECCE)*, 2016, pp. 1–8.

[66] X. Lei, B. Buchholz, and D. Povh, "Analysing subsynchronous resonance phenomena in the time- and frequency domain," *Eur. Trans. Electr. Power*, vol. 10, no. 4, pp. 203–211, Sep. 2007.

[67] S. Goldberg and W. Schmus, "Subsynchronous Resonance and Torsional Stresses in Turbine-Generator Shafts," *IEEE Trans. Power Appar. Syst.*, vol. PAS-98, no. 4, pp. 1233–1237, Jul. 1979.

[68] C. Concordia and G. K. Carter, “Negative Damping of Electrical Machinery,” *Trans. Am. Inst. Electr. Eng.*, vol. 60, no. 3, pp. 116–119, Mar. 1941.

[69] “Reader’s guide to subsynchronous resonance,” *IEEE Trans. Power Syst.*, vol. 7, no. 1, pp. 150–157, 1992.

[70] P. Kumar Ȧ, U. K. Agarwal Ḃ, and V. Kumar Sharma Ȧ, “Design of Controller for Chopper Fed DC Drive with Pulsating Load and Elastic Coupling under Resonance,” *Int. J. Curr. Eng. Technol.*, vol. 44, no. 44, 2450.

[71] D. Sen Gupta, Ce. N. MIEE Narahari ME I Boyd, and B. Hogg CEng, “An adaptive power-system stabiliser which cancels the negative damping torque of a synchronous generator List of symbols.”

[72] J. S. Joyce, T. Kulig, and D. Lambrecht, “Torsional Fatigue of Turbine-Generator Shafts Caused by Different Electrical System Faults and Switching Operations,” *Power Apparatus and Systems, IEEE Transactions on*, vol. PAS-97, no. 5. pp. 1965–1977, 1978.

[73] R. Dhaouadi, K. Kubo, and M. Tobise, “Analysis and compensation of speed drive systems with torsional loads,” *IEEE Trans. Ind. Appl.*, vol. 30, no. 3, pp. 760–766, 1994.

[74] B. A. Leishman, S. J. Drew, and B. J. Stone, “Torsional vibration of a back-to-back gearbox rig Part 1: frequency domain modal analysis,” *Proc. Inst. Mech. Eng. Part K J. Multi-body Dyn.*, vol. 214, no. 3, pp. 143–162, Jan. 2000.

[75] D. Melot de Beauregard, A. Conradi, B. Benthaus, and L. Golebiowski, “Electromechanical roller conveyor model with enhanced consideration of roller-belt interaction,” in *2012 IEEE International Conference on Automation and Logistics*, 2012, pp. 7–12.

[76] S. H. Kia, H. Henao, and G.-A. Capolino, “Torsional Vibration Effects on Induction Machine Current and Torque Signatures in Gearbox-Based

Electromechanical System," *IEEE Trans. Ind. Electron.*, vol. 56, no. 11, pp. 4689–4699, Nov. 2009.

[77] K.-S. Ou and K.-S. Chen, "Developing Electromechanical Coupling Macro Models for Dynamic Responses of MEMS Structures With Command Shaping Techniques," *IEEE Trans. Device Mater. Reliab.*, vol. 16, no. 2, pp. 123–131, Jun. 2016.

[78] P. Schmidt and T. Rehm, "(2)Notch Filter Tuning for Resonant Frequency Reduction in Dual Inertia Systems," *Transform*, vol. 3, no. 1, pp. 1730–1734, 1999.

[79] G. Ellis and R. D. Lorenz, "Resonant load control methods for industrial servo drives," *Conf. Rec. 2000 IEEE Ind. Appl. Conf.*, vol. 3, pp. 1438–1445, 2000.

[80] T. J. Hammons and L. Chanal, "Measurement of torque in steam turbine-generator shafts following severe disturbances on the electrical supply system-analysis and implementation," *IEEE Transactions on Energy Conversion*, vol. 6, no. 1. pp. 193–203, 1991.

[81] V. Atarod, P. L. Dandeno, and M. R. Iravani, "Impact of synchronous machine constants and models on the analysis of torsional dynamics," *IEEE Trans. Power Syst.*, vol. 7, no. 4, pp. 1456–1463, 1992.

[82] L. Feng, W. Gao, C. Tan, H. Qin, B. Xie, and Z. Hao, "Observer-Based Active Control of Torsional Vibration for Large Turbine-Generator Shaft System," in *2010 Asia-Pacific Power and Energy Engineering Conference*, 2010, pp. 1–5.

[83] R. Fadaeinedjad, M. Moallem, and G. Moschopoulos, "Simulation of a Wind Turbine With Doubly Fed Induction Generator by FAST and Simulink," *IEEE Trans. Energy Convers.*, vol. 23, no. 2, pp. 690–700, Jun. 2008.

[84] D. S. Ochs, R. D. Miller, and W. N. White, "Simulation of electromechanical interactions of permanent-magnet direct-drive wind turbines using the fast aeroelastic simulator," *IEEE Trans. Sustain. Energy*, vol. 5, no. 1, pp. 2–9,

2014.

[85] Hong Fu, Chao Feng, and Shan Xue, “Vibration suppression control of an integrated powertrain of electric and hybrid vehicles using LQR controller and reduced-order observer,” in *2014 IEEE Conference and Expo Transportation Electrification Asia-Pacific (ITEC Asia-Pacific)*, 2014, pp. 1–6.

[86] Q. Wang, K. Rajashekara, Y. Jia, and J. Sun, “A Real-time Vibration Suppression Strategy in Electric Vehicles,” *IEEE Trans. Veh. Technol.*, pp. 1–1, 2017.

[87] P. J. Norman, C. D. Booth, J. D. Schuddebeurs, G. M. Burt, J. R. McDonald, J. M. Apsley, M. Barnes, A. C. Smith, S. Williamson, E. Tsoudis, P. Pilidis, and R. Singh, “Integrated Electrical and Mechanical Modelling of Integrated-Full-Electric-Propulsion Systems,” *Power Electronics, Machines and Drives, 2006. The 3rd IET International Conference on*. pp. 101–105, 2006.

[88] T. Feehally and J. M. Apsley, “The Doubly Fed Induction Machine as an Aero Generator,” *IEEE Trans. Ind. Appl.*, vol. 51, no. 4, pp. 3462–3471, Jul. 2015.

[89] E. L. Owen, “Flexible shaft versus rigid shaft electric machines for petroleum and chemical plants,” *IEEE Trans. Ind. Appl.*, vol. 27, no. 2, pp. 245–253, 1991.

[90] S. M. M. Rahman, “A novel variable impedance compact compliant series elastic actuator for human-friendly soft robotics applications,” in *2012 IEEE RO-MAN: The 21st IEEE International Symposium on Robot and Human Interactive Communication*, 2012, pp. 19–24.

[91] T. Kakinoki, R. Yokoyama, G. Fujita, T. Nakano, K. Koyanagi, T. Funabashi, and H. Nara, “Estimation of turbine shaft torques using observer,” in *2001 IEEE Porto Power Tech Proceedings*, 2001, vol. 2, pp. 81–84.

[92] S. Higuchi, M. Ishida, and T. Hori, “Reduction of mechanical vibration of an induction motor with pulsating torque load by feedforward control utilizing an acceleration sensor and a timing sensor,” *Advanced Motion Control, 1996. AMC ’96-MIE. Proceedings., 1996 4th International Workshop on*, vol. 1. pp. 316–320 vol.1, 1996.

[93] D. Vrančić and P. M. Oliveira, “Design of feedback control for underdamped systems,” 2012.

[94] S. Garvey, Z. Chen, M. I. Friswell, and U. Prells, “Model reduction using structure-preserving transformations,” in *Proceedings of the International Modal Analysis Conference IMAC XXI*, 2003, no. 3, pp. 361–377.

[95] M. Friswell, J. E. T. Penny, and S. D. Garvey, “Model reduction for structures with damping and gyroscopic effects,” in *Proceedings of ISMA-25*, 2000, pp. 1151–1158.

[96] C.-M. Ong, *Dynamic Simulation of Electric Machinery: Using MATLAB/SIMULINK*. Prentice Hall PTR, 1998.

[97] S. D. Garvey, M. I. Friswell, and U. Prells, “Co-Ordinate Transformations for Second Order Systems. Part Ii: Elementary Structure-Preserving Transformations,” *J. Sound Vib.*, vol. 258, no. 5, pp. 885–909, Dec. 2002.

[98] Y. Chahlaoui, D. Lemonnier, K. Meerbergen, A. Vandendorpe, P. Van Dooren, and K. Gallivan, “Model reduction of second-order systems,” *Dimens. Reduct. …*, vol. 1, no. 2, pp. 1–23, 2005.

[99] R. Colgren, “Efficient Model Reduction for the Control of Large-Scale Systems,” in *Efficient Modeling and Control of Large-Scale Systems SE - 2*, J. Mohammadpour and K. M. Grigoriadis, Eds. Springer US, 2010, pp. 59–72.

[100] R. Guyan, “Reduction of stiffness and mass matrices,” *AIAA J.*, vol. 3, no. 2, p. 380, 1965.

[101] D. F. Enns, “Model reduction with balanced realizations: An error bound and a frequency weighted generalization,” *Decision and Control, 1984. The*

23rd IEEE Conference on, vol. 23. pp. 127–132, 1984.

[102] B. Moore, “Principal component analysis in linear systems: Controllability, observability, and model reduction,” *IEEE Trans. Automat. Contr.*, vol. 26, no. 1, pp. 17–32, Feb. 1981.

[103] T. Wu, S. Bozhko, G. Asher, P. Wheeler, and D. Thomas, “Fast Reduced Functional Models of Electromechanical Actuators for More-Electric Aircraft Power System Study,” in *SAE Power Systems Conference*, 2008, p. 12.

[104] C. Gan, R. Todd, and J. Apsley, “HIL emulation for future aerospace propulsion systems,” *Power Electronics, Machines and Drives (PEMD 2014), 7th IET International Conference on*. pp. 1–6, 2014.

[105] K. Ogata, *Modern control engineering*. Prentice-Hall, 2010.

[106] Department of Defense Armed Forced Supply Support, “MIL-STD-704 Military standard characteristics,” 1959.

[107] A. Shenkman, Y. Berkovich, and B. Axelrod, “Pulse converter for induction-heating applications,” *Electric Power Applications, IEE Proceedings -*, vol. 153, no. 6. pp. 864–872, 2006.

[108] F. Blaabjerg and S. Munk-Nielsen, “Power losses in PWM-VSI inverter using NPT or PT IGBT devices,” *Power Electronics, IEEE Transactions on*, vol. 10, no. 3. pp. 358–367, 1995.

[109] Gaoyu Zou and Zhengming Zhao, “Research on impacts of different parameters on transient power loss of IGBT,” in *2013 International Conference on Electrical Machines and Systems (ICEMS)*, 2013, pp. 490–495.

[110] O. J. M. Smith, “Posicast Control of Damped Oscillatory Systems,” *Proceedings of the IRE*, vol. 45, no. 9. pp. 1249–1255, 1957.

[111] E. W. Giloy, “An electric deicing system for aircraft,” *Transactions of the American Institute of Electrical Engineers*, vol. 69, no. 2. pp. 1051–1057,

1949.

[112] K. Veselić, *Damped Oscillations of Linear Systems*, 1st ed., vol. 2023. Berlin, Heidelberg: Springer-Verlag Berlin Heidelberg, 2011.

[113] C. W. de Silva, *Vibration: Fundamentals and Practice, Second Edition*. CRC Press, 2011.

[114] G. Tallman and O. Smith, "Analog study of dead-beat posicast control," *IRE Trans. Autom. Control*, vol. 4, no. 1, pp. 14–21, Mar. 1958.

[115] H. Ghorbani, J. I. Candela, A. Luna, and P. Rodriguez, "Posicast control A novel approach to mitigate multi-machine power system oscillations in presence of wind farm," in *2014 IEEE PES General Meeting | Conference & Exposition*, 2014, pp. 1–5.

[116] M. R. Aghamohammadi, A. Ghorbani, and S. Pourmohammad, "Enhancing transient and small signal stability in power systems using a posicast excitation controller," in *2008 43rd International Universities Power Engineering Conference*, 2008, pp. 1–5.

[117] L. Michel, X. Boucher, A. Cheriti, P. Sicard, and F. Sirois, "FPGA Implementation of an Optimal IGBT Gate Driver Based on Posicast Control," *IEEE Trans. Power Electron.*, vol. 28, no. 5, pp. 2569–2575, May 2013.

[118] Y. w. Li, B. Wu, N. Zargari, J. Wiseman, and D. Xu, "An Effective Method to Suppress Resonance in Input LC Filter of a PWM Current-Source Rectifier," in *2006 5th International Power Electronics and Motion Control Conference*, 2006, vol. 2, pp. 1–6.

[119] P. B. M. Oliveira and D. Vrančić, "Underdamped Second-Order Systems Overshoot Control," *IFAC Proc. Vol.*, vol. 45, no. 3, pp. 518–523, 2012.

[120] P. H. Meckl, "Control of Vibration in Mechanical Systems Using Shaped Reference Inputs," MIT Artificial Intelligence Laboratory, 1988.

[121] T. Singh and W. Singhose, "Input shaping/time delay control of

maneuvering flexible structures," in *Proceedings of the 2002 American Control Conference (IEEE Cat. No.CH37301)*, 2002, pp. 1717–1731 vol.3.

[122] J. Currie and D. I. Wilson, "OPTI: Lowering the Barrier Between Open Source Optimizers and the Industrial MATLAB User," in *Foundations of Computer-Aided Process Operations*, 2012.

[123] Huijun Wang, Dong-Hee Lee, Zhen-Guo Lee, and Jin-Woo Ahn, "Vibration Rejection Scheme of Servo Drive System with Adaptive Notch Filter," in *37th IEEE Power Electronics Specialists Conference*, 2006, pp. 1–6.

[124] C. Ahumada Sanhueza, A. Bristot, S. Kumar, N. Schneider, S. Garvey, and H. Morvan, "An Integrated System's Approach Towards Aero Engine Subsystems Design," 2016.

[125] F. M. Atay, "Magnetic saturation and steady-state analysis of electrical motors," *Appl. Math. Model.*, vol. 24, no. 11, pp. 827–842, 2000.

[126] ABB, *User's manual ACS150 drives*. ABB, 2016.

[127] Infineon, "AP16133 XE166 'Cookery-Book.'" pp. 1–130, 2008.

[128] W. Lu, X. Du, J. Ding, and X. Wang, "Modal parameter identification based on fast fourier transform and Hilbert Huang transform," in *2012 2nd International Conference on Consumer Electronics, Communications and Networks (CECNet)*, 2012, pp. 2703–2706.

[129] C. B. Smith and N. M. Wereley, "Transient analysis for damping identification in rotating composite beams with integral damping layers," *Smart Mater. Struct.*, vol. 5, no. 5, pp. 540–550, Oct. 1996.

[130] M. S. Arefeen, M. Ehsani, and A. Lipo, "Sensorless position measurement in synchronous reluctance motor," *IEEE Trans. Power Electron.*, vol. 9, no. 6, pp. 624–630, 1994.

[131] P. Phumiphak and C. Chat-uthai, "Induction motor speed measurement using motor current signature analysis technique," in *2009 International Conference on Electrical Machines and Systems*, 2009, pp. 1–5.

[132] D. Kumar and P. Radcliffe, “Sensorless speed measurement for brushed DC motors,” *IET Power Electron.*, vol. 8, no. 11, pp. 2223–2228, Nov. 2015.

[133] A.-C. Lee, C.-J. Fan, and G.-H. Chen, “Current Integral Method for Fine Commutation Tuning of Sensorless Brushless DC Motor,” *IEEE Trans. Power Electron.*, vol. 32, no. 12, pp. 9249–9266, Dec. 2017.

[134] H. Li, S. Zheng, and H. Ren, “Self-Correction of Commutation Point for High-Speed Sensorless BLDC Motor With Low Inductance and Nonideal Back EMF,” *IEEE Trans. Power Electron.*, vol. 32, no. 1, pp. 642–651, Jan. 2017.

[135] A. B. Ataji, Y. Miura, T. Ise, and H. Tanaka, “A Rotor-Current-Based Slip Angle Estimator for Grid-Connected Doubly Fed Induction Generator Requiring the Stator Inductance Only,” *IEEE Trans. Power Electron.*, vol. 32, no. 6, pp. 4827–4838, Jun. 2017.

[136] D. Liang, J. Li, and R. Qu, “Sensorless Control of Permanent Magnet Synchronous Machine Based on Second-Order Sliding-Mode Observer With Online Resistance Estimation,” *IEEE Trans. Ind. Appl.*, vol. 53, no. 4, pp. 3672–3682, Jul. 2017.

[137] A.-C. Lee, C.-J. Fan, and G.-H. Chen, “Current Integral Method for Fine Commutation Tuning of Sensorless Brushless DC Motor,” *IEEE Trans. Power Electron.*, vol. 32, no. 12, pp. 9249–9266, Dec. 2017.